國 立 交 通 大 學

光電工程研究所

博 士 論 文

成像與非成像光學系統之光學傳遞函數分析與應用

Optical transfer function and its applications to imaging and non-imaging optical systems

研 究 生：鄭竹明

指 導 教 授：陳志隆 教授

中 華 民 國 九十九 年 五 月

成像與非成像光學系統之光學傳遞函數分析與應用

Optical transfer function and its applications to imaging and non-imaging optical systems

研 究 生：鄭竹明　　Student：Chu-Ming Cheng

指導教授：陳志隆　　Advisor：Jyh-Long Chern

國 立 交 通 大 學

光 電 工 程 研 究 所

博 士 論 文

A Dissertation

Submitted to Institute of Electro-Optical Engineering
College of Electrical and Computer Engineering
National Chiao Tung University
in partial Fulfillment of the Requirements
for the Degree of
Doctor of Philosophy
in
Electro-Optical Engineering
May 2010
Hsinchu, Taiwan, Republic of China

中華民國 九十九 年 五 月

成像與非成像光學系統之
光學傳遞函數分析與應用

博士研究生 ： 鄭竹明　　指導教授 ： 陳志隆 教授

國立交通大學　　光電工程研究所

摘　　要

對於當今的光學儀器與光電消費性產品而言，除了被要求微型化系統設計之外，追求更優質的影像品質和高光學效率以及細緻的解析度畫質亦是未來光電產品的重要趨勢與主流。在成像光學系統的領域中，全幅對焦技術(EDOF, extending the depth of focus) 已然成為一個非常重要的光學設計議題。本論文利用光學傳遞函數 (OTF, optical transfer function) 和照明分布函數，開發出一套解析和半解析式數學模型，並將此方法應用於非同調成像光學系統之成像與非成像光學品質的評估與分析。由於照明光場會改變待測物的反射光強度分佈，因此我們不能再假設一成像系統中，待測物的光學傳遞函數值為一。所以，我們利用光闌方程式 (pupil function) 中的振幅穿透方程式 (一個描述非成像光學特性的項) 和波像差方程式(一個描述成像光學特性的項)，深入地探討光學傳遞函數和照明光分布之間的相互關係。本論文的學術貢獻之一，是在一光學系統的光學傳遞函數計算中，加入一”非成像光學”的有效因子，進而能夠完整地分析與評估光學系統的成像品質。我們也進一步地提出一種新的全幅對焦光學技術，並驗證於非同調成像光學系統之中。此技術利用在非成像系統中，設計一個空間光學調變器來產生一個結構光束(structured light)，如數位微鏡片元件(DMD, digital micromirror device)或是發光二極體陣列裝置(LED array module)，以提供一動態可程式化變形光闌 (a dynamically programmable shaped pupil)，並將此變形光闌投影在成像光學系統的孔徑位置。我們使用自行開發的光學傳遞函數之半解析式數學模型，驗證此新技術可以有效地補償光學像差，如失焦、球差和彗差等，同時亦可提升光

學系統的成像解析力。我們的研究是連結和整合成像與非成像光學系統的特性，開發出一新全幅對焦光學技術，應用一嵌入式照明調變器，達到提升傳統非同調光學系統的成像光學品質以及擴展其光學系統的對焦深度，並將此技術應用於光導管、攝影機、顯微鏡和投影機等光學系統中。

Optical transfer function and its applications to imaging and non-imaging optical systems

Doctoral Student：Chu-Ming Cheng　　Advisor：Dr. Jyh-Long Chern

Institute of Electro-Optical Engineering
National Chiao Tung University

Abstract

Today's optical instruments and electro-optical consumer products demand high imaging quality, optical efficiency and high resolution with the volume of the machine, nevertheless, being compact. At the same time, extending the depth of focus (EDOF) in an imaging system has been a long-standing issue in optical designs. This thesis develop either an analytical or a semi-analytical model by the use of optical transfer function (OTF) and illumination formations on the study of imaging and non-imaging qualities in the incoherent imaging system. Since the illumination light could vary the intensity distribution of the reflective light from an object, we could no longer assume the OTF of the object equal to unity in an imaging system. Hence, we make the in-depth investigation into the relationship between OTF and the illumination light distribution by calculating the OTF using the pupil function with the amplitude transmittance function which is the term given to the characteristic of a non-imaging system, and the wave aberration function which is the term given to the characteristic of an imaging system. One of main contributions of this thesis is to implement and demonstrate the effective factor of the non-imaging system (i.e., illumination light) in OTF calculation for assessing and specifying the performance of an imaging system. Then, a new approach for EDOF in an incoherent imaging system has been demonstrated. It provides a programmable shaped pupil using structured light which is generated by a non-imaging system with a spatial light modulator such as the digital micromirror device (DMD) or the light-emitting-diode (LED)-array module. The semi-analytical results using the OTF indicate that the limiting resolution of an

imaging system with a specific defocus coefficient, and the specific coefficients for spherical aberration and coma aberration can be improved significantly with a binary shaped pupil. The proposed structured light on aperture stop from the non-imaging system can offer a dynamically programmable approach for aberration compensation in an incoherent imaging system. Our proposed research provides the connection between non-imaging and imaging systems for extending the depth of focus and further enhancing the image quality in the conventionally incoherent imaging systems for light pipe, camera, microscope and projector with embedded illumination modulator.

誌 謝

投入光電產品的研發和光學工程的研究已有 12 多年的時間，自己很榮幸擁有這麼好的因緣際會，能夠在光電科學領域中，持續地從事技術的創新和學術的研究。首先，非常感謝交通大學光電工程研究所，能夠提供這麼優質地學習與研究的環境，以及特別地感謝指導教授陳志隆教授多年來的指導，其淵博的學識和嚴謹的研究精神，給予學生許多的教導與啟發。同時，感謝博士論文口試委員黃中垚教授、蘇德欽教授、趙于飛教授、施宙聰教授以及何明宗教授，提供學生許多寶貴的意見；亦感謝鄭伊凱同學、鄭介任同學和曹兆璽同學平時的幫忙與鼓勵。

此外，感謝揚明光學股份有限公司，提供學生在職進修的機會，以及由衷地感謝徐誌鴻總經理長期以來對後輩的提攜與教導；亦感謝林宗彥副總、邱賢琪副總、謝啟堂協理、鍾博任協理、張維勝協理、廖洽成協理、劉永光協理和康尹豪資深研究員等老長官們，長年來對我的勉勵與指導；同時，我更要特別地謝謝親密的工作夥伴林維賜、陳時偉、陳皇銘、蔡志賢、范萬昌、林清民、張美雲、李育宗、許志祿、陳錦怡、吳怡慧、陳孟萱、楊勝捷、黃習能和其他許多同事們相互的激勵，使得這麼多年來的工作充滿了衝勁與喜悅。

最後，謹將此論文獻給最親愛的父母、兄長以及最可愛的老婆和孩子們，謝謝他們平日來給予我最溫馨地關懷與支持。我會繼續努力地在光電工程領域上發明與創新，期許自己能夠為人類、科學與社會，創造出更多實質的福祉與貢獻。

Table of Contents

Figure Captions

Chapter 1

Introduction

1.1 Background and motivation

The current applications of electro-optical instruments and consumer products demand high imaging quality, optical efficiency and high resolution with the volume of the machine, nevertheless, being compact, for computer graphics involving digitized photography. In general two techniques were developed for enhancing the image quality. One is extending the depth of focus (EDOF) in an imaging system and the other is the high dynamic range (HDR) in the digital image processing. EDOF in an imaging system has been a long-standing issue in optical design. Enhancing the quality of an image can be achieved by the pupil function as well as by its amplitude transmittance and phase variation [1,2]. Non-uniform amplitude transmission filters can be employed to vary the response of an optical imaging system, for instance, to increase the focal depth and to decrease the influence of spherical aberration. Earlier EDOF investigations and experiments were carried out n annular apodizers [3,4], the radial Walsh filter [5], non-uniform shaped apertures [6,7] and wave-front coding [8,9] in imaging systems, where the nature of light is *incoherent*. High dynamic range (HDR) image processing produces a greater dynamic range of luminances between bright and dark areas of a scene by integrating a set of photographs which are taken with a range of exposures [10]. One of the earlier HDR investigations in digital photography was to combine the strengths of continuous flash/no-flash image pairs for enhancing the image's contrast and the sense of depth [11,12]. However, none of

those are programmable for amplitude transmission at the aperture stop using the structured light generated by a non-imaging system, such as illumination lighting and flash light. From the point of view of potential applications as well as from a purely academic interest perspective, it is worthwhile to explore the possibility of how to realize a dynamically programmable shaped pupil for incoherent imaging systems such as photography, projector and microscopy.

A light pipe is a commonly optical device that manages light properties in illumination systems, especially where extremely uniform illuminations with specific illuminance distributions are required [13]. Typical applications are the illuminations in the projection display [14], lithography [15], endoscopes [16], and in optical waveguides [17]. In those applications, the illumination system is mostly a combination of a light pipe and the corresponding imaging system with a projection lens. A light pipe is made with parallel reflective sides, either as a cylinder or with a square or rectangular cross section. The light source can be located on one end of the light pipe, and the other end is then the uniformly illuminated plane [18]. The uniform illumination on the exit end of the light pipe is determined by the ratio between the length to the diameter and also the cross-sectional shape of the light pipe [19]. The multiple reflections of the light source through the pipe can produce a spatially checkerboard-array-shaped light distribution at the aperture stop of the illumination system which is then projected to the aperture stop of the corresponding imaging system. Hence, we need to determine the pupil function with a specific shaped aperture generated by the light pipe in the optical transfer function (OTF) for the image evaluation in the optical system.

In the field of non-imaging optics for the illumination, the light emitting diode (LED) technology is widely applied in vehicles, architecture, signal lighting, backlighting and in projection microdisplays [20]. Most of these applications require

the shaping of a uniform beam illuminance profile, managing color quality and saving power consumption while maintaining high luminous efficiency in the illumination systems. There are two kinds of approaches to generate white light with LEDs. One is the phosphor-converted white LED, which provides a compact integrated package but has a relatively lower luminous efficiency. The other is the mixed-color LED, which provides more light throughput compared to a single phosphor-converted white LED with the same operating power. In practice, however, there are several technical challenges to creating a mixed-color LED, such as white light homogenizing with the acceptably lowest spatial variation, color mixing and color balancing with acceptably lowest chromatic variation. Rectangular light pipes are commonly optical elements that manage light properties in illumination systems, especially where extremely uniform illuminations with specific illuminance distributions are required. The light source can be located on one end of the light pipe and the other end is then the uniformly illuminated plane. The shape of the light pipe can modify the original characteristics of the spatial distribution of the light source but not the angular distribution. The uniform illumination on the exit end of the light pipe is determined by the ratio of the length to the cross-sectional dimension of the light pipe. In the literature, the mention of the properties of light pipes is mostly concentrated on transmittance, flux analysis and irradiance formation for the single light source. Although Derlofske and Hough developed a flux confinement diagram model to discuss the flux propagation of square light pipes and angular distribution [21], and Cheng and Chern developed a semi-analytical method to investigate the formation of irradiance distribution [19], to the best of our knowledge few articles have investigated the formation of illuminance and the color-differences in mixed-color light sources using an analytical method.

Projection display technology is widely applied in the large-screen display for business projector and rear-projection TV, mostly based on three differently light valves of transmissive LCDs, Digital Micromirror Device™ (DMD™) and liquid crystal on silicon (LCoS) [22]. In the field of optics, the technologies involved are being applied to very compact system with the higher image performance. Consequently, the designs for high optical collection efficiency, higher resolution image, smaller volume optical systems etc. are required. Examples are an off-axis wide-angle projection lens design with anamorphic mirrors [23], a TIR-prism optical system [14,24], and the hybrid projection screen [25]. The optical design with the appropriate *f*-number is the key to the illumination system and the *f*-number value is often constrained and determined by the light-valve's architecture in the projection display. Conventionally, single *f*-number and symmetric illumination pupil are generally utilized in optical system. However, these do limit optical collection efficiency and imaging quality.

1.2 Objectives of this dissertation study

Optics can broadly be classified into two fields of imaging and non-imaging optics. Imaging optics has been developed around for 300 years and is the optics of thick / thin lenses, mirrors, parabolas, ellipses and Fresnel lenses. The field of non-imaging optics was begun formulating the principles, theory and mathematics by Roland Winston until the 1970s [26]. One of its first applications was to the field of solar energy concentration for both photovoltaic and solar thermal system. Subsequently, applications such as fiber-optics couplers, backlights for liquid crystal displays, infrared countermeasures for heat seeking missiles, sensor for high energy particle physics, etc. all came to benefit from the increased optical efficiency and compactness that non-imaging optics could supply. In our experiences, so far the

knowledge of beam shaping technology, possibilities and limitations are thus applied into the illumination system in the field of non-imaging only. Therefore, the new and interesting subject in optics will be how to incorporate the already existing imaging optical technology into new optical systems. In this thesis, we would like to develop either an analytical or a semi-analytical model by the use of optical transfer function and illumination formation for the connection between the imaging and the non-imaging, and put emphasis on the study of imaging and non-imaging qualities in the severally specific optical systems, such as light pipe, photography, projector and microscopy.

1.3 Imaging optical system and its characterization

An imaging system is an optical system capable of being used for image-formation from an object field to a desired image field as shown in Fig. 1-1 (a). In the imaging system, all rays originating in one point of an object are mapped to be focused in one point of the image. The effective focal length and the diameter of the aperture (i.e., *f*-number, *f* /#) are common criteria for comparison among optical systems, such as telescopes, microscope, camera lens, endoscope, lithography, and projector and so on. The effective focal length gives the determination of the magnification and the *f* /# determines how much light intensity is able to be received in the optical system.

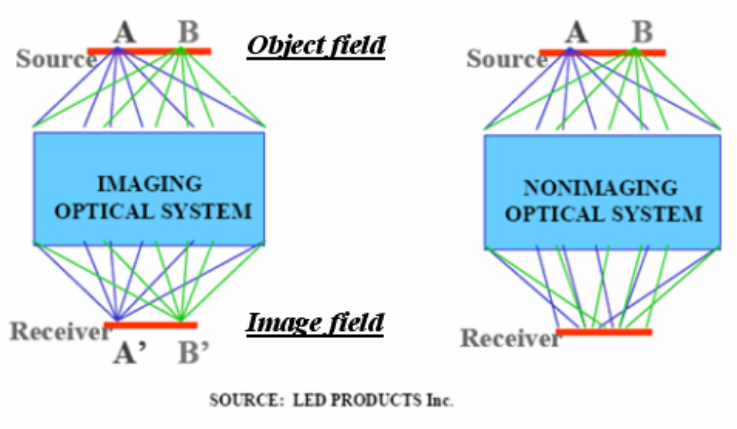

(a) (b)

Figure 1-1 Comparison of imaging and non-imaging optical systems

1.4 Non-imaging optical system and its characterization

As illustrated in Fig. 1-1 (b), in non-imaging systems, all rays of an extended source are directed to a target surface, i.e., a receiver. The distribution of the rays at the receiver and the collection efficiency through the system are the primary concerns rather than that points do map to points. Typical variables to be designed at the target include the total radiant flux, the angular distribution, and the spatial distribution of optical radiation. These variables on the target receiver are optimized while simultaneously considering the collection efficiency of the optical system at the source. That is an issue about the relationship between radiance (or luminance) and irradiance (or illuminance). Non-imaging optics is common applications where imaging formation is not included but where the efficient transfer and collection of light radiation is. Examples include many areas of illumination engineering in general lightings, automotive headlamps, solar concentrators, LCD backlights, fiber illumination devices and projection display systems, and so on.

1.5 Organization of the dissertation

The thesis is organized as follows. In Chapter 2, we describe the general

formations for imaging system and non-imaging system including the pupil function, optical transfer function for specific shaped pupil, illumination formation, color-difference function and Ètendue function for an asymmetric pupil. In Chapter 3, we investigate optical transfer functions for the specific-shaped apertures generated by illumination with a rectangular light pipe. In Chapter 4, a programmable apodizer for imaging quality enhancement in incoherent imaging system is developed and evaluated. In Chapter 5, we introduce a new approach for extending the depth of focus and improving the image quality with structured light in a conventional imaging system, such as photography, projector and microscopy, with the defocused, spherical and coma aberrations. In Chapter 6, we develop an analytical method of illuminance formation and color-difference for mixed-color LEDs in a rectangular light pipe. In Chapter 7, a dual-*f*-number illumination system and its application to DMD™ projection display is investigated. Finally we draw our conclusions and future works in Chapter 8.

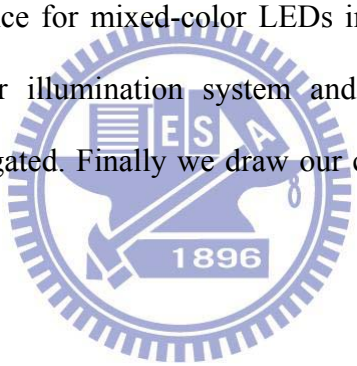

Chapter 2

General formalism for imaging and non-imaging optical systems

2.1 Optical systems and their general structures: light pipes, camera, projector and microscopy

The analysis of an optical system requires either analytical or numerical computation to determine the image quality on the image plane, which is taken by light rays as they come from an object and pass through the optical system. The general optical system with an imaging subsystem and a non-imaging subsystem is as schematically diagrammed in Fig. 2-1. The non-imaging system provides a desired illumination distribution and high optical collection efficiency in an incoherent imaging system. The function of the condenser is to project the light source directly into the aperture stop of the imaging lenses so that the lens aperture has the same brightness as the light source. The function of the imaging lens system is to image a bright and uniform illuminated object on the image plane. The platform of our investigations for the conventionally well-known optical systems will contain light pipe, photography, projector and microscopy as shown in Fig. 2-2, Fig. 2-3, Fig. 2-4 and Fig 2-5, respectively.

In this chapter we will introduce the optical tools for image performance evaluation in the general optical system. The subjects contain the pupil function and the optical transfer functions for an incoherent imaging system, and the illumination formation, color-difference function and Ètendue function for a non-imaging system.

In additional discussions of various aspect of the subjects, the reader may want to consult any of the following references: about Fourier optics [1] and wave aberration [2] of imaging optics, about non-imaging optics [26], about radiometry and photometry [27] and about color science [28].

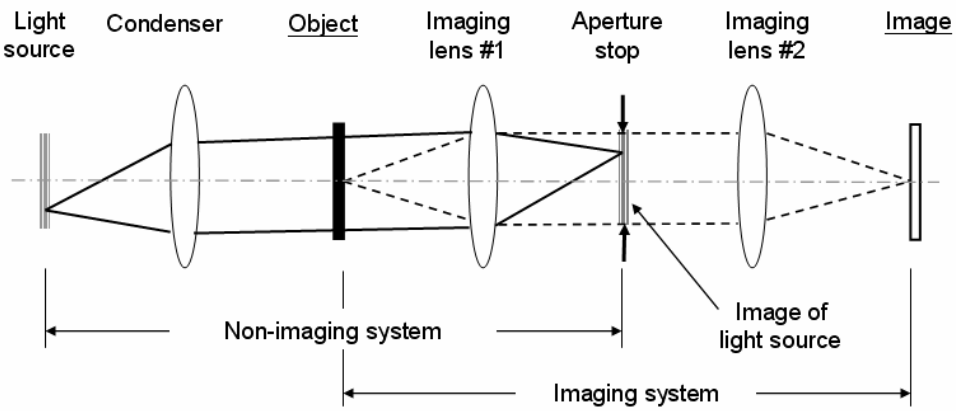

Figure 2-1 General schematic diagram of the optical system with an imaging subsystem and a non-imaging subsystem

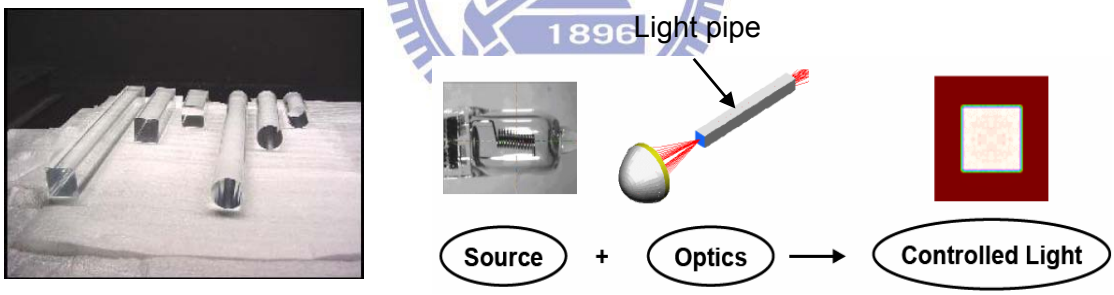

(a) (b)

Figure 2-2 (a) The photograph of the light pipe with circle and rectangular shapes [29] and (b) the illustration of an illumination system with a light source and a light pipe for a uniform light output [30]. Illumination system provides a desired light distribution that may have little or no relationship to light distribution from the light source. Figure (b) shows an illumination system with a filament in a reflector which can provides a uniform light distribution at the end of a square light pipe.

(a)

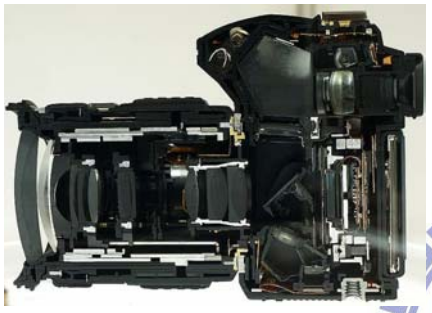

(b)

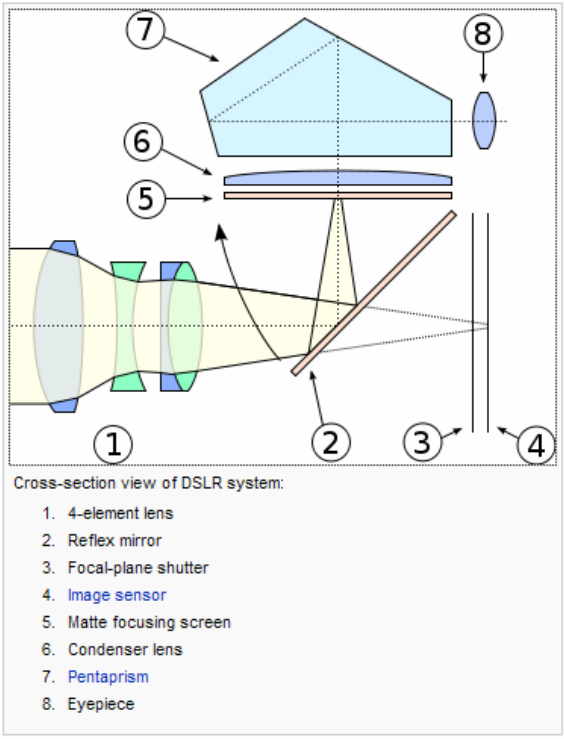

(c)

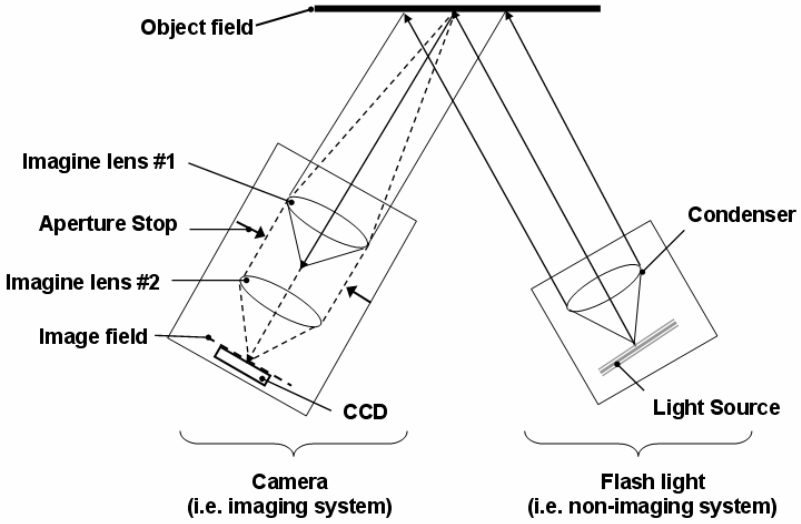

(d)

Figure 2-3 (a) The photograph of a DSLR camera with flash light [31], (b) cutaway of an Olympus E-30 DSLR camera [32], (c) cross-section view and introduction of a DSLR camera [32] and (d) the schematic diagram of a photographic system with a camera, an imaging system, and a flash light, a non-imaging system.

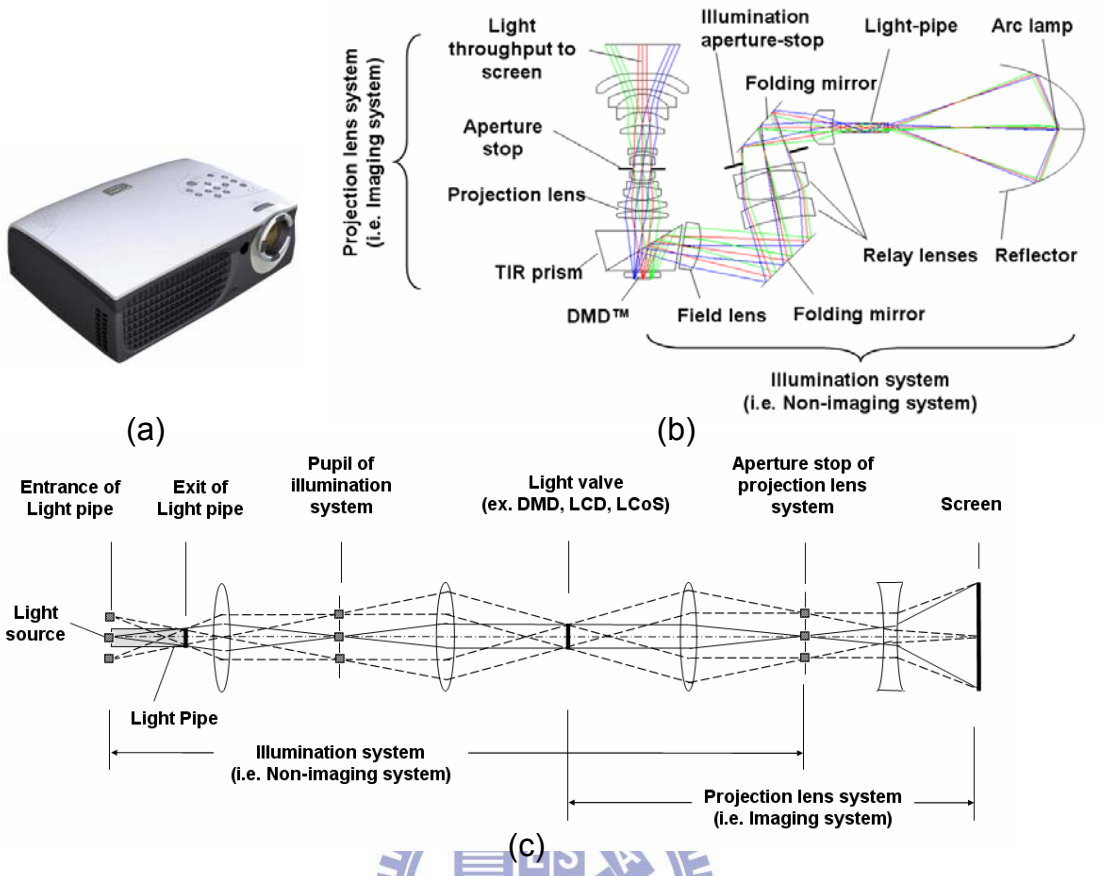

Figure 2-4 (a) The photograph of a projector- Optoma EP755 model [33], (b) cross-section view and introduction of a DLP projector, and (c) the schematic diagram of a projector system with a projection lens, an imaging system, and a light pipe illumination, a non-imaging system.

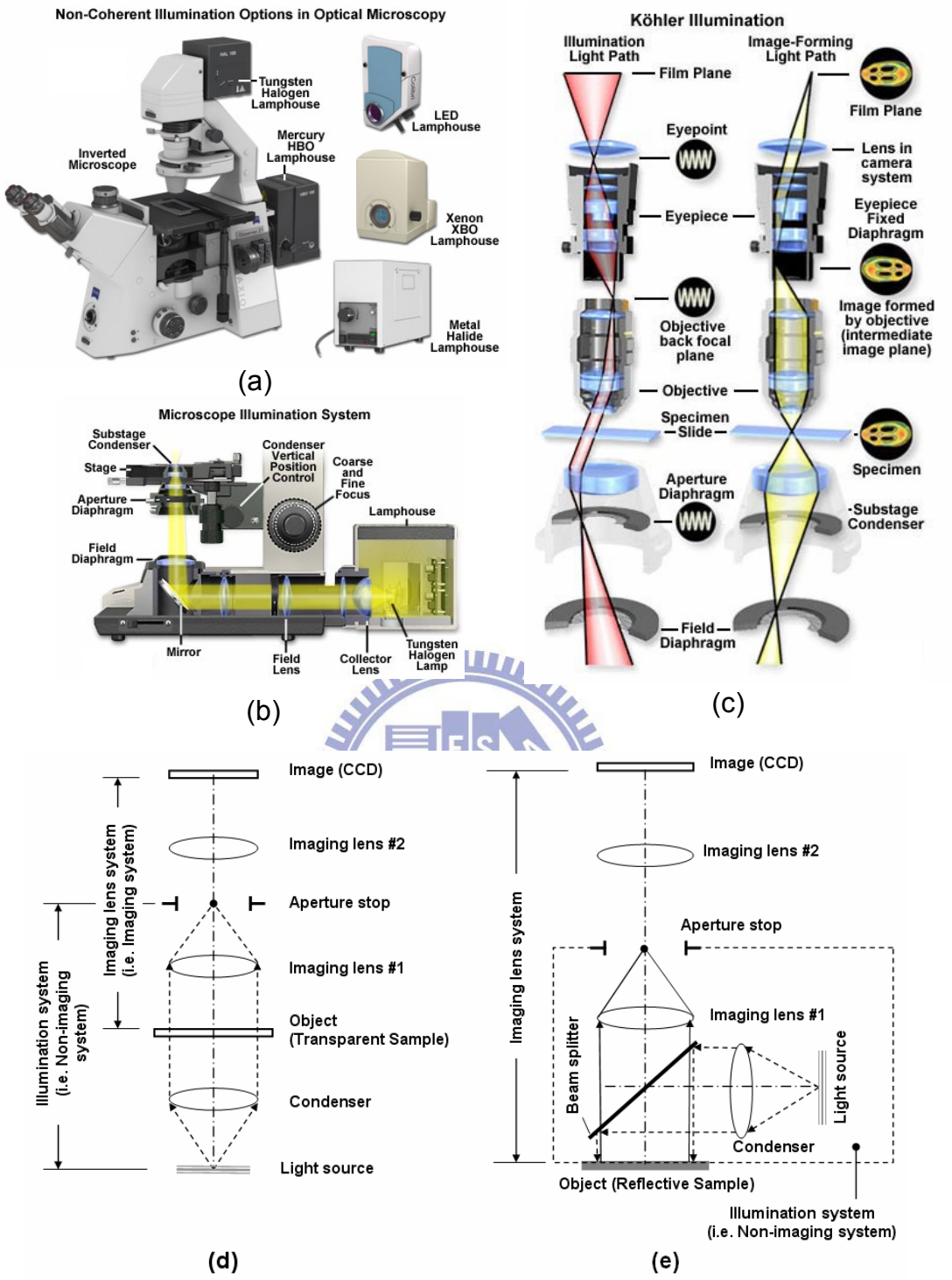

Figure 2-5 (a) The photograph of an optical microscope [34], (b) cross-section view and introduction of a microscopic illumination system [35], (c) cross-section view and introduction of the illumination light path and image-forming light path in microscope [35]. The schematic diagrams of a microscopic system with an imaging lens, an imaging system, and an illumination, a non-imaging system are for (d) a transparent sample and (e) a reflective sample.

2.2 Pupil function formalism

When an imaging system is diffraction limited, the point spread function (PSF) centering on the imaging point is the Fraunhofer diffraction pattern of the exit pupil. When there is a wavefront error in an imaging system, the exit pupil is illuminated by a perfect spherical wave, but that a phase-shifting plate exists in the aperture stop, thus deforming the wavefront passing the pupil. If the phase error at the point (x, y) in the exit pupil is represented by $kW(x, y)$, where $k=2\pi/\lambda$ and λ is the wavelength of the light. $W(x, y)$ is the aberration function of the effective path-length error accumulated by that ray as it passes from the Gaussian reference sphere to the actual wavefront, the latter wavefront also being defined to intercept the optical axis in the exit pupil as illustrated in Fig. 2-6. Then the complex amplitude transmittance $f(x, y)$ of the imaginary phase-shifting phase is given by

$$f(x,y)=T'(x,y)\exp\left[ikW(x,y)\right] \tag{2-1}$$

The complex function $f(x, y)$ is the generalized pupil function [1]. $T'(x,y)$ represents the amplitude transmittance over the normalized pupil coordinate.

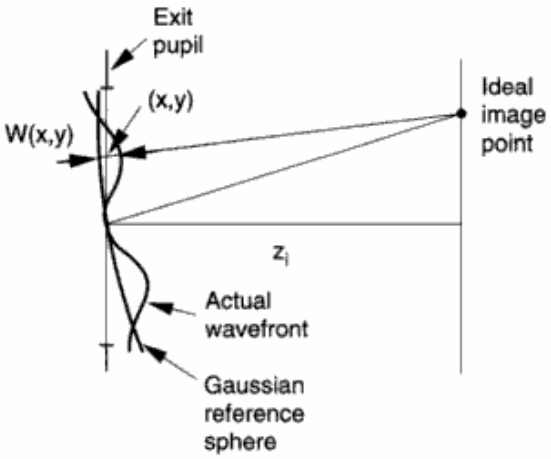

Figure 2-6 Illustration for defining the aberration function. [1]

The pupil function of an optical system with a circular symmetrical aperture is further given by [7]

$$f(x,y)=T'(x,y)\exp\left[ik\sum_{\alpha}\sum_{\beta}\omega_{\alpha\beta}\left(x^2+y^2\right)^{\frac{\alpha-\beta}{2}}y^{\beta} \right] \qquad x^2+y^2 \le 1$$
$$= 0 \qquad x^2+y^2 > 1 \tag{2-2}$$

where the term of the summation is the wave aberrations with the coefficients $\omega_{\alpha\beta}$ in the polynomial. For example, ω_{20} is the wave aberration of the defocus coefficient; ω_{40} denotes the coefficient for spherical aberration, and ω_{31} denotes the coefficient for coma aberration. (x ,y) are the normalized Cartesian coordinates, and $k = 2\pi/\lambda$, where λ is the wavelength of the light. Function $T'(x,y)$ in Eq. (2-1) represents the amplitude transmittance over the normalized pupil coordinate that is scaled and normalized to make the outer periphery the unit circle, $x^2 + y^2 \le 1$.

2.3 Optical transfer function

The optical transfer function (OTF) represents the ratio of image contrast to specimen contrast when plotted as a function of spatial frequency, taking into account the phase shift between positions occupied by the actual and ideal image [36]. The OTF describes either the spatial or angular variation as a function of either spatial or angular frequency. When the image is projected onto a flat plane, such as photographic film or a solid state detector, spatial frequency is the preferred domain, but when the image is referred to the lens alone, angular frequency is preferred. In general terms, the optical transfer function can be described as:

$$OTF(f_x,f_y)=MTF(f_x,f_y)\cdot PTF(f_x,f_y) \tag{2-3}$$

where

$$MTF\left(f_x, f_y\right) = \left|OTF\left(f_x, f_y\right)\right| \tag{2-4}$$

$$PTF\left(f_x, f_y\right) = e^{-i2\cdot\pi\cdot\lambda\left(f_x, f_y\right)} \tag{2-5}$$

and (f_x, f_y) are spatial frequency in the x-plane and y-plane, respectively. The OTF accounts for aberration. Its magnitude is known as the Modulation Transfer Function (MTF) and its phase is known as the Phase Transfer Function (PTF). Fig 2-7 shows the typical form the MTF and PTF curves of an imaging system can take and also show the most usual way in which these two parameters are plotted.

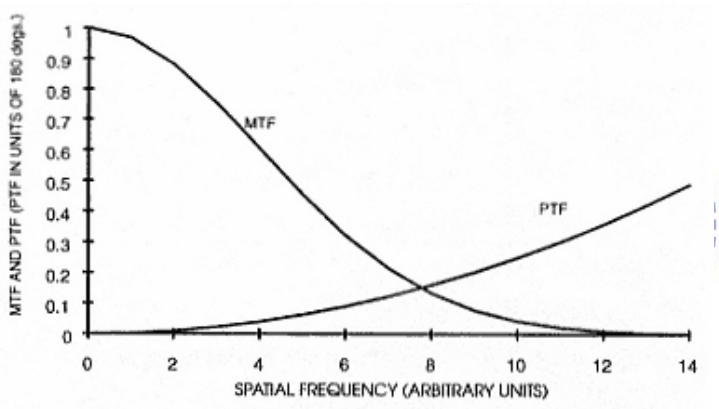

Figure 2-7 Typical plot of MTF and PTF versus spatial frequency. [36]

The OTF is derived from the autocorrelation of the pupil function by using the Hopkins canonical coordinate [37] and is given by

$$\tau(s) = \frac{\int_{-\infty}^{\infty}\int_{-\infty}^{\infty} f\left(x + s/2\,,\, y\right) f^{*}\left(x - s/2\,,\, y\right) dx\, dy}{\int_{-\infty}^{\infty}\int_{-\infty}^{\infty} f\left(x\,,\, y\right) f^{*}\left(x\,,\, y\right) dx\, dy} \tag{2-6}$$

where $f(x, y)$ is the pupil function shown in Eq. (2-2) , $f^{*}(x, y)$ is the complex conjugate of $f(x, y)$, and s is defined as the spatial frequency $s \equiv 2F\lambda N$. Here F is the f-number of the imaging lens system, λ is the wavelength, and N is the number of cycles per unit length in the image plane. The value of F is equal to the effective

focal length divided by D, where D is the diameter of the effective aperture stop and the effective focal length is determined by the optical magnification of the imaging lens.

2.4 Illumination formation and color difference

The equation of the luminous intensity of the light source with Lambertian characteristics is given as

$$J_\Omega = J(\theta) = J_0 \cos\theta \ , \quad -90^\circ \le \theta \le 90^\circ \tag{2-7}$$

where J_Ω is the luminous intensity (lumen sr^{-1}) of a small incremental area of the source in a direction at an angle θ from normal to the surface, and J_0 is the luminous intensity of the incremental area in the direction of normal. Thus, we can derive the illuminance distribution radiated from the Lambertian light source (i.e. LED) on an irradiated surface.

With reference to Fig. 2-8, we assume that the illuminance position on a surface is (x, y), length R is the distance from the light source to the incremental area, length L is the distance from the light source to the surface, and angle θ is the angle from normal to the incremental area.

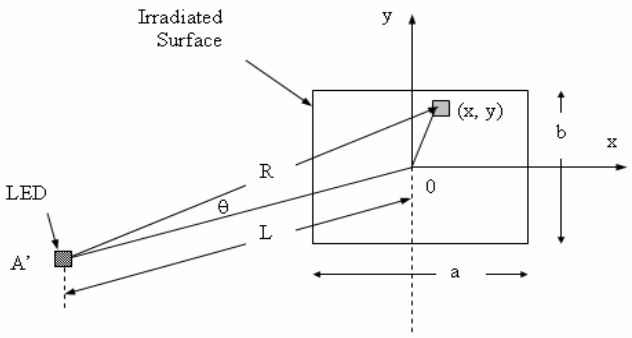

Figure 2-8 Illustration of an LED light source radiating into a surface.

The angle θ can be substituted by L, x, y and R, and is given by

$$\cos\theta = \frac{L}{\sqrt{L^2 + \left(x^2 + y^2\right)}} = \frac{L}{R} \tag{2-8}$$

The illuminance distribution on the irradiated surface is a function of $\cos^3\theta$, which can be expressed as a function of J_0, L, x and y according to Eqs. (2-7) and (2-8) as given by

$$H(x,y) = J(\theta)\frac{\cos^3\theta}{L^2} = J_0 \times \frac{L^2}{\left(L^2 + x^2 + y^2\right)^2} \tag{2-9}$$

To identify the uniformity on an irradiated surface, we introduce the ANSI light uniformity defined by [38]

$$Ur+ = \left(\frac{Maximum\ \left[H(x_l, y_l)\right]_{l=10,11,12,13}}{Average\ \left[H(x_l, y_l)\right]_{l=1,2,..9}} - 1\right) \times 100\% \tag{2-10}$$

$$Ur- = \left(\frac{Minimum\ \left[H(x_l, y_l)\right]_{l=10,11,12,13}}{Average\ \left[H(x_l, y_l)\right]_{l=1,2,..9}} - 1\right) \times 100\% \tag{2-11}$$

where the maximum deviation Ur+ or Ur- from the average of nine measurements is specified as a percentage of the average light output (9 measurement locations *l= 1, 2, 3…9*) using the measurement described in Fig. 2-9, and at the four corners (i.e. *l= 10, 11, 12, 13*) on the surface.

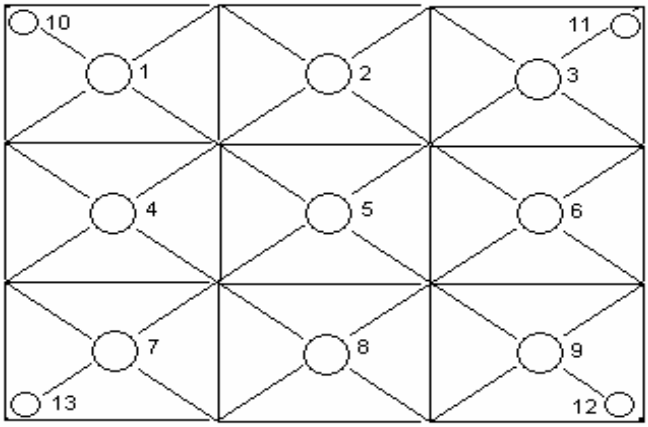

Figure 2-9 Measurement locations at the center of nine equal rectangles of a 100% exit plane on irradiant surface. The four corner points 10, 11, 12 and 13 are located at 10% of the distance from the corner itself to the center of the measurement location 5 [38].

To identify the color uniformity on an irradiated plane, we introduce the ANSI color uniformity defined by [28]

$$\Delta u'v' = \left[\left(u_1' - u_0' \right)^2 + \left(v_1' - v_0' \right)^2 \right]^{\frac{1}{2}} \tag{2-12}$$

where u_0' and v_0' are the average chromatic values of the nine measurements, and u_1' and v_1' are the value with the maximum deviation of the 13 measurements from the average chromatic values u_0' and v_0' using the measurement described in Fig. 2-9.

Finally we can derive the total color difference between two color stimuli, each given in the terms of L^*, a^*, b^*, in CIE 1976 ($L^*a^*b^*$) –space by [28]

$$\Delta E_{ab}^*(x,y) = 200\left[\left(\Delta L^* \right)^2 + \left(\Delta a^* \right)^2 + \left(\Delta b^* \right)^2 \right]^{\frac{1}{2}} \tag{2-13}$$

where ΔL^*, Δa^* and Δb^* are the values of the differences in L^*, a^* and b^* between two color stimuli, respectively. The quantities L^*, a^* and b^* are defined by

$$\begin{aligned} L^* &= 116\left(\frac{Y_w}{Y_n} \right)^{\frac{1}{3}} - 16 \\ a^* &= 500\left[\left(\frac{X_w}{X_n} \right)^{\frac{1}{3}} - \left(\frac{Y_w}{Y_n} \right)^{\frac{1}{3}} \right] \\ b^* &= 200\left[\left(\frac{Y_w}{Y_n} \right)^{\frac{1}{3}} - \left(\frac{Z_w}{Z_n} \right)^{\frac{1}{3}} \right]^{\frac{1}{2}} \end{aligned} \tag{2-14}$$

where $X_w = X_w(x,y)$, $Y_w = Y_w(x,y)$ and $Z_w = Z_w(x,y)$ are the tristimulus-values distribution and X_n, Y_n, Z_n are the tristimulus-values of the nominally white object-color stimuli given by the spectral radiant power of one of the CIE standard illuminants, for example, D65, reflected into the observer's eyes by the perfectly reflecting diffuser.

2.5 Ètendue function for an asymmetric pupil

Ètendue is an optical invariant of a light beam relative to the beam divergence and cross-section area in the illumination system [26]. It allows us to estimate the collection efficiency of the optical system. In this section, we develop the Ètendue model of the elliptic-shaped illumination-pupil system.

The formal definition of Ètendue is given by

$$E = \int_A dA \int_{\Omega(\theta,\phi)} \cos\theta d\Omega \,, \tag{2-15}$$

where E is the Ètendue, A is the cross-section area of light flux and $\Omega(\theta,\phi)$ is the solid angle of the beam divergence in the angular coordinate system [26,39]. θ is the half angles of the illumination cone and ϕ is the polar angle from 0 to 2π. In the elliptic-shaped illumination-pupil system, θ is a function of ϕ , so the Ètendue equation is given by

$$E = \int_A dA \int_0^{2\pi} \int_0^{\theta(\phi)} \sin\theta \cos\theta d\theta d\phi = \frac{A}{2} \int_0^{2\pi} \sin^2\theta(\phi) d\phi \tag{2-16}$$

The relationship between the half angle of the illumination cone and *f*-number is given by

$$f/\# = \frac{f}{D} = \frac{1}{2NA} = \frac{1}{2\sin\theta}, \tag{2-17}$$

where D is the diameter of aperture-stop, NA is the numerical aperture, and f is the effective focal length. In an elliptic-shaped illumination-pupil system, the illumination-pupil shape is elliptic and is expressed as the function of the polar angle ϕ,

$$D = 2r = \frac{2b}{\sqrt{1-\varepsilon^2\cos^2\phi}} \tag{2-18}$$

where r is the radius of the ellipse of the elliptic-shaped illumination-pupil; $\varepsilon = \frac{\sqrt{a^2 - b^2}}{a}$ is the numerical eccentricity of the ellipse; a and b are the major and minor semi-axis of the ellipse of the elliptic-shaped illumination-pupil and also described as the radii of aperture-stops in the tangential and sagittal axes, respectively. By putting Eqs. (2-17) and (2-18) into Eq. (2-16), the Ètendue expression of the elliptic-shaped illumination-pupil system is given by

$$E = \frac{A}{2}\int_0^{2\pi}\left(\frac{b}{f\sqrt{1-\varepsilon^2\cos^2\phi}}\right)^2 d\phi = \left(\frac{A}{2}\right)\left(\frac{b}{f}\right)^2 \int_0^{2\pi}\frac{1}{1-\varepsilon^2\cos^2\phi}\,d\phi \quad (2\text{-}19)$$

The integration about ϕ can be carried out by resolving Eq. (2-19) into the terms [40],

$$\int \frac{1}{1-\varepsilon^2\cos^2\phi}\,d\phi = \frac{1}{\sqrt{1-\varepsilon^2}}\tan^{-1}\left(\frac{\tan\phi}{\sqrt{1-\varepsilon^2}}\right), \qquad (1>\varepsilon^2) \qquad (2\text{-}20)$$

Then, the integral term in Eq. (2-20) can be deduced by Mathematica® software [41] as

$$\int_0^{2\pi}\frac{1}{1-\varepsilon^2\cos^2\phi}\,d\phi = \pi\left[\frac{(1+\varepsilon)\sqrt{\frac{1-\varepsilon}{1+\varepsilon}}+(1-\varepsilon)\sqrt{\frac{1+\varepsilon}{1-\varepsilon}}}{(1-\varepsilon^2)}\right] = \frac{2\pi\sqrt{1-\varepsilon^2}}{(1-\varepsilon^2)}$$

$$= \frac{2\pi}{\sqrt{1-\left(\frac{a^2-b^2}{a^2}\right)}} = 2\pi\left(\frac{a}{b}\right) \qquad (2\text{-}21)$$

By putting Eq. (2-21) into Eq. (2-19), the Ètendue formula of the elliptic-shaped illumination-pupil system is given by

$$E = \left(\frac{A}{2}\right)\left(\frac{b}{f}\right)^2 \times 2\pi\left(\frac{a}{b}\right) = \frac{\pi A}{f^2}(ab) = \frac{\pi A}{4\left(\frac{f}{2a}\right)\left(\frac{f}{2b}\right)} = \frac{\pi A}{4\,(f/\#)_T\,(f/\#)_S} \quad (2\text{-}22)$$

Where $(f/\#)_T = \frac{f}{2a}$ and $(f/\#)_S = \frac{f}{2b}$ are the *f*-numbers of the elliptic-shaped illumination-pupil in the tangential and sagittal axes, respectively. As an illustration, the variation of the Ètendue with the tangential *f*-numbers and the sagittal *f*-numbers is calculated if we assume the cross-section area of light flux A is unit and shown in Fig. 2-2.

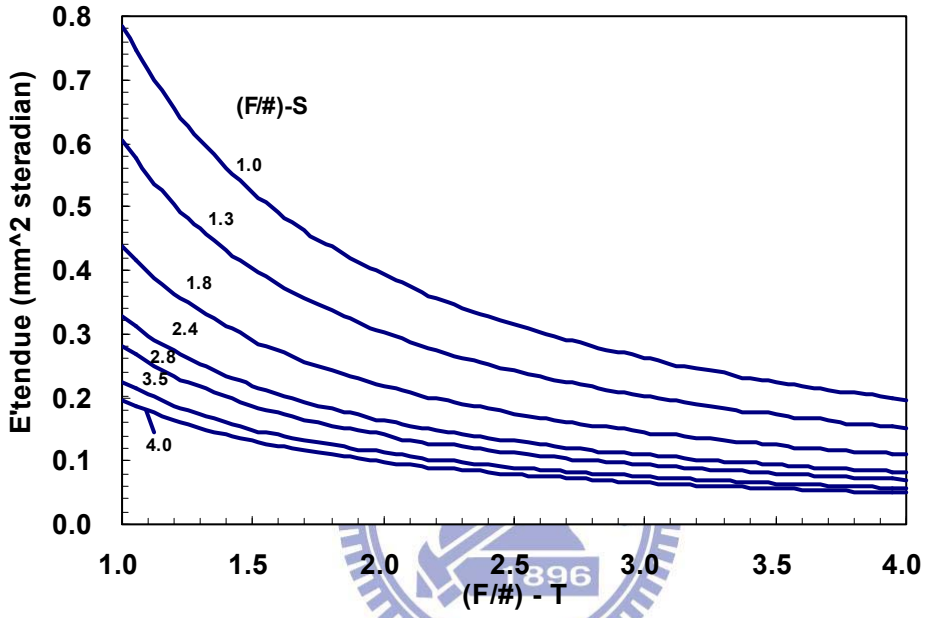

Figure 2-10 Variation of the Ètendue with the tangential *f*-number, (f / #)-T, for a variety of the sagittal *f*-number, (f / #)-S, i.e., from 1.0 to 4.0, in the optical system.

Furthermore, the shape equation of the aperture-stops of the illumination system and the projection lens is given by

$$D_S = \frac{(f/\#)_T}{(f/\#)_S} D_T = \frac{(f/\#)_T}{2.4} D_T \tag{2-23}$$

Where D_S and D_T are the diameters of the aperture-stops in the sagittal and tangential axes, respectively. It should be noted that because the ±12°-tilt angle of DMD™, the $(f/\#)_S$ should be limited by a value 2.4. On the contrast, $(f/\#)_T$ is determined by what the optical specifications are required; for examples, the trade-offs among the brightness, the resolution performance and the system volume, and so on. On the

other hand, D_T is determined by the designs of $(f/\#)_T$ and effective focal length in the illumination system and projection lens.

Besides the collection efficiency, *f*-number also affects the image aberrations on the illuminated plane, for example, the spherical aberration is inversely proportional to (*f*-number)^3 , the coma aberration is inversely proportional to (*f*-number)^2 and the astigmatism or field curvature is inversely proportional to (*f*-number) in terms of third-order aberration theory. Larger aberrations lead to the blurred projected image on the edge of the illuminated plane, for example the film and light valve. In order to keep the uniformity both on the center and edge of the illumination plane with the larger aberrations, it would be better to enlarge the overfill on the projected illumination spot to prevent the color band and shadow on the edge of illumination plane. However, when the overfill could be enlarged, the collection efficiency may be lost on the illumination plane and, hence, the overall throughout in the optical system will be reduced. Therefore, both the collection efficiency and the aberration for the specific *f*-number have to be considered in the initial phase of illumination system design.

2.6 Criteria on performance: aberration and modulation transfer function

Aberration is the departure and errors occurring in the resulting image which is not conformed to the real image in the optical system. Aberration leads to blurring of the image produced by an image-forming system. It occurs when light from one point of an object after transmission through the system does not converge into (or does not diverge from) a single point. There are the following five types of monochromatic aberration which are called the Seidel aberrations: Spherical aberration, Coma, Astigmatism difference, Curvature of field and Distortion. And, there are the following two types of chromatic aberration: Longitudinal chromatic

aberration and Lateral chromatic aberration [18]. In a real optical system, the above seven aberrations are mixed. The effect of those wavefront aberrations on image quality is a fairly complex subject. Any deviation in the form of the wavefront away from spherical causes degradation in the quality of point images, thus also the quality of image as a whole. The hard part is to define the specifics of this general fact. Assessing the relation between optical aberrations and image quality requires not only the knowledge of the mechanism by which the aberrations influence the determinants of optical quality, but also establishing the universal criteria applicable to any and all the aberrations. Such criteria need to define specific aberration tolerances as a reference point in fabrication, evaluation and the use of geometrical optics and diffraction optics.

The effect of aberrations on image quality is best assessed with the modulation transfer function (MTF) of the optical system. For that reason, this one quality indicator is addressed in more details. The MTF is a measure of the transfer of modulation (or contrast) from the subject to the image. In other words, it measures how faithfully the lens reproduces (or transfers) detail from the object to the image produced by the lens. Firstly, we have to define the type of test pattern being used. As shown in Fig 2-11, signal frequency of test pattern can be equated to a periodic line grating with the number of spacings per unit interval referred to as the spatial frequency. A common reference unit for spatial frequency is the number of line pairs per millimeter. As an example, a continuous series of black and white line pairs with a spatial period measuring 1 micrometer per pair would repeat 1000 times every millimeter and therefore have a corresponding spatial frequency of 1000 lines per millimeter.

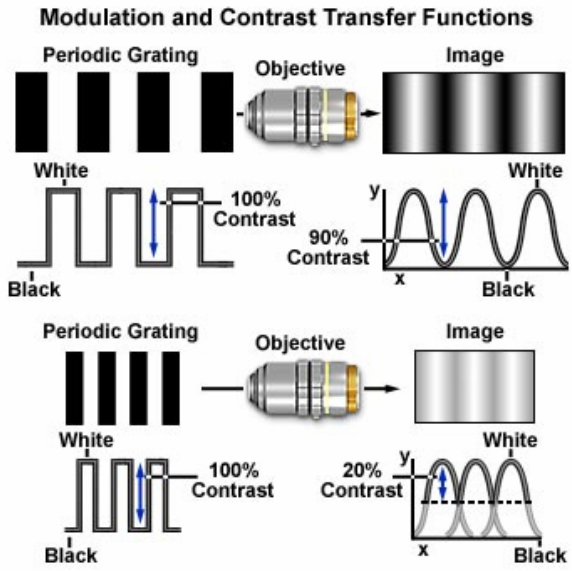

Figure 2-11 The illustration of the MTF and spatial frequency in a lens system. [42]

The formal definition of MTF:

$$MTF\left(f_x, f_y\right) = \frac{\left(Max\ \ Intensity - Min\ \ Intensity\right)}{\left(Max\ \ Intensity + Min\ \ Intensity\right)} \qquad (2\text{-}24)$$

In Fig. 2-11, for the first pattern group, the MTF is 0.9. For the second pattern set, the MTF can be calculated to be 0.2. The point at which you can no longer see any variation in the image is the point at which the MTF is zero, and that's the definition of the "limiting resolution" of the lens in an optical system. In this case, the final pattern set with an MTF of 0.1 would be classified as "just resolved" by this lens. In addition to the type of test pattern, the light used for illumination and the type of detector used for recording also influence MTF. When describing the performance of a lens using MTF, we typically use a plot of MTF against "spatial frequency" as shown in Fig 2-12 (a). This shows three plots. The blue curve is a perfect (diffraction limited) aberration-free lens operating at *f*-number equal to 4 (i.e. $f/4$). The black curve is the same lens operating at $f/8$. At $f/8$ many lenses are close to diffraction limited in the center of the optical field, so you could obtain a trace like this in

practice. Note that the "resolution" at *f*/4, defined as the spatial frequency at which the MTF drops so low that you can't see any modulation in the image, is around 450 line-pair/mm (lp/mm), while that of the perfect *f*/8 lens is exactly a half of that at 225 lp/mm. For a perfect lens, the resolution as defined in these terms (MTF~0) is linearly related to the aperture and is given by: Resolution (spatial frequency @ MTF=0) = 1800/(*f*-number). The red curve shows what you would expect from an *f*/4 lens with 1/2 wavelength of wavefront error (not an unreasonable amount to find in a typical camera lens). As you can see at *f*/8 a lens may actually be better (i.e. have a higher MTF) than the same lens at *f*/4 with 1/2 wavelength of wavefront error, at least for the region from 0 to about 175 lp/mm. This is the basis of the old rule that lenses are often best when stopped down a couple of stops from maximum aperture. In Fig 2-12 (b), the red region represents an MTF less than zero. What this means is that black areas appear as white and white areas appear as black, but in reality it can not be resolved. Resolution above the point at which the MTF first reaches zero is known as spurious resolution.

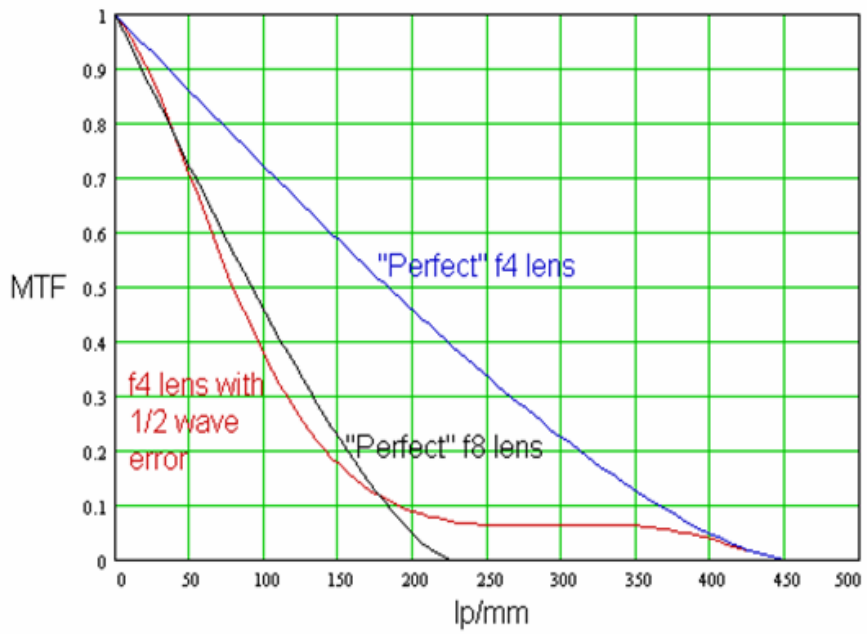

(a)

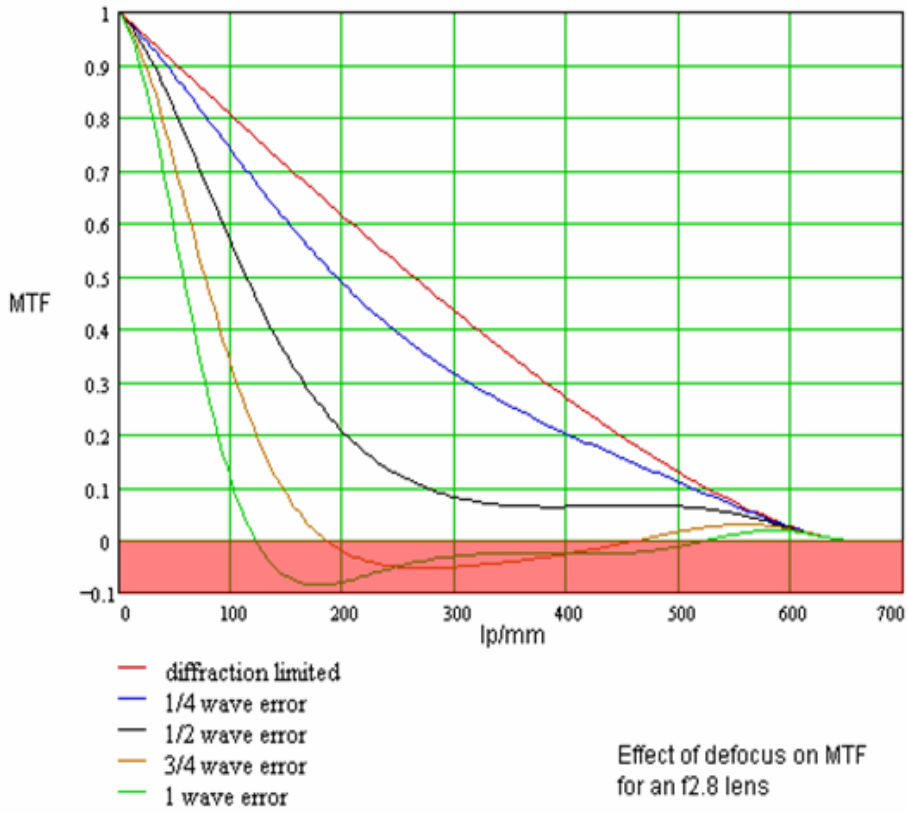

(b)

Figure 2-12 (a) A plot of MTF against "spatial frequency" for different designs of $f/4$ and $f/8$ lens, (b) the effect of defocus on MTF for an $f/2.8$ lens. [43]

Here is an example of an actual test pattern of USAF 1951 US Air Force resolution test chart [44] conform to MIL-STD-150A in Fig 2-13 (a), and recorded on film or detector in Fig 2-13 (b). As you can see the modulation in the finer spaced patterns with higher spatial frequencies in Group-II gets gradually more and more difficult to be resolved compared to the low spatial frequencies in Group-I. The higher the MTF of the lens, the finer spaced pattern that will be visible.

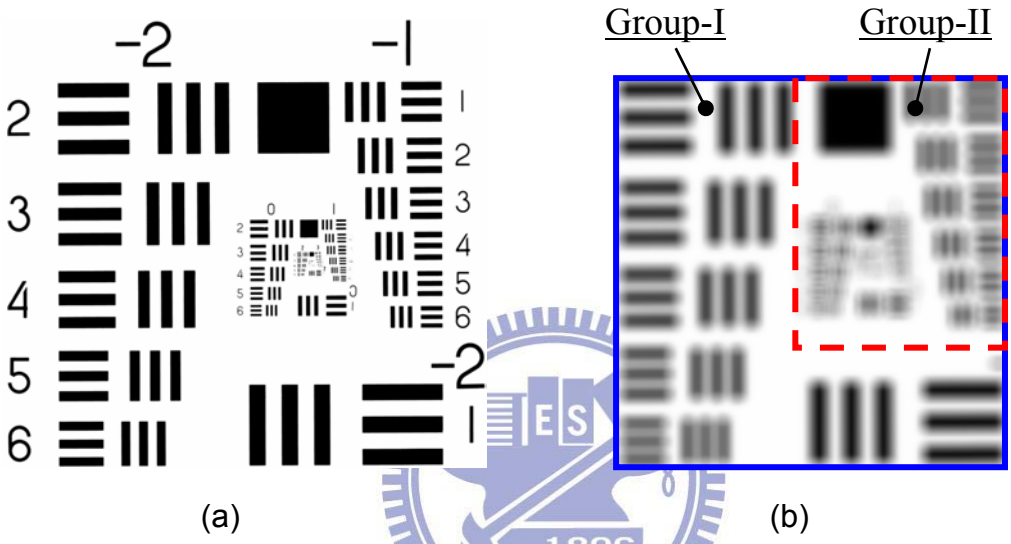

Figure 2-13 (a) An image of USAF 1951 US Air Force resolution test chart [44], (b) A record of the test chart in a film or a detector through the lens in an optical system.

The advantage of using OTF is both to analyzing and specifying the performance of imaging systems. One can compute the intensity distribution and contrast of an image if the intensity distribution of its corresponding object is known. The OTF of an imaging system can be calculated and simulated theoretically from the basic design data, so that it is feasible to design a lens system to meet OTF or MTF requirements with a desired image quality. The OTF of an entire system, such as a digital camera system can be predicted by computing the product of the OTFs of the individual sub-units in the system. The digital camera system consists of a lens, a CCD, an electronic circuit and a display, as shown in Fig 2-14. The MTF of an entire system at a spatial frequency s is given by

$$MTF_{System}(s) = MTF_{Lens}(k_1 s) \times MTF_{CCD}(k_2 s) \times MTF_{Electronic}(k_3 s) \times MTF_{Display}(k_4 s)$$

(2-25)

Where $MTF_{Lens}(k_1 s)$ etc are the MTFs of the sub-units in the system and k_1 etc are the constants that relate to the spatial frequency at that sub-unit with spatial frequency s of the entire system. The PTF of the entire system is given by

$$PTF_{System}(s) = PTF_{Lens}(k_1 s) + PTF_{CCD}(k_2 s) + PTF_{Electronic}(k_3 s) + PTF_{Display}(k_4 s)$$

(2-26)

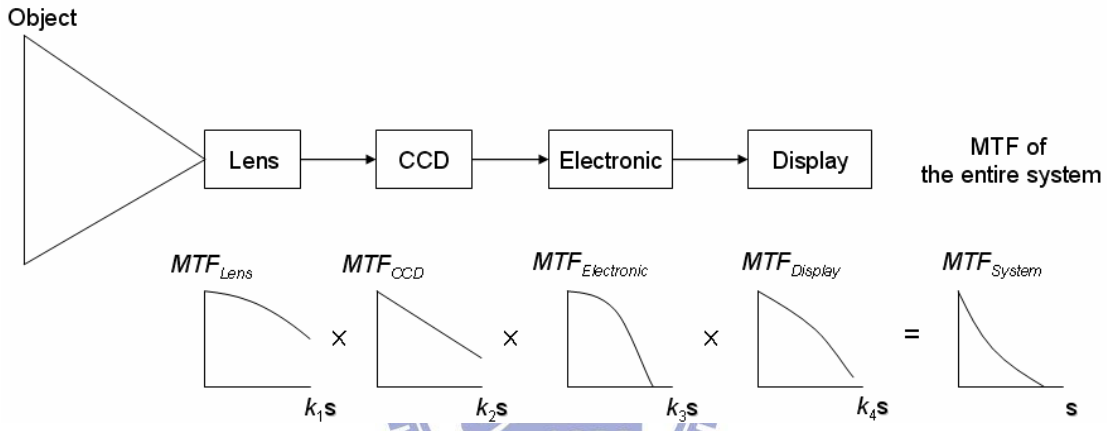

Figure 2-14 Schematic diagram of MTFs in an entire system

The MTF of a system by multiplying together the MTFs of the sub-units is very valuable in optical design. The designer can optimize the performance of each sub-unit individually and then match with each other for the final image quality of the entire system.

An important point of note is that an optical system, such as a photography or a microscopy consists of not only a lens system (an imaging system) but also an illumination system (a non-imaging system), but unfortunately MTF of an illumination light was generally assumed to be equal to unity in optical design. So, MTFs of a non-imaging system could be an effective factor for the final performance of an optical system. This issue will be investigated in this thesis as follows.

Chapter 3

Optical transfer functions for the specific-shaped apertures generated by illumination with a rectangular light pipe

3.1 Introduction

In this chapter, we investigate, both analytically and numerically, the imaging properties of the optical system with specific shaped apertures produced by the Lambertian illumination with a rectangular light pipe by calculating the OTF using the Hopkins method [37]. The different shaped apertures studied here are the types in which the amplitude transmittances vary with the different geometric structures of light pipes from the center of the pupil toward its rim. In order to do an image evaluation, the purpose of this study is to calculate the OTF of the aberration-free optical system (i.e. in-focus system and a diffraction-limited system) and the defocused optical system. For the purpose of comparison, this chapter also includes the OTFs of these two optical systems with a clear aperture as carried out by Hopkins [37].

The remainder of this chapter is organized as follows. In Section 2 we revisit on light pipes and light guides. In Section 3, we describe the optical projection system with a light pipe. In Section 4, we derive the pupil functions of different geometric structures of light pipes. In Section 5 we derive and analyze the corresponding OTFs and analyze the image quality in an aberration-free optical system and in a defocused optical system, respectively. Finally we draw our summary in Section 6.

3.2 Revisit on light pipes and light guides: academic interest and current trends

A light pipe is a commonly optical element that manages light properties in illumination systems, especially where extremely uniform illumination with specific illuminance distribution is required. Typical applications are in the illumination engines in the projectors, lithography, endoscopes and in optical waveguides. In those applications, the illumination system is mostly a combination of a light pipe and the corresponding imaging system with a projection lens. A light pipe is made with parallel reflective sides, either as a cylinder or with a square or rectangular cross section. The light source can be located on one end of the light pipe and the other end is then the uniformly illuminated plane [18]. The uniform illumination on the exit end of the light pipe is determined by the ratio between the length to the diameter and also the cross-sectional shape of the light pipe [19]. The multiple reflections of the light source through the pipe can produce a spatially checkerboard-array-shaped light distribution at the aperture stop of the illumination system which is then projected to the aperture stop of the corresponding imaging system. Hence, we need to determine the pupil function with a specific shaped aperture generated by the light pipe in the optical transfer function (OTF) for the image evaluation in the optical system. The earlier investigations of the use of shaped apertures are all in annular apodizers [3], radial Walsh filters [5], multiple mirror telescopes [45], and the diffraction by an aperture with central obstruction [46], and non-uniform amplitudes [6,7].

There are two kinds of the light pipes in term of the properties of the materials: hollow light pipe and solid light pipe. A hollow light pipe is made with parallel mirrors where the sidewalls join together and where coatings have the reflectivity of less than 100 and angular/color dependence. A solid light pipe is made of the dielectric material with the addition of the refraction, Fresnel loss, material absorption and a total internal reflection. Additionally, such a dielectric-filled light pipe brings a

factor of an index through Snell's law into the treatment of the angular profile and requires a longer length to obtain a given uniformity [13]. In order to have a convenient form of the pupil function, we employed the hollow straight light pipe in the calculation of the OTF in this chapter. The consideration of a hollow straight light pipe may be limited, but the study will provide a semi-analytical base of the connection between the non-imaging and the imaging in order to have a "uniform" source for imaging applications.

3.3 Configuration of the optical system

The schematic sketch of an optical projection system using a rectangular light pipe is illustrated in Fig. 3-1 showing the relationships between the pupils and fields. The system consists of the following subsystems: a light source with Lambertian angular distribution, an illumination system using a rectangular light pipe, a light valve and a projection system.

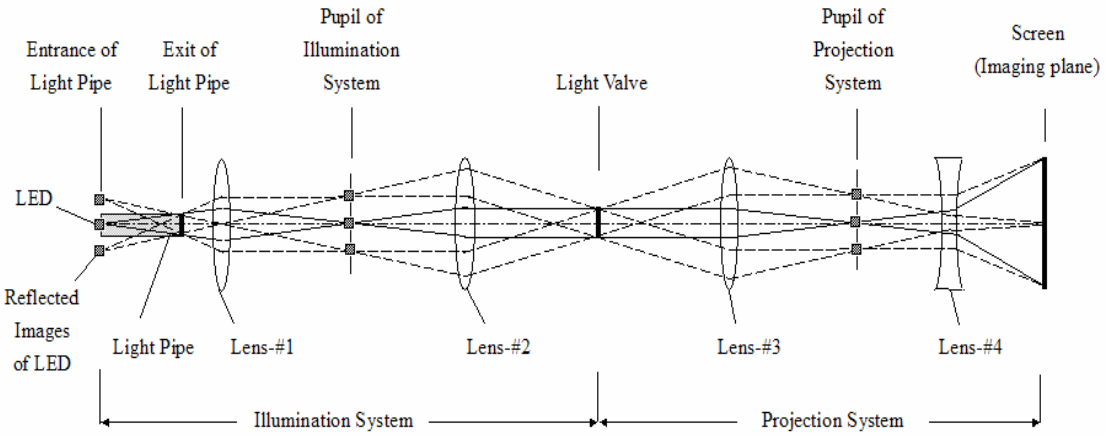

Figure 3-1 Schematic diagrams of the optical projection system with the light pipe and light-valve to illustrate the relationship between pupils and fields.

The Lambertian light source is located at the entrance of the light pipe, and the light source has an angular distribution extending from +90° to -90°. The exit is

uniformly illuminated by the multiple reflections through the light pipe. The uniform illuminance on the exit plane of the light pipe is transferred to its conjugate imaging plane on the light valve. The multiple reflections of the light source through the pipe can produce a spatial checkerboard-array-shaped light distribution that is a virtual image at the entrance of the light pipe. This virtual image is imaged onto the aperture stop of the illumination system by lens #1. Then, the image at the pupil of the illumination system is conjugately imaged onto the aperture stop of the corresponding projection lens system by lens #2 in the illumination system and lens #3 in the projection system. Finally, the image on the light valve is projected onto the screen by the projection lenses lens #3 and lens #4.

The dimension of the light pipe and the light source is shown in Fig. 3-2, where *a* and *b* are the width and the height of the cross section of the light pipe, respectively, where *L* is the length of the light pipe and *c* is the size of the square light source.

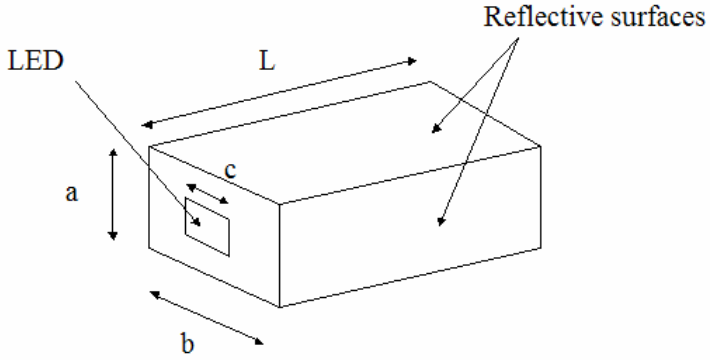

Figure 3-2 Schematic diagrams and Dimension of the light pipe and LED source.

The light pipe is made with parallel reflective sides with a rectangular cross section. The multiple reflections of the light source through the pipe can produce a spatial checkerboard-array-shaped light distribution that is the virtual image of the light at the entrance of the light pipe as shown in Fig. 3-3 (a). The spaces between each adjacent light spot are: *a* on the vertical axis and *b* on the horizontal axis, which

are equal to the width and height of the cross section of the light pipe, respectively. And, the size of each light spot is equal to that of the light source. The luminous flux of each light spot is noted as $F_{m,n}$ as shown in Fig. 3-3 (b). The subscripts m and n stand for the reflective times on the horizontal axis and vertical axis, respectively, and the plus and minus values of m and n denote the opposite directions of the light source. For example, $F_{1,2}$ means the luminous flux of the light spot is reflected one time on the horizontal axis and two times on the vertical axis and its location is shown in Fig. 3-3 (b).

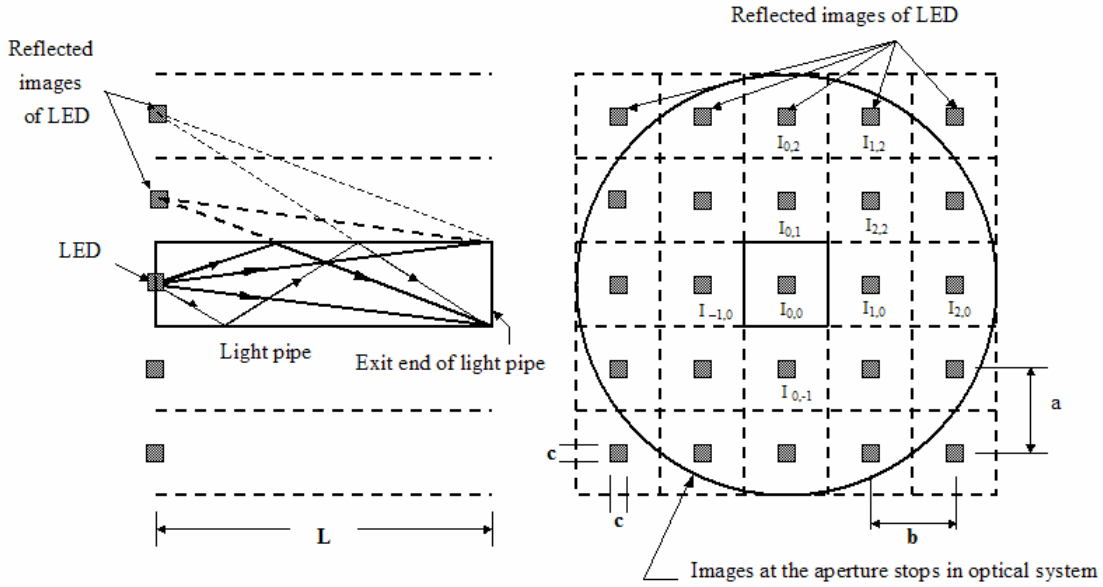

(a) (b)

Figure 3-3 (a) Principle operation of light pipe. (b) Image at the aperture stop in the optical system. The light pipe is made with the parallel reflective sides with the rectangular cross section. The multiple reflections of the light source through the pipe can produce the spatially checkerboard-array-shaped light distribution, a virtual image at the entrance of the light pipe.

3.4 Optical computation for pupil function

The equation of the luminous exitance from the light source is assumed as one pulse function shown in Fig. 3-4.

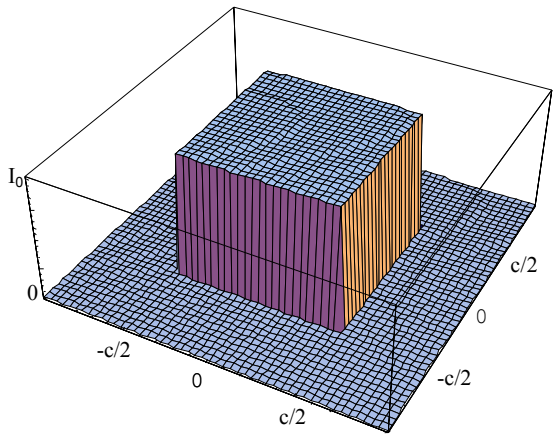

Figure 3-4 LED spatial light-intensity distribution's chart.

and expressed as,

$$B(x,y)=B_0\ ,\quad |x|\le\frac{c}{2},\ |y|\le\frac{c}{2}\ =\ [\,H(x+c/2)-H(x-c/2)\,]\times[\,H(y+c/2)-H(y-c/2)\,]$$
$$=0\ ,\quad |x|>\frac{c}{2},\ |y|>\frac{c}{2}, \tag{3-1}$$

where c is the size of the square light source, B_0 is the luminous exitance (lumen cm^{-2}) of the uniform light source, and *H(x+c/2), H(x-c/2), H(y+c/2) and H(y-c/2)* are the step functions. The luminous intensity of the light source with Lambertian characteristics is given by

$$I_\Omega = I(\theta) = I_0\cos\theta\ ,\quad -90^\circ\le\theta\le 90^\circ \tag{3-2}$$

where I_Ω is the luminous intensity (lumen $ster^{-1}$) of a small incremental area of the source in a direction at an angle θ from normal to the surface, and I_0 is the luminous intensity of the incremental area in the direction of normal. Then, we can derive the luminous flux (lumen) radiated from the Lambertian light source into the exit end of the light pipe.

With reference to Fig. 3-5, we assume that the incremental rectangular area *dA* on the end plane of the light pipe is *dxdy,* length *R* is the distance from the light source to the incremental area, length *L* is the distance from the light source to the end plane of the light pipe, and angle θ is the angle from normal to the incremental area.

The values a and b are the width and the height of the cross section of the light pipe, respectively.

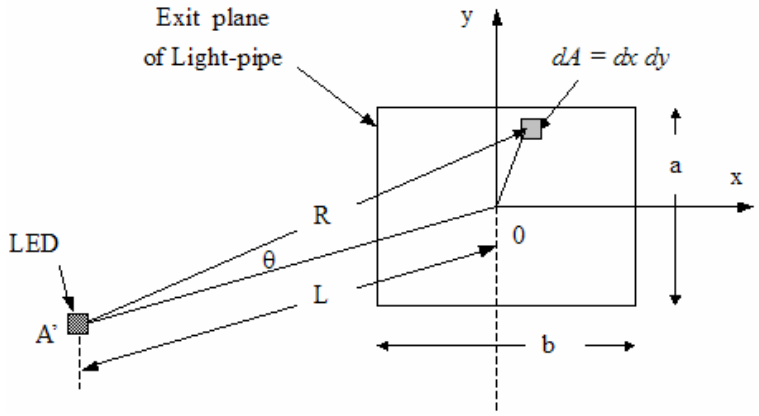

Figure 3-5 Geometry of a LED source radiating into the exit plane of the light pipe.

The angle θ can be substituted by L, x, y and R, and is given by

$$\cos\theta = \frac{L}{\sqrt{L^2 + \left(x^2 + y^2\right)}} = \frac{L}{R} \tag{3-3}$$

The luminous flux intercepted by the incremental area is the product of the luminous intensity of the light source and the solid angle, which can be expressed as the function of I_0, L, x and y according to Eqs. (3-2) and (3-3) as given by

$$dF = I_\Omega d\Omega = I_0 \cos\theta \frac{dA}{R^2} = I_0 \frac{L}{R}\frac{dA}{R^2} = \frac{I_0 L}{R^3} dA = \frac{I_0 L}{\left[L^2 + \left(x^2 + y^2\right)\right]^{3/2}} dxdy \tag{3-4}$$

Then, we determine the individual luminous fluxes of the virtual light spots on the entrance plane of the light pipe. The luminous flux $F_{0,0}$ of the virtual light spot on the entrance plane of the light pipe is equivalent to the luminous flux $F'_{0,0}$ on the exit end of the light pipe, which is radiated without any reflection through the light pipe as shown in Fig. 3-6. We integrate Eq. (3-4) about x from $-b/2$ to $+b/2$ and about y from $-a/2$ and $+a/2$ to find the luminous flux $F_{0,0}$ as given by

$$F_{0,0} = \int_{-b/2}^{b/2}\int_{-a/2}^{a/2} \frac{I_0 L}{\left[L^2 + \left(x^2 + y^2\right)\right]^{3/2}} dxdy \tag{3-5}$$

Also, we can derive the powers $F_{0,1}$ and $F_{0,2}$ that are radiated with one time reflection and a two times reflection through the light pipe, respectively, as shown in Fig. 3-6.

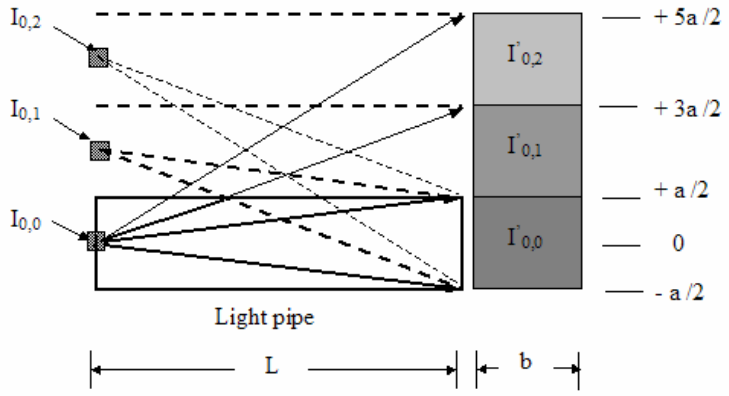

Figure 3-6 Illustration of a LED source radiating into the exit plane of the light pipe for the different virtual light spot on the entrance plane of the light pipe.

and they are given by

$$F_{0,1} = \int_{-b/2}^{b/2}\int_{a/2}^{3a/2} \frac{\rho\, I_0 L}{\left[L^2 + \left(x^2 + y^2\right)\right]^{3/2}} dxdy \tag{3-6}$$

$$F_{0,2} = \int_{-b/2}^{b/2}\int_{3a/2}^{5a/2} \frac{\rho^2\, I_0 L}{\left[L^2 + \left(x^2 + y^2\right)\right]^{3/2}} dxdy \tag{3-7}$$

where ρ is the reflectivity and the exponent of ρ is the reflective time. Finally we can then summarize the expression of the luminous flux for each virtual light spot on the entrance plane of the light pipe as follows,

$$F_{mn} = \int_{(2n-1)b/2}^{(2n+1)b/2}\int_{(2m-1)a/2}^{(2m+1)a/2} \frac{\rho^{|m|}\,\rho^{|n|}\, I_0 L}{\left[L^2 + \left(x^2 + y^2\right)\right]^{3/2}} dxdy \qquad m, n = \ldots -3, -2, -1, 0, 1, 2, 3 \ldots \tag{3-8}$$

where $|m|$ and $|n|$ stand for the reflective times through the light pipe on the horizontal and vertical axis, respectively.

In order to have a convenient form for the numerical evaluation, we make the reasonable assumption, $\left(\frac{x}{L}\right)^2 + \left(\frac{y}{L}\right)^2 << 1$. In most application cases that means that the dimension of the cross section of the light pipe should be much less than the

length of the light pipe. In this case, it is certain that the Lambertian light source is uniformly transferred on the exit plane of the light pipe [19]. The numerical aperture N.A. can be generally assumed around 0.5 as a minimum (i.e., the corresponding *f*-number is equal to unity) because of "Ètendue limited" in most of projection systems [39] and reducing an optical system to the commercial practice. Based on the assumptions, the term in the integration in Eq. (3-8) can be approximately derived as the following expression,

$$\frac{L}{\left(L^2+\left(x^2+y^2\right)\right)^{3/2}}=\frac{1}{L^2}\left(1+\left(\frac{x}{L}\right)^2+\left(\frac{y}{L}\right)^2\right)^{-3/2}\approx\frac{1}{L^2}\left(1-\frac{3}{2}\cdot\left(\frac{x}{L}\right)^2-\frac{3}{2}\cdot\left(\frac{y}{L}\right)^2\right)$$

$$=\frac{1}{2L^4}\left(2L^2-3x^2-3y^2\right) \tag{3-9}$$

Then, the integration of Eq. (3-8) can be carried out by substituting Eq. (3-9). Finally, the expression of the luminous flux for each virtual light spot on the entrance plane of the light pipe is given by

$$F_{mn}=\frac{I_0}{2L^4}\int_{(2n-1)b/2}^{(2n+1)b/2}\int_{(2m-1)a/2}^{(2m+1)a/2}\rho^{|m|}\rho^{|n|}\left(2L^2-3x^2-3y^2\right)dxdy$$

$$=\frac{\rho^{|m|}\rho^{|n|}I_0}{2L^4}\left(-\frac{a^3b}{4}-\frac{ab^3}{4}+2abL^2-3a^3bm^2-3ab^3n^2\right) \tag{3-10}$$

$$m,n=\ldots-3,-2,-1,0,1,2,3\ldots$$

From Eq. (3-10), we know that the luminous flux $F_{m,n}$ of the light spot can be nonlinearly decreased with the different reflective times *m* and *n* through the light pipe because of the characteristics of the angular profile for luminous intensity of a Lambertian light source.

The pupil function of a defocused optical system with a circular aperture is referring to Eq. (2-2) and given by [6]

$$f(x,y) = T(x,y)\exp\left[ik\omega_{20}\left(x^2+y^2\right)\right] \qquad x^2+y^2 \le 1$$
$$= 0 \qquad x^2+y^2 > 1 \tag{3-11}$$

where ω_{20} is the wave aberration of the defocused coefficient, (x ,y) are the normalized Cartesian coordinates, and $k = 2\pi/\lambda$, where λ is the wavelength of the light. Function $T(x, y)$ in Eq. (3-11) represents the amplitude distribution over the pupil. The amplitude transmittance $T(x, y)$ has a circular symmetrical pupil coordinate that is scaled and normalized to make the outer periphery of the unit circle, $x^2 + y^2 \le 1$.

It is assumed that the corresponding diameter of the effective aperture stop in the projection lens system with be D. With reference to the array theorem [47], and by combining Eq. (3-1) and Eq. (3-10), we can derive the amplitude transmittance of the shaped aperture $T(x, y)$ due to the multiple reflections through the light pipe as follows,

$$T(x,y) = E'(x,y) \otimes A_\delta(x,y)$$
$$= E'(x,y) \otimes \sum_m \sum_n \left(\frac{F_{m,n}}{A'}\right) \times \delta\left(x - \frac{2ma}{D}\right) \delta\left(y - \frac{2nb}{D}\right) \tag{3-12}$$

$$m = Int\left[\frac{D/a - 1}{2}\right], n = Int\left[\frac{D/b - 1}{2}\right] \tag{2-13}$$

where $F_{m,n}$ denotes the luminous flux for the individual light spot on the entrance plane of the light pipe, $\delta\left(x - \frac{2ma}{D}\right)\delta\left(y - \frac{2nb}{D}\right)$ denotes the delta function indicating the location of the individual light spot in the normalized coordinate on the entrance plane, $E'(x,y) = \left[H(x + c/D) - H(x - c/D)\right] \times \left[H(y + c/D) - H(y - c/D)\right]$ is the individual light spot illuminated by the Lambertian light source, then scaled and normalized in to the pupil coordinate, $A' = \left(\frac{c}{D}\right)^2$ is the area of the individual light

spot at the pupil and $\left(\frac{F_{m,n}}{A'}\right)$ is the illuminance (lux or lumen-cm^{-2}) of the individual light spot at the pupil , while $Int\left[\frac{D/a - 1}{2}\right]$ and $Int\left[\frac{D/b - 1}{2}\right]$ are the inter parts of $\left[\frac{D/a - 1}{2}\right]$ and $\left[\frac{D/b - 1}{2}\right]$, respectively. It is evident that the total aperture function is formed by convolving the individual aperture function with an appropriate array of the delta function, each located at one of the coordinate origins $(x_m, y_n) = \left(\frac{2ma}{D}, \frac{2nb}{D}\right)$, where *m, n* = …-2, -1, 0, 1, 2, … The quality and location for the individual aperture on the pupil depends on the dimension of the light pipe's cross-section and length, and the specific diameter of the effective aperture stop in the optical system. The total aperture function is a direct result of the convolution theorem.

Next we quantitatively investigate the relationship between the geometric structure of the square light pipe and the amplitude transmittance of the shaped aperture. And, it is assumed that there are no losses of the reflectivity (i.e., ρ =1), the absorption and the scatter in the light pipe for the simplification. The computer program for evaluating Eq. (3-12) is written in Mathematica software [41]. We evaluate three cases for the amplitude transmittance of the shaped aperture $T(x, y)$ as follows,

(1) Case-1: D=20, a= b= 2.5, L= 60 and c= 0.5, 1.0, 1.5 and 2.0, respectively. The distributions are shown in Fig. 3-7. The result shows that the individual aperture size can be shrunk with the dimension of the Lambertian light source shrunk to the specific diameter of the pupil. This is due to the fact that the size of the individual aperture is the same as the projection mapped from the Lambertian light source in the illumination system. That is equivalent to the term $E'(x, y)$ varied with c in Eq (3-12).

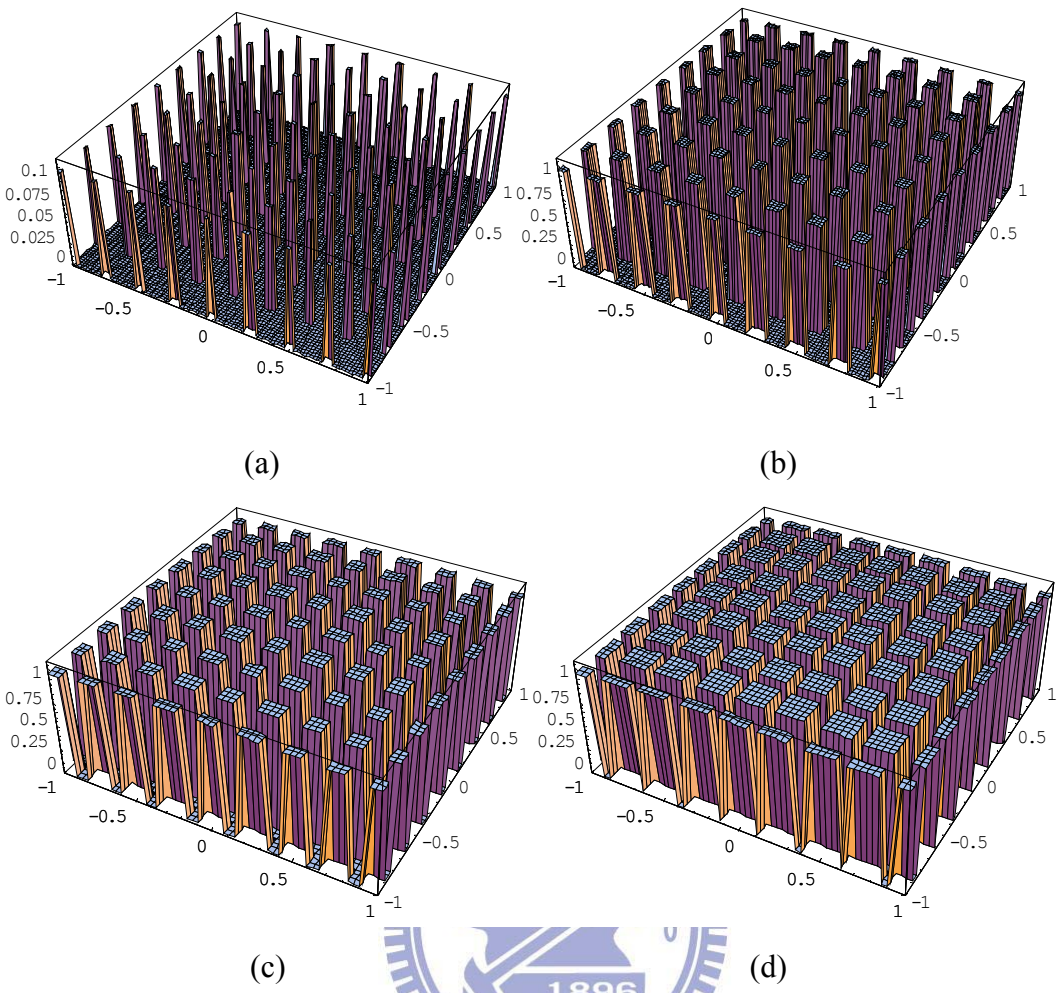

Figure 3-7 Total aperture functions on the normalized pupil in the condition of D=20, a=b=2.5 and L= 60 with (a) c=0.5, (b) c=1.0, (c) c=1.5, (d) c=2.0.

(2) Case-2: *D*=20, *c* = 2.0, *L*= 60 and *a* = *b*= 2.5, 3.5, 5.0, 7.5 and 10.0, respectively. The distributions are shown in Fig. 3-8. The result shows us that the total aperture function consists of many individual aperture functions due to the light's multiple reflection through the light pipe as mentioned in the previous section. The distance between the individual apertures can be increased with the dimensions of the cross-section of the light pipe, i.e. *a* and *b* values, becoming bigger for the specific diameter of the pupil. This is due to the fact that the cross-section size of the light pipe can affect the locations of the multiple reflected images through the

light pipe on the pupil as shown in Fig. 3-3(b). This is equivalent to the term $\delta(x-\frac{2ma}{D})\delta(y-\frac{2nb}{D})$ varied with a and b in Eq (3-12).

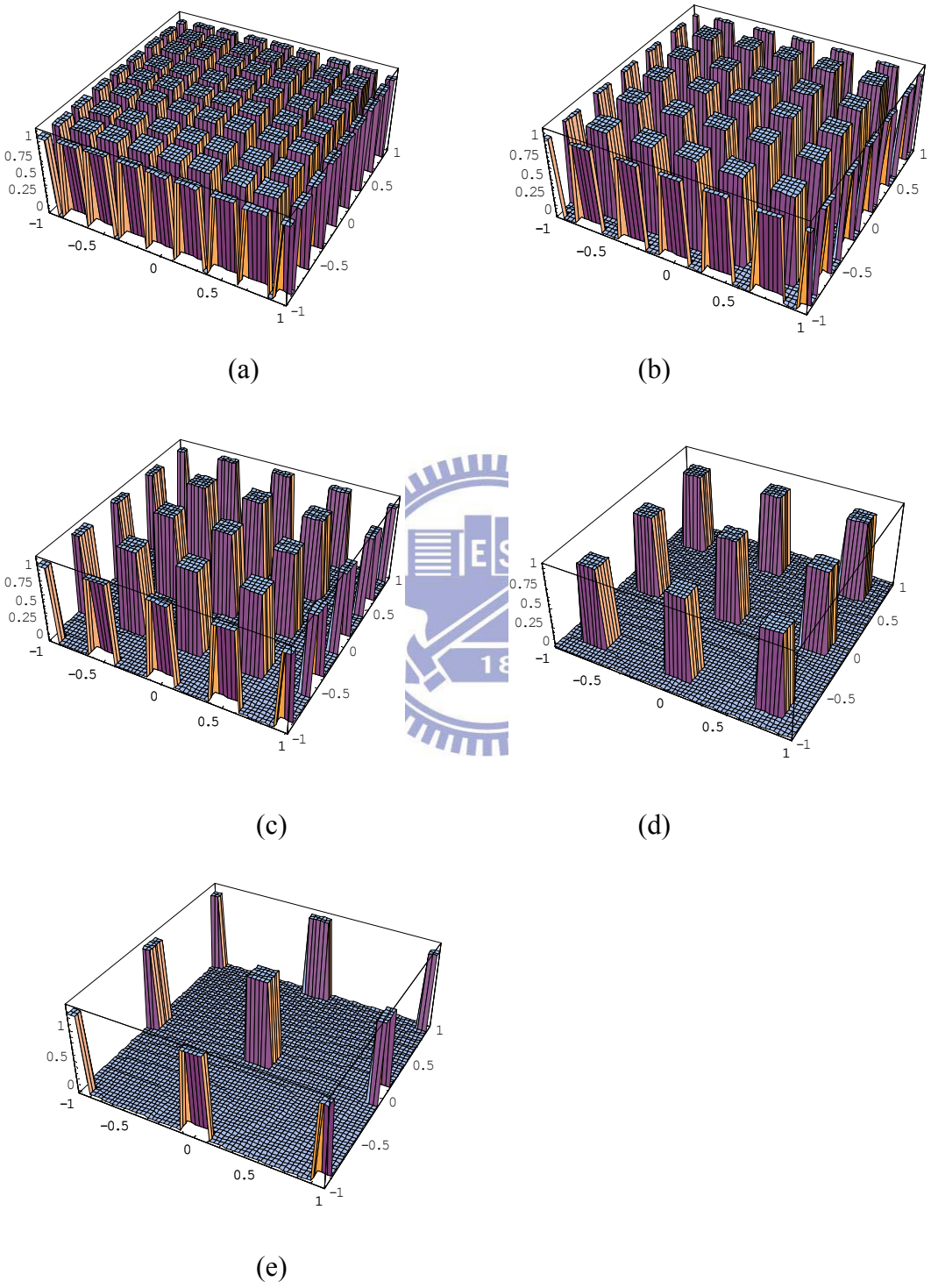

Figure 3-8 Total aperture functions on the normalized pupil in the condition of D=20, c=2.0 and L=60 with (a) a=b=2.5, (b) a=b=3.5, (c) a=b=5.0, (d) a=b=7.5, (e) a=b=10.0.

(3) Case-3: D=20, a= b= 2.5, c= 2.0 and L= 20, 30, 60 and 120, respectively. The distributions are shown in Fig. 3-9. The result shows that the amplitude of the individual aperture can decrease from the center to the periphery when the light pipe's length increases. The reason for this is that the length of the light pipe can affect the radiated solid angle and consequently the power of each individual light spot on the exit plane of the light pipe as shown in Fig. 3-6. That is to say, equivalent to the terms $I_{m,n}$ varied with L in Eq. (3-10) and Eq. (3-12).

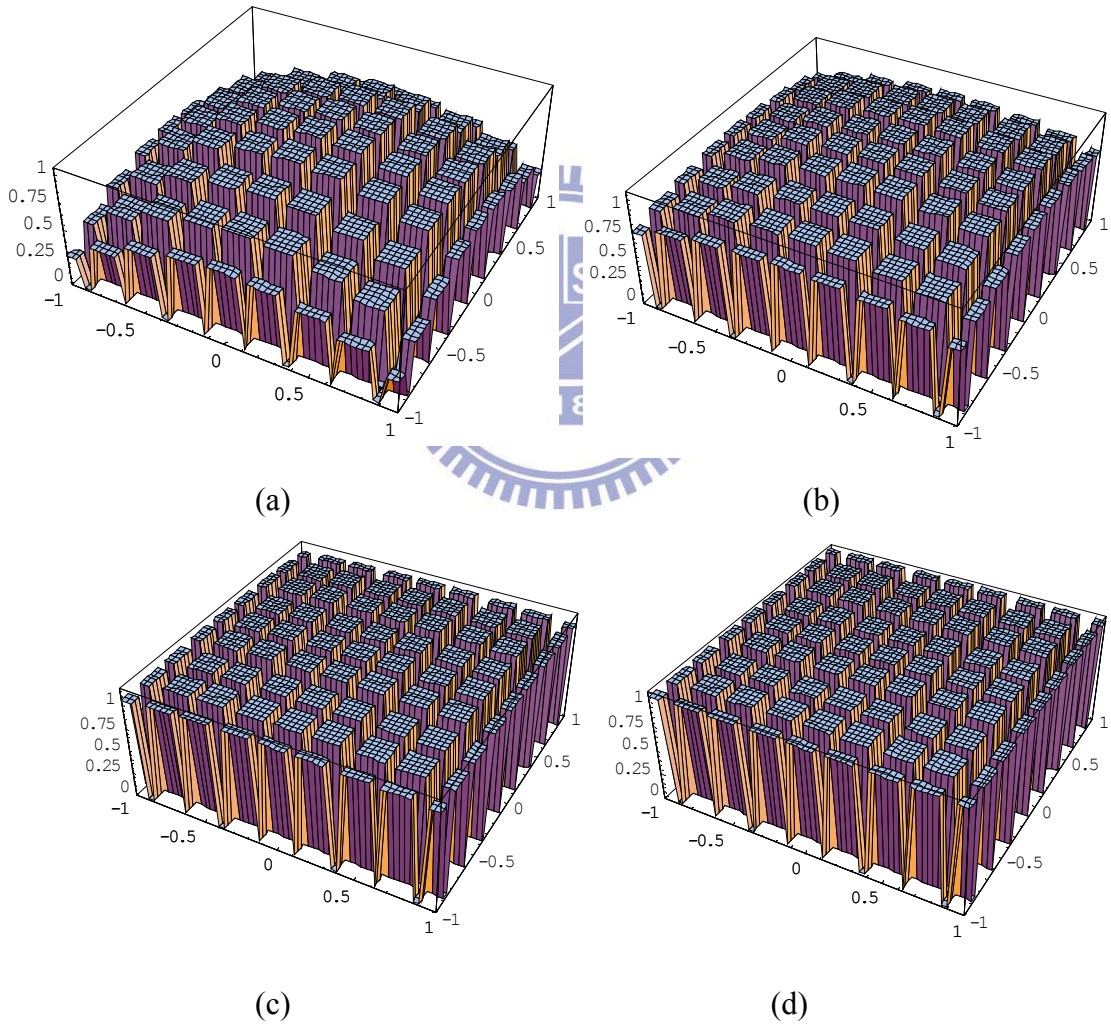

Figure 3-9 Total aperture functions on the normalized pupil in the condition of D=20, a=b=2.5 and c=2.0 with (a) L=20, (b) L=30, (c) L=60, (d) L=120.

3.5 Optical transfer function and image performance evaluation

The optical transfer function (OTF) is derived from the autocorrelation of the pupil function [37] by using the Hopkins canonical coordinates [48,49] and is given by

$$D(s)=\frac{g(s,0)}{g(0,0)}=\frac{\int_{-\infty}^{\infty}\int_{-\infty}^{\infty}f(x+s/2\,,y)\,f^{*}(x+s/2\,,y)\,dx\,dy}{\int_{-\infty}^{\infty}\int_{-\infty}^{\infty}f(x\,,y)\,f^{*}(x\,,y)\,dx\,dy} \tag{3-14}$$

where $f(x,\ y)$ is the pupil function shown as Eq. (3-11) , $f^{*}(x,\ y)$ is the complex conjugate of $f(x,\ y)$, and s is defined as the spatial frequency, $s \equiv 2\,(f/\#)\,\lambda\,N$, where $f/\#$ is the F-number of the projection lens system , λ is the wavelength and N is the number of cycles per unit length in the image plane. The denominator of Eq. (3-14) is the normalizing factor to make $D_0\,(0) = 1$. Then the $g\,(s,\ 0)$ and $g(0,\ 0)$ in OTF for the pupil function $f\,(x,\ y)$ can be given by

$$g(s,0)=\int_{-\left[1-(s/2)^2\right]^{1/2}}^{\left[1-(s/2)^2\right]^{1/2}}\int_{-\left[\left(1-y^2\right)^{1/2}-s/2\right]}^{\left[\left(1-y^2\right)^{1/2}-s/2\right]}\left[T(x,y)\right]^2\cdot exp\,\left[iKx\right]dxdy \tag{3-15}$$

and

$$g(0,0)=\int_{-1}^{1}\int_{-\left(1-y^2\right)^{1/2}}^{\left(1-y^2\right)^{1/2}}\left[T(x,y)\right]^2\,dxdy \tag{3-16}$$

where $K = 2\,k\,\omega_{20}\,s$. Because the pupil function is an even function, the term of $exp[iKx]$ can be reduced to $cos[iKx]$ in the integral of Eq. (3-15). Then $g(s,\ 0)$ is rewritten as

$$g(s,0)=\int_{-\left[1-(s/2)^2\right]^{1/2}}^{\left[1-(s/2)^2\right]^{1/2}}\int_{-\left[\left(1-y^2\right)^{1/2}-s/2\right]}^{\left[\left(1-y^2\right)^{1/2}-s/2\right]}\left[T(x,y)\right]^2\cdot cos\,\left(iKx\right)dxdy \tag{3-17}$$

In order to have the numerical computation in the Mathematica software [41], we need to modify the Eq. (3-16) and Eq. (3-17) to the following convenient forms, i.e.,

$$g(0,0)=\sum_{q=-p}^{p}\left\{\int_{-\left(1-y^2\right)^{1/2}}^{\left(1-y^2\right)^{1/2}}\left[T(x,y)\right]^2\,dx\right\}\cdot\Delta y \tag{3-18}$$

where $y=\frac{1}{p}\times q$, $\Delta y=\frac{1}{p}$.

$$g(s,0)=\sum_{q'=-p'}^{p'}\left\{\int_{-\left[\left(1-y^2\right)^{1/2}-s/2\right]}^{\left[\left(1-y^2\right)^{1/2}-s/2\right]}\left[T(x,y)\right]^2\cdot\cos\left(iKx\right)dx\right\}\cdot\Delta y \tag{3-19}$$

where $y=\frac{\left[1-(s/2)^2\right]^{1/2}}{p'}\times q'$, $\Delta y=\frac{\left[1-(s/2)^2\right]^{1/2}}{p'}$. By substituting the integral in Eq. (3-16) and Eq. (3-17) with y-axis for the summation in Eq. (3-18) and (3-19), an initial setting of p=100 is made for the number of the interval used to find the value of $\Delta y=\frac{\left[1-(s/2)^2\right]^{1/2}}{p'}$ and $\Delta y=\frac{1}{p}$ for $g(s,\ 0)$ and $g\ (0,\ 0)$, respectively. Different numbers of y, from $-\left[1-(s/2)^2\right]^{1/2}$ to $\left[1-(s/2)^2\right]^{1/2}$, are then used to calculate the OTF.

The OTF of different pupil functions is numerically calculated using the Mathematica software based on the Eq. (3-11)-(3-13), (3-18) and (3-19). The OTF of the aberration-free and defocused system with the clear aperture $T_0(x, y)$ =1 ($x^2+y^2\leqq 1$) and 0 ($x^2+y^2>1$), already investigated by Hopkins [37], was calculated as a comparison. We calculated and analyzed the OTFs of the four cases that are with specific shaped aperture generated by the illumination with light pipe as follows,

(1) Case-1: the OTF in the aberration-free system with specific shaped apertures of different geometric structure of the light pipe: a = b= 2.5 is fixed, L= 60 is fixed, but c varies from 0.5, 1.0, 1.5 to 2.0, as shown in Fig. 3-7. The OTF's calculation results are shown in Fig. 3-10. The general tendency of the OTF curve versus the number of the individual aperture within the pupil in readily evident. There are a total of 9 × 9 =81 individual apertures within the pupil. Meanwhile, there are 9 peaks on the OTF curve at the near-periodically spatial frequencies around 0, 0.25, 0.50, 0.75, 1.00, 1.25, 1.50, 1.70 and 1.90. The OTF values of the odd-peak

frequencies for different sizes of the Lambertian light sources (i.e. value c) remain very similar to the values of the OTF's of the corresponding frequencies for the clear aperture. However, the OTF values of the even-peak frequencies can decrease with the decrease in the light-source size. Therefore, if the size of an individual aperture is much less than that of the pupil, then OTF values of the even-peak frequencies will be almost zero.

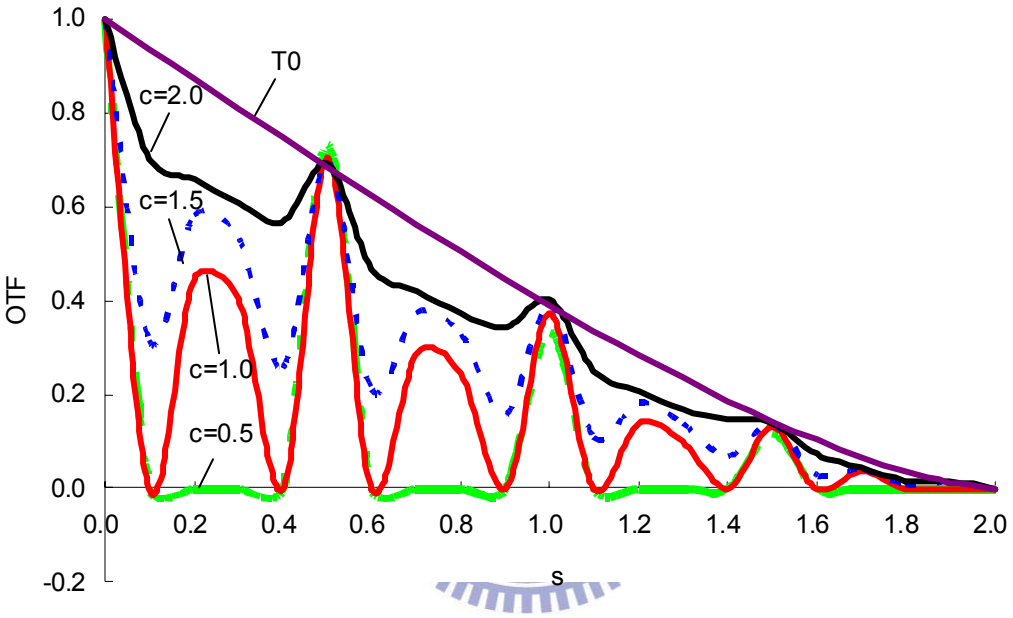

Figure 3-10 Optical transfer functions in aberration-free system with a clear aperture T_0 and specific apertures generated by different light pipe's geometric structure with fixed a=b=2.5 and fixed L= 60 and different conditions of c=0.5, c=1.0, c=1.5 and c=2.0.

(2) Case-2: the OTF in the aberration-free system with specific shaped apertures of different geometric structure of the light pipe: c = 2.0 is fixed, L= 60 is fixed, but a = b varies with 2.5, 3.5, 5.0, 7.5 and 10.0, as shown in Fig. 3-8. The results of the OTF's calculation are shown in Fig. 3-11. For a=b=2.5, there are a total of 9 × 9 = 81 individual apertures within the pupil, and there are 9 peaks on the OTF curve. For a=b=3.5, there are a total of 7 × 7 = 63 individual apertures within the pupil, and there are 7 peaks on the OTF curve. Together with the other cases,

we can conclude that if there are a total of $n \times n$ individual apertures within the pupil then there will be n peaks on the OTF curve. Furthermore, the peaks show at nearly periodic responses to the OTF curve.

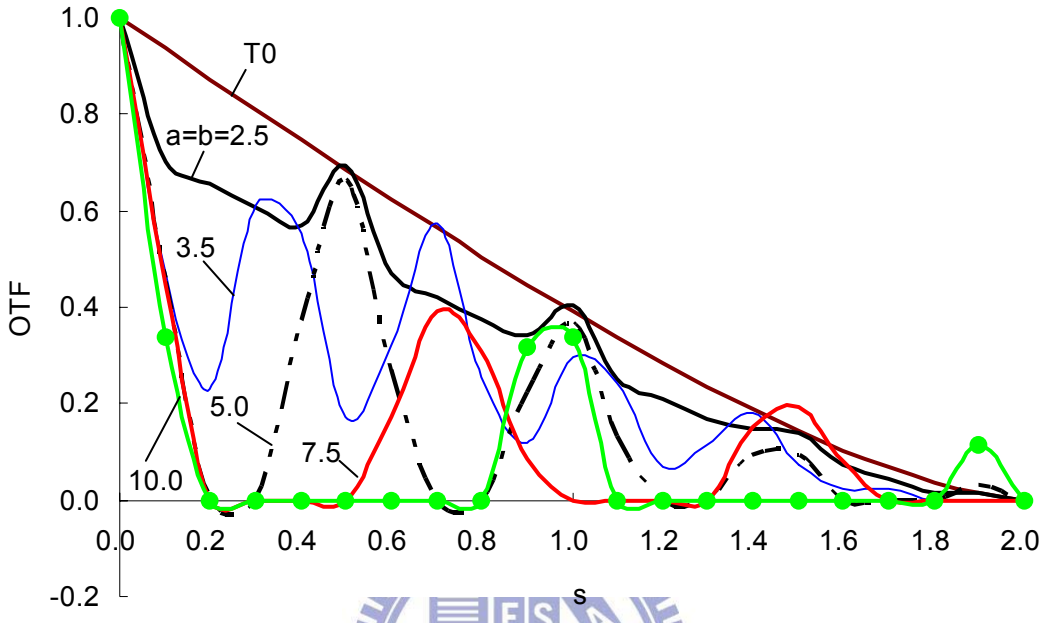

Figure 3-11 Optical transfer functions in aberration-free system with a clear aperture T_0 and specific apertures generated by different light pipe's geometric structure with fixed c=2.0 and fixed L= 60 and different conditions of a=b=2.5, a=b=3.5, a=b=5.0, a=b=7.5 and a=b=10.0.

(3) Case-3: the OTF in the aberration-free system with specific shaped apertures of different geometric structure of the light pipe: $a = b$= 2.5 is fixed, c= 2.0 in fixed but L varies with 20, 30, 60 and 120, as shown in Fig. 3-9. The OTF's calculation results are shown in Fig. 3-12. We can see that the values of the OTF remain almost unchanged with the different lengths of the light pipe (i.e. the value of L.) even though the amplitude of the individual aperture decreases from the center to the peripheral when the length of the light pipe is increases.

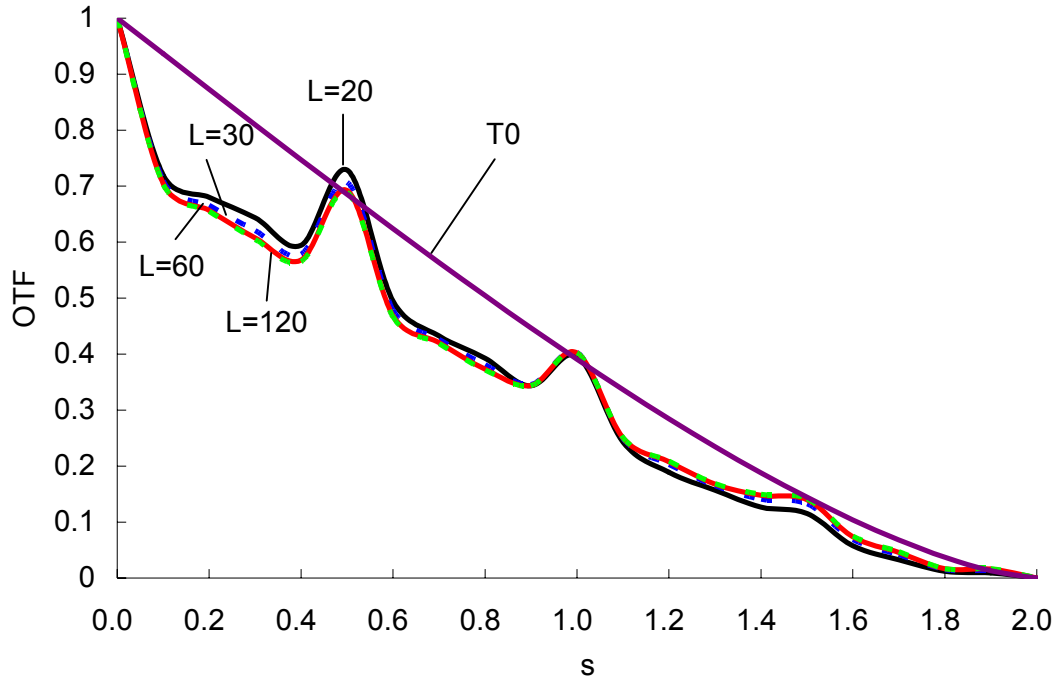

Figure 3-12 Optical transfer functions in aberration-free system with a clear aperture T_0 and specific apertures generated by different light pipe's geometric structure with fixed a=b=2.5 and fixed c= 2.0 and different conditions of L=20, L=30, L=60 and L=120.

(4) Case-4: the OTF in the defocused system with the clear shape and the fixed shaped apertures and with a geometric structure of the fixed light pipe: $a = b = 2.5$ is fixed, $c = 2.0$ is fixed, and $L = 60$ is fixed too, as shown in Fig. 3-8 (a). The OTFs are calculated for the different defocused coefficients for $\omega_{20} = 0, \lambda/\pi, 2\lambda/\pi, 3\lambda/\pi, 5\lambda/\pi$ and $10\lambda/\pi$, as shown in Fig. 3-13 (a) and Fig. 3-13 (b), respectively. The spatial frequency of the first zero is commonly defined as the resolution limit of the optical system with aberration, and we can assume that the first corresponding zero is the degree of the defocused system. When we compare Fig. 3-13 (a) to Fig. 3-13 (b), it is evident that the degree of defocus for the optical system with a clear aperture is equal to that of the optical system with specific shaped apertures generated by the light pipe. Therefore, we can conclude that the geometric structure of the light pipe does not affect the resolution limit of

the optical system. We also find that the OTFs of the defocused system can coincide with those of the aberration-free system under the condition of a larger ω_{20}.

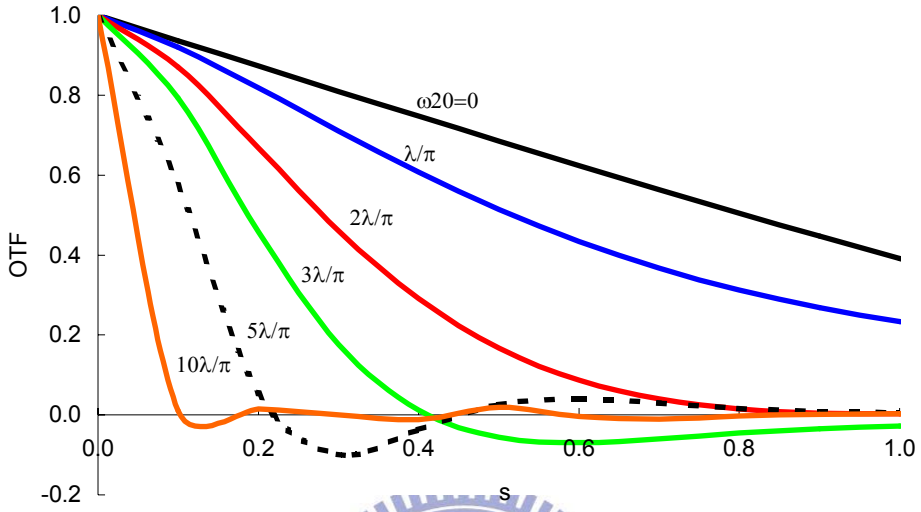

(a)

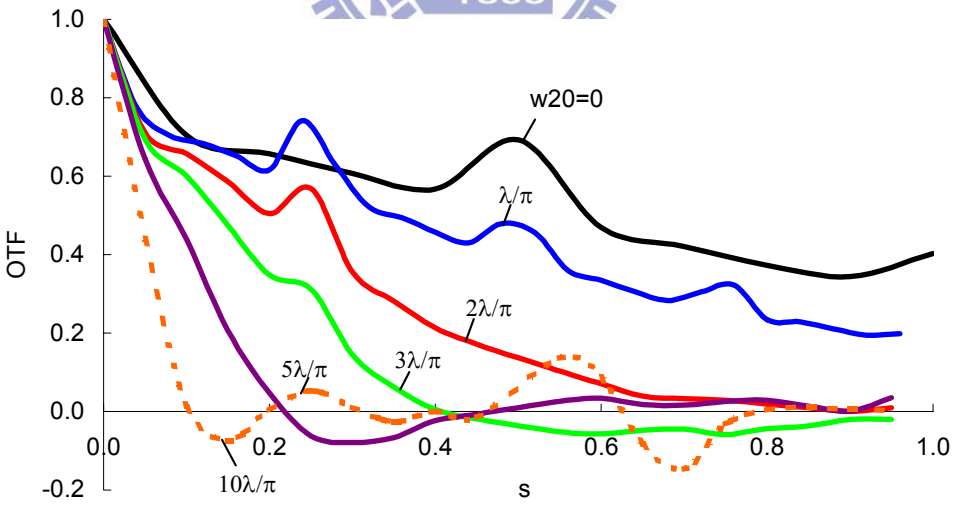

(b)

Figure 3-13 Optical transfer functions in defocused system with (a) a clear aperture and (b) one specific aperture generated by different light pipe's geometric structure with a=b=2.5, c= 2.0 and L=60 for the different defocused coefficients ω20= 0, λ/π, 2λ/π, 3λ/π, 5λ/π and 10λ/π.

3.6 Summary and remarks

The pupil function of the specific shaped aperture generated by illumination with a rectangular hollow light pipe has been investigated. The corresponding OTFs were derived in the aberration-free and defocused optical systems, respectively. The semi-analytical results indicate that the OTF's curve of the optical system can vary with the different shaped apertures that are generated by the illumination with light pipes and light sources of different geometric structures.

In summary, (1) the OTF values of the even-peak frequencies can decrease when the size of the Lambertian light source decreases, (2) if there are a total of $n \times n$ individual apertures within the pupil, then there are n near-periodical peaks on the OTF curve, (3) the OTF's values remain almost unchanged with the different length of the light pipe, (4) the geometric structure of the light pipe does not affect the resolution limit of the optical system, and the case of the defocused system can coincide with that of the aberration-free system under the condition of a larger defocused coefficient ω_{20}.

The semi-analytical method can be extended for any symmetrical cross-section shape of the light pipe, for example, the hexagonal cross-section shape or elliptical one, and any asymmetrical cross-section shape of the light pipe, which can generate the symmetrical and asymmetrical forms of the pupil function, respectively. For these cases, it is difficult to describe the pupil functions of the specific shaped apertures using the photometric method, as we did for rectangular light pipes. However, by utilizing a simulation package, one can easily verify the illumination distribution for the specific light pipes by Monte Carlo non-sequential ray tracing. Then, we can obtain an approximating pupil function which performs a fit for a sequence of ray-tracing data using the interpolation method, and we can calculate and analyze the OTFs of the specific cases finally.

Furthermore, the semi-analytical method can be extended for the lithography optical system with the mercury arc lamp and quartz rectangular light pipe, for the color-LED array with specific light pipe, or for the endoscope optical system with circular light pipe and so on. Also, this method can also be applied to other kinds of light integrator in an optical system, such as for example, the fly-eye integrator. Because the level of the requirements of the resolution for the object, the light-valve and the light-mask will continue to increase, an investigation into the relationship between the projection system and the illumination system is certainly worthwhile and will be explored in the future.

Chapter 4

Programmable apodizer in incoherent imaging system using a digital micromirror device

4.1 Introduction

This chapter proposes a programmable apodizer using a digital micromirror device and the total-internal-reflection prism subsystem for incoherent imaging systems. It is shown that the proposed programmable apodizer can extend the depth of focus with the specific shaped aperture generated by the digital micromirror device. With a scale ratio K equal to or less than 0.05, one can achieve almost the same level of imaging quality as provided by the conventional annular apodizer, where K represents the ratio between the integer multiple of the micromirror's square pixel size and the diameter of the effective aperture stop.

The remainder of this chapter is organized as follows. In Section 2, we revisit on expending the depth of focus (EDOF) and digital micromirror device (DMD). In Section 3, we describe the configuration of the proposed system which consists of a digital micromirror device and a total-internal-reflection prism subsystem is illustrated. In section 4, we derive the pupil functions of the differently shaped apertures which are generated by the digital micromirror device. Then, in section 5, we calculate the optical transfer function and analyze the image quality in such an incoherent imaging system. Furthermore, the corresponding OTFs is evaluated and then to identify the imaging performance for a system of perfect imaging (aberration-free) as well as the defocused one in section 5. Finally, the summary and remark are given in section 6.

4.2 Revisit on extending the depth of focus (EDOF) and digital micromirror device (DMD): technology impact

Extending the depth of focus (EDOF) in an imaging system has been a long-standing issue in optical designs. Enhancing the quality of an image can be achieved and determined not only by the pupil function but also by its amplitude transmittance [1]. Non-uniform amplitude transmission filters can be employed to vary the response of an optical imaging system, for instance, to increase the focal depth and to decrease the influence of spherical aberration. Earlier EDOF investigations and experiments were carried out on annular apodizers [3,4], non-uniform shaped apertures [6,7] and wave-front coding [8,9] in imaging systems, where the nature of light is *incoherent*. However, none of those are programmable for the amplitude transmission at the aperture stop. From the point of view of potential applications as well as from a purely academic interest perspective, it is worthwhile to explore the possibility of how to realize a programmable apodizer for incoherent imaging systems.

In the literature, amplitude-transmitting filters for apodizing and hyper-resolving can be implemented with a programmable liquid-crystal spatial light modulator operating in a transmission-only mode in a *coherent* imaging system with the laser light source, polarizers and quarter-wavelength plates [50,51]. In this chapter, we proposed a programmable apodizer using the digital micromirror device (DMD™; Texas Instrument, Dallas, Tex.) [52] and the total-internal-reflection (TIR) prism subsystem in a polarization-free mode in an *incoherent* imaging system. We evaluated the imaging properties of the incoherent imaging system with a specific shaped aperture generated by DMD™ by calculating the optical transfer function (OTF) using the Hopkins method [37]. We also included the OTF of the specific shaped aperture for the conventional annular apodizer, which has been demonstrated,

both theoretically and experimentally, by Mino and Okano [6] to show that the proposed programmable apodizer can not only extend the depth of focus but can also achieve almost the same level of imaging quality as the conventional annular apodizer in an incoherent imaging system.

4.3 Configuration of the optical system with digital micromirror device

The schematic sketch of an incoherent imaging system using one DMD™ and a charge-coupled device (CCD) imager is illustrated in Fig. 4-1. The system is formed by an image-taking lens module and a prism module. By following the paths of the axial rays as indicated by the solid lines in Fig. 4-1, the rays starting from a point in the object pass through Lens #1 and a prism module. The size of the axial cone of energy from the object is limited by the aperture stop on the DMD™. The DMD™ consists of hundreds of thousands of moving micromirrors that are made to rotate to either +12° or -12° positions depending on the binary state, i.e. on-state or off-state, of the underlying Complementary Metal Oxide Semi-conductor Synchronized Dynamic Random Access Memory (CMOS SRAM) cells below each micromirror [52].

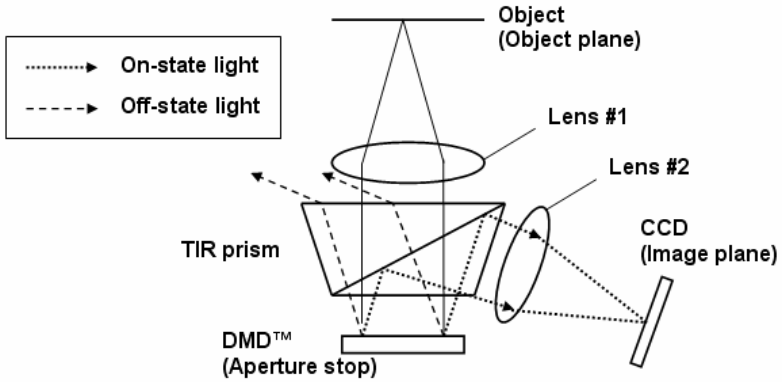

Figure 4-1 Schematic diagram of the incoherent imaging system with the DMD™ and the total-internal-reflection (TIR) prism subsystem.

The DMD™ array size is 1024×768, and the pixel micromirrors measure ~13.7 μm square to form a matrix having a high fill factor of around 90%. The prism system comprises two transparent prisms, with an air gap between them. Total internal reflection (TIR) at the interface between the prism and the air gap is utilized to separate the rays by their angle. Total-internal-reflection (TIR) prism has been applied into the DMD™-based projection display in practice [14]. The prism system can guide the rays onto and away from the DMD™ simultaneously. The rays indicated by the dotted lines in Fig. 4-1 from the object are imaged and focused onto the CCD by Lens #2 when the configuration of the DMD™ is the on-state. When the configuration of the DMD™ is the off-state, the rays indicated by the dashed lines in Fig. 4-1 are steered away in the opposite direction, and the rays from the object are not imaged on the CCD. The DMD™ performs a spatial light modulation to rapidly generate a specific shaped aperture with either uniform or non-uniform illumination distribution at the aperture stop in an imaging system within the limited exposure time. This digital micromirror device can provide a programmable apodizer with a specific binary transmission for the incoherent imaging system. This implementation is not limited by this practical device. The TIR prism performs light separation to manage the illuminations and also make the normal vectors of the object, aperture stop and image planes, respectively, coincide with the optical axis of the optical imaging system with the most compact volume.

4.4 Optical computation for pupil function

The pupil function of a defocused optical system with a circular symmetrical aperture is referring to Eq. (2-2) and given by [6]

$$f(x,y) = T'(x,y)\exp\left[ik\omega_{20}\left(x^2+y^2\right)\right] \qquad x^2+y^2 \le 1$$
$$= 0 \qquad x^2+y^2 > 1 \tag{4-1}$$

where ω_{20} is the wave aberration of the defocused coefficient, (x ,y) are the normalized Cartesian coordinates, and $k = 2\pi/\lambda$, where λ is the wavelength of the light. Function $T'(x,y)$ in Eq. (4-1) represents the binary amplitude distribution over the normalized pupil coordinate that is scaled and normalized to make the outer periphery the unit circle, $x^2+y^2 \le 1$. The binary amplitude transmittance $T'(x,y)$ is generated by the DMD™ as shown in Fig. 4-2.

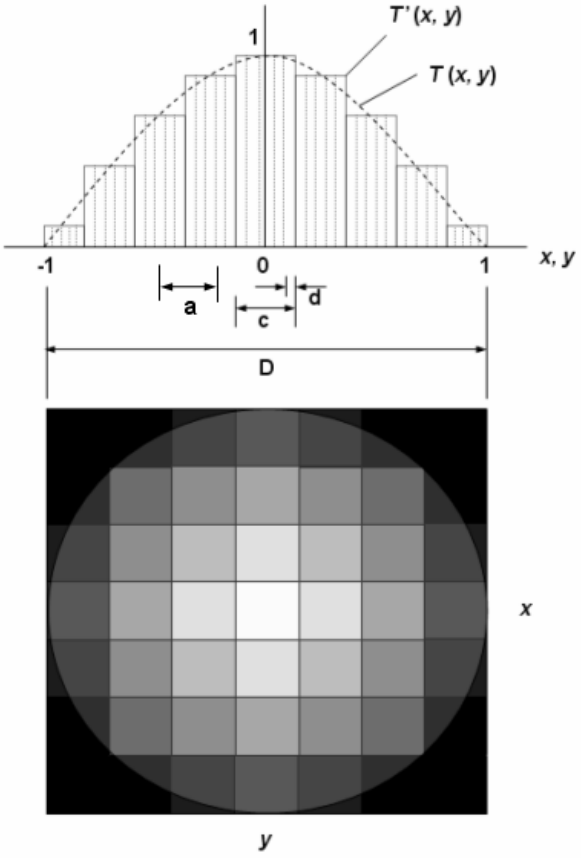

Figure 4-2 Illustration of the binary amplitude transmittance $T'(x,y)$ for the normalized circular aperture which is generated by the DMD™. $T(x,y)$ represents a specifically shaped aperture for a conventional annular apodizer.

We can derive the amplitude transmittance of the shaped aperture $T'(x,y)$ in an on-state configuration as follows,

$$T'(x,y) = E'(x,y) \otimes \sum_m \sum_n T(x,y)\delta(x - \frac{2mc}{D})\,\delta(y - \frac{2nc}{D}) \tag{4-2}$$

$$0 \le |m|, |n| \le Int\left[\frac{D/c - 1}{2}\right] \tag{4-3}$$

where $\otimes$ represents the convolution operation. $T(x,y) = 1 - (x^2 + y^2)$ denotes the amplitude transmittance with a continuous profile at the aperture stop which can extend the focal depth in the imaging system with a conventional annular apodizer [6]. D is the corresponding diameter of the effective aperture stop. c represents the width of each square individual aperture generated by DMD™ in the pupil plane, which is equal to an integer multiple of the value d, with d being the width of each square pixel in the DMD™. $\delta[x - (2mc/D)]\delta[y - (2nc/D)]$ denotes the delta function indicating the location of the individual aperture in the normalized coordinate on the aperture stop. $E'(x,y) = [H(x + c/D) - H(x - c/D)] \times [H(y + c/D) - H(y - c/D)]$ is the binary amplitude transmittance of the individual shaped aperture, which is then scaled and normalized into the pupil coordinate. $Int[(D/c - 1)/2]$ is the interpart of $[(D/c - 1)/2]$. $H(x + c/D)$, $H(x - c/D)$, $H(y + c/D)$ and $H(y - c/D)$ are the step functions. It is evident that the total aperture function is formed by convolving the individual aperture function with an appropriate array of the delta function, each located at one of the coordinate origins $(x_m, y_n) = (2mc/D, 2nc/D)$, where m, n = …-2, -1, 0, 1, 2, …

The quality and location of the individual aperture on the pupil depends on the scale ratio defined as

$$K \equiv (c/D) \tag{4-4}$$

for the specific diameter of the effective aperture stop on the DMD™ in the imaging system. The value of the scale ratio K determinates how many resolutions, how many gray levels and how fast the DMD™ can dynamically generate the shaped apertures within a specific exposure time.

It is worthwhile to give an example for illustration. If the DMD™ array is 1024×768 with a pixel size of 13.7 μm square, and the active area is 14.03 mm × 10.52 mm = 147.60 mm^2 [52], then the number of D is ~10.52mm (i.e. equal to the width of the active area of the DMD) if the effective aperture stop is located on the circular area centered at the actual DMD™. In the case of K =0.05, the width of each individual square aperture c is 0.53mm and is equivalent to 38 square pixels with the same amplitude transmittance. There are 10 (i.e. $Int\left[(D/c - 1)/2\right]+1$) gray levels for a specific shaped aperture including the full bright mode and full dark mode. The current DMD™- based system can offer 8 bits or 256 gray levels within a time period of 5.6 ms per primary color [52]. Thus, the DMD™ can rapidly generate one shaped aperture with 10 gray levels within the very short exposure time of 0.22 ms (i.e. 5.6×10/256) in the case of K =0.05.

The computer program for evaluating Eq. (4-2)-(4-4) is written in MATHEMATICA software [41]. We assumed D=2 for the simplification and evaluated four cases for the scale ratios K=0, K =0.05, K =0.1 and K =0.3. The binary amplitude transmittances of the shaped apertures $T'(x, y)$ are shown in Fig. 4-3. The scale ratio K=0 stands for the amplitude transmittance with a continuous profile. It is evident that the scale level of the binary amplitude transmission at the aperture stop increases with the reduction of scale ratio K, and the distribution of the binary amplitude transmission gets close to the continuous profile if the scale ratio K decreases.

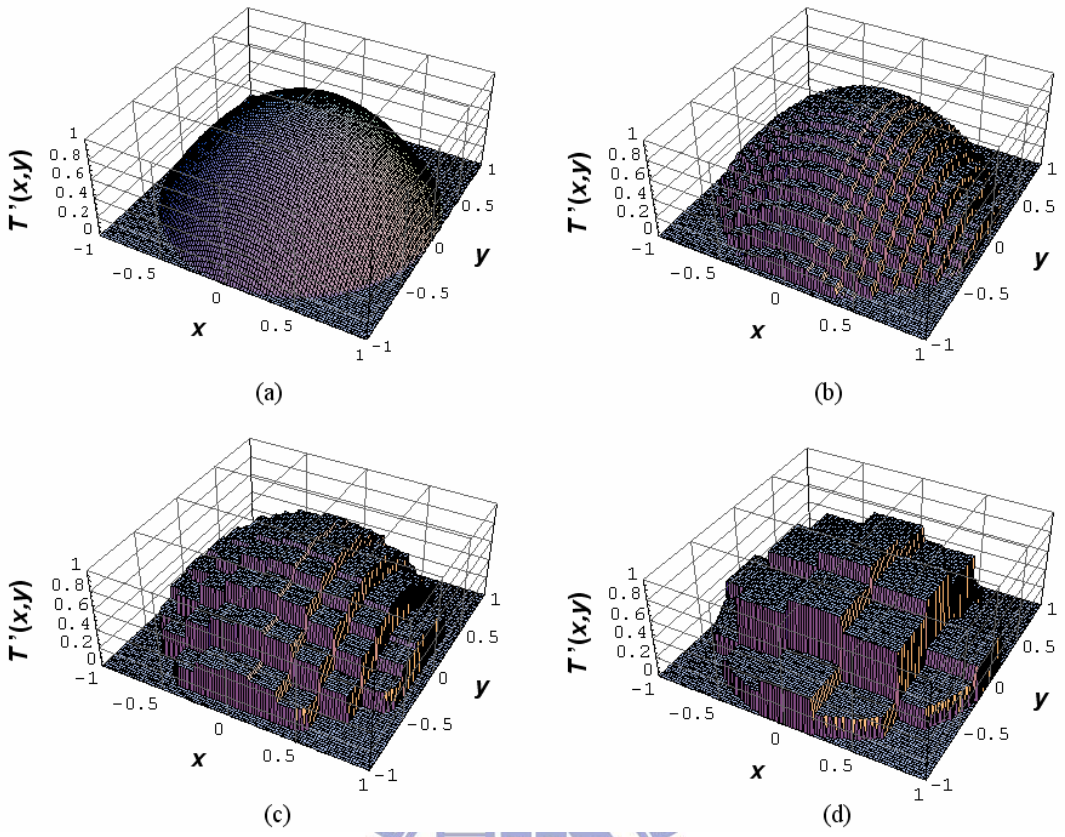

Figure 4-3 Binary Amplitude transmittance $T''(x,y)$ with $T(x, y)$ =1- (x^2+y^2) on the normalized pupil in the condition of D=2, and scale ratios at (a) K=0, (b) K=0.05, (c) K=0.1, and (d) K=0.3, which are generated by DMD™.

In order to evaluate the relationship between the image performance and the size of the individual square aperture on the normalized pupil, we modified Eq. (4-2) and (4-3) to the following equations.

$$T'(x,y) = E'(x,y) \otimes \sum_m \sum_n T(x,y)\delta(x - \frac{2ma}{D})\,\delta(y - \frac{2na}{D}) \tag{4-5}$$

$$0 \le |m|, |n| \le Int\left[\frac{D/a - 1}{2}\right] + 1 \tag{4-6}$$

where $\otimes$ represents the convolution operation. $T(x,y) = 1$ denotes the amplitude transmittance with a clear aperture. D is the corresponding diameter of the effective aperture stop. c represents the width of each square individual aperture generated by DMD™ in the pupil plane. The parameter a represents the distance between each square individual aperture as shown in Fig.

4-2. $\delta[x-(2ma/D)]\delta[y-(2na/D)]$ denotes the delta function indicating the location of the individual aperture in the normalized coordinate on the aperture stop. $E'(x,y)=[H(x+c/D)-H(x-c/D)]\times[H(y+c/D)-H(y-c/D)]$ is the binary amplitude transmittance of the individual shaped aperture, which is then scaled and normalized into the pupil coordinate. $Int[(D/a-1)/2]$ is the interpart of $[(D/a-1)/2]$. $H(x+c/D)$, $H(x-c/D)$, $H(y+c/D)$ and $H(y-c/D)$ are the step functions. It is evident that the total aperture function is formed by convolving the individual aperture function with an appropriate array of the delta function, each located at one of the coordinate origins $(x_m, y_n)=(2ma/D, 2na/D)$, where m, n = …-2, -1, 0, 1, 2, … We assumed D=2 and a=0.25 in Eq. (4-5) and (4-6). Four cases of the binary amplitude transmittances $T'(x,y)$ for c=0.05, c =0.1, c =0.15 and c =0.2 were computed and shown in Fig. 4-4. There are nine individual apertures along x-axis and y-axis within the pupil, respectively. The results show that the individual aperture size on the normalized pupil is shrunk with the width of each square individual aperture (i.e. the value c) generated by DMD™. That is equivalent to the term $E'(x,y)$ varied with c in Eq. (4-5).

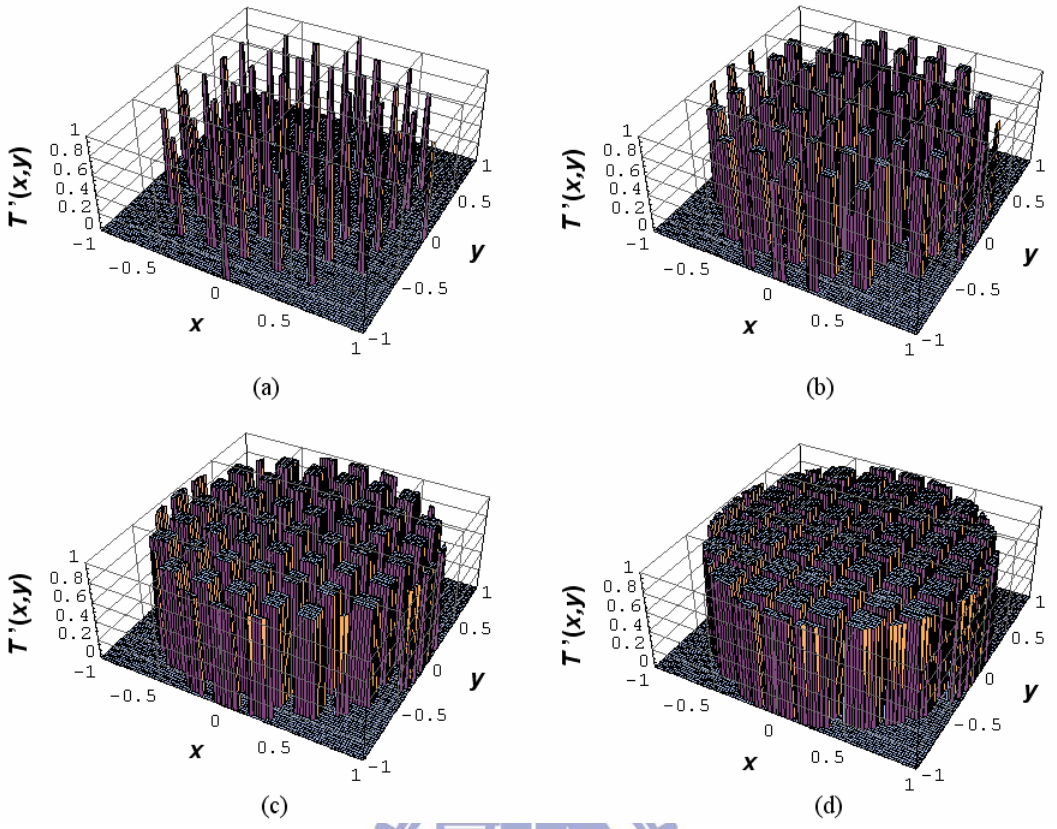

Figure 4-4 Binary Amplitude transmittance $T'(x,y)$ with $T(x, y)$ =1 on the normalized pupil in the condition of D=2 in different conditions of (a) c=0.05, (b) c=0.1, (c) c=0.15 and (d) c=0.2, which are generated by DMD™.

4.5 Optical transfer function and image performance evaluation

The OTF is derived from the autocorrelation of the pupil function by using the Hopkins canonical coordinate [37, 48-49] and is given by

$$\tau(s) = \frac{g(s,0)}{g(0,0)} = \frac{\int_{-\infty}^{\infty}\int_{-\infty}^{\infty} f(x+s/2\,,\,y)\,f^{*}(x-s/2\,,\,y)\,dx\,dy}{\int_{-\infty}^{\infty}\int_{-\infty}^{\infty} f(x\,,\,y)\,f^{*}(x\,,\,y)\,dx\,dy} \tag{4-7}$$

where $f(x, y)$ is the pupil function shown in Eq. (4-1) , $f^{*}(x, y)$ is the complex conjugate of $f(x, y)$, and s is defined as the spatial frequency $s \equiv 2F\lambda N$. Here F is the f-number of the imaging lens system, λ is the wavelength and N is the number of cycles per unit length in the image plane. The denominator of Eq. (4-7) is the

normalizing factor for making $\tau_0(0) = 1$. The $g(s, 0)$ and $g(0, 0)$ in the OTF for the pupil function $f(x, y)$ can then be given by

$$g(s,0) = \int_{-\left[1-(s/2)^2\right]^{1/2}}^{\left[1-(s/2)^2\right]^{1/2}} \int_{-\left[\left(1-y^2\right)^{1/2}-s/2\right]}^{\left[\left(1-y^2\right)^{1/2}-s/2\right]} T'\left(x+\frac{s}{2}, y\right) \cdot T'\left(x-\frac{s}{2}, y\right) exp\,[iAx]\,dxdy \quad (2\text{-}8)$$

and

$$g(0,0) = \int_{-1}^{1} \int_{-\left(1-y^2\right)^{1/2}}^{\left(1-y^2\right)^{1/2}} [T'(x, y)]^2\, dxdy \quad (2\text{-}9)$$

where $A = 2k\,\omega_{20}\,s$. Because the pupil function is an even function, the term of $exp[\,iAx]$ can be reduced to $cos\,[\,Ax]$ in the integral of Eq. (2-8). Then $g(s, 0)$ can be rewritten as

$$g(s,0) = \int_{-\left[1-(s/2)^2\right]^{1/2}}^{\left[1-(s/2)^2\right]^{1/2}} \int_{-\left[\left(1-y^2\right)^{1/2}-s/2\right]}^{\left[\left(1-y^2\right)^{1/2}-s/2\right]} T'\left(x+\frac{s}{2}, y\right) \cdot T'\left(x-\frac{s}{2}, y\right) \cdot cos\,(Ax)\,dxdy \quad (2\text{-}10)$$

Eqs. (2-9) and (2-10) can be further modified as

$$g(0,0) = \sum_{q=-p}^{p} \left\{ \int_{-\left(1-y^2\right)^{1/2}}^{\left(1-y^2\right)^{1/2}} [T'(x, y)]^2\, dx \right\} \cdot \Delta y \quad (2\text{-}11)$$

where $y = (1/p) \times q$, $\Delta y = (1/p)$.

$$g(s,0) = \sum_{q'=-p'}^{p'} \left\{ \int_{-\left[\left(1-y^2\right)^{1/2}-s/2\right]}^{\left[\left(1-y^2\right)^{1/2}-s/2\right]} T'\left(x+\frac{s}{2}, y\right) \cdot T'\left(x-\frac{s}{2}, y\right) \cdot cos\,(Ax)\,dx \right\} \cdot \Delta y \quad (2\text{-}12)$$

where $y = \dfrac{\left[1-(s/2)^2\right]^{1/2}}{p'} \times q'$, $\Delta y = \dfrac{\left[1-(s/2)^2\right]^{1/2}}{p'}$. By replacing the integral in Eqs. (2-9) and (2-10) with the y-axis for the summation in Eqs. (2-11) and (2-12), an initial setting of p=100 is made for the number of intervals used to find the value of $\Delta y = \left[1-(s/2)^2\right]^{1/2} / p'$ and $\Delta y = 1/p$ for $g(s, 0)$ and $g(0, 0)$, respectively. Different numbers of y, from $-\left[1-(s/2)^2\right]^{1/2}$ to $\left[1-(s/2)^2\right]^{1/2}$, are then used to calculate the OTF.

The OTF of the different pupil functions are numerically computed using MATHEMATICA software [41] based on Eqs. (4-2)-(4-4), (4-11) and (4-12) for binary amplitude transmittances of the aperture functions for K=0.05, K=0.1, and K=0.3 which are shown in Fig. 4-3. The OTF of the aberration-free and defocused system with a clear aperture $T(x, y) = 1$ (i.e. a uniform-shaped aperture) and one specific shaped aperture $T(x, y) = 1 - (x^2+y^2)$, as $x^2+y^2 \leqq 1$, and $T(x,y)=0$ as $x^2+y^2 > 1$, over the normalized pupil coordinate which is scaled to make the outer periphery as one unit circle, i.e., $x^2 + y^2 \leq 1$, respectively, already investigated theoretically and experimentally in the literature [6], are calculated again here for comparison.

The results for the aberration-free system i.e., $\omega_{20}= 0$ is shown in Fig. 4-5(a), and the defocused systems with $\omega_{20}= \lambda/\pi$, $3\lambda/\pi$, $5\lambda/\pi$, $10\lambda/\pi$ and $15\lambda/\pi$ are shown in Figs. 4-5 (b)-(f), respectively. We compared the OTF of the different scale ratios K to the OTF of a clear aperture $T(x, y) = 1$. For the large values of ω_{20}, e.g., $5\lambda/\pi$, $10\lambda/\pi$ and $15\lambda/\pi$ as shown in Fig. 4-5(d)-(f), the spatial frequency corresponding to the first zero becomes smaller. Since the spatial frequency of the first zero generally represents the resolution limit of a defocused imaging system, we can take the first zero as defining the degree of focus. The larger degree of focus in the larger value of ω_{20} commonly represents the longer depth of focus in a defocused system. For the large values of ω_{20}, the degree of focus for the aperture with scale ratio K less than 0.3 is larger than for the aperture $T(x, y) = 1$. It is evident that the specific shaped aperture, which is generated by the DMD™ with scale ratio K=0.3 or less, can then extend the depth of focus compared to a clear aperture in the conventional imaging system. We also compared the OTF of the different scale ratios K to the OTF of one specific shaped aperture $T(x, y) = 1 - (x^2+y^2)$. The OTF value of the former increased and got close to the OTF value of the latter when the scale ratio K decreased gradually, especially in the low spatial frequency region. This

shows that the OTFs of the specifically shaped aperture, which are generated by the DMD™, with scale ratio K=0.05 or less can coincide with the OTF of the conventional annular apodizer with continuously-shaped aperture.

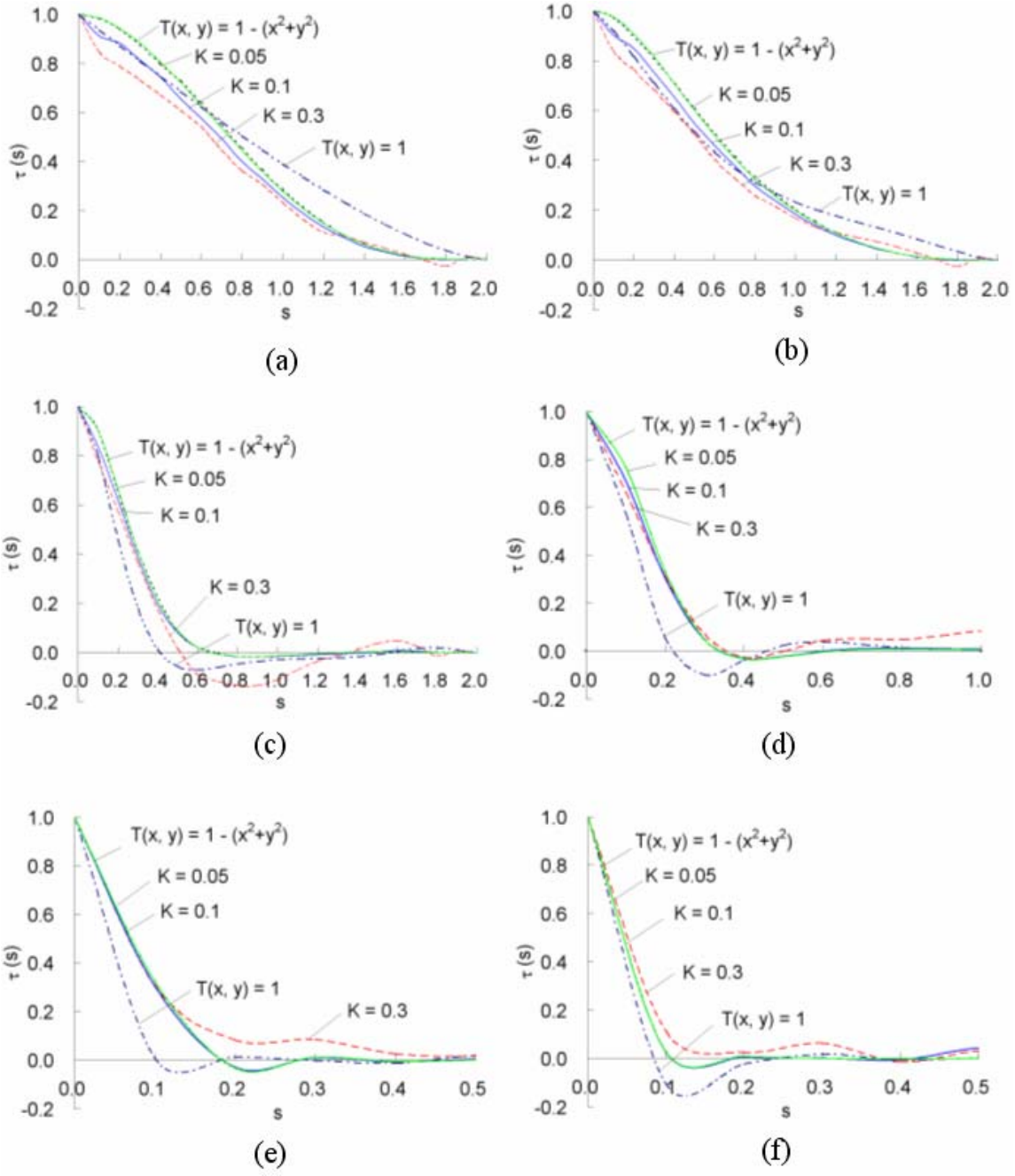

Figure 4-5 Optical transfer functions in an aberration-free system and a defocused system with different defocused coefficients (a) ω_{20}= 0, (b) ω_{20}= λ/π, (c) ω_{20}= 3λ/π, (d) ω_{20}= 5λ/π, (e) ω_{20}= 10λ/π and (f) ω_{20}= 15λ/π, for binary amplitude transmittances of the aperture functions for K=0.05, K=0.1, and K=0.3, which are generated by the DMD™, and for a clear aperture $T(x, y)$ = 1 and one specific shaped aperture $T(x, y)$ =1- (x^2+y^2) of a conventional annular apodizer, respectively.

To highlight the capability of our approach, we take a spoke pattern to explore imaging performance. Referring to Fig. 4-6, in column A, one could see the images for the clear aperture, while in column B, the images for the specific shaped aperture with scale ratio K=0.05 are shown. Furthermore, the lines (a)-(d) correspond to the images obtained with the defocused coefficients of ω_{20}= 0, ω_{20}= 5λ/π, ω_{20}= 10λ/π, and ω_{20}= 15λ/π, respectively. Comparing with the images for the specific shaped aperture, the images for the clear aperture show a more critical loss of contrast at high spatial frequencies with larger ω_{20}. Hence, we can conclude that the image quality will be enhanced as the specific shaped aperture is used, especially for the large defocus coefficients in an imaging system. In other words, as for a real implementation of the DMD™, the specific shaped aperture can extend the depth of focus compared to a clear aperture in the conventional imaging system.

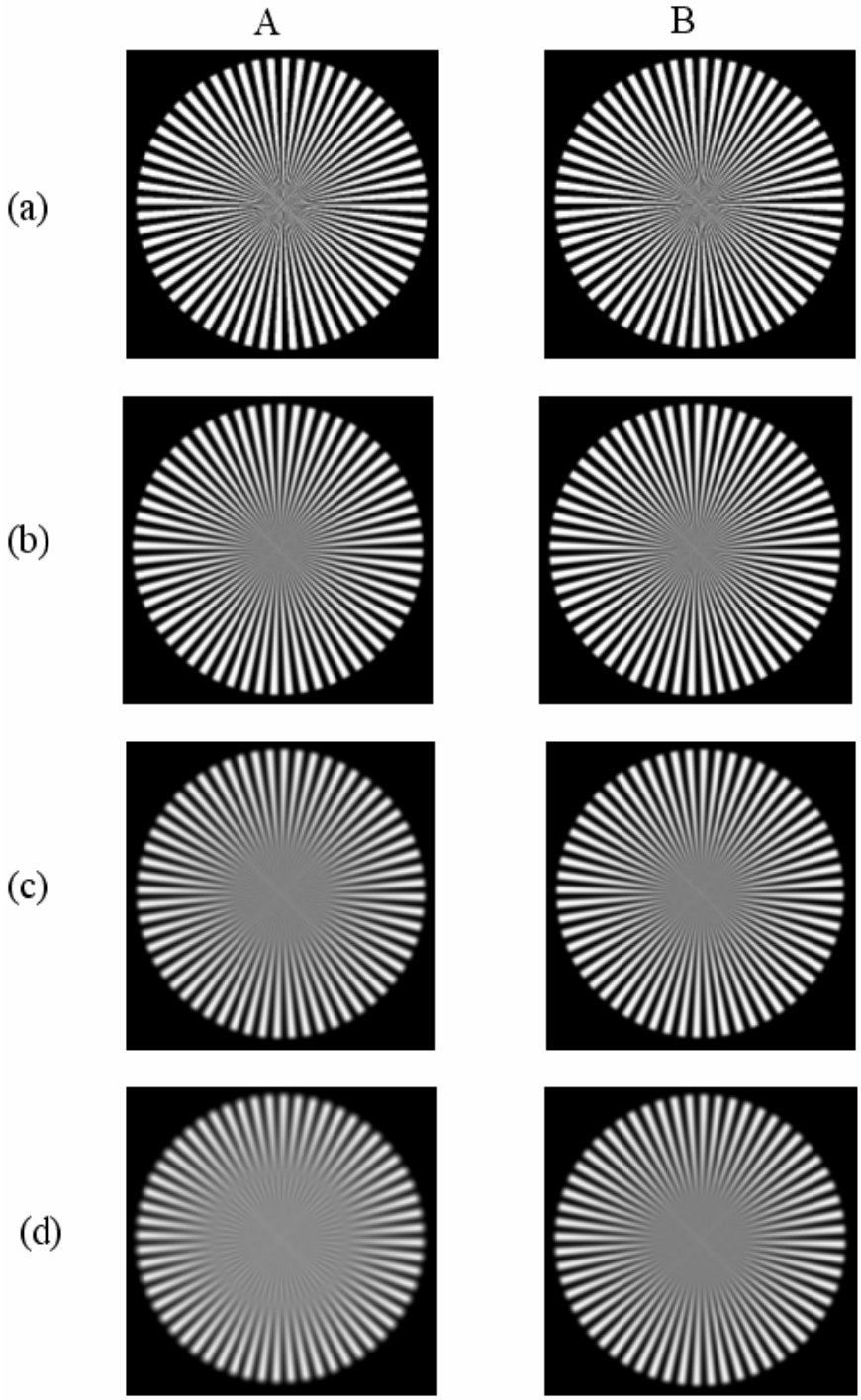

Figure 4-6 The computer-simulated images of spoke patterns for A, a clear aperture, and B, a specific shaped aperture with the scale ratio K=0.05 obtained with different defocused coefficients: (a) ω_{20}= 0, (b) ω_{20}= 5λ/π, (c) ω_{20}= 10λ/π and (d) ω_{20}= 15λ/π.

In order to evaluate the relationship between the image performance and the size of the individual square aperture on the normalized pupil, we computed the OTF of the other types of pupil functions based on Eqs. (4-5)-(4-6), (4-11) and (4-12) for

the binary amplitude transmittances $T'(x,y)$ for c=0.05, c =0.1, c =0.15 and c =0.2 in the conditions of $T(x,y)=1$, D=2 and a=0.25 which is shown in Fig. 4-4. The OTF of the aberration-free system with a clear aperture $T(x, y) = 1$ was also calculated here for comparison. The OTF's calculation results for the aberration-free system are shown in Fig. 4-7. The general tendency of the OTF curve versus the number of the individual aperture within the pupil is readily evident. There are nine individual apertures along x-axis and y-axis within the pupil, respectively. Meanwhile, there are nine peaks on the OTF curve at the near-periodic spatial frequencies around 0, 0.25, 0.50, 0.75, 1.00, 1.25, 1.50, 1.70 and 1.90. The OTF values of the odd-peak frequencies for different sizes of the individual apertures (i.e., value c) remain very similar to the values of the OTF's of the corresponding frequencies for the clear aperture. However, the OTF values of the even-peak frequencies can decrease with decrease in the size of the individual aperture. Therefore, if the size of an individual aperture is much less than that of pupil, then OTF values of the even-peak frequencies will almost be zero.

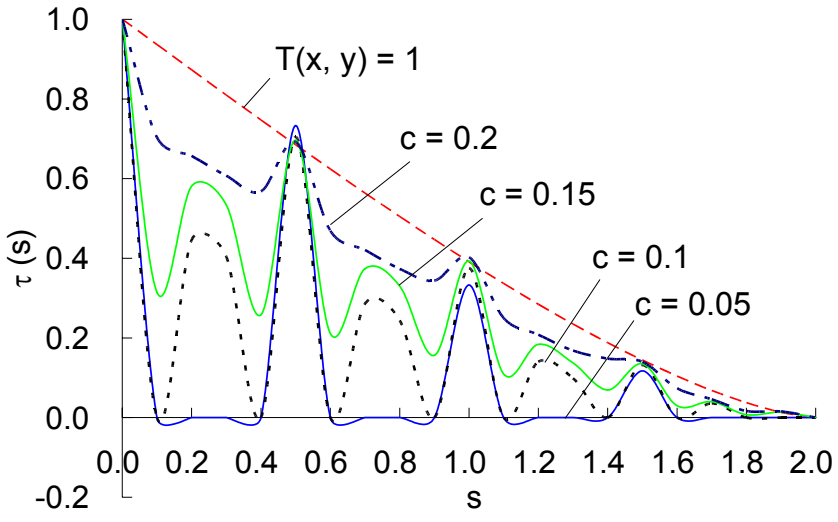

Figure 4-7 Optical transfer functions in an aberration-free system with a clear aperture and the binary amplitude transmittances of the aperture functions for different conditions of c=0.05, c=0.1, c=0.15 and c=0.2, which are generated by the DMD™.

4.6 Summary and remarks

One programmable apodizer using the digital micromirror device (DMD™) and the total-internal-reflection (TIR) prism system has been applied to incoherent imaging systems. The OTF model semi-analytically demonstrated that the proposed programmable apodizer for the specifically shaped aperture generated by a digital micromirror device can extend the depth of focus compared to a clear aperture in a defocused system. It shows that the specifically shaped aperture with scale ratio K equal to or less than 0.05 can achieve the same improved imaging quality as that of the conventional annular apodizer. Meanwhile, the general tendency of the OTF curve versus the number of the individual aperture and the binary amplitude transmittances with the discontinuous peak profile within the pupil has been investigated. It is evident that the OTF values of the even-peak frequencies can decrease when the size of the individual aperture decreases.

It is worth noting that the proposed model can rapidly generate one specifically shaped aperture with 10 gray levels within the very short exposure time of 0.22 ms in the case of K =0.05. On the other hand, the TIR prism can make the normal vectors of the object, aperture stop and image planes, respectively, coincide with the optical axis of the optical imaging system for a very compact volume. Further refinement of the shaped aperture design should be able to dynamically provide improved imaging quality for many varied scenes.

Chapter 5

Extending the depth of field in conventional imaging system with structured light at aperture stop

5.1 Introduction

In this chapter we propose a programmable structured light to shape one binary incoherent source of illumination to improve the depth of focus and numerically demonstrate the improvement of image quality in conventional imaging system such as photography, projector and optical microscopy. As a theoretical demonstration and as a reference for further practical implementation, we also propose to use a digital micromirror device (DMD™; Texas Instrument, Dallas, Tex.) [58] or light emitting diode (LED) array module in a non-imaging subsystem. The shaped pupil with this specific incoherent illumination, i.e., the proposed structured light, is projected onto the aperture stop in an incoherent imaging system. We will evaluate the imaging properties of the projection system with defocus, spherical aberration and coma, where a specifically shaped pupil on the aperture stop is embedded, by calculating the optical transfer function (OTF) using the Hopkins method [37]. We then take the computer-simulated images of resolution patterns to explore the image performance. We also include the OTF of the specifically shaped aperture for the conventional annular apodizer, as demonstrated, both theoretically and experimentally by Mino and Okano [6], to show that the proposed programmable shaped pupil does not only extend the depth of focus but can also achieve almost the same level of

imaging quality as the conventional annular apodizer in an incoherent imaging system.

The remainder of this chapter is organized as follows. In Section 2, we introduce what structured lighting and smart lighting are. In Section 3, we revisit Kohler illumination and its applications. We design and illustrate three configurations of (1) a photography system with structured light, (2) a projector system with embedded illumination modulator and (3) a microscopic system with structured illumination in Sections 4, 5 and 6, respectively. Then, in Section 7, we compute the pupil functions of the differently shaped pupil that are generated by DMD and LED, and we calculate the optical transfer function for those optical systems of perfect imaging (aberration-free) as well as the defocused, spherical and coma aberrations. Furthermore, the corresponding image performances are evaluated and identified in Section 8. Finally, the conclusions are given in section 9.

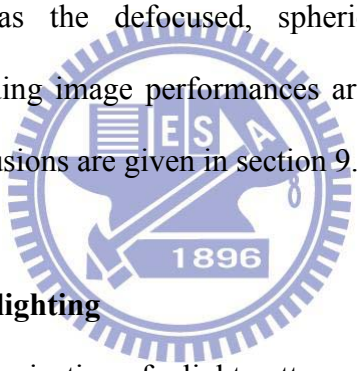

5.2 Revisit on structured lighting

Structured light is the projection of a light pattern, such as a plane, grid, or more complex shape, at a known angle onto an object as illustrated in Fig 5-1. This technique can be very useful for imaging and acquiring dimensional information [53,54]. The most often used light pattern is generated by fanning out a light beam into a sheet-of-light using a laser scanning system or an optical projector. When a sheet-of-light intersects with an object, a bright line of light can be seen on the surface of the object. By viewing this line of light from an angle, the observed distortions in the line can be translated into height variations. Either scanning or projecting the object with the light constructs 3-D information about the shape of the object. This is the basic principle behind depth perception for machines, or 3D machine vision. Another method of obtaining optical sectioning is using structured light in a

conventional wide-field microscope by projecting a single-spatial-frequency grid pattern onto the object [55] as shown in Fig. 5-2. It provides a method with partially coherent illumination to resolve the entire image volume of an object that is substantially similar to those obtained with confocal microscopes. Above investigations are to project the specific structured light onto the object to produce an optically sectioned image for detecting the depth of field in photography or extending the depth of focus in microscopy.

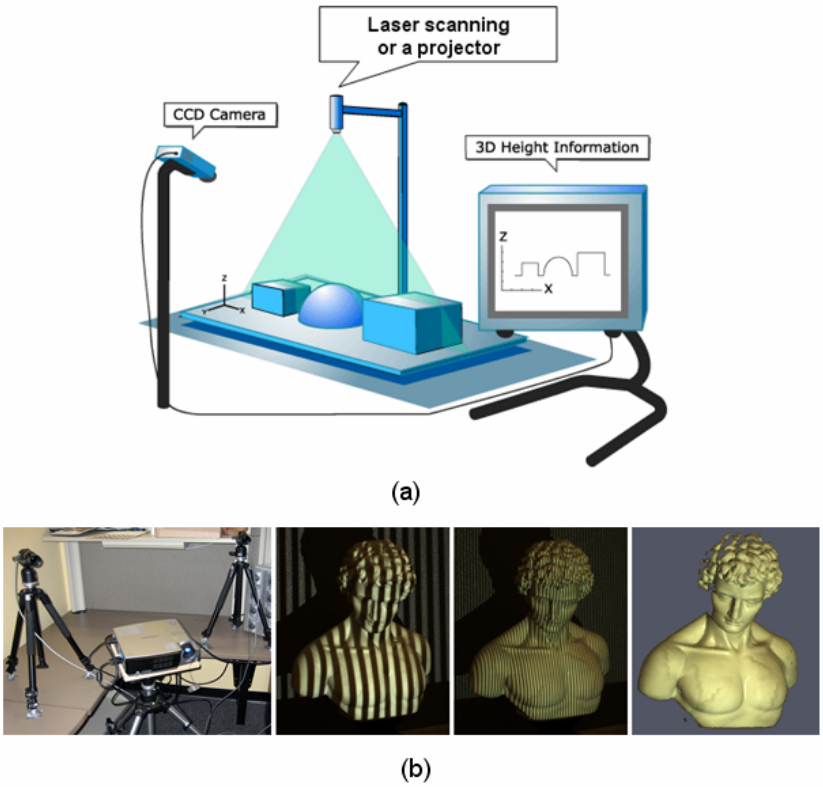

Figure 5-1 (a) A schematic diagram of structured lighting system for 3D Scanning [56]. (b) From left to right: a structured light scanning system containing a pair of digital cameras and a single projector, two images of an object illuminated by different bit planes of a gray code structured light sequence, and a reconstructed 3D point cloud [57].

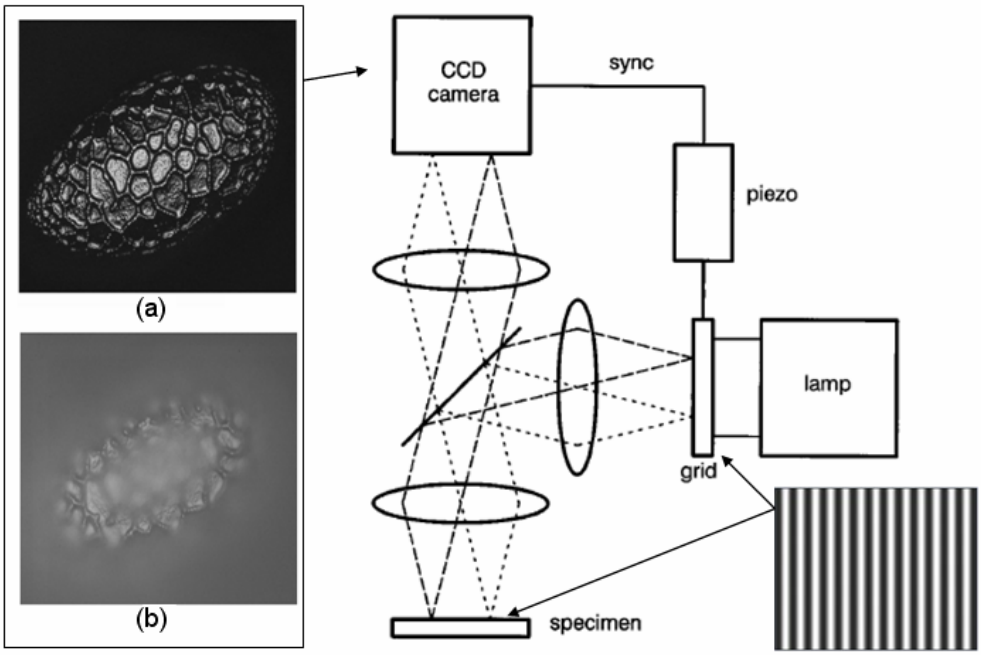

Figure 5-2 A schematic diagram of the structured lighting system for a conventional wide-angle microscopy [55] where (a) is an autofocus image of lily pollen grain, obtained by the structured lighting microscopic system. The field size is 100μm × 70μm. (b) Conventional image of lily pollen grain when the microscope is focused in a mid-depth plane.

5.3 Köhler illumination and its modification

Köhler illumination [18] is a popular method used in optical microscopy and projector. The general configuration of Köhler illumination is schematically diagrammed in Fig. 5-3. It provides a uniform illumination and high optical collection efficiency in an incoherent imaging system. The function of the condenser is to image the light source directly into the aperture stop of the imaging lens system so that the lens aperture has the same brightness as the light source. The function of the imaging lens system is to produce a bright and uniform illuminated object on the image plane. For optical microscopy, the object is either a transparent or a reflective sample, and the image plane is human eyes or a charge-coupled device (CCD) imager. For optical projector, the object is a film or a light valve, such as liquid crystal device (LCD), and the image plane is a screen. It is apparent that the maximum illumination on the image plane is limited by the size of the aperture stop in the imaging lens system. Therefore,

if the imaging size of light source is equal to or greater than the size of the aperture stop, the illumination is optimized, and if the condenser is sufficiently larger so that the illumination light is not vignetted, the illumination over the full image filed is as uniform as possible.

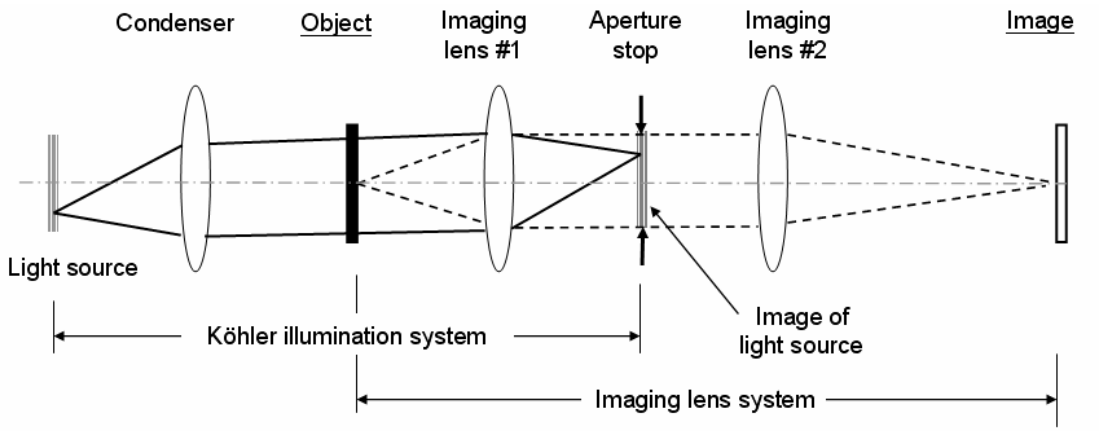

Figure 5-3 General schematic diagram of the Köhler illumination system and the conjugate focal planes.

The primary aberrations which are concerned in Köhler illumination system are spherical and chromatic aberrations; coma, field curvature, astigmatism, and distortion are of secondary importance [18]. The spherical aberration could be controlled by splitting one condenser into two or three spherical lens elements, or by replacing the condenser with the aspherical lens element in order to correct the illumination light at the marginal zone of the condenser and the edge of the field. The chromatic aberration could be corrected by designing one achromatic doublet as usual. It should be noted that if the imagine lens aperture is only partially filled by the light source image, the diffraction effects will differ from those associated with a fully illuminated aperture. For example, if only the center of the aperture is illuminated, this “semi-coherent illumination” causes the modulation transfer function (MTF) at

low spatial frequencies to be increased, and the MTF at high spatial frequencies to be reduced.

In this chapter we will expend this principle and investigate what the image quality will be if we modulate the illumination distribution at the aperture stop in an incoherent imaging system as shown in Fig 5-4. We design a programmable structured light to shape one binary incoherent source of illumination using a spatial light modulator (SLM), such as DMD and LED array, which is imaged into the aperture stop in an incoherent imaging system and calculate the optical transfer function (OTF) for evaluating the corresponding image performance.

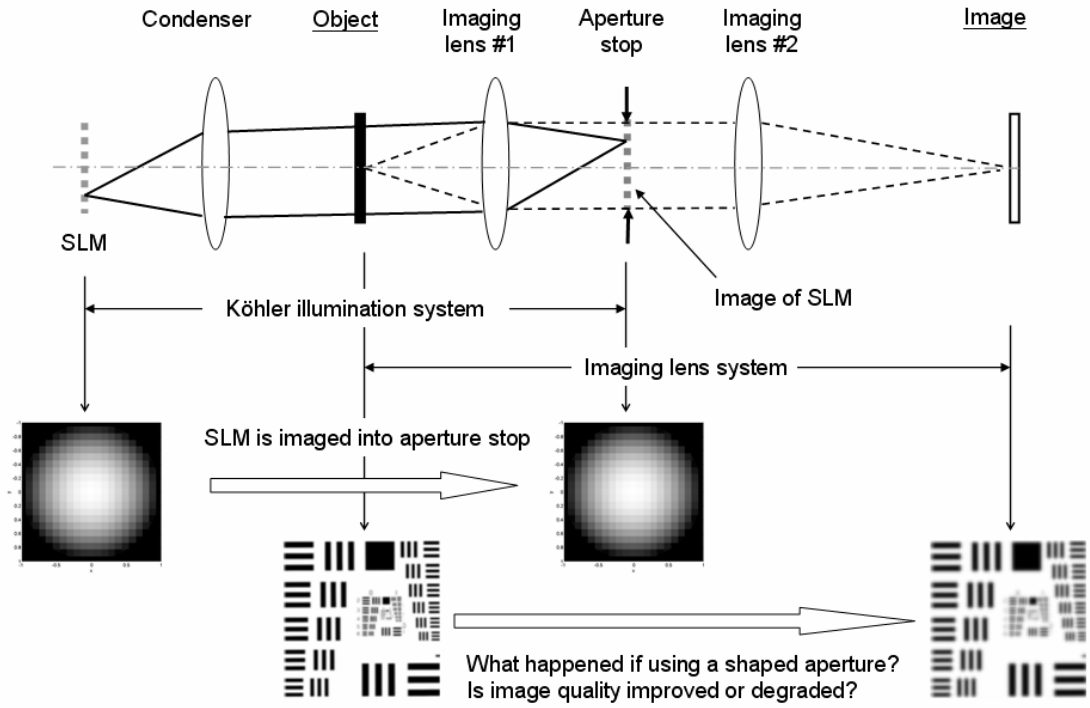

Figure 5-4 Schematic diagram of the modified Köhler illumination system with a shaped aperture using the structured light and the conjugate focal planes.

5.4 Configuration of the photography systems with structured light

The schematic sketch of an optical system with the programmable shaped pupil in photography is illustrated in Fig. 5-5. The system consists of a non-imaging

subsystem and an incoherent imaging subsystem. The non-imaging subsystem is formed by an illumination optical module, a uniform white light source (for example, a white high-brightness light emitting diode, LED) and a digital micromirror device (DMD™; Texas Instrument, Dallas, Tex.) [58] The DMD is a means of creating the structured light. This implementation is not limited by this practical device. The imaging subsystem is formed by an image-taking lens module and a charge-coupled device (CCD) imager.

Two kinds of incoherent imaging systems for a reflective object and a transparent one are shown in Fig. 5-5(a) and Fig 5-5(b), respectively. In the non-imaging subsystem, by following the paths of the axial rays, as indicated by the dotted lines in Fig. 5-5, the rays starting from a uniform white light source pass through Lens #1 and project on DMD™. Then, the uniform illumination is projected on the object field using Lens #1 and Lens #2. The size of the axial cone of energy from the object is limited by the active area on the DMD™. The DMD™ consists of hundreds of thousands of moving micromirrors that are made to rotate to either +10° or -10° positions depending on the binary state, i.e. on-state or off-state, of the underlying Complementary Metal Oxide Semi-conductor Synchronized Dynamic Random Access Memory (CMOS SRAM) cells below each micromirror [58]. The DMD array size is 800×600, and the pixel micromirrors measure ~17.0μm square to form a matrix having a high fill factor of around 90%. The rays, indicated by the solid lines in Fig. 5-5 from the DMD™, are imaged onto the aperture stop in imaging system by Lens #2 and Lens #3 when the configuration of the DMD™ is in the on-state. When the configuration of the DMD™ is in the off-state, the rays are steered away in the opposite direction, and the rays from DMD™ are not imaged onto the aperture stop.

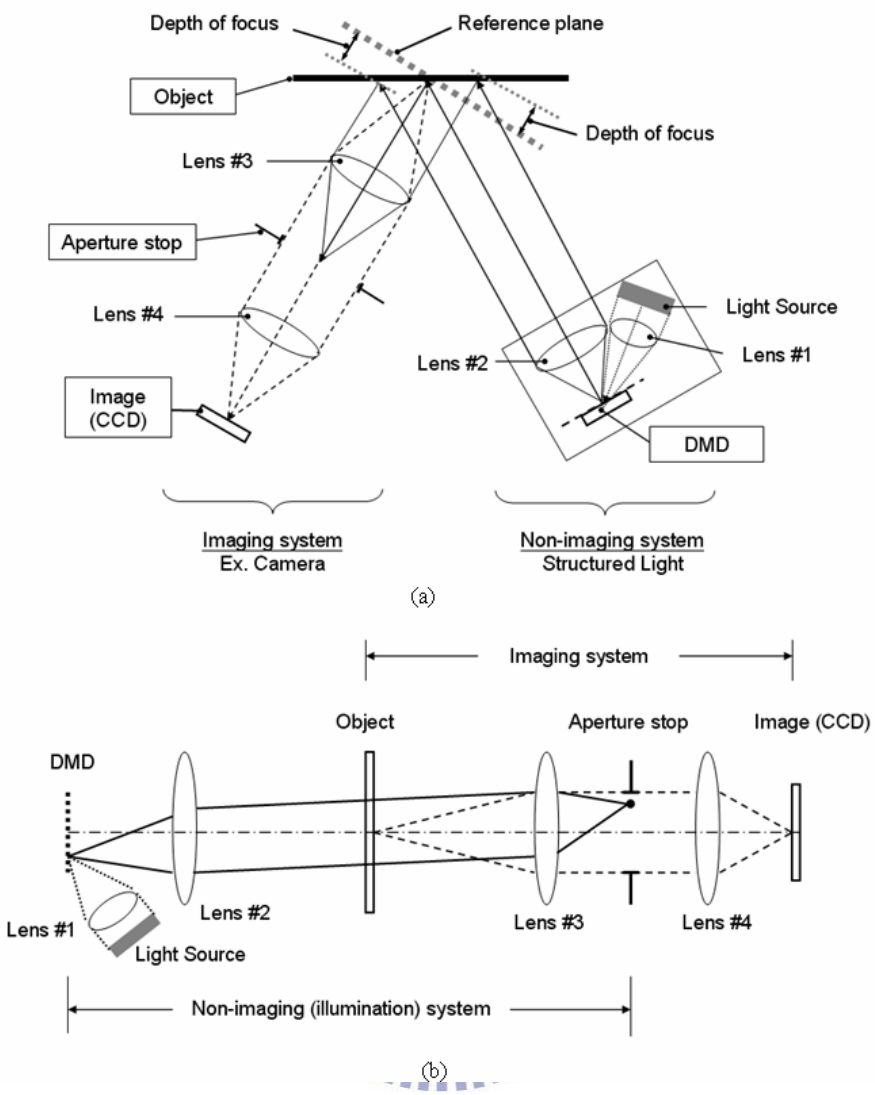

Figure 5-5 Schematic diagrams of the optical systems with one incoherent imaging subsystem and one non-imaging subsystem to illustrate the relationship between the aperture stop and the field for (a) a reflective object and (c) a transparent object.

In the imaging subsystem, the paths of the of the axial rays as indicated by the dashed lines in Fig. 5-5, start from the object and pass through Lens #3 and Lens #4 and are imaged onto the image field on CCD. The size of the axial cone from the object is limited by the *f*-number of the image-taking lens module. By following the paths of the axial rays as indicated by the solid lines, the aperture stop in the imaging subsystem is designed to be a conjugate with the DMD™ plane in the non-imaging subsystem by using Lens #2 and Lens #3. We assume the aberration free in this

non-imaging subsystem. In most cases of an imaging system, there is a difference in the depth of focus between the two extreme sides of the object, compared to the reference plan on the central field of the object plan as shown in Fig. 5-5.

For the entire optical system, the DMD™ performs a spatial light modulation to rapidly and field-sequentially generate a specific structured lighting with either uniform or non-uniform illumination distribution on the aperture stop of the imaging subsystem. This structured flash light can provide a programmable shaped pupil with a specific binary transmission for the incoherent imaging system in photography.

5.5 Configuration of the projector system with embedded illumination modulator

The schematic diagram of the projector system is illustrated in Fig. 5-6. The system consists of an illumination modulator and a projection module. The illumination modulator is formed by a uniform white light source (typically, for example, a white high-brightness light emitting diode or high pressure mercury lamp), a prism module and a digital micromirror device (DMD™; Texas Instrument, Dallas, Tex.) [58]. Obviously, the implementation is not limited by this kind of practical device. The projection module is a projection lens.

In the illumination modulator, by following the optical path of the illumination rays as indicated by the dotted lines in Fig. 5-6, the rays starting from a uniform light source pass through Lens #1 and a prism module. The size of the axial cone of energy from the light source is limited by the active area on the DMD™. The DMD™ consists of hundreds of thousands of moving micromirrors that are made to rotate to either +12° or -12° positions depending on the binary state, i.e. on-state or off-state, of the underlying Complementary Metal Oxide Semi-conductor Synchronized Dynamic Random Access Memory (CMOS SRAM) cells below each micromirror [58]. The

DMD™ array size is 1024×768, and the pixel micromirrors measure ~13.7 μm square to form a matrix having a high fill factor of more than 90%. The prism system comprises two transparent prisms with an air gap between them. Total internal reflection (TIR) at the interface between the prism and the air gap is utilized to separate the rays by their angles. Total-internal-reflection (TIR) prism has been applied into the DMD™-based projection display [14]. The prism system can guide the rays onto and away from the DMD™ simultaneously. The rays, indicated by the solid lines in Fig. 5-6 from the DMD™, are imaged onto the aperture stop in projection system by Lens #2 and Lens #3 when the configuration of the DMD™ is in the on-state. When the configuration of the DMD™ is in the off-state, the rays are steered away in the opposite direction, and the rays from DMD™ are not imaged onto the aperture stop.

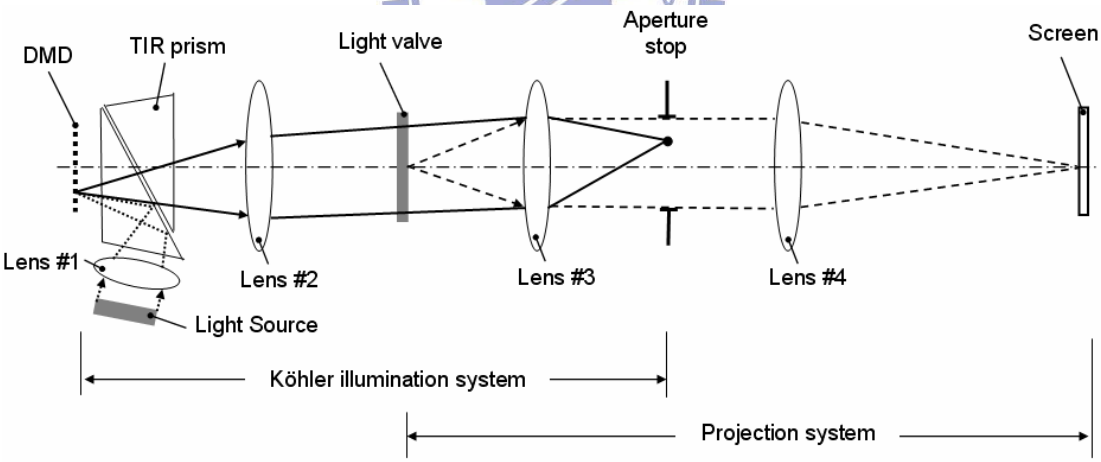

Figure 5-6 Schematic diagram of the projector system with a Köhler illumination subsystem and a projection subsystem to illustrate the relationship between the aperture stop and the digital micromirror device. The dotted and solid lines indicate the optical path of the illumination rays in a Köhler illumination system. The dashed lines indicate the optical path of the imaging rays in a projection system.

In the projection system, the optical path of the imaging rays as indicated by the dashed lines in Fig. 5-6, start from the light valve and pass through Lens #3 and Lens

#4 and then are imaged onto the screen. The light valve utilized here is a transmissive liquid crystal device (LCD) with the angular dependence of the transmittance which could reduce the amplitude transmittance especially on the peripheral area of the aperture stop. We assume the angular dependence of the transmissive LCD could be ignored for simplification because the incident angle of the illumination light onto LCD panel is about 12°~14.5°,which is equivalent to *f*-numbers 2.0~2.4 in a typical projector system, much smaller than the viewing angle of a typical LCD panel [59]. Obviously, the implementation is not limited by this kind of device, for example, we could also use DMD™ and liquid crystal on silicon (LCoS). The size of the axial cone from the light valve is limited by the *f*-number of the projection lens module, the acceptable cone angle and the physical size of the light valve, and the *f*-number of the illuminator modulator according to Ètendue theorem which is an optical invariant of a light beam relative to the beam divergence and cross-sectional area for estimating maximum collection efficiency in a projection system [22].

By following the optical path of the illumination rays as indicated by the solid lines in Fig. 5-6, the aperture stop in the projection system is designed to be a conjugate with DMD™ plane by using Lens #2 and Lens #3. For simplification in illustration, we assume that the pupil aberration is corrected and could be ignored for this Köhler illumination system. For the entire optical system, the DMD™ performs a spatial light modulation to rapidly and field-sequentially generate a specifically shaped pupil with either uniform or non-uniform illumination distribution on the aperture stop of the projection system.

5.6 Configuration of the microscopic system with structured illumination

The schematic diagram of the optical system with programmable structured illumination in a microscope is illustrated in Fig. 5-7, where two kinds of microscopic

systems, transparent type and reflective one, are shown with (a) and (b) respectively. The system consists of a Köhler-illumination subsystem and an imaging subsystem. The Köhler-illumination subsystem includes a condenser lens module and one set of illumination modulator with DMD™ which is mentioned in Section 5.5. The imaging subsystem has an image-taking lens module and a charge-coupled device (CCD) imager.

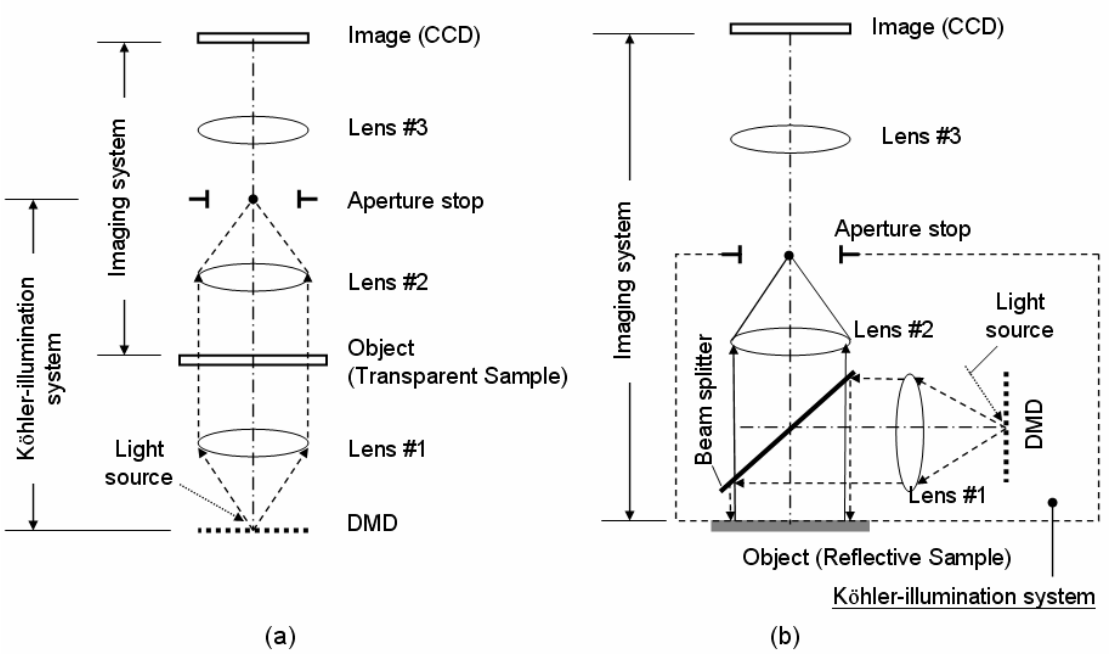

Figure 5-7 Schematic diagrams of the optical systems in microscopy with DMD illumination modulator for (a) a transparent sample and (b) a reflective sample.

For a transparent object in the Köhler-illumination subsystem, by following the paths of the marginal rays, as indicated by the dashed lines in Fig. 5-7 (a), the rays starting from DMD pass through Lens #1 (i.e. a condenser) and the transparent object. Then, the light of DMD is projected on the aperture stop of the image subsystem using Lens #1 and Lens #2. The size of the axial cone of energy from the DMD is limited by the size of aperture stop. In the imaging subsystem, the object is imaged onto the image field on CCD by the use of Lens #2 (i.e. objective lens) and Lens #3

(i.e. eyepiece). For a reflective object, by following the paths of the marginal rays, as indicated by the dashed lines in Fig. 5-7 (b), the rays starting from DMD pass through Lens #1 (i.e. a condenser), and the illumination light is folded by a beam splitter and arrives the object plane. Then, the illumination of DMD is reflected from object and projected on the aperture stop in the image subsystem using Lens #2 by following the paths of the rays, as indicated by the solid lines. In the imaging subsystem, the object is imaged onto the image field on CCD by the use of Lens #2 (i.e. objective lens) and Lens #3 (i.e. eyepiece). We assume there is no aberration in this Köhler-illumination subsystem to simplify the analysis.

For the entire optical system, the DMD performs a spatial light modulation to rapidly generate a specific structured illumination with either uniform or non-uniform illumination distribution on the aperture stop of the imaging subsystem. This structured illumination can provide a programmable shaped pupil with a specific transmission for the imaging system in microscope.

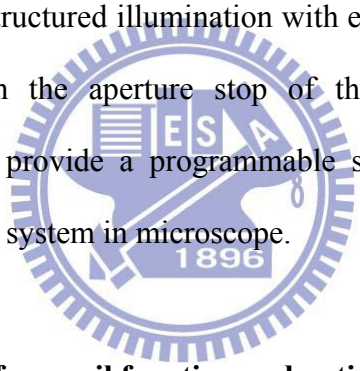

5.7 Optical computation for pupil function and optical transfer function

The pupil function of an imaging system with defocused, spherical aberration and coma for a circular symmetrical aperture is referring to Eq. (2-2) and given by

$$f(x,y) = T'(x,y)\exp\left\{ik\left[\omega_{20}\left(x^2+y^2\right)+\omega_{40}\left(x^2+y^2\right)^2+\omega_{31}\left(x^2+y^2\right)\times y\right]\right\} \qquad x^2+y^2 \le 1 \quad (5\text{-}1)$$

$$= 0 \qquad x^2+y^2 > 1$$

where ω_{20} is the wave aberration of the defocus coefficient, ω_{40} denotes the coefficient for spherical aberration, and ω_{31} denotes the coefficient for coma aberration. (x,y) are the normalized Cartesian coordinates, and $k = 2\pi/\lambda$, where λ is the wavelength of the light. Function $T'(x,y)$ in Eq. (5-1) represents the binary amplitude distribution over the normalized pupil coordinate that is scaled and

normalized to make the outer periphery the unit circle, $x^2 + y^2 \le 1$. The binary amplitude transmittance $T'(x, y)$ is generated by the DMD™ as shown in Fig. 5-8.

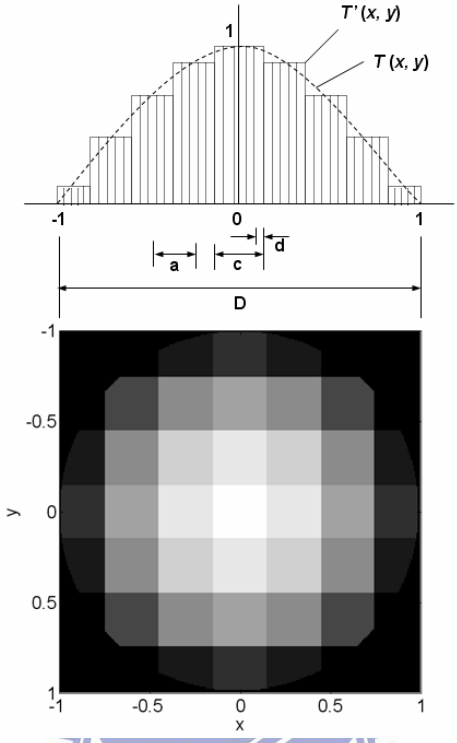

Figure 5-8 Illustration of the binary amplitude transmittance $T'(x, y)$ for the normalized circular aperture which is generated by the DMD™. $T(x, y)$ represents a specifically shaped aperture for a conventional annular apodizer.

We can derive the amplitude transmittance of the shaped aperture $T'(x, y)$ in an on-state configuration as follows,

$$T'(x, y) = E'(x, y) \otimes \sum_m \sum_n T(x, y) \delta(x - \frac{2mc}{D}) \, \delta(y - \frac{2nc}{D}) \tag{5-2}$$

$$0 \le |m|, |n| \le Int\left[\frac{D/c - 1}{2}\right] \tag{5-3}$$

where $\otimes$ represents the convolution operation, $T(x, y) = 1 - (x^2 + y^2)$ denotes the amplitude transmittance with a continuous profile at the aperture stop which can extend the focal depth in the imaging system with a conventional annular apodizer [6], D is the corresponding diameter of the effective aperture stop, and c represents the width of each square individual aperture generated by DMD™ in the pupil plane,

which is equal to an integer multiple of the value *d,* with *d* being the width of each square pixel in the DMD™. Furthermore, $\delta[x-(2mc/D)]\delta[y-(2nc/D)]$ denotes the delta function indicating the location of the individual aperture in the normalized coordinate on the aperture stop. $E'(x,y)=[H(x+c/D)-H(x-c/D)]\times[H(y+c/D)-H(y-c/D)]$ is the binary amplitude transmittance of the individual shaped aperture, which is then scaled and normalized into the pupil coordinate. $Int[(D/c-1)/2]$ is the interpart of $[(D/c-1)/2]$. $H(x+c/D)$, $H(x-c/D)$, $H(y+c/D)$ and $H(y-c/D)$ are the step functions. It is evident that the total aperture function is formed by convolving the individual aperture function with an appropriate array of the delta function, each located at one of the coordinate origins $(x_m, y_n)=(2mc/D, 2nc/D)$, where m, n = …-2, -1, 0, 1, 2, …

As to be shown below, the quality of performance could be identified by a scale ratio which is defined as

$$K \equiv (c/D) \tag{5-4}$$

The value of the scale ratio *K* determinates how many resolutions, how many gray levels and how fast the DMD™ can dynamically generate the shaped apertures within a specific exposure time. It is worthwhile to give an example for quantity reference. If the DMD™ array is 1024×768 with a pixel size of 13.7 μm square, and the active area is 14.03 mm × 10.52 mm = 147.60 mm^2 [58], then the number of *D* is ~10.52mm (i.e. equal to the width of the active area of the DMD) provided that the effective aperture stop is located on the circular area centered at the actual DMD™. In the case of *K* =0.05, the width of each individual square aperture *c* is 0.53mm and is equivalent to 38 square pixels with the same amplitude transmittance. There are 10 (i.e. $Int[(D/c-1)/2]+1$) gray levels for a specifically shaped aperture including the full bright mode and full dark mode. The current DMD™- based system can offer 8 bits or 256 gray levels within a time period of 5.6 ms per primary color [58]. Thus, the

DMD™ can rapidly generate one shaped aperture with 10 gray levels within the very short exposure time of 0.22 ms (i.e. 5.6×10/256) in the case of K =0.05.

The computer program for evaluating Eq. (5-2)-(5-4) is written in MATHEMATICA software [41]. We assumed D=2 for simplification and evaluated three different scale ratios, i.e., K=0, K =0.05, and K =0.3. The binary amplitude transmittances of the shaped apertures $T'(x,y)$ are shown in Fig. 5-9. The scale ratio K=0 stands for the amplitude transmittance with a continuous profile. It is evident that the scale level of the binary amplitude transmission at the aperture stop increases with the reduction of scale ratio K, and the distribution of the binary amplitude transmission gets close to the continuous profile if the scale ratio K decreases.

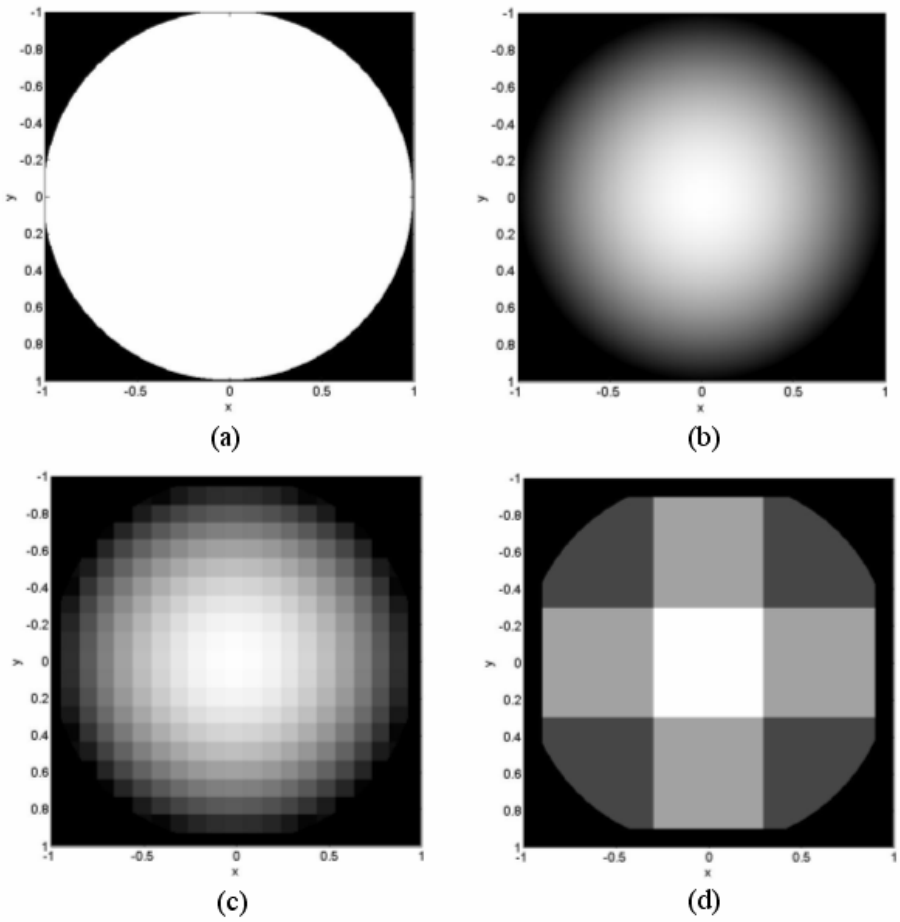

Figure 5-9 Total aperture functions on the aperture stop, which are generated by the DMD™ in the conditions of (a) clear aperture, (b) K=0, (c) K= 0.05 and (d) K= 0.3.

In order to evaluate the relationship between the image performance and the size of the individual square aperture on the normalized pupil (i.e., fill factor or aperture ratio), we modified Eqs. (5-2) and (5-3) to the following equations.

$$T'(x,y) = E'(x,y) \otimes \sum_m \sum_n T(x,y)\delta(x - \frac{2ma}{D})\,\delta(y - \frac{2na}{D}) \tag{5-5}$$

$$0 \le |m|, |n| \le Int\left[\frac{D/a - 1}{2}\right] + 1 \tag{5-6}$$

where $\otimes$ represents the convolution operation. $T(x,y) = 1 - (x^2 + y^2)$ is the amplitude transmittance with a continuous profile at the aperture stop, D is the corresponding diameter of the effective aperture stop, c represents the width of each square individual aperture generated by DMD in the pupil plane. The parameter a represents the distance between each square individual aperture as shown in Fig. 5-8. $\delta[x - (2ma/D)]\delta[y - (2na/D)]$ denotes the delta function, indicating the location of the individual aperture in the normalized coordinate on the aperture stop. $E'(x,y) = [H(x + c/D) - H(x - c/D)] \times [H(y + c/D) - H(y - c/D)]$ is the amplitude transmittance of the individual shaped aperture, which is then scaled and normalized into the pupil coordinate. $Int[(D/a - 1)/2]$ is the interpart of $[(D/a - 1)/2]$ and $H(x + c/D)$, $H(x - c/D)$, $H(y + c/D)$ and $H(y - c/D)$ are the step functions. It is evident that the total aperture function is formed by convolving the individual aperture function with an appropriate array of the delta function, each located at one of the coordinate origins $(x_m, y_n) = (2ma/D, 2na/D)$, where m, n = …-2, -1, 0, 1, 2, … We also take D=2 and a/D=0.3 in Eq. (5-5) and (5-6). The fill factor represents the ratio of c and a. Six cases of the amplitude transmittances $T'(x,y)$ with the fill factors ranged from 100% to 50% were computed as shown in Fig. 5-10. There are 9 apertures (3× 3 array) within the pupil. The results show that the individual aperture size on the normalized pupil is shrunk when the fill factor decreased. That is equivalent to the term $E'(x,y)$ varied with c in Eq. (5-5).

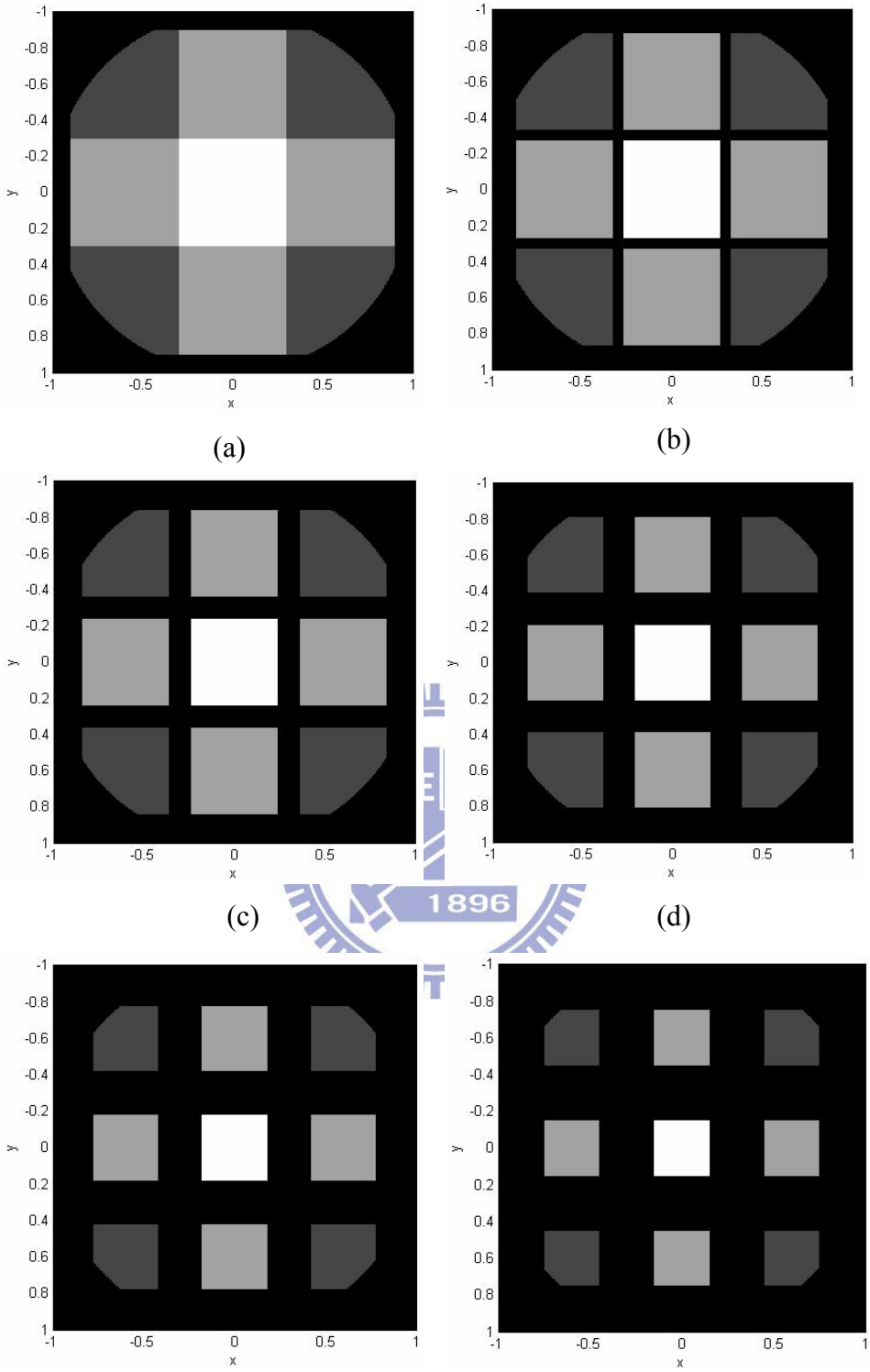

Figure 5-10 Amplitude transmittance $T'(x,y)$ with $T(x, y)$ =1 on the normalized pupil in the condition of D=2 and the fill factors (a) 100%, (b) 90%, (c) 80%, (d) 70%, (e) 60% and (f) 50%.

The OTF is derived from the autocorrelation of the pupil function by using the Hopkins canonical coordinate [37, 48-49] and is given by

$$\tau(s) = \frac{g(s,0)}{g(0,0)} = \frac{\int_{-\infty}^{\infty}\int_{-\infty}^{\infty} f(x+s/2\,,\,y)\, f^{*}(x-s/2\,,\,y)\,dx\,dy}{\int_{-\infty}^{\infty}\int_{-\infty}^{\infty} f(x\,,\,y)\, f^{*}(x\,,\,y)\,dx\,dy} \tag{5-7}$$

where $f(x, y)$ is the pupil function shown in Eq. (5-1), $f^{*}(x, y)$ is the complex conjugate of $f(x, y)$, and s is defined as the spatial frequency $s \equiv 2F\lambda N$. Here F is the f-number of the projection lens system, λ is the wavelength, and N is the number of cycles per unit length in the image plane. The value of F is equal to the effective focal length divided by D, where D is the diameter of the effective aperture stop and the effective focal length is determined by the optical magnification of the projection lens. The denominator of Eq. (5-7) is the normalizing factor for making $\tau_0(0) = 1$. The $g(s, 0)$ and $g(0, 0)$ in the OTF for the pupil function $f(x, y)$ can then be given by

$$g(s,0) = \int_{-\left[1-(s/2)^2\right]^{1/2}}^{\left[1-(s/2)^2\right]^{1/2}} \int_{-\left[(1-y^2)^{1/2}-s/2\right]}^{\left[(1-y^2)^{1/2}-s/2\right]} T'\left(x+\frac{s}{2}, y\right)\cdot T'\left(x-\frac{s}{2}, y\right) \times exp\left\{i2ksx\left[\omega_{20} + \omega_{40}\left(2x^2 + 2y^2 + \frac{s^2}{2}\right) + \omega_{31}y\right]\right\} dxdy \tag{5-8}$$

and

$$g(0,0) = \int_{-1}^{1}\int_{-\left(1-y^2\right)^{1/2}}^{\left(1-y^2\right)^{1/2}} \left[T'(x,y)\right]^2 dxdy \tag{5-9}$$

Eqs. (5-8) and (5-9) can be further modified as

$$g(s,0) = \sum_{q'=-p'}^{p'} \left\{ \int_{-\left[(1-y^2)^{1/2}-s/2\right]}^{\left[(1-y^2)^{1/2}-s/2\right]} T'\left(x+\frac{s}{2}, y\right)\cdot T'\left(x-\frac{s}{2}, y\right) \times exp\left\{i2ksx\left[\omega_{20} + \omega_{40}\left(2x^2 + 2y^2 + \frac{s^2}{2}\right) + \omega_{31}y\right]\right\} dx \right\} \Delta y \tag{5-10}$$

where $y = \frac{\left[1-(s/2)^2\right]^{1/2}}{p'} \times q'$, $\Delta y = \frac{\left[1-(s/2)^2\right]^{1/2}}{p'}$, and

$$g(0,0)=\sum_{q=-p}^{p}\left\{\int_{-(1-y^2)^{1/2}}^{(1-y^2)^{1/2}}[T'(x,y)]^2\,dx\right\}\cdot\Delta y \tag{5-11}$$

where $y=(1/p)\times q$, $\Delta y=(1/p)$.

By replacing the integral in Eqs. (5-8) and (5-9) with the y-axis for the summation in Eqs. (5-10) and (5-11), an initial setting of p=100 is made for the number of intervals used to find the value of $\Delta y=\left[1-(s/2)^2\right]^{1/2}/p'$ and $\Delta y=1/p$ for $g(s, 0)$ and $g(0, 0)$, respectively. Different numbers of y, from $-\left[1-(s/2)^2\right]^{1/2}$ to $\left[1-(s/2)^2\right]^{1/2}$, are then used to calculate the OTF.

The OTFs of the different pupil functions are numerically computed using MATHEMATICA software [41] based on Eqs. (5-1)-(5-4), (5-10) and (5-11). We calculated the OTFs and analyzed the image performances of five different cases for the differently shaped apertures in an aberration-free system and incoherent imaging systems with defocused aberration, spherical aberration, the coma aberration.

Case 1: Defocus

We calculated the OTFs of the clear aperture, one conventional annual apodizer and two specifically shaped pupils with the scale ratios K= 0.05 and 0.3, respectively, for defocused systems with the defocus coefficients ω_{20}= 0, λ/π, 3λ/π, 5λ/π, 10λ/π and 20λ/π, as shown in Fig. 5-11, where we assumed that spherical and coma aberration are free, i.e.,$\omega_{40}=\omega_{31}=0$.

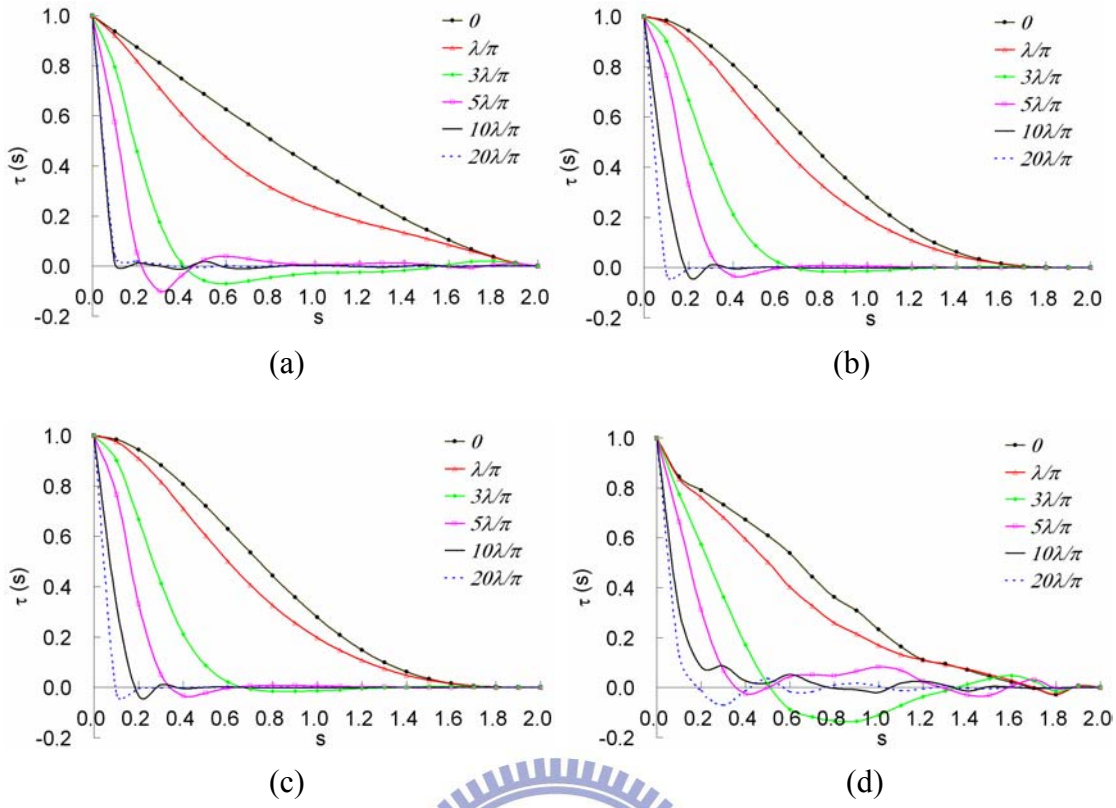

Figure 5-11 Optical transfer functions in an aberration-free imaging system and a defocused imaging system without spherical aberration ω_{40}= 0 and coma aberration ω_{31}= 0, but with different defocus coefficients ω_{20}= 0, ω_{20}= λ/π, ω_{20}= 3λ/π, ω_{20}= 5λ/π, ω_{20}= 10λ/π and ω_{20}= 20λ/π for amplitude transmittances of the aperture functions for (a) clear aperture, (b) K= 0, (c) K= 0.05, and (d) K= 0.3.

For the large values of ω_{20} from 5λ/π to 20λ/π, the spatial frequency corresponding to the first zero becomes smaller. Since generally the spatial frequency of the first zero represents the resolution limit of a defocused imaging system, we can take the first zero as defining the degree of focus for each case. The larger degree of focus in the larger value of ω_{20} commonly represents the longer depth of focus in a defocused system. The OTF of a clear aperture $T(x, y)$ = 1 (i.e. a uniform-shaped aperture), is shown in Fig. 5-11 (a), and was investigated in the literature [6]. The OTF of one annual apodizer $T(x, y)$ =1- (x^2+y^2), at $(x^2+y^2 \leqq 1)$ and 0 at $(x^2+y^2 > 1)$ with K= 0, is shown in Fig. 5-11 (b), and was previously investigated and proven by the use of the theoretical and experimental approaches in literature [6]. Two former cases are computed again here for comparison. For the large values of ω_{20} especially

greater than $5\lambda/\pi$, the degree of focus for the shaped pupil with a scale ratio K of less than 0.3, as shown in Fig. 5-11 (c) and (d), is significantly larger than that for the clear aperture $T(x, y) = 1$. It is evident that the specifically shaped pupil, which is generated by DMD™ with a scale ratio K=0.3 or less, can significantly extend the depth of focus compared to a clear aperture in the conventional imaging system. We also compared the OTF of the different scale ratios K to the OTF of the conventional annual apodizer $T(x, y) = 1 - (x^2+y^2)$. The OTF value of the former increased and came close to the OTF value of the latter when the scale ratio K decreased gradually. In Fig. 5-11 (b) and (c), it shows that the OTFs of the specifically shaped pupil with a scale ratio K=0.05 or less can coincide with the OTF of the conventional annular apodizer with continuously-shaped aperture. For the case of K=0.3, i.e., the scale ratio K now increases, as shown in Fig. 5-11 (d), the OTF value decreases in the low spatial frequency region especially for the defocus coefficients ω_{20} less than λ/π. But, the OTF value increases in the high spatial frequency region especially for ω_{20} greater than $10\lambda/\pi$ when K= 0.3. It indicates that the degree of focus can increase for the specifically shaped pupil in the defocused imaging system when K increases. This is as a result of weighting the light intensity from the airy disk to the rings of the diffraction pattern when designing the specifically shaped pupil in the imaging system for extending the depth of focus [1].

Case 2: Spherical aberration

Here we turn to focus on the clarification of the influence of spherical aberration. The spherical aberration is the essential aberration along optical axis, i.e., on-axis aberration. We calculated the OTFs of the clear aperture, one conventional annual apodizer and two specifically shaped pupils with the scale ratios K= 0.05 and 0.3, respectively, for the imaging systems with the coefficients for spherical aberration

ω_{40}= 0, λ/π, 3λ/π, 5λ/π, 10λ/π and 20λ/π, as shown in Fig. 5-12, if we assumed that defocused and coma aberration are free, i.e. $\omega_{20} = \omega_{31} = 0$. The OTF of a clear aperture $T(x, y) = 1$ (i.e. a uniform-shaped aperture), is shown in Fig. 5-12 (a). The OTF of one annual apodizer $T(x, y) = 1 - (x^2+y^2)$, at $(x^2+y^2 \leq 1)$ and 0 at $(x^2+y^2 > 1)$ with $K = 0$, is shown in Fig. 5-12 (b). The OTFs for the shaped pupil with a scale ratio K of less than 0.3, as shown in Fig. 5-12 (c) and (d), are significantly larger than that for the clear aperture $T(x, y) = 1$ in Fig. 5-12 (a) at all spatial frequency.

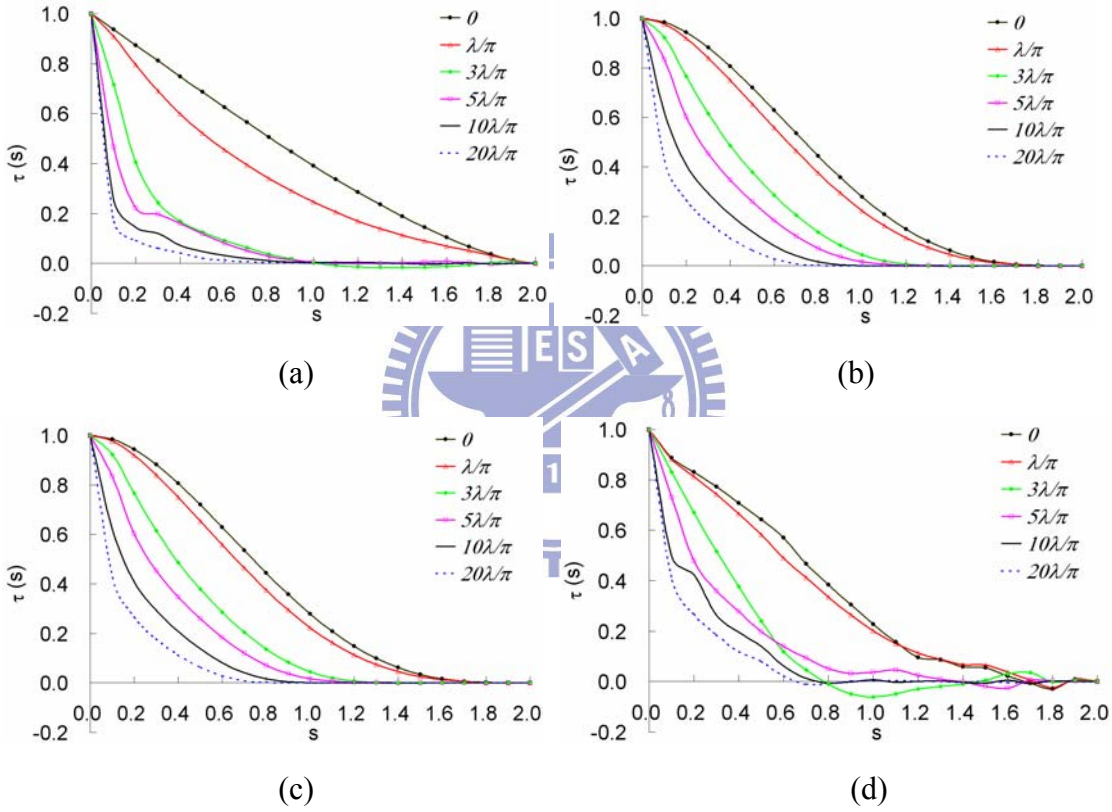

Figure 5-12 Optical transfer functions in an aberration-free imaging system and an imaging system without defocus aberration ω_{20}= 0 and coma aberration ω_{31}= 0, but with different spherical aberration coefficients ω_{40}= 0, ω_{40}= λ/π, ω_{40}= 3λ/π, ω_{40}= 5λ/π, ω_{40}= 10λ/π and ω_{40}= 20λ/π for amplitude transmittances of the aperture functions for (a) clear aperture, (b) K= 0, (c) K= 0.05, and (d) K= 0.3.

It is evident that the specifically shaped pupil, which is generated by DMD™ with a scale ratio K=0.3 or less, can significantly extend the depth of focus compared to a clear aperture in the conventional imaging system with spherical aberration. The OTF

of K=0.3 is slightly lower than but similar to that of K=0.05 in Fig 5-12 (c) and (d). It indicates that the degree of focus could be similar for the specifically shaped pupil in the imaging system with spherical aberration when K varies from 0.05 to 0.3. We also compared the OTF of the different scale ratios K to the OTF of the conventional annual apodizer $T(x, y)$ =1- (x^2+y^2). The OTF value of the former increased and came close to the OTF value of the latter when the scale ratio K decreased gradually. In Fig. 5-12 (b) and (c), it shows that the OTFs of the specifically shaped pupil with a scale ratio K=0.05 or less can coincide with the OTF of the conventional annular apodizer with continuously-shaped aperture.

Case 3: Coma aberration

In this subsection, we consider the influence of coma and its compensation. The coma is treated as the essential off-axis aberration. We calculated the OTFs of the clear aperture, one conventional annual apodizer and two specifically shaped pupils with the scale ratios K= 0.05 and 0.3, respectively, for the imaging systems with the coefficients for coma aberration ω_{31}= 0, λ/π, 3λ/π, 5λ/π, 10λ/π and 20λ/π, as shown in Fig. 5-13, where we assumed that defocused and spherical aberration are free, i.e. ω_{20}= ω_{40}=0. The OTF of a clear aperture $T(x, y)$ = 1, is shown in Fig. 5-13 (a). The OTF of one annual apodizer $T(x, y)$ =1- (x^2+y^2), at $(x^2+y^2 \leqq 1)$ and 0 at $(x^2+y^2 > 1)$ with K= 0, is shown in Fig. 5-13 (b). The OTFs for the shaped pupil with a scale ratio K of less than 0.3, as shown in Fig. 5-13 (c) and (d), are significantly larger than that for the clear aperture $T(x, y)$ = 1 in Fig. 5-13 (a) at all spatial frequency.

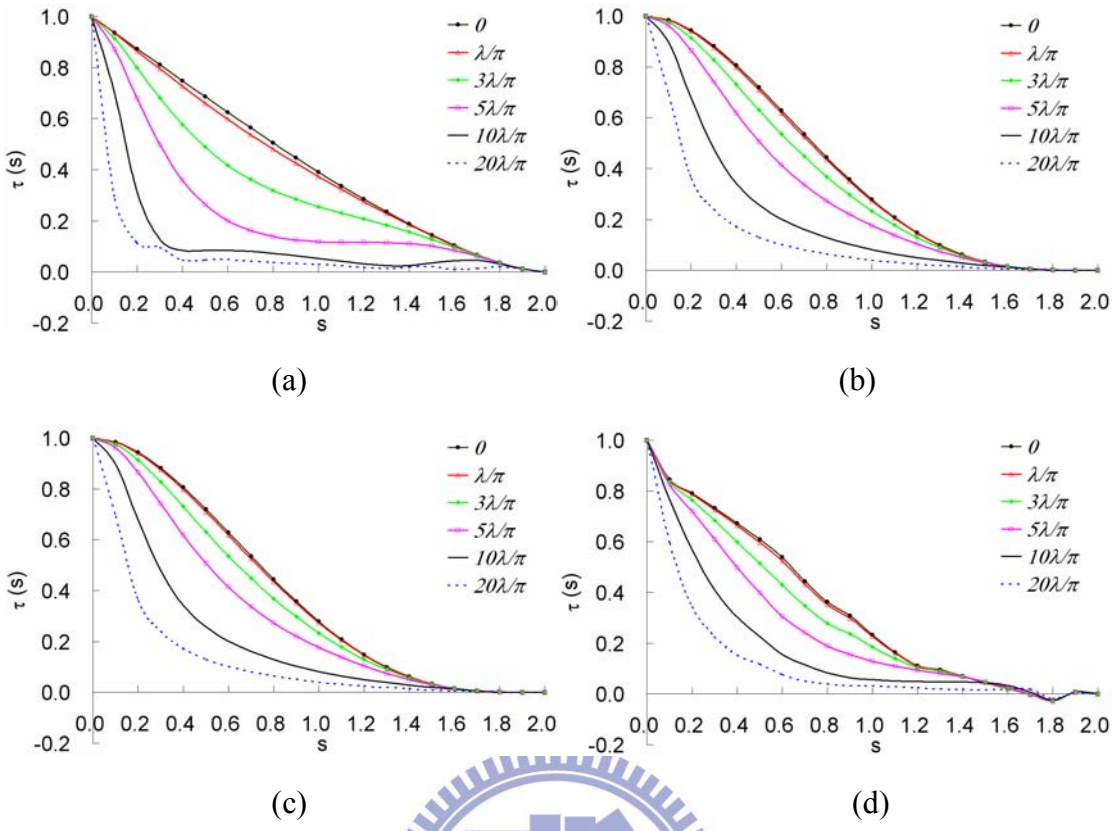

Figure 5-13 Optical transfer functions in an aberration-free imaging system and a projection system without defocus aberration ω_{20}= 0 and spherical aberration ω_{40}= 0 ,but with different coma aberration coefficients ω_{31}= 0, ω_{31}= λ/π, ω_{31}= 3λ/π, ω_{31}= 5λ/π, ω_{31}= 10λ/π and ω_{31}= 20λ/π for amplitude transmittances of the aperture functions for (a) clear aperture, (b) K= 0, (c) K= 0.05, and (d) K= 0.3.

It is evident that the specifically shaped pupil, which is generated by DMD™ with a scale ratio K=0.3 or less, can significantly extend the depth of focus compared to a clear aperture in the conventional imaging system with coma aberration. The OTF of K=0.3 is slightly lower than but similar to that of K=0.05 in Fig. 5-13 (c) and (d). It indicates that the degree of focus could be similar for the specifically shaped pupil in the imaging system with coma aberration when K varies from 0.05 to 0.3. We also compared the OTF of the different scale ratios K to the OTF of the conventional annual apodizer $T(x, y)$ =1- (x^2+y^2). The OTF value of the former increased and came close to the OTF value of the latter when the scale ratio K decreased gradually. In Fig. 5-13 (b) and (c), it shows that the OTFs of the specifically shaped pupil with a

scale ratio K=0.05 or less can coincide with the OTF of the conventional annular apodizer with continuously-shaped aperture.

Case 4: Combined aberration (defocus, Spherical aberration, and Coma)

Now, we can consider the whole influence with all aberrations discussed above. We calculated the OTFs of the clear aperture, one conventional annual apodizer and two specifically shaped pupils with the scale ratios K= 0.05 and 0.3, respectively, for the imaging systems with a specific defocus coefficient ω_{20}, and the specific coefficients for spherical aberration ω_{40} and coma aberration ω_{31}. For variable spherical aberration, the best focal plane in the condition of $\omega_{20} = -\omega_{40}$ is supposed [2]. The OTFs for $-\omega_{20} = \omega_{40} = \omega_{31} = 0$, $5\lambda/\pi$, $10\lambda/\pi$, and $20\lambda/\pi$ are shown in Fig. 5-14, respectively. For the large value of the coefficient especially for $20\lambda/\pi$, the degree of focus for the shaped pupil with a scale ratio K of less than 0.3, as shown in Fig. 5-14 (c) and (d), is significantly larger than that for the clear aperture $T(x, y)$ = 1 in Fig 5-14 (a). It is evident that the specifically shaped pupil, which is generated by DMD™ with a scale ratio K=0.3 or less, can significantly extend the depth of focus compared to a clear aperture in the conventional imaging system. We also compared the OTF of the different scale ratios K to the OTF of the conventional annual apodizer $T(x, y) = 1-(x^2+y^2)$. The OTF value of the former increased and came close to the OTF value of the latter when the scale ratio K decreased gradually. In Fig. 5-14 (b) and (c), it shows that the OTFs of the specifically shaped pupil with a scale ratio K=0.05 or less can coincide with the OTF of the conventional annular apodizer with continuously-shaped aperture.

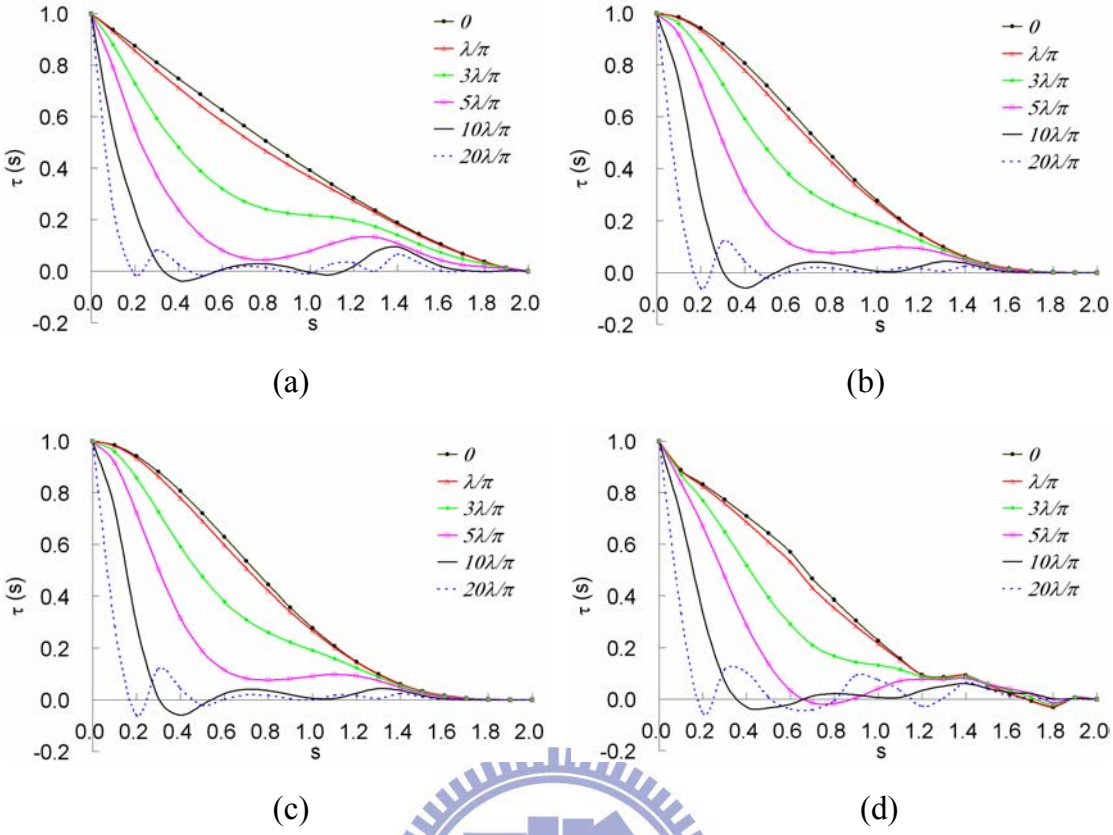

Figure 5-14 Optical transfer functions in an aberration-free imaging system and a projection system with different defocus coefficients ω_{20} , different spherical aberration coefficients ω_{41} , and different coma aberration coefficients ω_{31} , when $-\omega_{20} = \omega_{40} = \omega_{31} = 0$, λ/π, 3λ/π, 5λ/π, 10λ/π and 20λ/π for amplitude transmittances of the aperture functions for (a) clear aperture, (b) K= 0, (c) K= 0.05, and (d) K= 0.3.

Finally, we investigated an example of a real implement for a light value with a typical pixel size equal to 13μm square in a projection system with $f/\#$ =2.0 and the dominant wavelength λ= 550nm. $N = 1/2(13\times10^{-6})$ which is the number of cycles per unit length in image plane. In this case, $s \equiv 2F\lambda N = 0.085$ which is defined as the spatial frequency. Referring to Fig. 5-11, Fig. 5-12, Fig. 5-13 and Fig. 5-14, we calculated and summarized the OTF's values of the clear aperture and two specifically shaped pupils with the scale ratios K= 0.05 and K= 0.3, respectively, in the cases of ω_{20}, ω_{40}, $\omega_{31} = 0$, 5λ/π, 10λ/π, and 20λ/π in the condition of a specifically spatial frequency s =0.085 in Table 5-1. It indicates that the OTFs of a specifically shaped

aperture with K=0.05 and K= 0.3 are greater than the OTFs of a clear aperture especially when the aberration coefficients ≥5λ/π. Hence, we can conclude that the projection quality will be enhanced as the specifically shaped aperture is used, especially for the imaging system with large aberration coefficients including defocus, spherical and come aberrations. In other words, as for a real implementation of an illumination modulator with DMD, the specifically shaped pupil can improve the image quality compared to a clear aperture in the conventional imaging system.

Table 5-1 OTF's values of the clear aperture and two specifically shaped pupils with the scale ratios K= 0.05 and K= 0.3, respectively, in the cases of ω_{20}, ω_{40}, $\omega_{31}=0$, 5λ/π, 10λ/π, and 20λ/π in the condition of a specifically spatial frequency s =0.085.

Aberration coefficient	0			5λ/π			10λ/π			20λ/π		
Pupil shape (K factor)	CA*[1]	0.05	0.3	CA*[1]	0.05	0.3	CA*[1]	0.05	0.3	CA*[1]	0.05	0.3
defocus (w_{20})	0.95	0.98	0.86	0.64	0.81	0.71	0.13	0.41	0.38	0.00	0.07	0.22
Spherical (w_{40})	0.95	0.98	0.90	0.55	0.87	0.77	0.28	0.68	0.54	0.17	0.47	0.41
Coma (w_{31})	0.95	0.98	0.86	0.90	0.97	0.84	0.75	0.92	0.80	0.36	0.74	0.65
Combination*[2]	0.95	0.98	0.90	0.83	0.94	0.87	0.60	0.78	0.75	0.33	0.37	0.37

Note:

1. CA is "Clear Aperture".

2. Combination consists of defocused aberration (w_{20}= -w_{40}), spherical aberration (w_{40}) and coma aberration (w_{31}).

Case 5: the influence of fill factor

In order to evaluate the relationship between the image performance and the size of the individual square aperture on the normalized pupil, we computed the OTFs of the other types of pupil functions based on Eqs. (5-1), (5-5), (5-10) and (5-11) in a

defocused system with the defocused coefficient ω_{20}= 10λ/π and the amplitude transmittances of the aperture functions for *a/D*=0.3 with different fill factors ranged from 100% to 60% in Fig. 5-15 (a) and in Fig. 5-15 (b), the range is from 60%, to 10%. The degree of focus (i.e. the resolution limit) reduces, but the OTF (i.e. image quality) increases at the specific spatial frequency when the fill factor decreased from 100% to 60%. However, both of the degree of focus and the OTF reduces when the fill factor decreases from 60% to 10%, which is mainly because the pin-hole effect reduces the diffractive limit significantly.

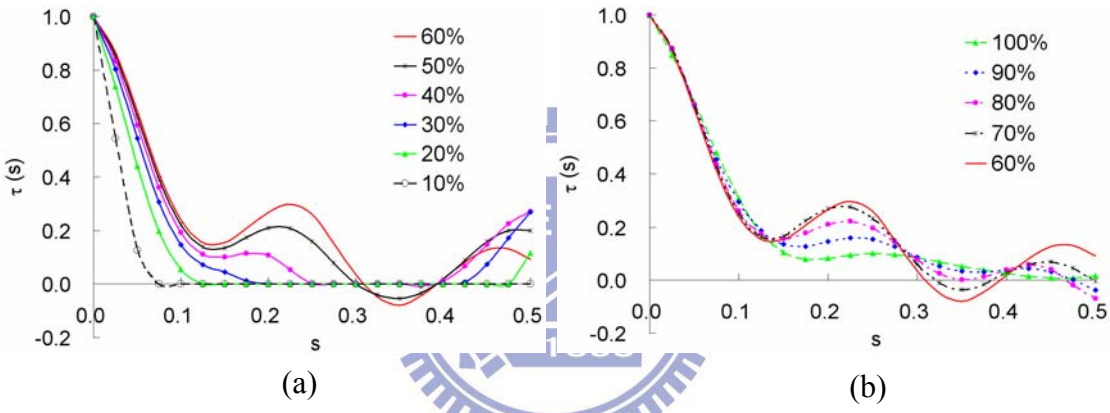

Figure 5-15 Optical transfer functions in a defocused system with amplitude transmittances of the aperture functions for *a/D*=0.3 and the defocused coefficient ω_{20}= 10λ/π for different fill factors (a) 100%, 90%, 80%, 70%, 60% and (b) 60%, 50%, 40%, 30%, 20%, 10%.

5.8 Image performance evaluation

To highlight the capability of our approach, we took a resolution pattern to explore the image performance in an incoherent imaging system. This pattern is 1951 USAF resolution test chart [44] conforms to MIL-STD-150A standard with resolution 600 (dpi) × 600 (dpi).

Case 1: Defocus

Referring to Fig. 5-16, in column (a), one could see the images for the clear aperture, while in column (b) and (c), the images for the specifically shaped apertures with scale ratios K=0.05 and K=0.3 are shown, respectively. The images were generated by the multiplication of OTF in the Fourier domain using the convolution technique. Furthermore, the images with defocus coefficients of ω_{20}= 5λ/π, ω_{20}= 10λ/π, ω_{20}= 15λ/π, and ω_{20}= 20λ/π, are shown with lines (1)-(4) respectively. Comparing with the images for the specifically shaped apertures, the images of typical aperture show a clearer loss in contrast at high spatial frequencies with larger ω_{20}. Especially for ω_{20} ≥10λ/π, there is a significant enhancement of the image resolution at high spatial frequency by the use of a specifically shaped aperture with K=0.3.

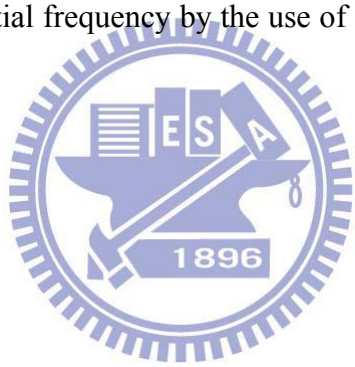

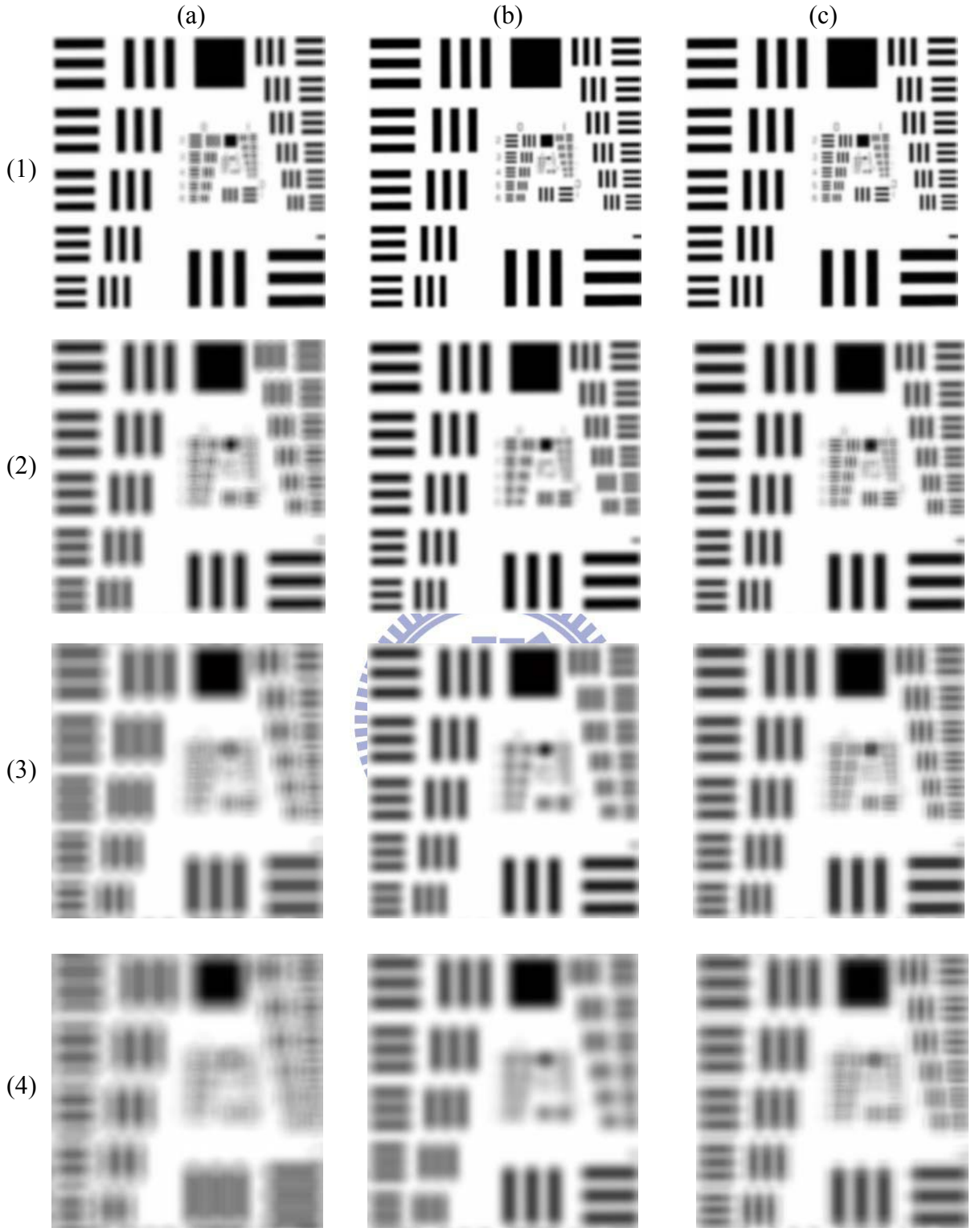

Figure 5-16 The computer-simulated images of resolution patterns for (a), a clear aperture, and (b), a specifically shaped aperture with the scale ratio K=0.05, and (c), a specifically shaped aperture with the scale ratio K=0.3, obtained with different defocus coefficients: (1)ω_{20}= 5λ/π, (2) ω_{20}= 10λ/π, (3) ω_{20}= 15λ/π and (4) ω_{20}= 20λ/π.

Case 2: Spherical aberration

Referring to Fig. 5-17, in column (a), one could see the images for the clear aperture, while in column (b) and (c), the images for the specifically shaped apertures with scale ratios K=0.05 and K=0.3 are shown, respectively. Furthermore, the images with spherical-aberration coefficients of ω_{40} = 5λ/π, ω_{40} = 10λ/π, ω_{40} = 15λ/π, and ω_{40} = 20λ/π, are shown with lines (1)-(4), respectively. Spherical aberration could make the image of a bright point source surrounded by a halo of light. The effect of spherical aberration on an extended image is to soften the contrast of the image and to blur its details with symmetrical distribution. Comparing with the images for the specifically shaped apertures, the images of the clear aperture show a clearer loss in contrast and a seriously blurred flare at all spatial frequency with larger ω_{40} even tough the three-bar charts for all spatial frequencies is resolved for the clear aperture. Especially for $\omega_{40} \geq 10\lambda/\pi$, there is a significant enhancement of the imaging contrast by the use of a specifically shaped aperture with K=0.3 and 0.05.

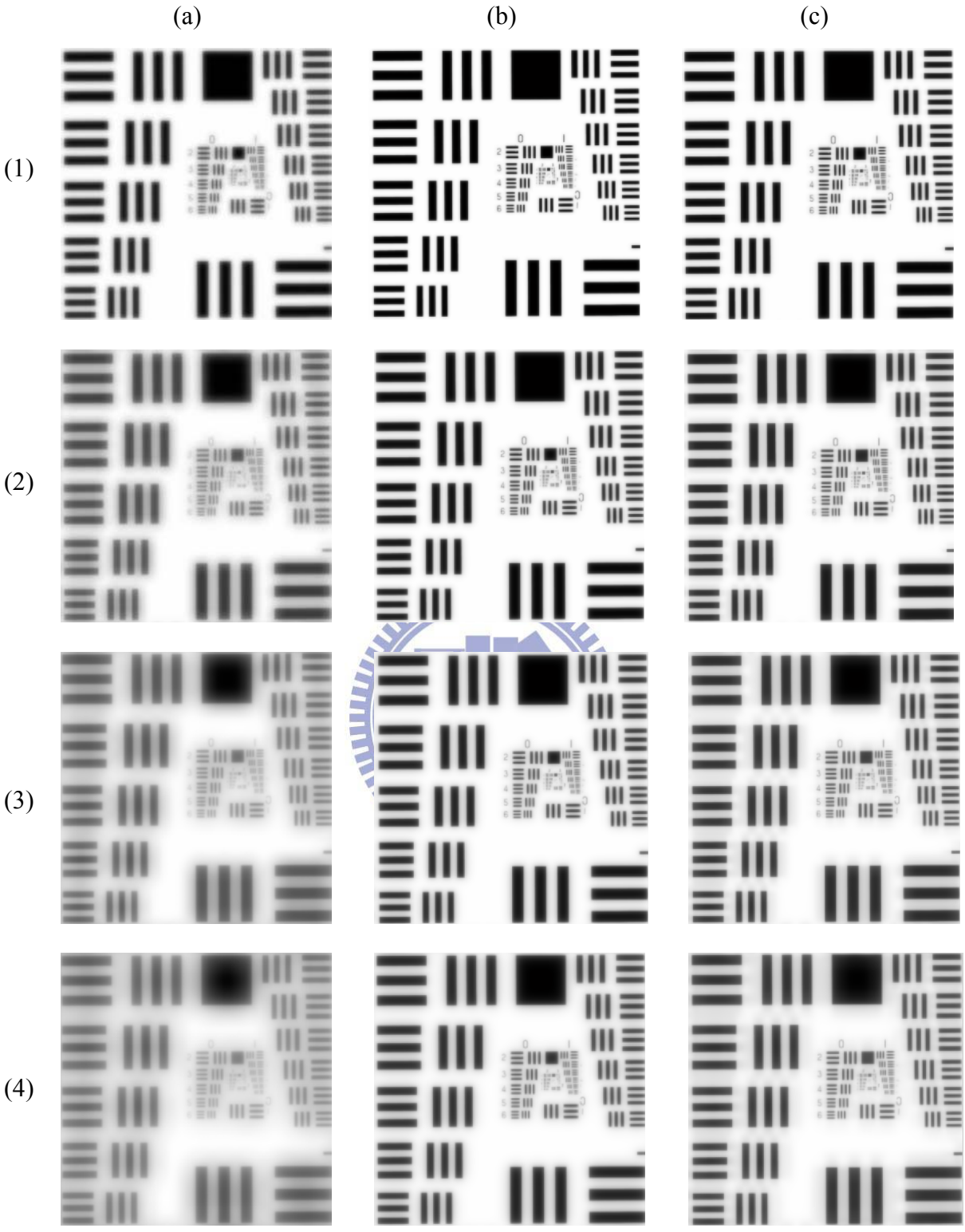

Figure 5-17 The computer-simulated images of resolution patterns for (a), a clear aperture, and (b), a specifically shaped aperture with the scale ratio K=0.05, and (c), a specifically shaped aperture with the scale ratio K=0.3, obtained with different spherical aberration coefficients: (1) ω_{40}= 5λ/π, (2) ω_{40}= 10λ/π, (3) ω_{40}= 15λ/π and (4) ω_{40}= 20λ/π.

Case 3: Coma aberration

In order to obviously show the effect of coma aberration by the use of a suitable test chart, we utilized a concentric-circles pattern with resolution 96 (dpi) × 96 (dpi) [60]. Referring to Fig. 5-18, in column (a), one could see the images for the clear aperture, while in column (b) and (c), the images for the specifically shaped apertures with scale ratios K=0.05 and K=0.3 are shown, respectively. Furthermore, the images with coma-aberration coefficients of $\omega_{31} = 5\lambda/\pi$, $\omega_{31} = 10\lambda/\pi$, $\omega_{31} = 15\lambda/\pi$, and $\omega_{31} = 20\lambda/\pi$, are shown with lines (1)-(4) respectively. Coma aberration could make the image of a point source spread out into a comet-shaped flare with the non-symmetrical distribution. Comparing with the images for the specifically shaped apertures, the images of the clear aperture show a seriously blurred flare at all spatial frequency with larger ω_{31} along the vertical direction. Especially for $\omega_{31} \geq 10\lambda/\pi$, there is a significant enhancement of the imaging resolution by the use of a specifically shaped aperture with K=0.3 and 0.05.

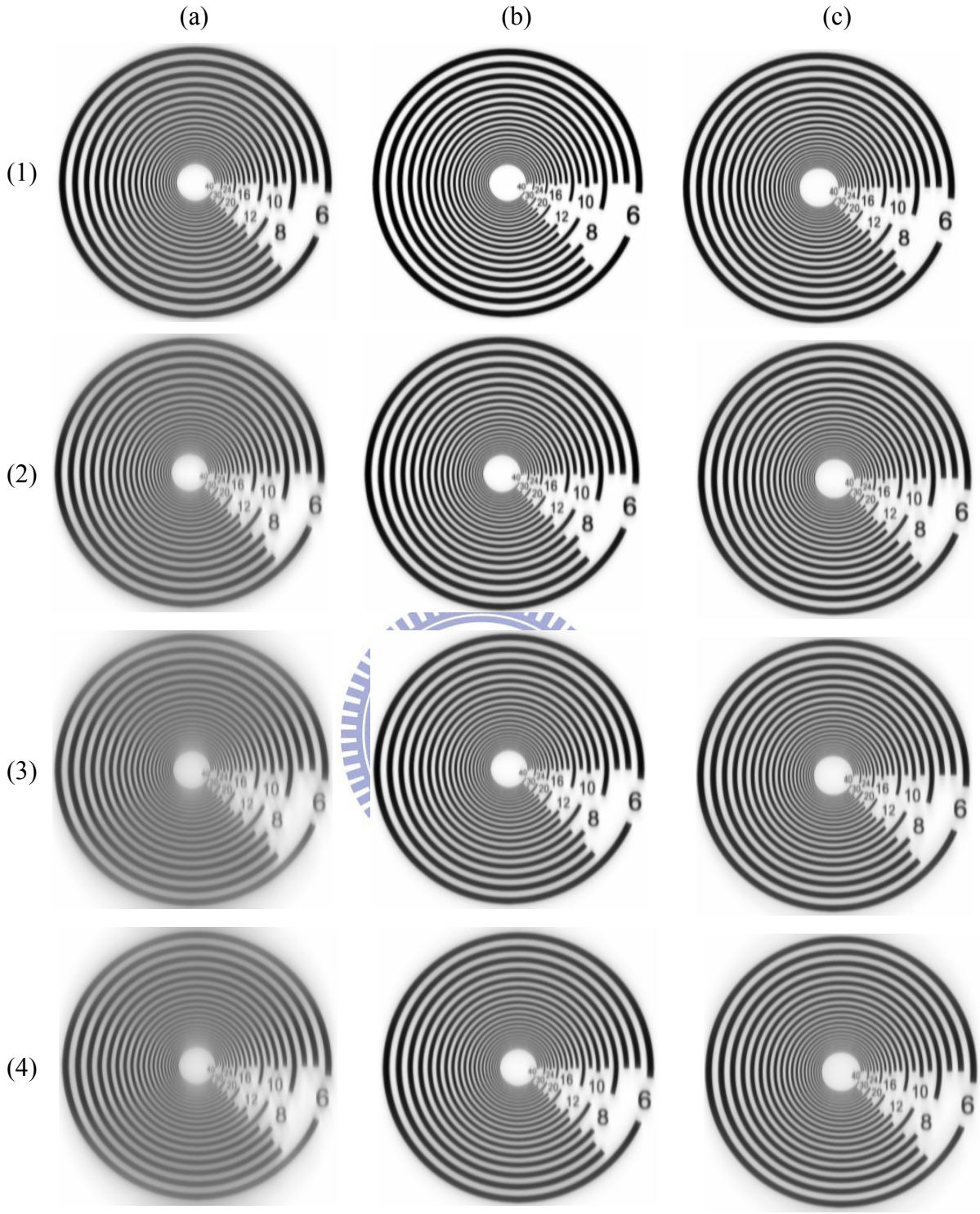

Figure 5-18 The computer-simulated images of resolution patterns for (a), a clear aperture, and (b), a specifically shaped aperture with the scale ratio K=0.05, and (c), a specifically shaped aperture with the scale ratio K=0.3, obtained with different coma aberration coefficients: (1) ω_{31}= 5λ/π, (2) ω_{31}= 10λ/π, (3) ω_{31}= 15λ/π and (4) ω_{31}= 20λ/π.

Case 4: Combined aberration (defocus, Spherical aberration, and Coma)

Referring to Fig. 5-19, in column (a), one could see the images for the clear aperture, while in column (b) and (c), the images for the specifically shaped apertures with scale ratios K=0.05 and K=0.3 are shown, respectively. Furthermore, the images with the aberration coefficients of $-\omega_{20} = \omega_{40} = \omega_{31} = 5\lambda/\pi$, $10\lambda/\pi$, and $20\lambda/\pi$ including defocus, spherical and come aberrations are shown with lines (1)-(3), respectively. Comparing with the images for the specifically shaped apertures, the images of typical aperture show a significant loss in contrast at all spatial frequency. Especially for the aberration coefficients $\geq 5\lambda/\pi$, there is a significant enhancement of the image resolution at all spatial frequency by the use of a specifically shaped aperture with K=0.05 and K=0.3.

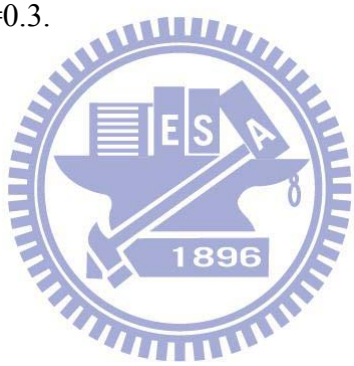

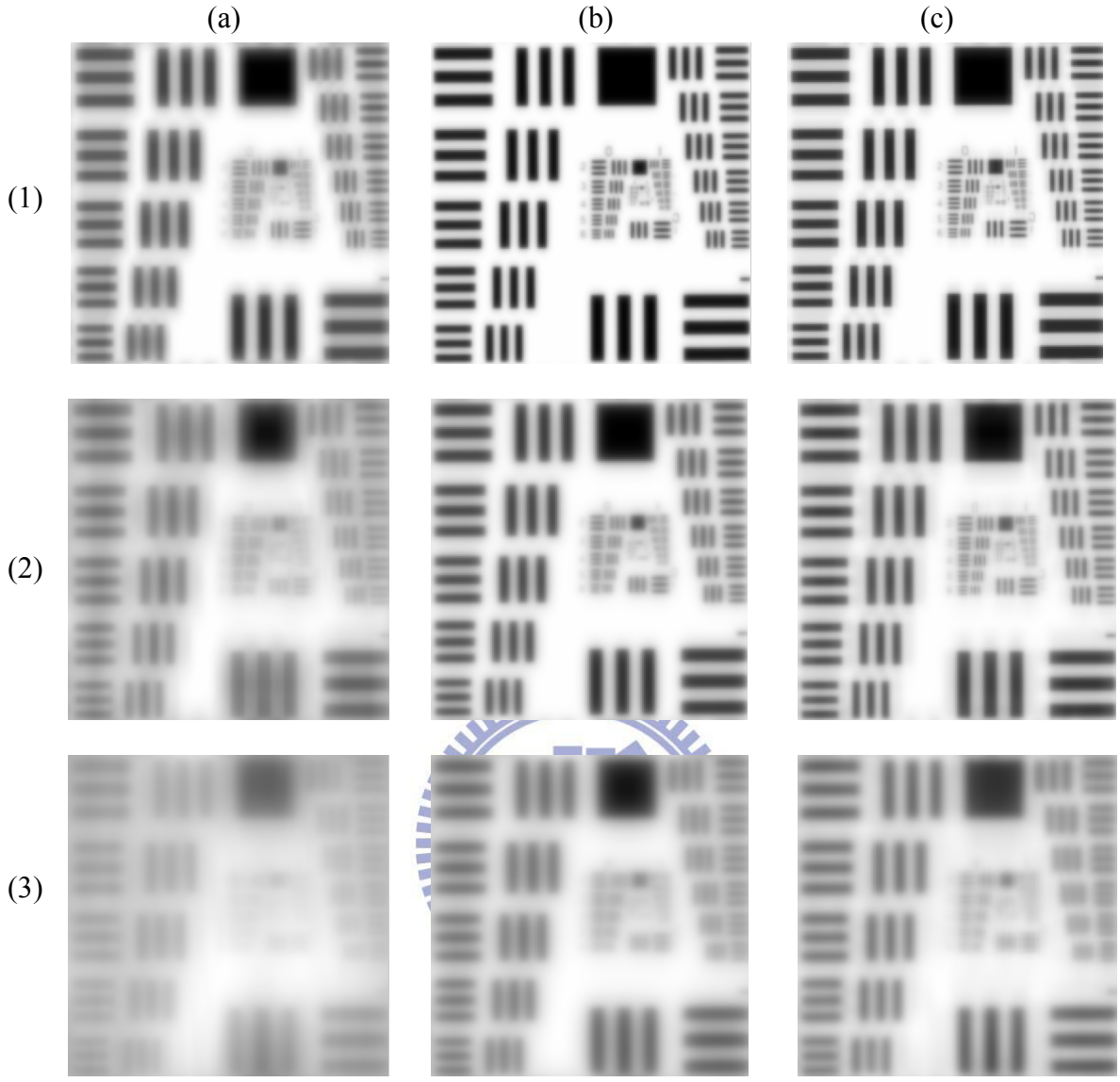

Figure 5-19 The computer-simulated images of resolution patterns for (a), a clear aperture, and (b), a specifically shaped aperture with the scale ratio K=0.05, and (c), a specifically shaped aperture with the scale ratio K=0.3, obtained with different defocus coefficients ω_{20} , different spherical aberration coefficients ω_{41} , and different coma aberration coefficients ω_{31} , when $-\omega_{20} = \omega_{40} = \omega_{31}$ = (1) 5λ/π, (2) 10λ/π, and (3) 20λ/π.

Case 5: the influence of fill factor

We take a resolution pattern to simulate the imaging performance for this specific shaped aperture with the scale ratio a/D =0.3 and different fill factors ranged from 100% to 50% in a defocus system with the defocused coefficient ω_{20}= 10λ/π as shown in Fig. 5-20. Comparing with the images in the red frames shown in the figures, the image of the specific shaped aperture with the fill factor 60% shows a higher resolution at the middle spatial frequencies. Hence, it is evident that the image quality at specific spatial frequency will be improved once the specific shaped aperture is implemented.

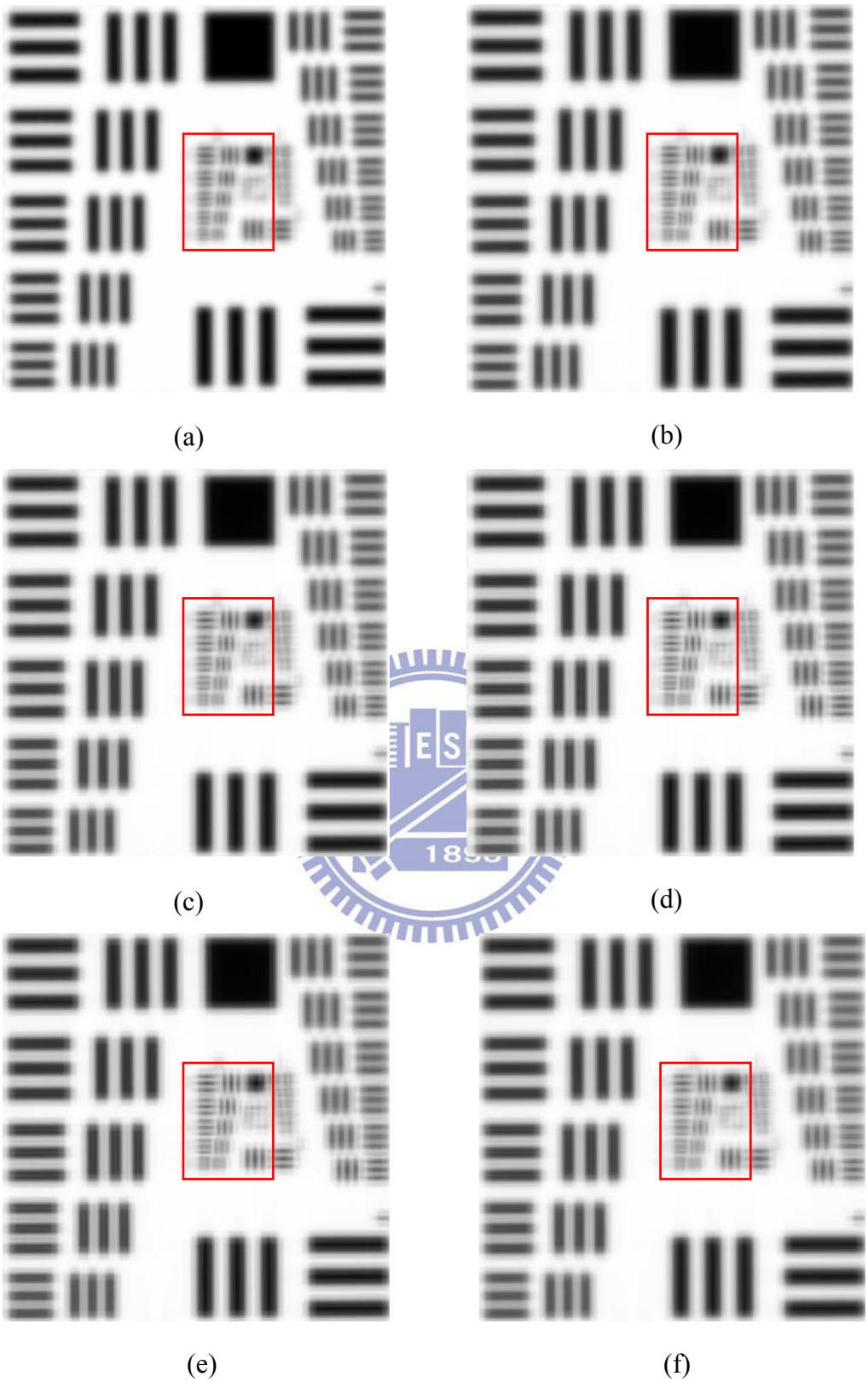

Figure 5-20 The computer-simulated images of resolution patterns for a specific shaped aperture with the scale ratio a/D =0.3 and different fill factors (a) 100%, (b) 90%, (c) 80%, (d) 70%, (e) 60% and (f) 50%, in a defocus system with the defocused coefficient ω_{20}= 10λ/π.

5.9 Summary and remarks

We have provided a new approach for improving the image quality for the incoherent imaging systems, including photography, projector and microscopy, with a specific illuminator modulator. The semi-analytical results using the optical transfer function (OTF) indicated that the depth of focus can be extended with specifically shaped illumination, which is generated by a digital micromirror device and LED array, on the aperture stop in the imaging system with a specific defocus coefficient, and the specific coefficients for spherical aberration and coma aberration.

In summary, (1) The limiting resolution of a defocused imaging system with a specific defocus coefficient can be improved by its corresponding binary shaped pupil. It has been shown that a shaped pupil with a scale ratio K equal to 0.05 is more helpful for extending the depth of focus at low spatial frequency, while a shaped pupil with a scale ratio K equal to 0.3 is more useful for extending the depth of focus at high spatial frequency. (2) In an imaging system with the coefficient for spherical aberration or coma aberration, respectively, the OTF for the shaped pupil with a scale ratio K of less than 0.3 is significantly larger than that for the clear aperture at all spatial frequencies. Especially for $\omega_{40} \geq 10\lambda/\pi$ and $\omega_{31} \geq 10\lambda/\pi$, there is a significant enhancement of the imaging contrast by the use of a specifically shaped aperture with K=0.3 and 0.05 according to the computer-simulated image. (3) the OTFs of a specifically shaped aperture with K=0.05 and K= 0.3 are greater than the OTFs of a clear aperture especially when the aberration coefficients $\geq 5\lambda/\pi$. It is evident that the image quality will be enhanced as the specifically shaped aperture is used, especially for the imaging system with large aberration coefficients including defocus, spherical and come aberrations. (4) The image quality could not be significantly influenced as the fill factor (i.e. aperture ratio) of the spatially shaped pupil varied from 100% to 80%.

In the point of view of optical design, the pupil plane at the aperture stop in the imaging subsystem should be designed to be a conjugate at the other pupil plane on the digital micromirror device for the non-imaging subsystem. The pupil matching between the imaging unit and the non-imaging one could significantly affect its practical implementation and hence the matching sets one limitation on performance. Overall, the pupil matching will be determined by the precise alignment between the digital micromirror device and the lens elements in the whole optical system.

Overall, the proposed approach of shaped pupil from an illumination modulator is a dynamically programmable method to achieve aberration compensation for imaging applications, such as photography, projector and microscopy. This method provides a connection between non-imaging and imaging systems for enhancing the image quality. Regarding the pupil aberration is considered in the illumination system, this influence may be incorporated with the corresponding spherical aberration and even off-axis coma with different levels of coefficients. Hence, practically, the pupil aberration could be included partially and further explored once the spherical aberration and coma are included. It is worth noting that this proposed model can rapidly and field-sequentially generate a specifically shaped pupil with 10 gray levels within the very short image processing time of 0.22 ms in the case of K =0.05. Different spatial frequencies represent different imaging information from an object in photography or a sample in microscopy or a light valve in a projector. High spatial frequencies represent sharp spatial changes in the image, such as edges, and generally correspond to local information and fine detail, while the portion of low spatial frequencies represent global information about the shape, such as general proportion and orientation. On the other hand, this programmable structured light can be substituted for the conventional flash light and illumination light in the conventional incoherent imaging system, in order to extend the depth of

focus (EDOF), and for dynamically providing improved imaging quality for many varied scenes combined with the technology of high dynamic range (HDR) imaging. For instance, by the use of this dynamically programmable structured light with EDOF and HDR technologies, we can capture an sense-of-depth-enhanced image by combining a sub-image with global information (i.e., low spatial frequencies) within first half period of exposure time and another sub-image with local information (i.e., high spatial frequencies) within the other half period of exposure time, which have different shaped pupils with specific scale ratios K.

Chapter 6

Illuminance formation and color-difference of mixed-color LEDs in a rectangular light pipe: an analytical approach

6.1 Introduction

In this section we developed an analytical method of illuminance formation and color-difference for mixing colored LEDs in a rectangular light pipe using the methods of non-imaging optics [26], photometry [27], and colorimetry [28]. The different illuminance formations and color-differences studied in this chapter are the types in which ANSI light uniformity [38] and ANSI color uniformity [38] vary with the different geometric structures of light pipes. For the purpose of comparison, this chapter also includes the formation of illuminance distribution for a single LED source using the same analytical method.

In order to obtain a convenient form of the illuminance formation, we employed the hollow straight light pipe with a perfect reflectivity of 100% for the calculations in this chapter. In reality, the finite absorption loss is inevitable. With more times of reflection, the flux of the ray will decrease, which can affect the illuminance distribution. This influence has been explored by Cheng and Chern [19]. For a common coating with a reflectivity of 90%, the difference of the uniformity deviation from that of 100% reflectivity is less than 1% at the length scale L/A equal and greater than unity, where L is the length of the light pipe and A is a constant which is a geometric parameter for the scale unit of the light pipe's input face. To have a best

approximation for the analytical evaluation, we make another assumption that the LED is a point light source with Lambertian characteristics. In most applications this means that the dimension of LED source should be much less than the cross-sectional dimension of the light pipe. The considerations of a hollow straight light pipe with a perfect reflectivity and a point light source may limit this study, but it will provide an analytical base for the connection between non-imaging and coloring in order to obtain a "uniform" source for illumination applications.

The remainder of this section is organized as follows. In Section 2 we revisit on the chromatic issue and LED RGB color mixing. In Section 3, we describe the light pipe illumination system. In Section 4, we derive illumination formation and function of color difference. In Section 5 we analyze the non-imaging performance for a rectangular light pipe system with mixed-color LEDs. Finally we draw our summary in Section 6.

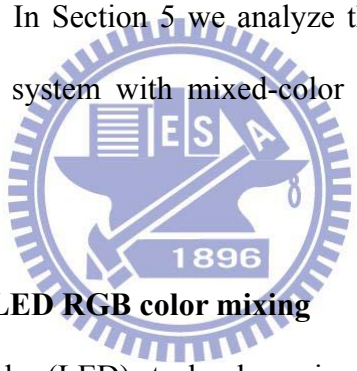

6.2 Chromatic issue and LED RGB color mixing

Today's light emitting diode (LED) technology is widely applied in vehicles, architecture, signal lighting, backlighting and in projection microdisplays [20]. Most of these applications require the shaping of a uniform beam illuminance profile, managing color quality and saving power consumption while maintaining high luminous efficiency in the illumination systems. There are two kinds of approaches to generate white light with LEDs. One is the phosphor-converted white LED which provides a compact integrated package but has a relatively lower luminous efficiency. The other is the mixed-color LED which provides more light throughput compared to a single phosphor-converted white LED with the same operating power. In practice, however, there are several technical challenges to creating a mixed-color LED, such as white light homogenizing with the acceptably lowest spatial variation, color mixing

and color balancing with acceptably lowest chromatic variation.

Rectangular light pipes are commonly optical devices that manage light properties in illumination systems, especially where extremely uniform illuminations with specific illuminance distributions are required [13]. Typical applications are the illuminations in the projection display [22], lithography [15], endoscopes [16] and in optical waveguides [17]. A rectangular light pipe is made with parallel reflective sides with a square or rectangular cross section. The light source can be located on one end of the light pipe and the other end is then the uniformly illuminated plane [18]. The shape of the light pipe can modify the original characteristics of the spatial distribution of the light source but not the angular distribution. The uniform illumination on the exit end of the light pipe is determined by the ratio of the length to the cross-sectional dimension of the light pipe [19].

In the literature, the mention of the properties of light pipes is mostly concentrated on transmittance, flux analysis and irradiance formation for the single light source. Although Derlofske and Hough developed a flux confinement diagram model to discuss the flux propagation of square light pipes and angular distribution [21], and Cheng and Chern developed a semi-analytical method to investigate the formation of irradiance distribution, [19] to the best of our knowledge few articles have investigated the formation of illuminance and the color-differences in mixed-color light sources. An earlier investigation of the use of mixed-color LEDs in a light pipe was done by Zhao et al., and it comprised two parts: a computer simulation using a commercial ray tracing software package with Monte Carlo algorithm; and an experimental study verifying the results obtained from the simulation [30].

6.3 Configuration of the light pipe illumination system

A schematic sketch of an optical system using a rectangular light pipe is shown in Fig. 6-1. The optical system consists of an LED light source with Lambertian angular distribution and a rectangular light pipe, where *a* and *b* are the width and the height of the cross section of the light pipe, respectively, *L* is the length of the light pipe, *c* is the size of the square light source and n is the optical index of the light pipe's material. The LED light source is located at the entrance of the light pipe, and the light source has an angular distribution extending from +90° to -90°. The exit is uniformly illuminated by the multiple reflections throughout the light pipe.

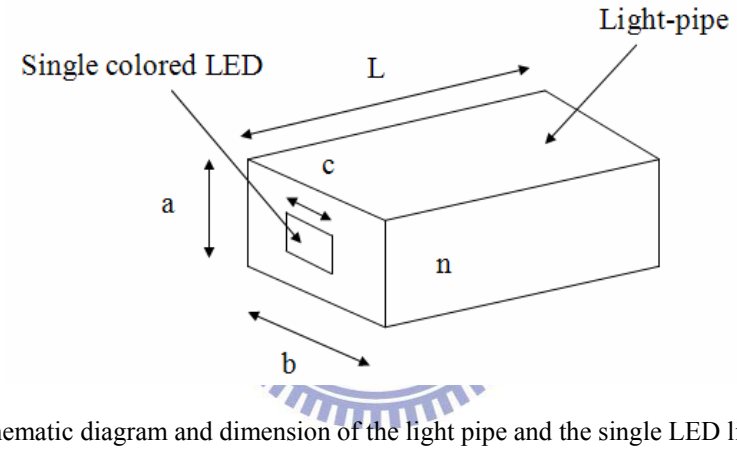

Figure 6-1 Schematic diagram and dimension of the light pipe and the single LED light source.

The light pipe is made with parallel reflective sides with a rectangular cross section. The virtual image of the light at the entrance of the light pipe has the checkerboard-array-shaped light distribution which results from the multiple reflections of the light source through the pipe as shown in Fig. 6-2. The spaces between each adjacent light spot are: *a* on the vertical axis and *b* on the horizontal axis, which are equal to the width and height of the cross section of the light pipe, respectively. And, the size of each light spot is equal to that of the light source. The radiant intensity of each light spot is denoted as $J'_{i,j}$ as shown in Fig. 6-2 (b). The subscripts *m* and *n* stand for the reflective times on the horizontal axis and vertical

axis, respectively, and the plus and minus values of i and j denote the opposite directions of the light source. For example, $J'_{1,2}$ means that the luminous flux of the light spot is reflected one time on the horizontal axis and two times on the vertical axis and its location is shown in Fig. 6-2 (b).

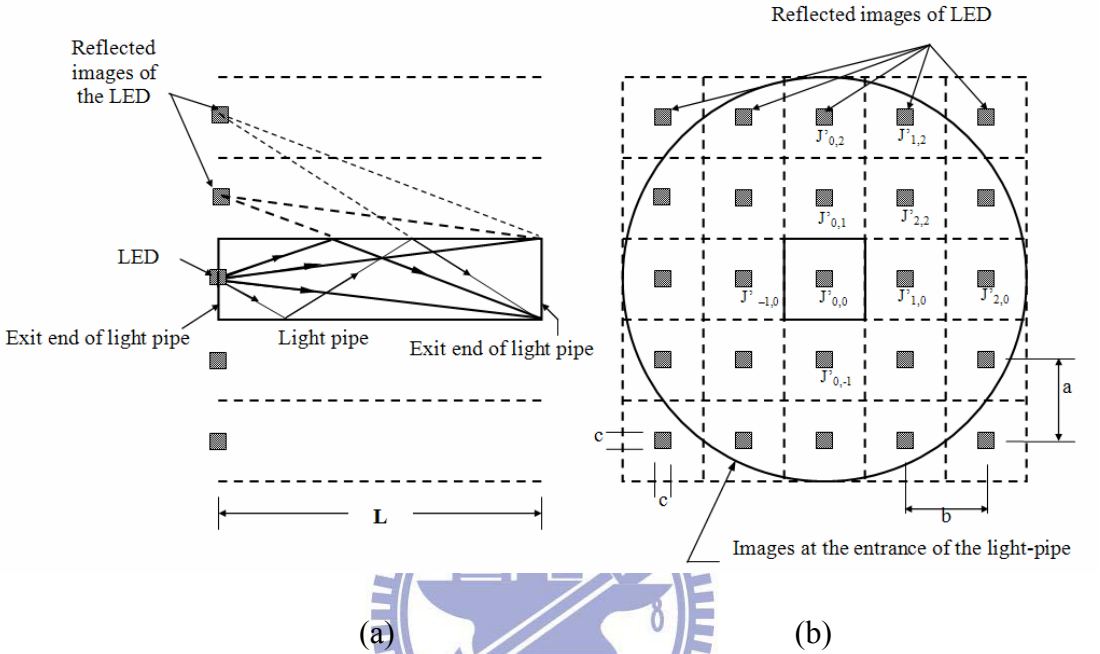

Figure 6-2 (a) Principal of the operation of a light pipe. (b) Virtual image at the entrance of the light pipe. The light pipe is made with parallel reflective sides with a rectangular cross section. The multiple reflections of the light source through the pipe can produce a spatial checkerboard-array-shaped light distribution.

The schematic sketch of one specific light pipe optical system with mixed-color LEDs is illustrated in Fig. 6-3 (a). The optical system consists of four colored LED light sources, including one red-colored LED, two green-colored LEDs and one blue-colored LED, and a rectangular light pipe, where a and b are the width and the height of the cross section of the light pipe, respectively, where L is the length of the light pipe, c is the side of the square light source, and n is the optical index of the light pipe material. The light sources are located at the entrance of the light pipe as shown in Fig. 6-3 (b), where the red LED is located at the coordinate (-P, Q), the first green

LED is located at (P, Q), the second green LED is located at (-P, -Q) and the blue LED is located at (+P, -Q), respectively, assuming that the coordinate of the center for the entrance of the light pipe is (0, 0).

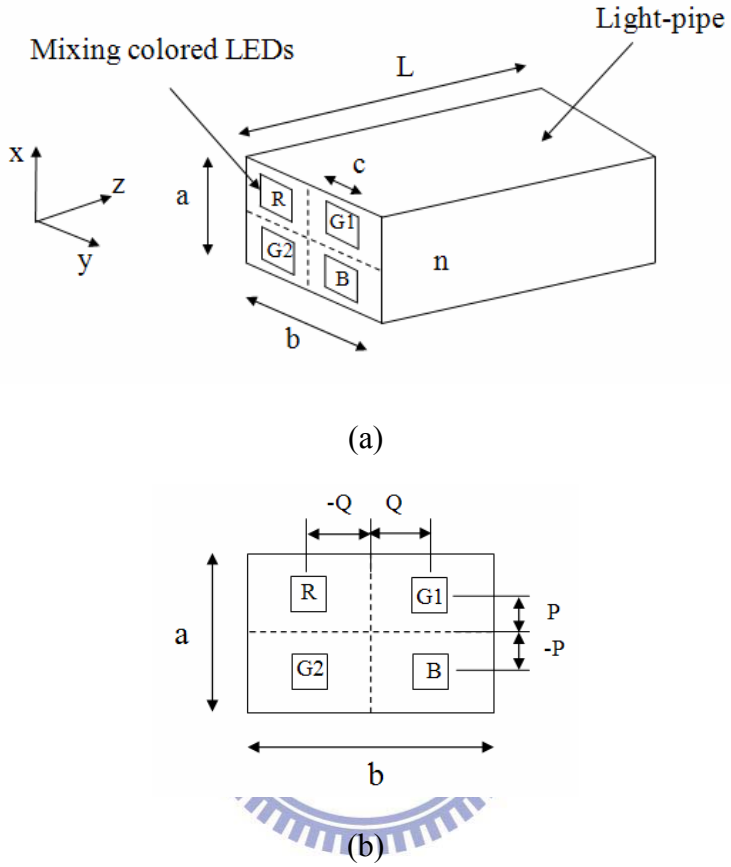

Figure 6-3 (a) Schematic diagram and dimension of the light pipe. (b) Locations of red, green and blue LED light sources, i.e. mixed-color LEDs, on the entrance of light pipe.

6.4 Optical computation for illumination formation and function of color difference

The illuminance distribution on the end plane of the light pipe is referring to Eq. (2-9) ands given by

$$H(x,y) = J(\theta)\frac{\cos^3\theta}{L^2} = J_0 \times \frac{L^2}{\left(L^2 + x^2 + y^2\right)^2} \tag{6-1}$$

Then, we determine the individual contribution of illuminance by the virtual light spots on the entrance plane of the light pipe. The illuminance $H_{0,0}$ is radiated without

any reflection through the light pipe about x from $-a/2$ to $+a/2$ and about y from $-b/2$ and $+b/2$ as shown in Fig. 6-4.

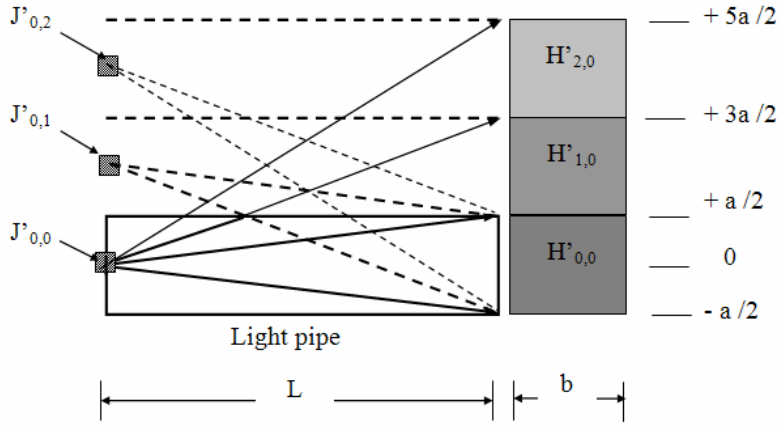

Figure 6-4 Illustration of a Lambertian light source radiating into the exit plane of the light pipe for the different virtual light spot on the entrance plane of the light pipe

and as given by

$$H_{00}(x,y) = J_0 \times \frac{L^2}{\left(L^2 + x^2 + y^2\right)^2}, \qquad -\frac{a}{2} \le x \le \frac{a}{2}, -\frac{b}{2} \le y \le \frac{b}{2} \tag{6-2}$$

Where the values a and b are the width and the height of the cross section of the light pipe, respectively. Also, we can derive the illuminances $H'_{1,0}$ and $H'_{2,0}$ that are radiated with one time reflection and a two times reflection , respectively, through the light pipe along the +x axis direction, as shown in Fig. 5 . They are given by

$$H'_{10}(x,y) = J_0 \times \frac{\rho L^2}{\left(L^2 + x^2 + y^2\right)^2}, \qquad \frac{a}{2} \le x \le \frac{3a}{2}, -\frac{b}{2} \le y \le \frac{b}{2}. \tag{6-3}$$

$$H'_{20}(x,y) = J_0 \times \frac{\rho^2 L^2}{\left[L^2 + x^2 + y^2\right]^2}, \qquad \frac{3a}{2} \le x \le \frac{5a}{2}, -\frac{b}{2} \le y \le \frac{b}{2}. \tag{6-4}$$

where ρ is the reflectivity, and the exponent of ρ is the reflective time. Then, we can derive the practical illuminance distribution, which is radiated from the individual virtual light spot on the entrance plane of the light pipe, on the exit plane of the light

pipe about x from $-a/2$ to $+a/2$ and about y from $-b/2$ and $+b/2$ using the mirror mapping method according to Eq. (6) and Eq. (7) as given by

$$H_{10}(x,y) = J_0 \times \frac{\rho L^2}{\left[L^2 + (-x+a)^2 + y^2\right]^2}, \qquad -\frac{a}{2} \le x \le \frac{a}{2}, -\frac{b}{2} \le y \le \frac{b}{2} \tag{6-5}$$

$$H_{20}(x,y) = J_0 \times \frac{\rho^2 L^2}{\left[L^2 + (x+2a)^2 + y^2\right]^2}, \qquad -\frac{a}{2} \le x \le \frac{a}{2}, -\frac{b}{2} \le y \le \frac{b}{2} \tag{6-6}$$

Then, we can extend the expression of the illuminance for each virtual light spot on the exit plane of the light pipe with one time reflection and a two times reflection through the light pipe along the ±x axes and the ±y axes directions about x from $-a/2$ to $+a/2$ and about y from $-b/2$ and $+b/2$, respectively as follows,

$$H_{\pm 1 \pm 1}(x,y) = J_0 \times \frac{\rho\,\rho\, L^2}{\left[L^2 + (-x \pm a)^2 + (-y \pm b)^2\right]^2}, \quad -\frac{a}{2} \le x \le \frac{a}{2}, -\frac{b}{2} \le y \le \frac{b}{2} \tag{6-7}$$

$$H_{\pm 2 \pm 2}(x,y) = J_0 \times \frac{\rho^{|\pm 2|}\,\rho^{|\pm 2|}\,\rho\, L^2}{\left[L^2 + (x \pm 2a)^2 + (y \pm 2b)^2\right]^2}, \quad -\frac{a}{2} \le x \le \frac{a}{2}, -\frac{b}{2} \le y \le \frac{b}{2} \tag{6-8}$$

Finally we can summarize the expression of the total illuminance for each virtual light spot on the entrance plane of the light pipe as follows,

$$\begin{aligned} H_0(x,y) = & \sum_{j=-\infty}^{\infty}\sum_{i=-\infty}^{\infty} \frac{J_0 \rho^{|i|+|j|}\, L^2}{\left\{L^2 + \left[-x + (2i+1)a\right]^2 + \left[-y + (2j+1)b\right]^2\right\}^2} \\ & + \sum_{j=-\infty}^{\infty}\sum_{i=-\infty}^{\infty} \frac{J_0 \rho^{|i|+|j|}\, L^2}{\left\{L^2 + \left[x + 2ia\right]^2 + \left[y + 2jb\right]^2\right\}^2} \\ & + \sum_{j=-\infty}^{\infty}\sum_{i=-\infty}^{\infty} \frac{J_0 \rho^{|i|+|j|}\, L^2}{\left\{L^2 + \left[-x + (2i+1)a\right]^2 + \left[y + 2jb\right]^2\right\}^2} \\ & + \sum_{j=-\infty}^{\infty}\sum_{i=-\infty}^{\infty} \frac{J_0 \rho^{|i|+|j|}\, L^2}{\left\{L^2 + \left[x + 2ia\right]^2 + \left[-y + (2j+1)b\right]^2\right\}^2}, \quad -\frac{a}{2} \le x \le \frac{a}{2}, -\frac{b}{2} \le y \le \frac{b}{2} \end{aligned} \tag{6-9}$$

where the exponent of ρ indicates the reflective times through the light pipe on the x and y axis, respectively. The first term of Eq. (6-9) represents the illuminance for the virtual light spots with an odd times reflection along the ±x axes and an odd times reflection along the ±y axes. The second term of Eq. (6-9) represents the illuminance

for the virtual light spots without any reflection through the light pipe and with an even times reflection along the ±x axes and an even times reflection along the ±y axes, respectively. The third term of Eq. (6-9) represents the illuminance for the virtual light spots with an odd times reflection along the ±x axes and an even times reflection along the ±y axes. The fourth term of Eq. (6-9) represents the illuminance for the virtual light spots with an even times reflection along the ±x axes and an odd times reflection along the ±y axes. Eq. (6-9) can be simplified as following,

$$H_0(x,y)=\sum_{j=-\infty}^{\infty}\sum_{i=-\infty}^{\infty}\frac{J_0\rho^{|i|+|j|}\ L^2}{\left\{L^2+\left[(-1)^i x+ia\right]^2+\left[(-1)^j y+jb\right]^2\right\}^2}\quad ,\quad -\frac{a}{2}\le x\le\frac{a}{2},-\frac{b}{2}\le y\le\frac{b}{2} \tag{6-10}$$

With reference to Fig. 6-3, we assume that the light sources are located at the entrance of the light pipe, where the red LED is located at coordinate (-P, +Q), the first green LED is located at (+P, +Q), the second green LED is located at (-P, -Q) and the blue LED is located at (+P, -Q), respectively. The expression of the illuminance distribution radiated from each LED on the exit plane of light pipe can be derived from the Eq. (6-10) by shifting on the x-axis and the y-axis, as follows,

$$H_{G1}(x,y)=H_0(x-P,y-Q) \tag{6-11}$$

$$H_{G2}(x,y)=H_0(x+P,y+Q) \tag{6-12}$$

$$H_R(x,y)=H_0(x+P,y-Q) \tag{6-13}$$

$$H_B(x,y)=H_0(x-P,y+Q) \tag{6-14}$$

Where $H_{G1}(x,y)$, $H_{G2}(x,y)$, $H_R(x,y)$ and $H_B(x,y)$ are the illuminance distributions radiated from the first green LED, second green LED, red LED and blue LED, respectively. And, the J_{G1}, J_{G2}, J_R and J_B represent the luminous intensity of the incremental area in the normal direction for each color LEDs, respectively.

Finally we can summarize the total illuminance distribution for the mixed-colors LEDs on the exit plane of the rectangular light pipe as given by,

$$H_T(x,y)=H_{G1}(x,y)+H_{G1}(x,y)+H_R(x,y)+H_B(x,y) \tag{6-15}$$

To identify the uniformity on the exit plane of the rectangular light pipe, we introduce the ANSI light uniformity referring to Eq. (2-10) and Eq. (2-11) and defined by [38]

$$Ur+ = \left(\frac{Maximum\ [H_T(x_l, y_l)]_{l=10,11,12,13}}{Average\ [H_T(x_l, y_l)]_{l=1,2,..9}} - 1 \right) \times 100\% \tag{6-16}$$

$$Ur- = \left(\frac{Minimum\ [H_T(x_l, y_l)]_{l=10,11,12,13}}{Average\ [H_T(x_l, y_l)]_{l=1,2,..9}} - 1 \right) \times 100\% \tag{6-17}$$

The general equations that define the tristimulus-values distribution for each colored LEDs in the CIE 1931 system on the exit plane of the rectangular light pipe are given by [28]

$$\begin{aligned} X_m(x,y) &= k\ H_m(x,y) \times \sum_{\lambda} \beta_m(\lambda) S_m(\lambda)\ \bar{x}(\lambda) \Delta\lambda \\ Y_m(x,y) &= k\ H_m(x,y) \times \sum_{\lambda} \beta_m(\lambda) S_m(\lambda)\ \bar{y}(\lambda) \Delta\lambda \quad , m = R,\ G1,\ G2,\ B \\ Z_m(x,y) &= k\ H_m(x,y) \times \sum_{\lambda} \beta_m(\lambda) S_m(\lambda)\ \bar{z}(\lambda) \Delta\lambda \end{aligned} \tag{6-18}$$

where $\bar{x}(\lambda)$, $\bar{y}(\lambda)$, and $\bar{z}(\lambda)$ denote the set of color-matching functions, k is the normalized factor, $\beta_m(\lambda)$ is the total spectral reflectance of the illuminated parallel reflective sides in the light pipe for each light source and $S_m(\lambda)$ is the relative spectral concentration of the radiant power for each light source, and $H_m(x,y)$ denotes the illuminance distribution radiated from each light source.

Then, we determine the tristimulus-values distribution for the mixed- color LEDs in the CIE 1931 system and the chromaticity coordinates in the CIE 1976 system on the exit plane of the rectangular light pipe which are given by

$$\begin{aligned} X_w(x,y) &= X_R(x,y) + X_{G1}(x,y) + X_{G2}(x,y) + X_B(x,y) \\ Y_w(x,y) &= Y_R(x,y) + Y_{G1}(x,y) + Y_{G2}(x,y) + Y_B(x,y) \\ Z_w(x,y) &= Z_R(x,y) + Z_{G1}(x,y) + Z_{G2}(x,y) + Z_B(x,y) \end{aligned} \tag{6-19}$$

$$u'(x,y) = \frac{4X_w}{X_w + 15Y_w + 3Z_w}$$
$$v'(x,y) = \frac{9X_w}{X_w + 15Y_w + 3Z_w} \quad (6\text{-}20)$$

Finally, we identify the color uniformity by referring to Eq. (2-12), and the total color difference between two color stimuli, each given in the terms of L^*, a^*, b^*, in CIE 1976 ($L^*a^*b^*$) –space by referring to Eq. (2-13) and Eq. (2-14),on the exit plane of the rectangular light pipe.

6.5 Non-imaging performance evaluation

First, we select OSTAR® – Projection (Type name: LE ATB A2A) as our LED light sources [61], whose relative spectral concentrations of radiant powers $S_R(\lambda)$, $S_G(\lambda)$and $S_B(\lambda)$, are shown in Fig. 6-6 with a typical luminous intensity per color of 18 cd for one red-colored LED, 14 cd for one green-colored LED and 3.5 cd for one blue-colored LED, respectively, and with its natural white coordinate (0.360, 0.242) in the CIE 1931 system. Besides the natural white color point of the specific LED light source employed in this chapter, it can also be extended to other more common white color points, such as the color coordinate (0.333, 0.333), by adjusting the relative luminous intensity of each colored LED but decreasing the total output of the luminous intensity.

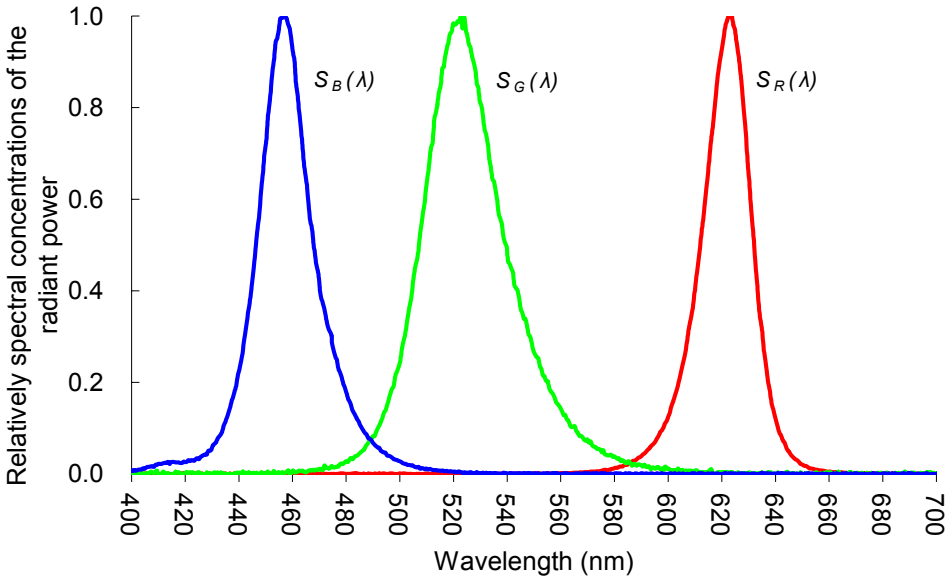

Figure 6-6 Relative spectral concentrations of the radiant powers $S_R(\lambda)$, $S_G(\lambda)$ and $S_B(\lambda)$. For OSTAR® – Projection (Type name: LE ATB A2A) as our LEDs light sources.

In order to have a convenient form for the numerical evaluation we assume the following. The reflectivity ρ is unity in Eq. (6-10) and the total spectral reflectance $\beta_m(\lambda)$ is also unity in Eq. (6-18). Finally, we calculate and analyze the total illuminance distribution using Eq. (6-10) and Eq. (6-15), the ANSI uniformity using Eq. (2-16) and Eq. (2-17), the ANSI color uniformity using Eq. (2-12) and the total color-difference distribution using Eq. (2-13) on the exit plane of the rectangular light pipe for a single color LED and mixed- color LEDs, respectively. In calculating Eq. (2-13), $X_n = 94.825$, $Y_n = 100$, $Z_n = 107.381$ are the tristimulus-values of the nominally white object-color stimuli given by the spectral radiant power of one of the CIE standard illuminants D65 which represents a phase of the natural daylight with a correlated color temperature of approximately 6504 K. The CIE standard illuminant D65 is recommended a method of calculating the relative spectral radiant power distributions of any daylight illuminant [28].

The computer programs for the above mentioned evaluations are written in Mathematica software [41]. We calculated and analyzed four cases as follows,

Case 1

There is a single LED point light source located at the center of the entrance plane of the light pipe with c=0, P=Q=0, a= b= A, L= 0.10A, 0.25A, 0.50A, 1.00A and 2.00A, respectively, where A is a constant. The distributions of the illuminances for L= 0.10A, 0.50A and 1.00A are shown in Fig. 6-7 (a), Fig. 6-7 (c) and Fig. 6-7 (e), respectively, and the contours of the illuminances for L= 0.10A, 0.50A and 1.00A are shown in Fig. 6-7 (b), Fig. 6-7 (d) and Fig. 6-7 (f), respectively. The variation of the ANSI light uniformity versus the length L of the light pipe is shown in the linear chart of Fig 6-7 (g) and in the exponential chart of Fig. 6-7 (h), respectively. The result shows us that the ANSI light uniformity at the exit plane of the light pipe with a single LED light source can be reduced exponentially with the increase in the length of the light pipe. In the case of the length scale L/A being greater than unity, a single LED source at the center of the entrance plane is uniformly illuminated with the acceptable uniformly brightness image, i.e. +2.7% / -2.16% ANSI light uniformity, on the exit plane of the light pipe. Once the light pipe is long enough with L/A over 2.0, then the ANSI light uniformity can be achieved to +0.006%/-0.006% as being perfect. This result was also demonstrated and proven in the paper of Cheng and Chern [19] using the semi-analytical methods of the sequential ray tracing and the statistical method of the Monte Carlo non-sequential ray tracing.

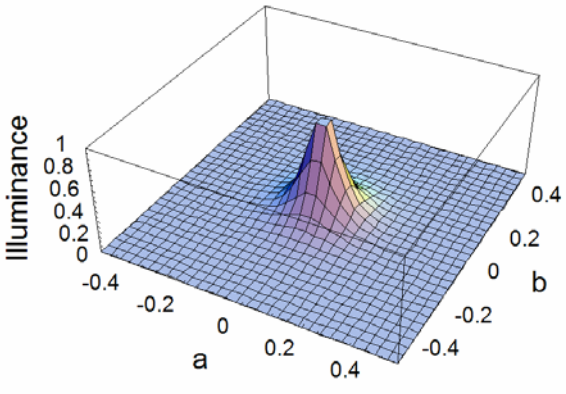
Illuminance
1
0.8
0.6
0.4
0.2
0
-0.4
-0.2
0
0.2
0.4
a
b

(a)

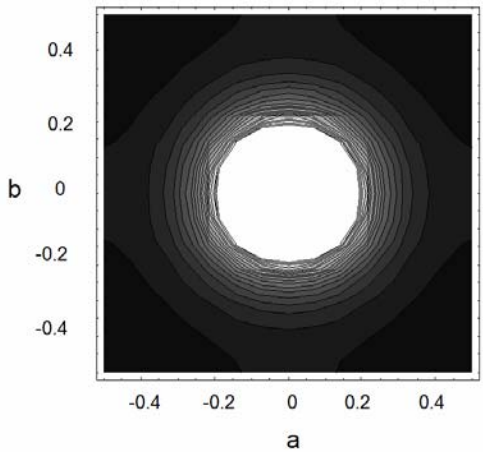
0.4
0.2
0
-0.2
-0.4
b
-0.4
-0.2
0
0.2
0.4
a

(b)

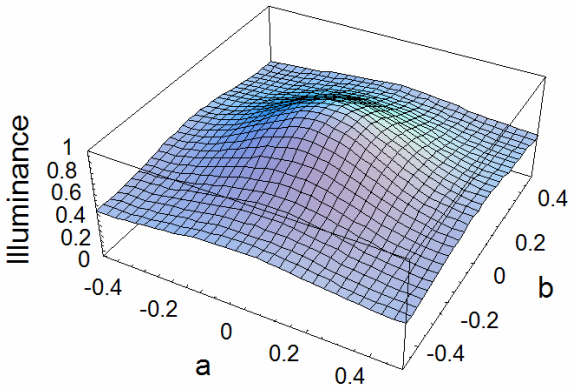
Illuminance
1
0.8
0.6
0.4
0.2
0
-0.4
-0.2
0
0.2
0.4
a
b

(c)

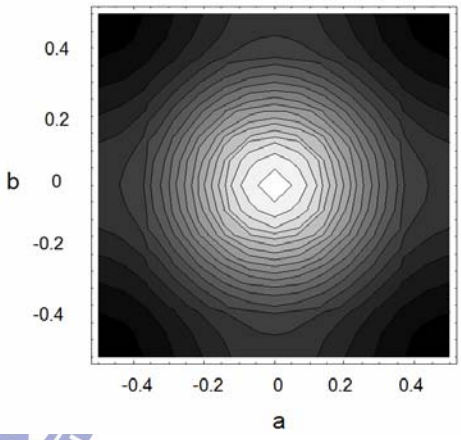
0.4
0.2
0
-0.2
-0.4
b
-0.4
-0.2
0
0.2
0.4
a

(d)

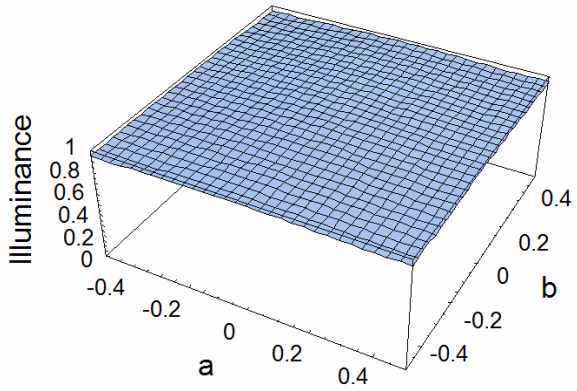
Illuminance
1
0.8
0.6
0.4
0.2
0
-0.4
-0.2
0
0.2
0.4
a
b

(e)

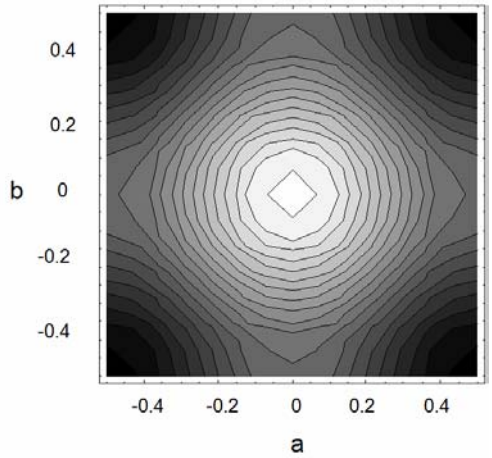
0.4
0.2
0
-0.2
-0.4
b
-0.4
-0.2
0
0.2
0.4
a

(f)

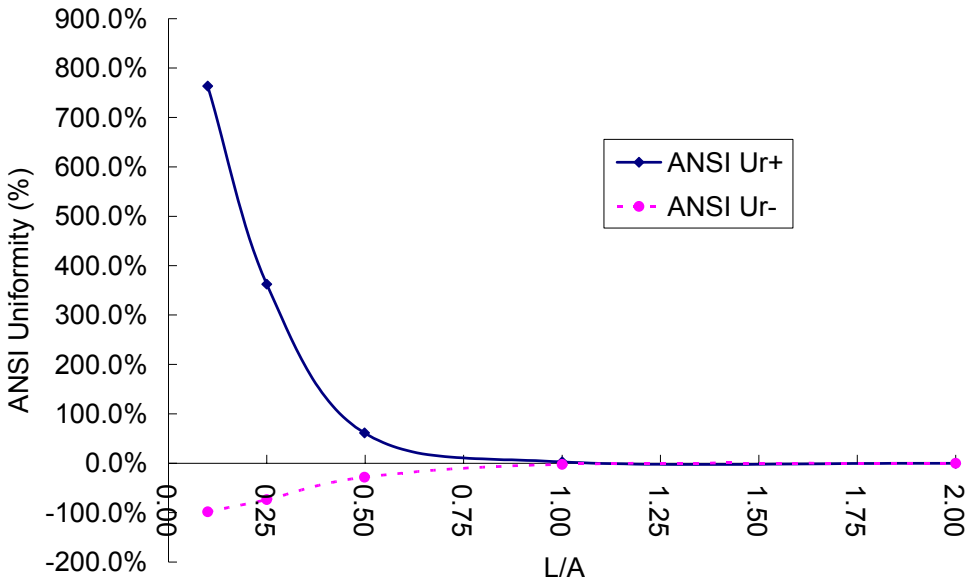

(g)

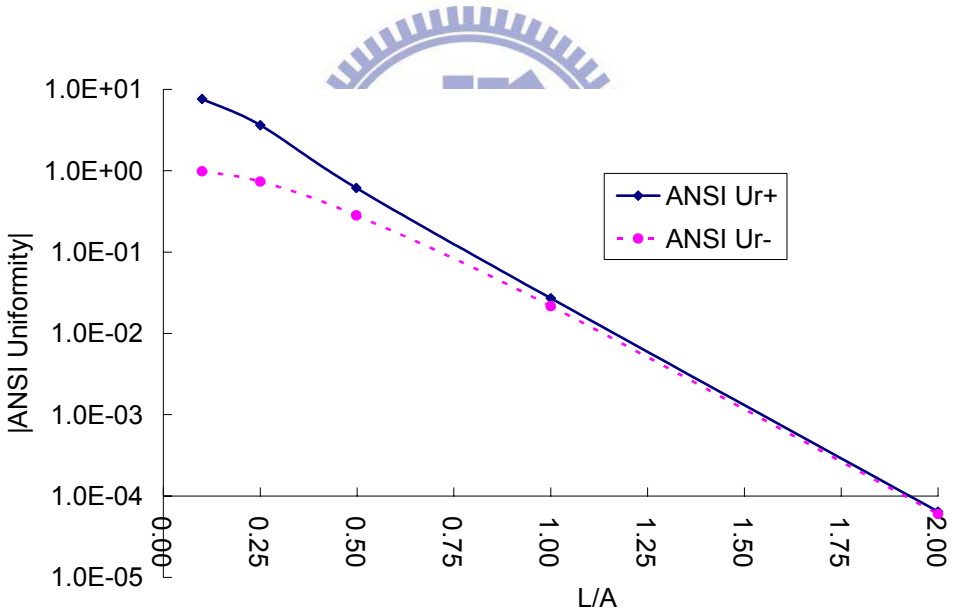

(h)

Figure 6-7 Distributions and contours of illuminance for single LEDs under the condition of P=Q=0 and *a*=*b*=A with (a) and (b) *L*=0.1A, (c) and (d) *L*=0.5A, (e) and (f) *L*=1.0A. Also, the variation of ANSI light uniformity versus the length L of a light pipe with (g) linear chart and (h) exponential chart.

Case 2

As shown in Fig. 6-3, the point light sources are located at specific locations on the entrance plane of the light pipe with c=0, P=Q=A/4, a= b= A, L= 0.10A, 0.25A, 0.50A, 1.00A and 2.00A, respectively, where A is a constant. The distributions of the illuminances for L= 0.10A, 0.50A and 2.00A are shown in Fig. 6-8 (a), Fig. 6-8 (c) and Fig. 6-8 (e), respectively, and the contours of the illuminances for L= 0.10A, 0.50A and 2.00A are shown in Fig. 6-8 (b), Fig. 6-8 (d) and Fig. 6-8 (f), respectively. The variation of ANSI light uniformity versus the length L of the light pipe is shown in the linear chart of Fig 6-8 (g) and in the exponential chart of Fig. 6-8 (h), respectively. The result shows us that the ANSI light uniformity at the exit plane of the light pipe with mixed-color LED light sources can also be reduced exponentially with the increase in length of the light pipe with a similar result as in Case-1. In the case of the length scale L/A being greater than unity, the mixed-color LED sources on the entrance plane are uniformly illuminated with an acceptable uniform brightness, i.e. +0.61% / -0.65% ANSI uniformity, on the exit plane of the light pipe. Once the light pipe is long enough with L/A over 2.0, then the ANSI uniformity can be achieved to +0.0016%/-0.0016% as being perfect.

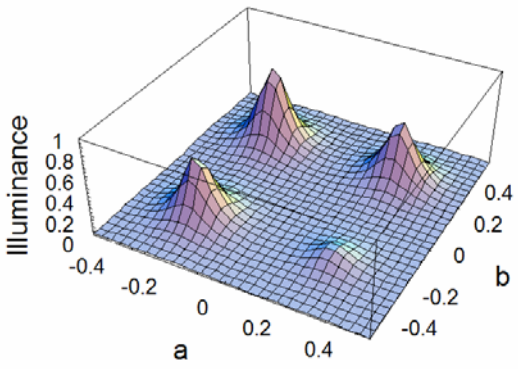
Illuminance
1
0.8
0.6
0.4
0.2
0
-0.4
-0.2
0
0.2
0.4
a
b

(a)

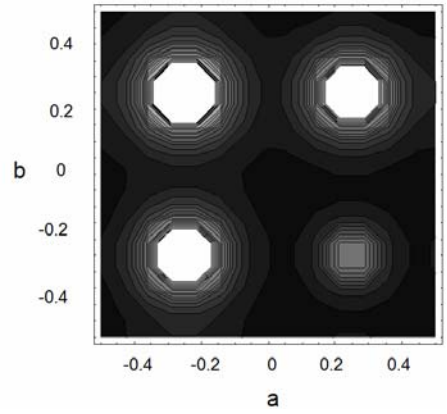
0.4
0.2
b 0
-0.2
-0.4
-0.4
-0.2
0
0.2
0.4
a

(b)

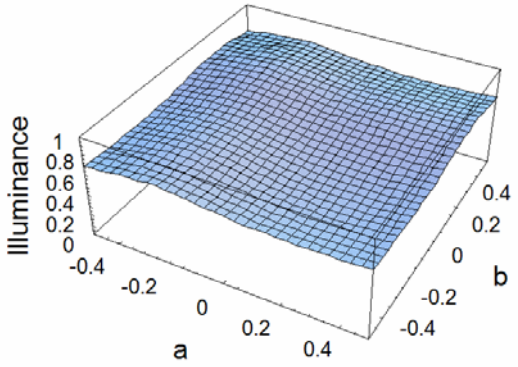
Illuminance
1
0.8
0.6
0.4
0.2
0
-0.4
-0.2
0
0.2
0.4
a
b

(c)

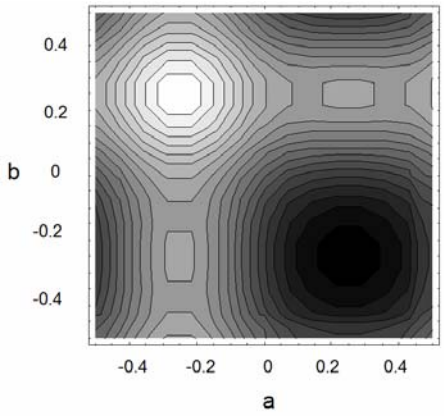
0.4
0.2
b 0
-0.2
-0.4
-0.4
-0.2
0
0.2
0.4
a

(d)

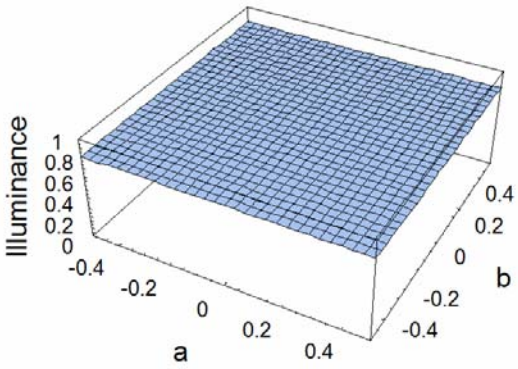
Illuminance
1
0.8
0.6
0.4
0.2
0
-0.4
-0.2
0
0.2
0.4
a
b

(e)

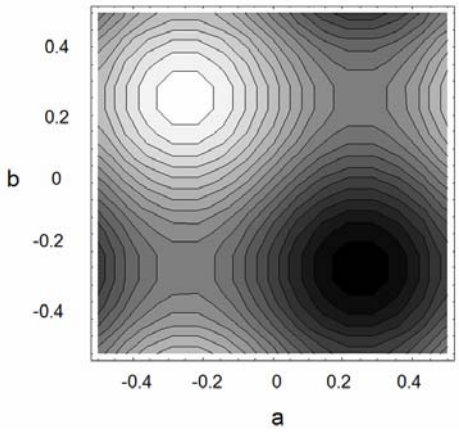
0.4
0.2
b 0
-0.2
-0.4
-0.4
-0.2
0
0.2
0.4
a

(f)

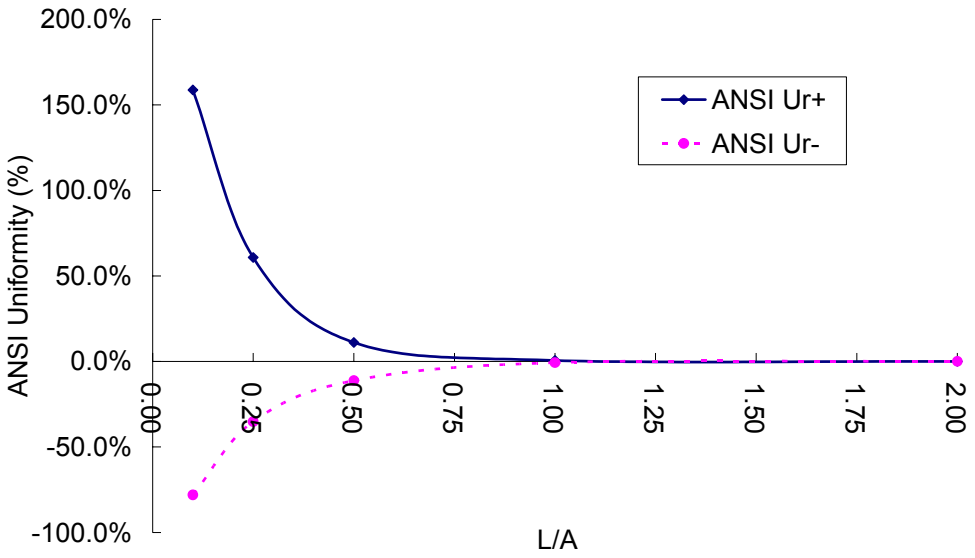

(g)

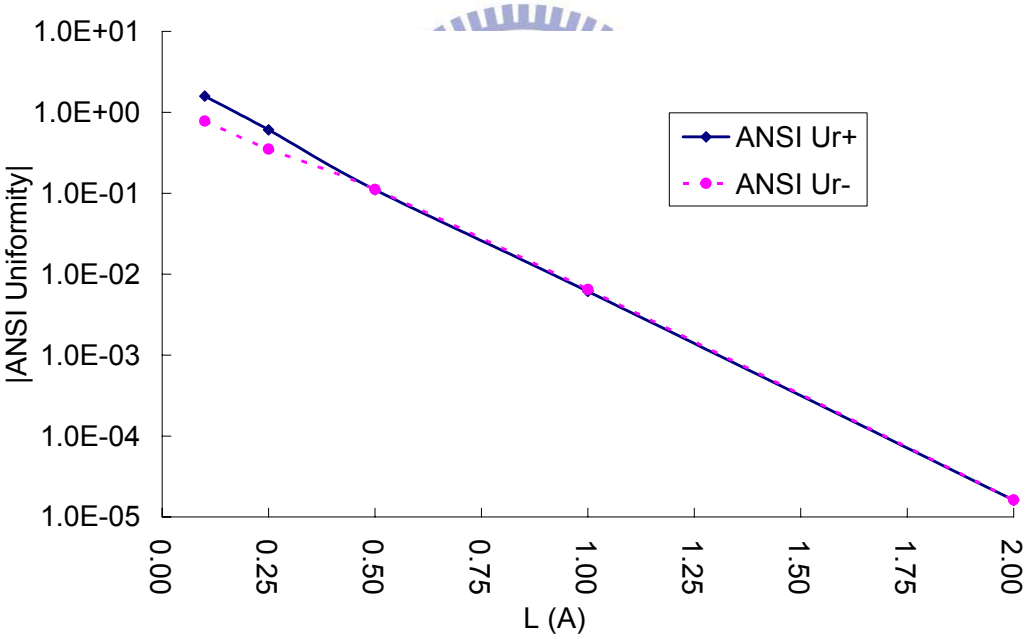

(h)

Figure 6-8 Distributions and contours of illuminance for mixed-color LEDs in the condition of P=Q=A/4 and *a*=*b*=A with (a) and (b) *L*=0.1A, (c) and (d) *L*=0.5A, (e) and (f) *L*=2.0A. Also, the variation of ANSI light uniformity versus the length L of a light pipe with (g) linear chart and (h) exponential chart.

Furthermore, the distributions of the color-differences for L= 0.10A, 0.50A , 1.00A and 2.00A are shown in Fig. 6-9 (a), Fig. 6-9 (c), Fig. 6-9 (e) and Fig. 6-9 (g), respectively, and the contours of the color-differences for L= 0.10A, 0.50A , 1.00A and 2.00A are shown in Fig. 6-9 (b), Fig. 6-9 (d), Fig. 6-9 (f) and Fig. 6-9 (h), respectively. The variation of the ANSI color uniformity versus the length L of the light pipe is shown in the linear curve and the exponential curve of Fig 6-9 (i). The result shows us that the ANSI color uniformity at the exit plane of the light pipe with a mixed-color LED light source can also be reduced exponentially by increasing the length of the light pipe. In the case of the length scale L/A being greater than unity, the mixed-color LED sources on the entrance plane are uniformly illuminated with an acceptable uniform color image, i.e. 0.27% ANSI color uniformity, on the exit plane of the light pipe. Once the light pipe is long enough with L/A over 2.0 then a perfect ANSI uniformity can be achieved to 7.3×10^{-6} %.

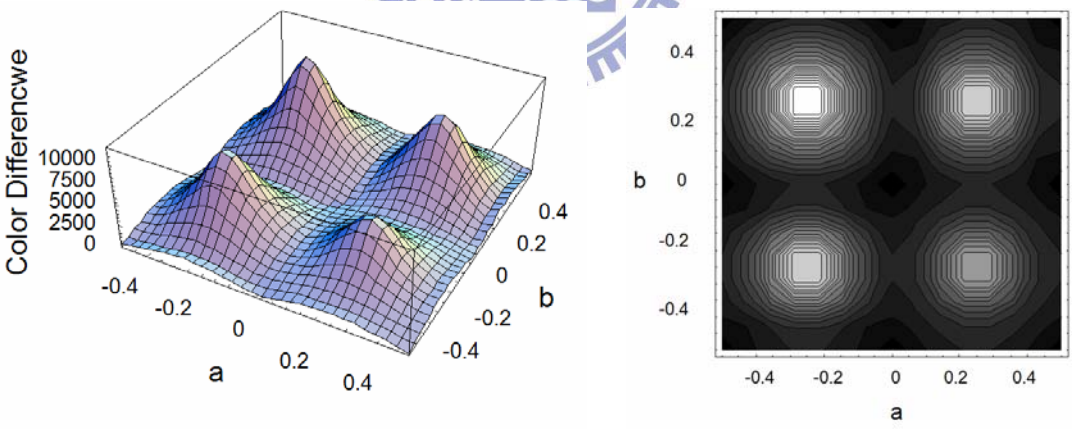

(a) (b)

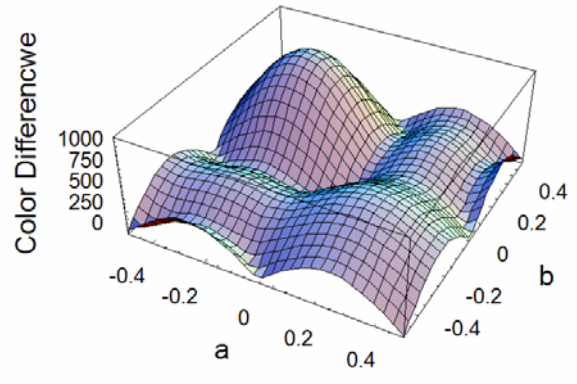
Color Differencwe
1000
750
500
250
0
-0.4
-0.2
0
0.2
0.4
a
b

(c)

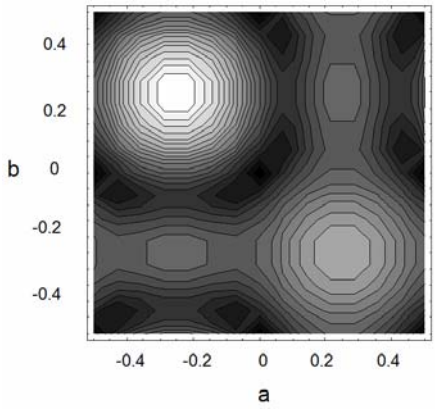
b
a

(d)

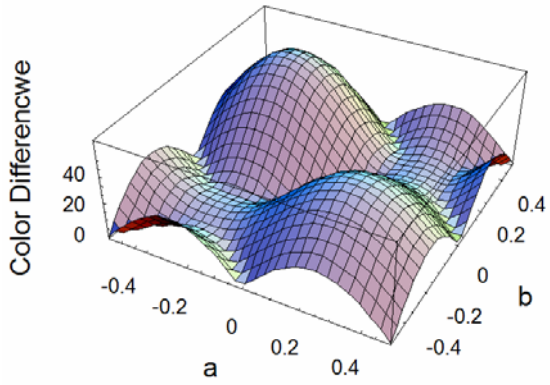
Color Differencwe
40
20
0
-0.4
-0.2
0
0.2
0.4
a
b

(e)

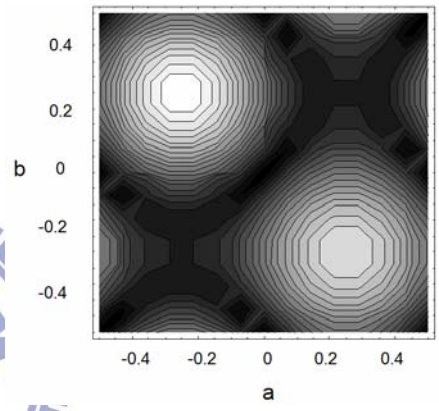
b
a

(f)

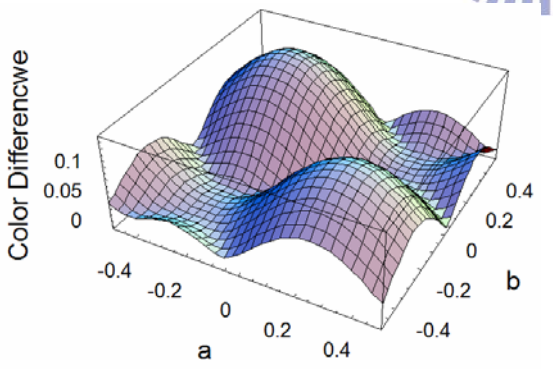
Color Differencwe
0.1
0.05
0
-0.4
-0.2
0
0.2
0.4
a
b

(g)

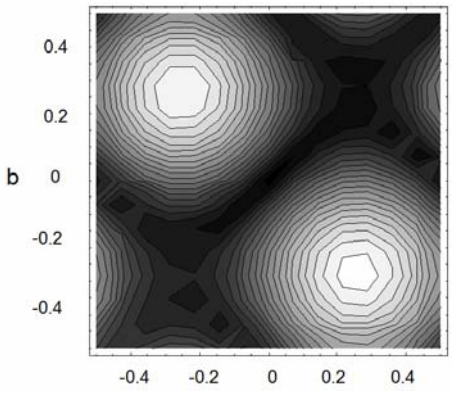
b
a

(h)

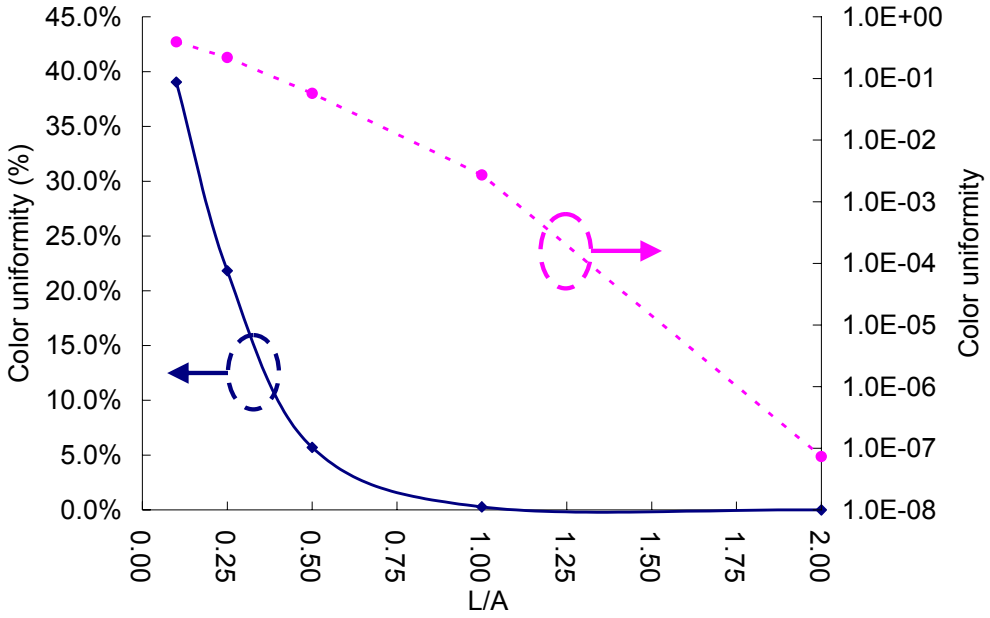

(i)

Figure 6-9 Distributions and contours of the color-difference for mixed-color LEDs in the condition of P=Q=A/4 and *a*=*b*=A with (a) and (b) *L*=0.1A, (c) and (d) *L*=0.5A, (e) and (f) *L*=1.0A, (g) and (h) *L*=2.0A. Also, (i) the variation of ANSI color uniformity versus the length *L* of a light pipe with linear chart and exponential chart.

Case 3

As shown in Fig. 6-3, the point light sources are located at specific locations on the entrance plane of the light pipe with c=0, P=Q=A/4, *a*= *L*= A, *b*= 0.5A, 1.0A, 1.5A, 2.0A and 3.0A, respectively, where A is a constant. The distributions of the illuminances for *b*= 1.5A, 2.0A and 3.0A are shown in Fig. 6-10 (a), Fig. 6-10 (c) and Fig. 6-10 (e), respectively, and the contours of the illuminance for *b*= 1.5A, 2.0A and 3.0A are shown in Fig. 6-10 (b), Fig. 6-10 (d) and Fig. 6-10 (f), respectively. The variation of the ANSI light uniformity versus the height *b* of the light pipe is shown in the linear chart of Fig 6-10 (g) and in the exponential chart of Fig. 6-10 (h), respectively. The result shows us that the ANSI light uniformity at the exit plane of the light pipe with mixed-color LED light sources can also be increased exponentially by increasing the height of the light pipe opposite to that of Case-2. In the case of the

height scale L/A being greater than 2.0, the mixed- color LED sources on the entrance plane is not able to be uniformly illuminated with an acceptable uniform brightness image, i.e. +6.2% / -5.3% ANSI uniformity, on the exit plane of the light pipe.

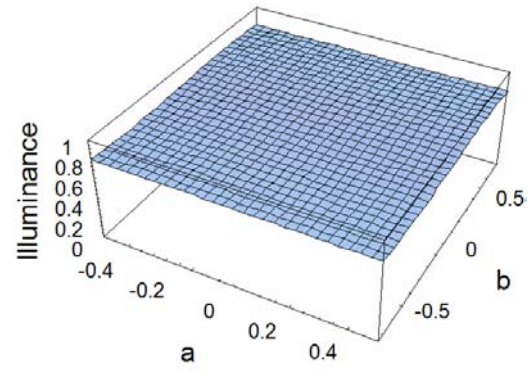

(a)

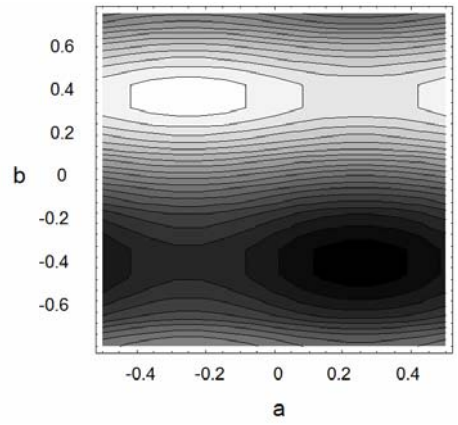

(b)

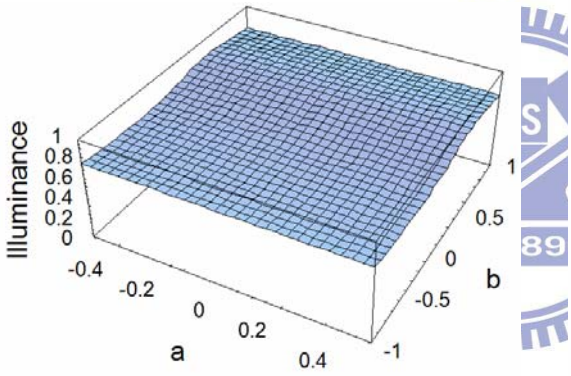

(c)

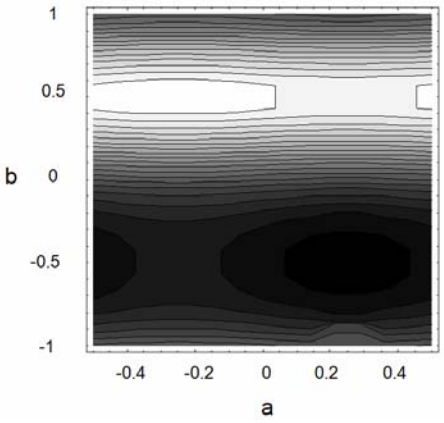

(d)

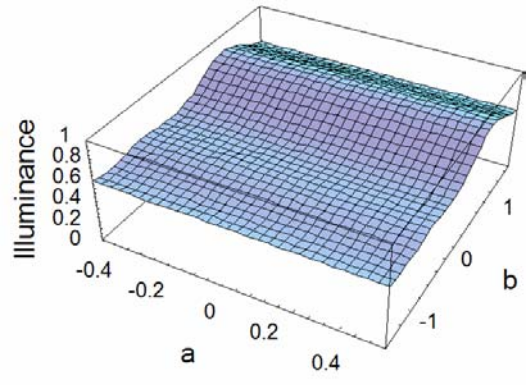

(e)

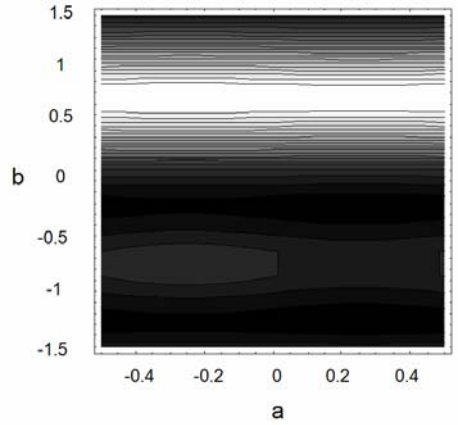

(f)

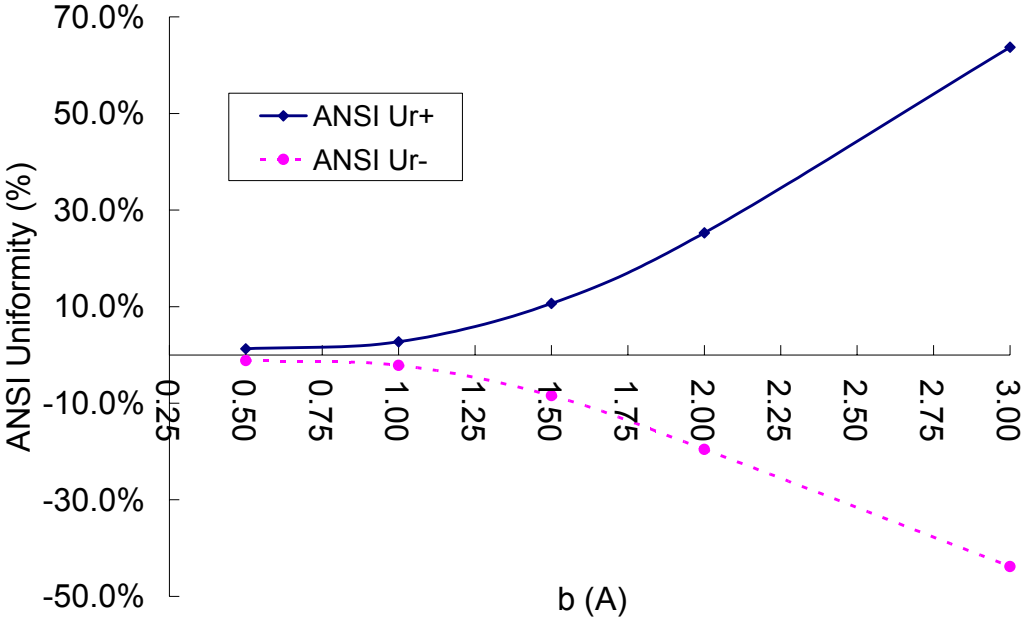

(g)

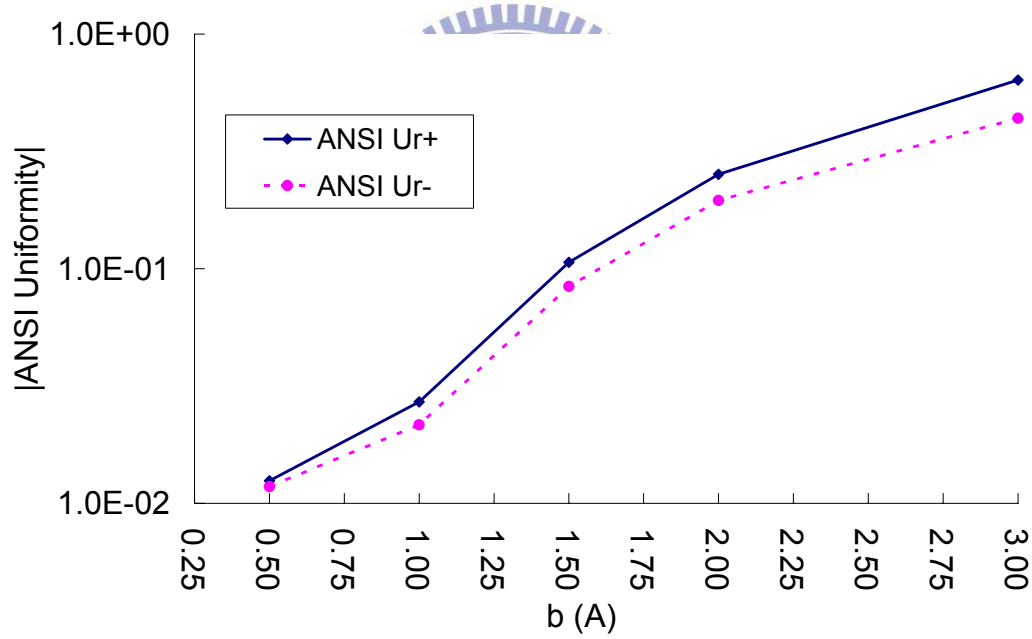

(h)

Figure 6-10 Distributions and contours of illuminance for mixed-color LEDs in the condition of P=Q=A/4 and *a*=*L*=A with (a) and (b) *b*=1.5A, (c) and (d) *b*=2.0A, (e) and (f) *b*=3.0A. Also, the variation of ANSI light uniformity versus the height *b* of a light pipe with (g) linear chart and (h) exponential chart.

Furthermore, the distributions of the color-differences for *b*= 1.5A, 2.0A and 3.0A are shown in Fig. 6-11 (a), Fig. 6-11 (c) and Fig. 6-11 (e), respectively, and the contours of the color-differences for *b*= 1.5A, 2.0A and 3.0A are shown in Fig. 6-11 (b), Fig. 6-11 (d) and Fig. 6-11 (f), respectively. The variation of the ANSI color uniformity versus the length *L* of light pipe is shown in the linear curve and the exponential curve of Fig 6-11 (g). The result shows us that the ANSI color uniformity at the exit plane of the light pipe with mixed-color LED light source can also be increased exponentially by increasing the height of the light pipe. In the case of the height scale L/A being greater than 2.0, the mixed-color LED sources on the entrance plane is not able to be uniformly illuminated with an acceptable uniform color image, i.e. 2.3% ANSI color uniformity, on the exit plane of the light pipe.

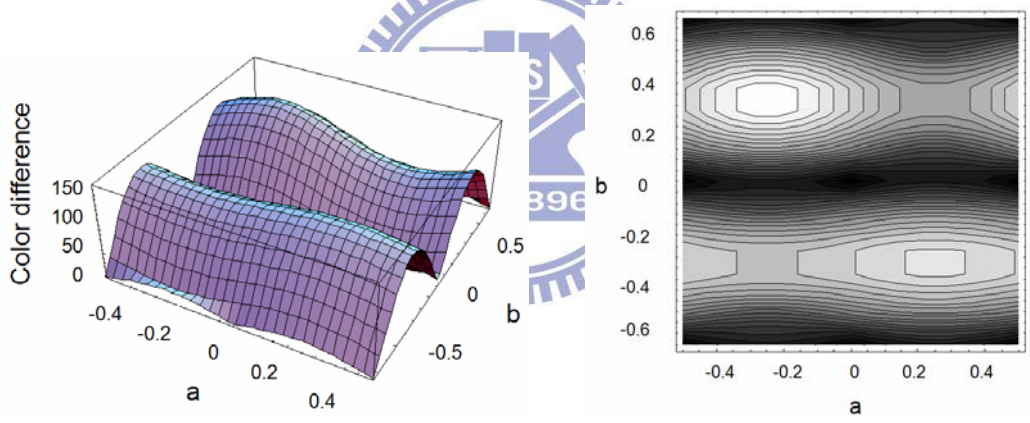

(a) (b)

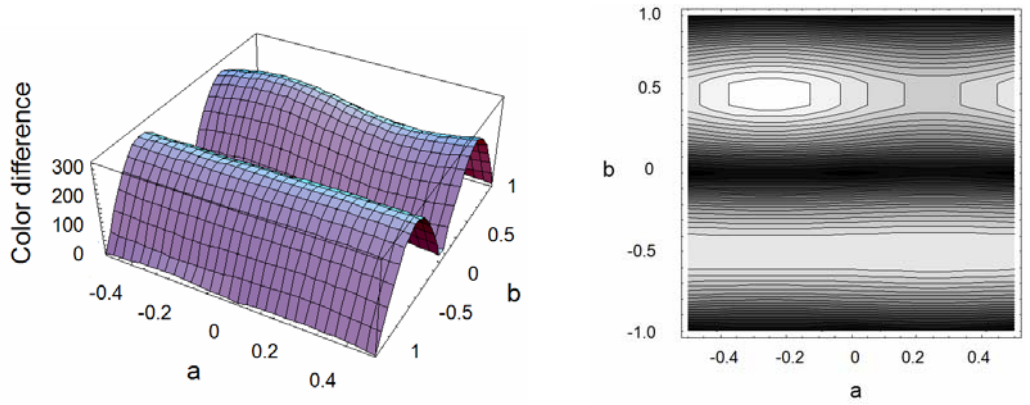

(c) (d)

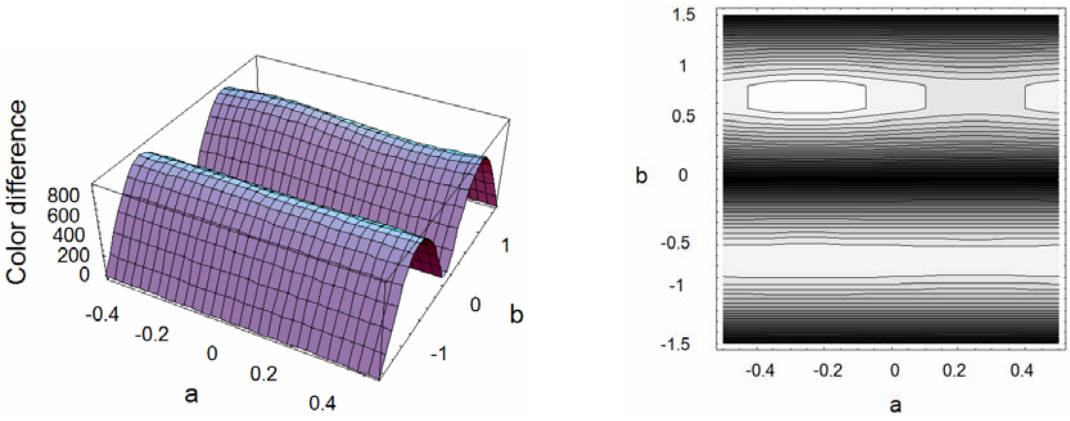

(e) (f)

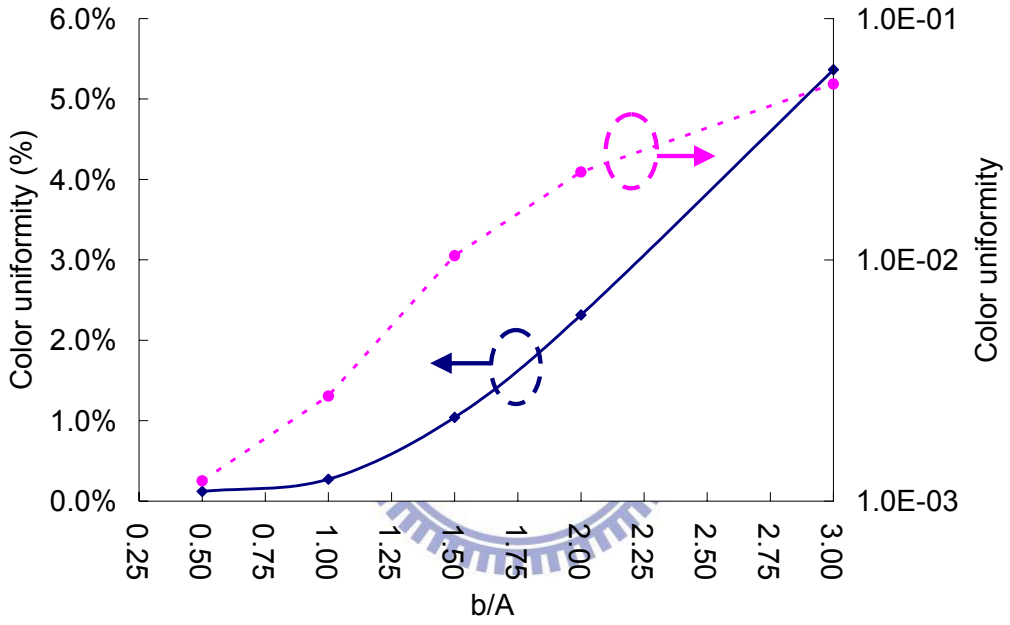

(g)

Figure 6-11 Distributions and contours of the color-difference for mixed-color LEDs in the condition of P=Q=A/4 and *a*=*L*=A and (a) and (b) *b*=1.5A, (c) and (d) *b*=2.0A, (e) and (f) *b*=3.0A. Also, (g) the variation of ANSI color uniformity versus the height *b* of a light pipe with linear chart and exponential chart.

Case 4

As shown in Fig. 6-3, the point light sources are located at specific locations on the entrance plane of the light pipe with c=0, *a*=*b*=*L*=A, P=Q= A/8, A/4, 3A/8 and 1A, respectively, where A is a constant. The distributions of the illuminances for P=Q= A/8, A/4, 3A/8 and 1A are shown in Fig. 6-12 (a), Fig. 6-12 (c), Fig 6-12 (e) and Fig.

6-12 (g), respectively and the contours of the illuminances for P=Q= A/8, A/4, 3A/8 and 1A are shown in Fig. 6-12 (b), Fig. 6-12 (d), Fig. 6-12 (f) and Fig. 6-12 (h), respectively. The variation of the ANSI light uniformity versus the location of the mixed-color light sources is shown in Fig 6-12 (i). The result shows us that the ANSI light uniformity on the exit plane of the light pipe with mixed-color LED light sources can also be minimized at +0.61% / + 0.65% under the condition of the locations P=Q= A/4.

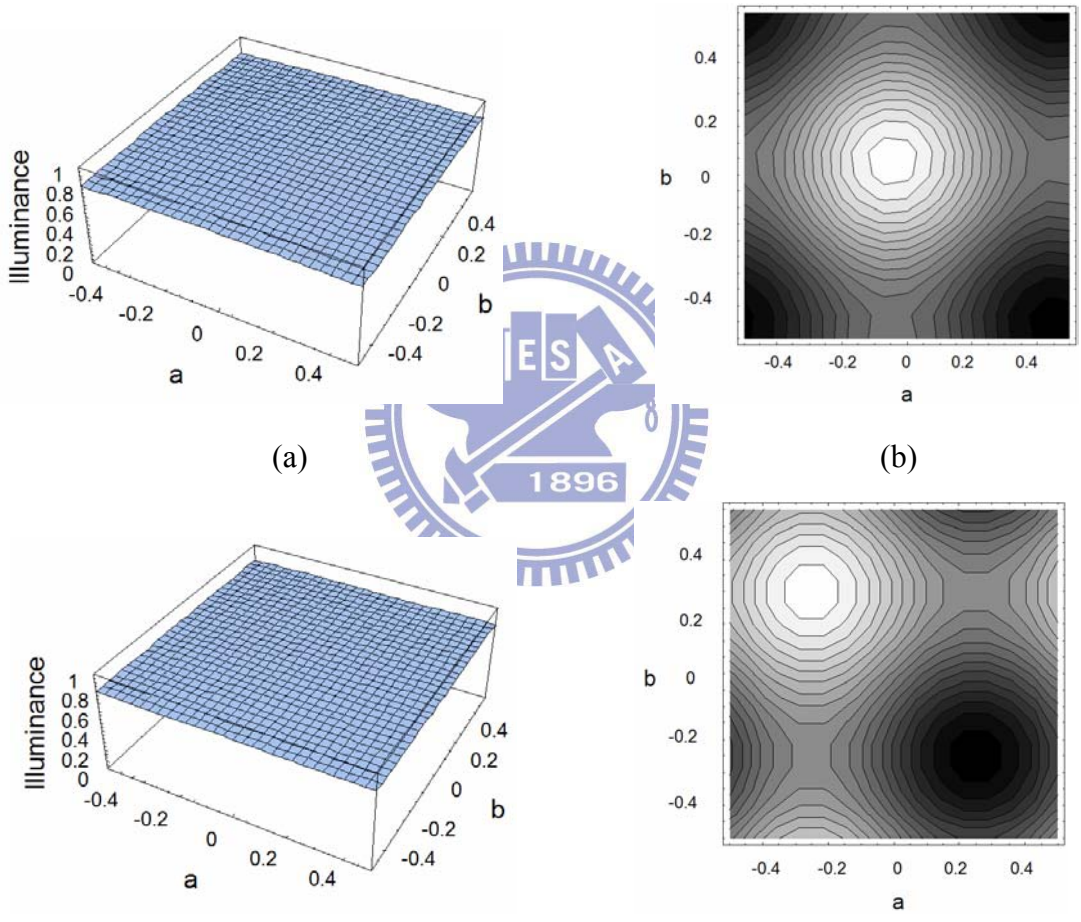

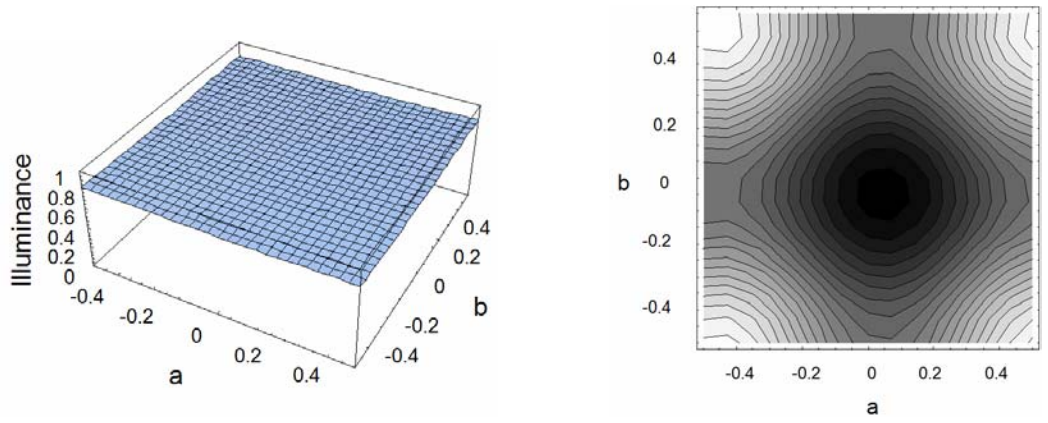

(e) (f)

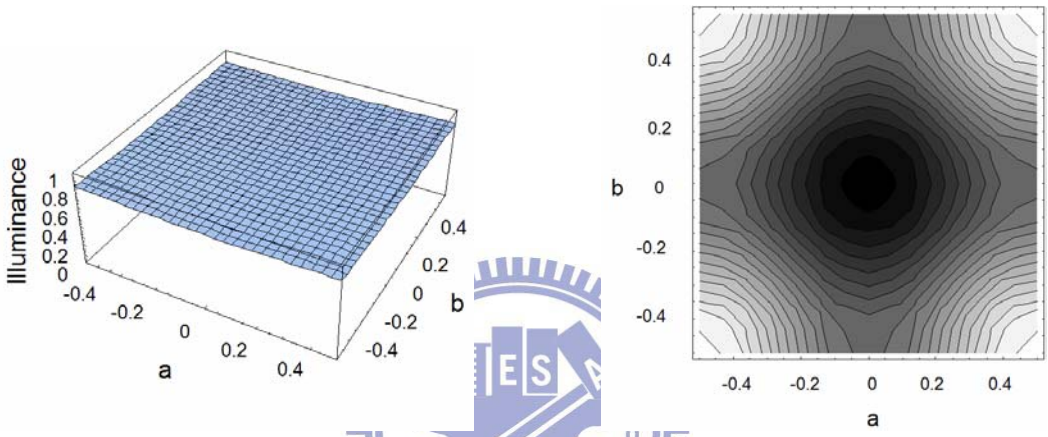

(g) (h)

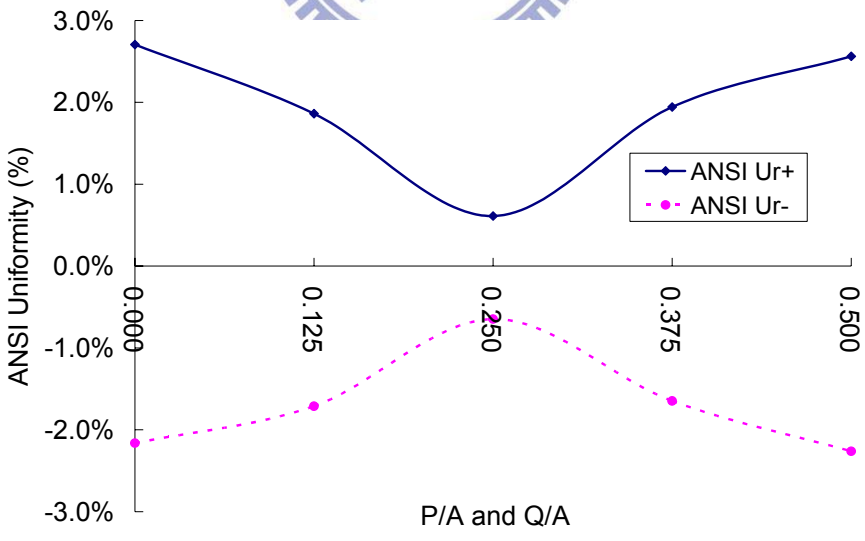

(i)

Figure 6-12 Distributions and contours of illuminance for mixed-color LEDs in the condition of *a*=*b*=*L*=A with (a) and (b) P=Q= A/8, (c) and (d) P=Q= A/4, (e) and (f) P=Q=3A/8 A, (g) and (h) P=Q= 1A. Also, (i) the variation of ANSI light uniformity versus the locations P and Q of a light pipe with linear chart.

Furthermore, the distributions of the color-difference for P=Q= A/8, A/4, 3A/8 and 1A are shown in Fig. 6-13 (a), Fig. 6-13 (c) Fig. 6-13 (e) and Fig. 6-13 (g), respectively, and the contours of the color-differences for P=Q= A/8, A/4, 3A/8 and 1A are shown in Fig. 6-13 (b), Fig. 6-13 (d), Fig. 6-13 (f) and Fig. 6-13 (h), respectively. The variation of the ANSI color uniformity versus the locations of the mixed-color light sources is shown in the linear curve and the exponential curve of Fig 6-13 (i). The result shows us that the ANSI color uniformity at the exit plane of light pipe with mixed-color LED light source can be maximized at 0.27% under the condition of the locations P=Q= A/4 contrary to the case for ANSI uniformity. However, it will be a trade-off between ANSI brightness uniformity and color uniformity for the human eye.

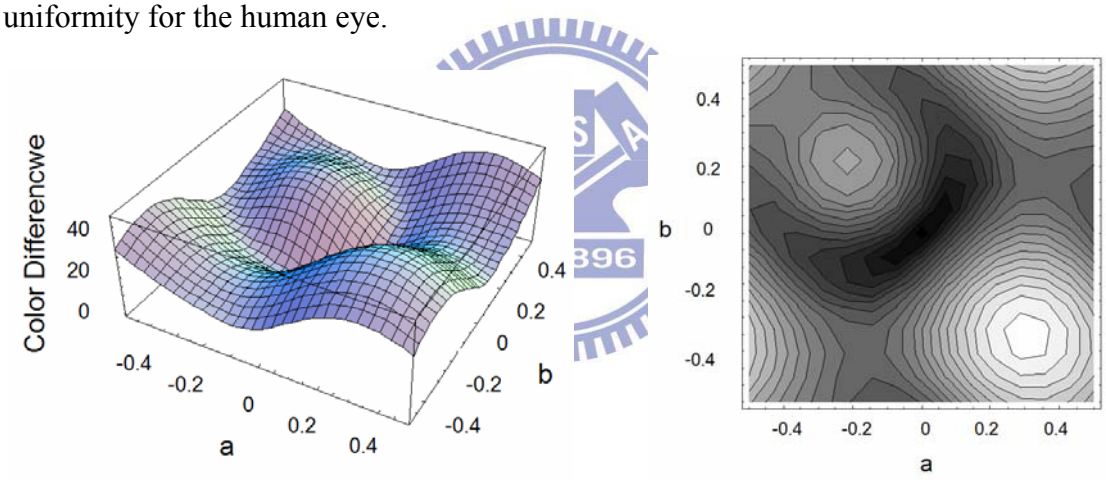

(a) (b)

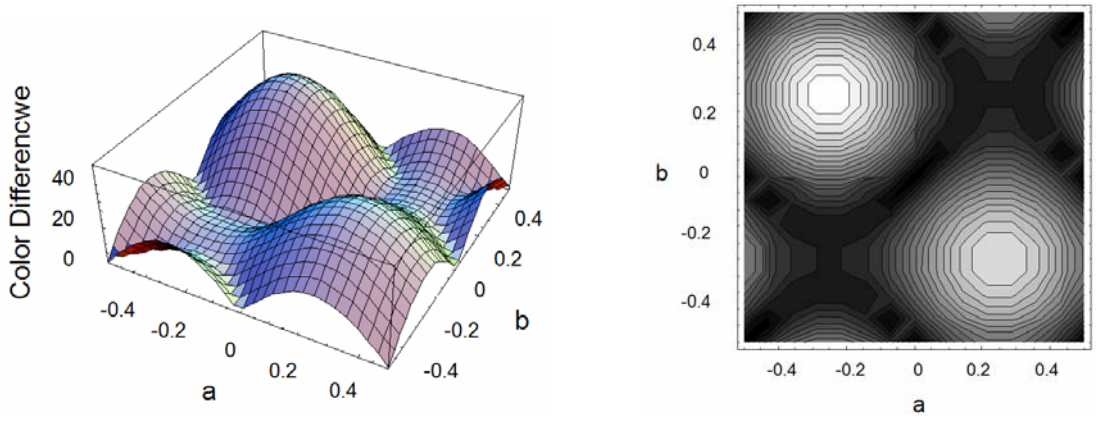

(c) (d)

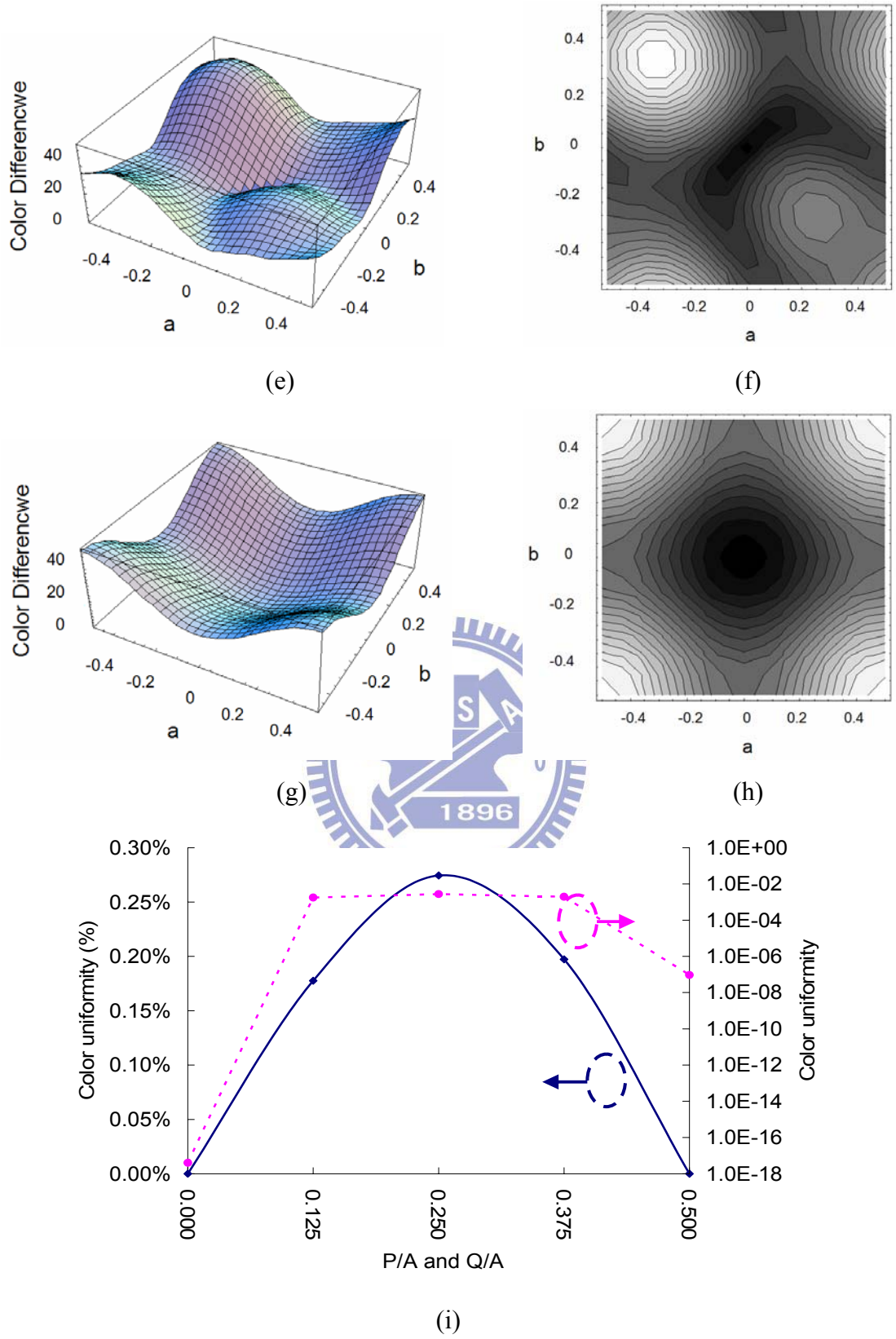

Figure 6-13 Distributions and contours of the color-difference for mixed-color LEDs in the condition of *a*=*b*=*L*=A with (a) and (b) P=Q= A/8, (c) and (d) P=Q= A/4, (e) and (f) P=Q=3A/8, (g) and (h) P=Q= 1A. Also, (i) the variation of ANSI color uniformity versus the locations P and Q of a light pipe with linear chart and exponential chart.

6.6 Summary and remarks

This Chapter investigated an analytical method of illuminance formation generated by illumination using a rectangular hollow light pipe and mixed-color LEDs. The corresponding ANSI light uniformity, ANSI color uniformity and color-difference were derived for single LED and multi mixed-color LEDs. The analytical results indicate that the distributions of illuminance and color-difference vary with the different geometric structures of the light pipes and the location of the light sources.

In summary, (1) ANSI light uniformity at the exit plane of the light pipe with single LED light source can be reduced exponentially by increasing the length of the light pipe. (2) Both ANSI light and color uniformity at the exit plane of the light pipe with mixed-color LED light sources can also be reduced exponentially by increasing the length of the light pipe. In the case of the length scale L/A being greater than unity, the mixed-color LED sources on the entrance plane are uniformly illuminated with the acceptable uniform brightness and color images with the brightness uniformity less than 1% and color uniformity less than 0.01. (3) Both ANSI light and color uniformity at the exit plane of the light pipe with mixed-color LED light sources can also be increased exponentially by increasing the height ratio *b/a* of the light pipe. (4) The ANSI light uniformity can be minimized while the ANSI color uniformity can be maximized on the exit plane of the light pipe with mixed-color LED light sources under the condition of the multi light-source locations P=Q= A/4.

We can conclude that rectangular light pipes provide extremely uniform illuminations with the highest light efficiency and the most compact package for the optical system with mixed-color LEDs compared to lenses, prisms and optical diffusers. The optimum form factor of a light pipe is the fact that the cross-section is square, and that the length scale L/A is equal to unity and that the multi light-sources are locate on positions of A/4, individually.

Chapter 7

Design of a dual-f-number illumination system and its application to DMD™ projection displays

7.1 Introduction

The optical design with the appropriate *f*-number is the key to the illumination system and the *f*-number value is often constrained and determined by the light-valve's architecture in the projection display. Conventionally, single *f*-number and symmetric illumination pupil are generally utilized in optical system. However, these do limit optical collection efficiency and imaging quality. Digital Light Processing™ (DLP™) is one of the light-valve technologies, based on DMD™ that is a reflective digital light valve developed by Texas Instruments. The DMD™ architecture can yield the projector with compact size, high resolution, good digital image quality and exceptional durability. But, there is still one critical issue of brightness improvement stemming from the size of DMD™ that have been being developed smaller and smaller by the advanced semiconductor technology for the commercially ultra-portable projector in business and home entertainment use [58].

The brightness is not only a most important specification of the projector but also always a challenge of the optical design in projection systems. Because of the narrow tilt angle of DMD™, the *f*-number-limited optical system design is required and restricts the Ètendue (or said optical collection efficiency) in DMD™-based projection system. In case the *f*-number were not restricted within the specific value, there would be a poor contrast ratio or ghost image observed on the screen [62].

The DMD™ consists of hundreds of thousands of moving micromirrors that are made to rotate to either +12° or -12° positions depending on the binary states (said on-state and off-state, respectively) of the underlying SRAM cells below each micro-mirror [52], as shown in Fig. 7-1. On-state reflected light from DMD™ chip is directed into the entrance pupil of the projection lens and the corresponding image on the screen is bright. Off-state light is steered away from the entrance pupil of projection lens and the corresponding image on the screen is dark. The specular light (said flat-state light) reflected while micromirrors are flat (no deflection), also should be directed out of the entrance pupil of projection lens for the high contrast ratio and eliminating the ghost or stray light through the pupil onto the screen. The conceptual principle of the optical design in DMD™ based projection system is to prevent the overlaps of on-, off-, and flat-state pupils for the high contrast ratio and high quality image controls. Because of the light-steering action of ±12°-tilt angles on DMD™ mentioned above, the half cone-angle of illumination light should be bounded within ±12°, (i.e. numerical aperture N.A. 0.2079), which corresponds to the *f*/2.4 optical design in the illumination system. The constraint on *f*-number is a critical factor to result in the low optical collection efficiency in the conventional DMD™-based projection system. Once this bottleneck could be overcome, the optical efficiency and the brightness on the screen for the small size DMD™-based projectors would be enhanced.

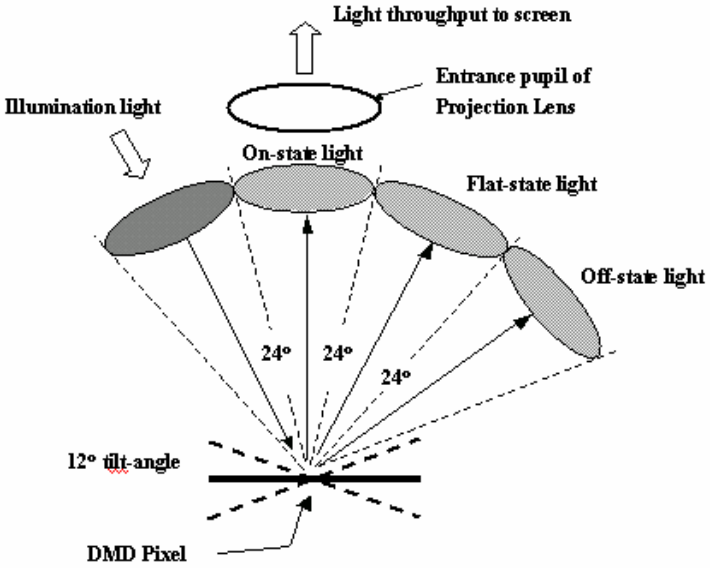

Figure 7-1 Schematic diagram of the light-steering action of a ±12°-tilt angles on DMD™. The half cone-angles of the illumination light and on-, flat-, off-states lights are ±12°. The included angle between each pair light is 24°. On-state reflected light from DMD™ chip is directed into the entrance pupil of the projection lens and the corresponding image on the screen is bright. Off- and flat- state lights are steered away from the entrance pupil of projection lens and the corresponding image on the screen is dark.

In this chapter we propose new optical design that can solve the *f*-number constraint mentioned above. The proposed optical design employ an elliptic-shaped illumination-pupil, which corresponds to the dual *f*-number, for example *f*/2.0 x *f*/2.4, to overcome the *f*/2.4 constraint, due to the light-steering action of the narrow ±12°-tilt angles on DMD™, and to enhance the optical collection efficiency and screen's brightness with an adequate contrast ratio in the DMD™ -based projector.

7.2 Optical system design with Cooke triplet

The Cooke triplet has been a classical optical design [18, 63]. It was also proposed as the projection lens in the over-head projector system [64]. Here, as an illustration of dual *f*-number illumination system, we design three types of Cooke triplet lens for the illumination systems with *f*/2.4× *f*/2.4, *f*/2.0× *f*/2.4 and *f*/2.0× *f*

/2.0 by OSLO program [65], respectively, as shown in Fig. 7-2. The effect of dual *f*-number on the aberration on the illuminated plane can be seen.

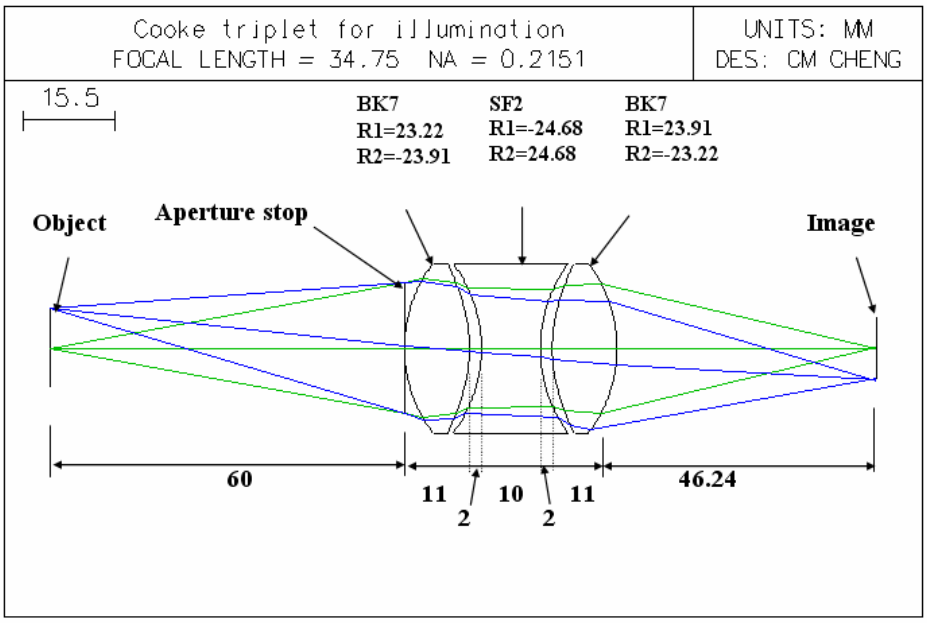

Figure 7-2 Schematic diagrams of the illumination system layouts for an air-spaced triplet lens design.

As shown in Fig. 7-3, the dimensions and footprints of the aperture stops are different between each configuration according to the different *f*-number values, where x-axis stands for the tangential axis and y-axis stands for the sagittal axes, respectively, on the aperture stops in the optical illumination system that is shown in Fig. 7-2. The round-shaped illumination-pupil of $f/2.4\times f/2.4$ is shown in Fig. 7-3 (a), the elliptic-shaped illumination-pupil of $f/2.0\times f/2.4$ is shown in Fig. 7-3 (b) and the round-shaped illumination-pupil of $f/2.0\times f/2.0$ is shown in Fig. 7-3 (c).

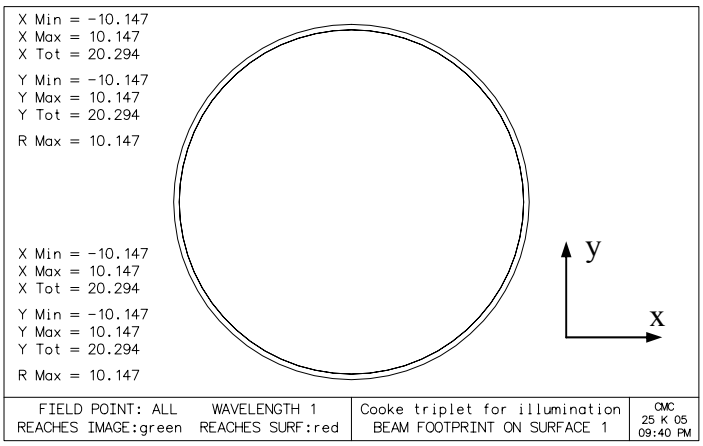

(a)

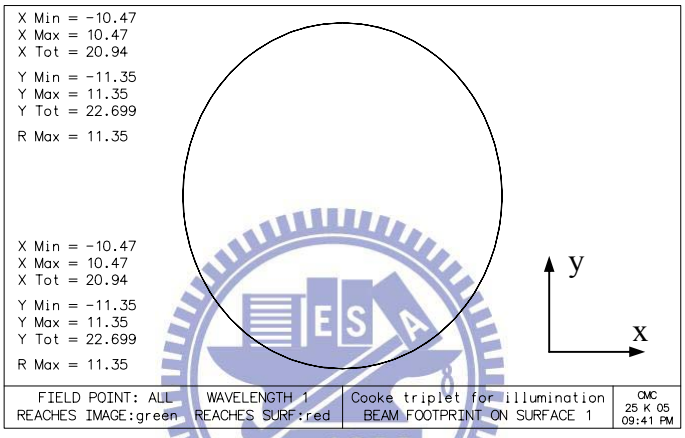

(b)

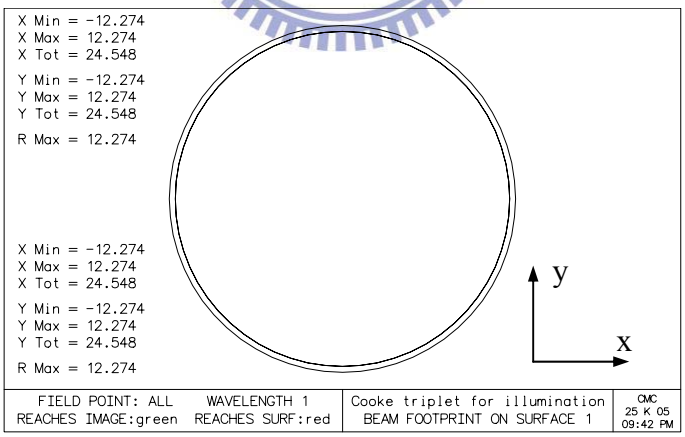

(c)

Figure 7-3 Beam footprint outline at aperture stop. (a) $f/2.4 \times f/2.4$ illumination system. (b) $f/2.0 \times f/2.4$ illumination system. (c) $f/2.0 \times f/2.0$ illumination system, where x-axis stands for the tangential axis and y-axis stands for the sagittal axes, respectively.

The MTF values of those three types of *f*-number design for the "maximum field of view" are calculated and performed in Fig. 7-4, that is considered by the edge-ray principle in the illumination system [26]. In the result of the design, MTF value of $f/2.4\times f/2.4$ is 34.46% on tangential plane and 34.18% on the sagittal plane; MTF value of $f/2.0\times f/2.4$ is 25.37% on tangential plane and 33.67% on the sagittal plane; MTF value of $f/2.0\times f/2.0$ is 20.67% on tangential plane and 19.90% on the sagittal plane. That indicates the performance of the imaging resolution of dual *f*-number $f/2.0\times f/2.4$ system is between those of $f/2.4\times f/2.4$ and $f/2.0\times f/2.0$. And, the astigmatism of $f//2.0\times f//2.4$, i.e. the aberration difference of the tangential MTF and sagittal MTF, is worse than those of $f/2.4\times f/2.4$ and $f/2.0\times f/2.0$, due to the nature of dual-*f*-number.

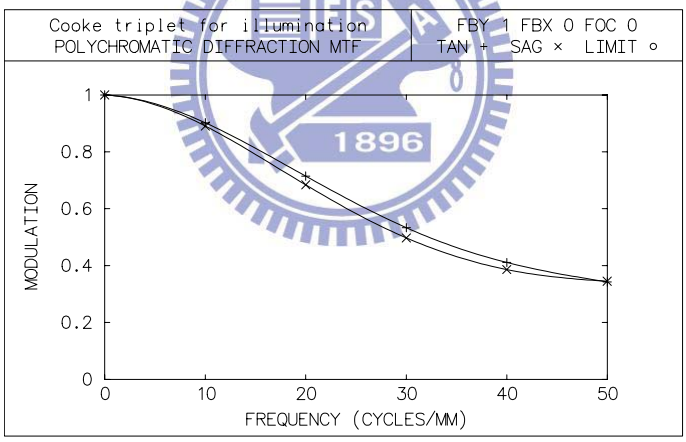

(a)

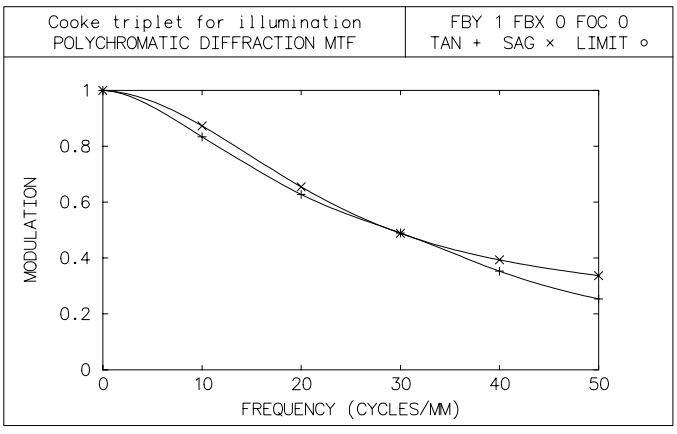

(b)

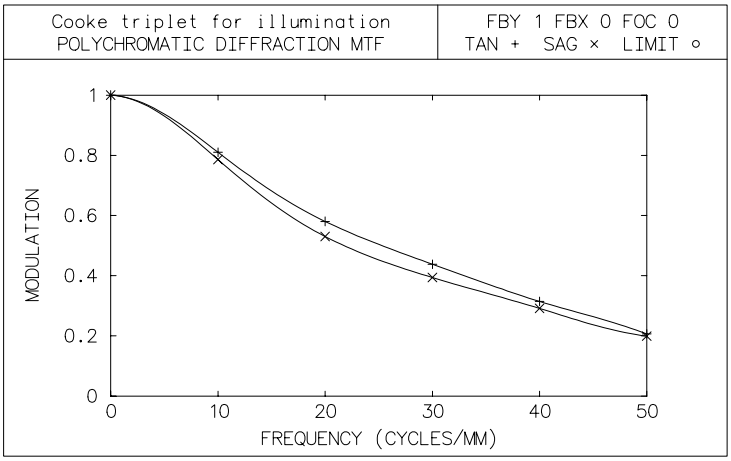

(c)

Figure 7-4 Modulation transfer functions for the illumination systems. (a) f/2.4× f/2.4 illumination system. (b) f/2.0 × f/2.4 illumination system. (c) f/2.0 × f/2.0 illumination system.

This kind of the optical design is for the illumination system but not the imaging system, so the astigmatism is not a significant index to judge the dual-*f*-number functionality but the average MTF is. Generally, the reasonable resolution of the illumination system design is round 30% MTF value at 50 line-pairs per mm for controlling the around 7% overfill value with the 10μm imaging RMS spot size on the illumination plane. Therefore, the dual *f*-number design should keep the above minimum criterion with the reasonably acceptable resolution performance in the illumination system. As shown by the above-simulated results in Fig. 2-10 and 7-4, we can conclude that dual *f*-number is not only able to enhance the collection efficiency but also keep the reasonable aberrations in the illumination system.

7.3 Extension to the DMD™-based projector system

For single-DMD™-based projector, because of the light-steering action of ±12°-tilt angles, a f/2.4 constraint has been documented on DMD™ architecture. In the following, a dual *f*-number f/2.0× f/2.4 optical system will be developed for the

single-DMD™-based projector. The advantages of the dual *f*-number illumination system will be further analyzed.

The optical system layout for the single-DMD™-based projector is illustrated in Fig. 7-5 (a) and Fig. 7-5 (b). The optical system is a telecentric system that is defined as the location of exit pupil of the illumination system or the entrance pupil of the projection lens at or near infinity from the objective surface. It consists of one lamp light-coupling system, the illumination system, a light separator, DMD ™ and a projection lens system.

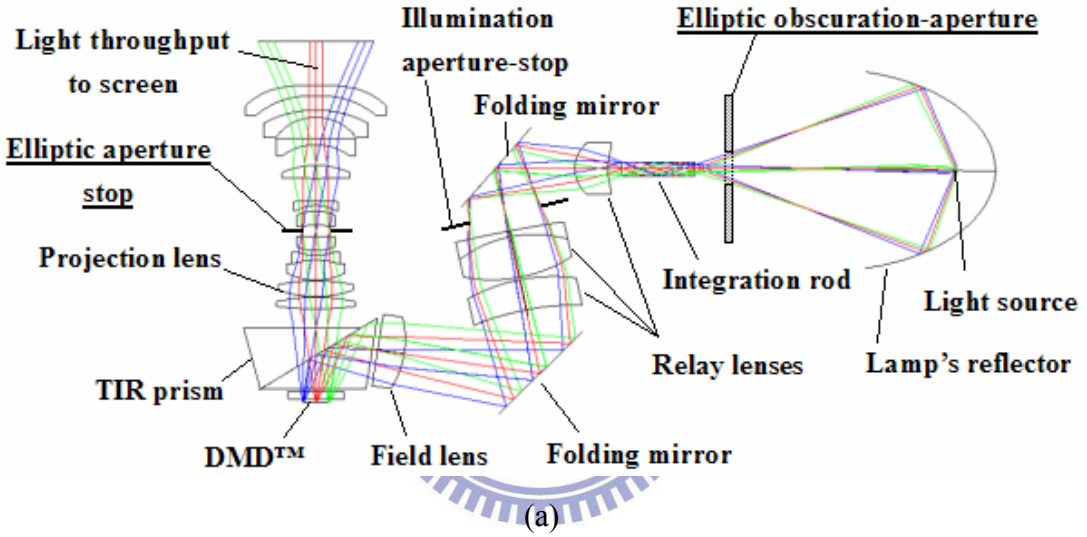

(a)

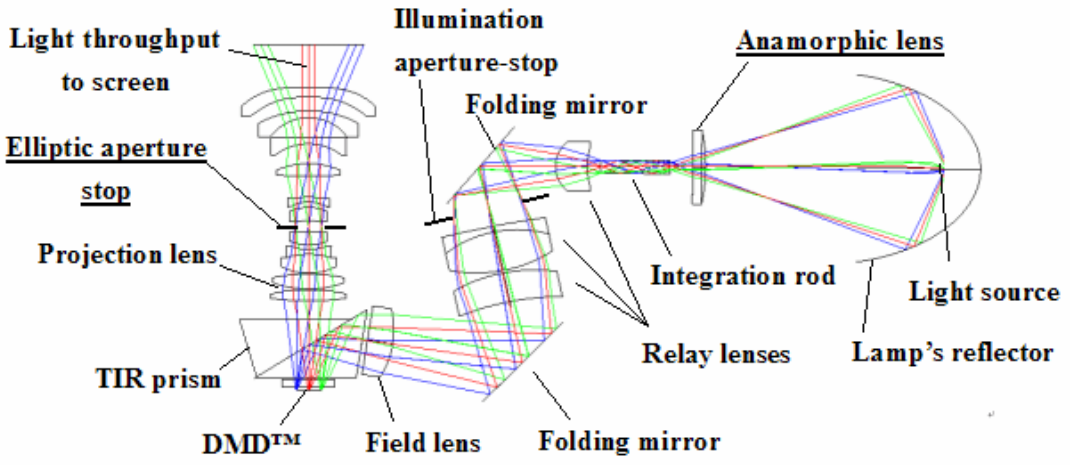

(b)

Figure 7-5 Schematic diagrams of the optical system layouts for the elliptic-shaped illumination-pupil design in the DMD™-based projection systems. (a) Elliptic obscuration-aperture design. (b) Anamorphic lens design, between the lamp's reflector and the integration rod.

The illumination system consists of one ultra-high-pressure-mercury lamp with short arc, one elliptic reflector (f/1 and maximum cone-angle= ±30°), one integration rod (dimension = 7.35 mm × 5.51 mm × 42 mm), one set of the relay and the field lenses, one light separator, one DMD™ chip and one projection lens. The illumination system is f/2 optical system that consists of three singlet lenses, one achromatic doublet and one illumination aperture-stop. The light separator is one TIR-prism [24]. The DMD™ chip is 0.7-in diagonal size, 1024×768 pixels resolution, 4:3 aspect ratio and ±12°-tilt angles. The projection lens is with f/2, focal length 28.3mm and the elliptic aperture-stops. There are extra components, either one elliptic obscuration aperture as shown in Fig. 7-5 (a) or one anamorphic lens as shown as Fig 7-5 (b) between the lamp reflector and the integration rod for the new optical design.

The arc of lamp is located on the first focus-point of the elliptic reflector and is imaged on the second focus point by the elliptic reflector. The light from the lamp is collected by the reflector and is incident on the entrance end of the integration rod. And, the light beam passes through either one elliptic obscuration aperture or one anamorphic lens that is located between the lamp reflector and the integration rod. Then, the non-uniform light from the lamp is uniformly illuminated on the exit end of the integration rod through the multiple reflections inside. The uniformly rectangular-shaped light spot on the exit surface of the integration rod is imaged onto the active area of DMD™ by the illumination optics (i.e. three singlet lenses and one achromatic doublet) and one TIR prism. TIR prism is a light separator that is a compound prism system to guide the light onto and away from DMD™ in the illumination system and the projection system simultaneously by the air-gap and one total internal reflection surface between two prisms. The image of the DMD™ is projected and imaged onto the screen by the TIR-prism and the projection lens while DMD™ is in the condition of the on-state configuration. While the configuration of

DMD™ is in either the flat-state or the off-state, the light beam is steered away from the entrance pupil of the projection lens and the light is not projected on the screen.

In the illumination system, there is one aperture-stop that limits the size and the axial cone of light energy. The entrance and the exit pupils are the conjugate images of the aperture stop in the object and image spaces of the illumination system, respectively. In order to attain the maximum optical collection efficiency, the entrance pupil of the illumination system should be designed on the entrance end of the integration rod that limits the light beam from the lamp and the reflector, and the exit pupil of the illumination system should be designed on the entrance pupil of projection lens to attain the maximum throughput on the screen, as shown in Fig. 7-5 (a) and Fig. 7-5 (b).

In the conventional optical design for ±12°-tilt-angles DMD™-based projection system, the *f*-number should be limited on the value of the *f* /2.4 that corresponds to the ±12°-half-cone angles of the illumination system because of the light-steering action for on-, flat- and off-states of ±12°-tilt-angles DMD™ architecture, as shown in Fig. 7-6 (a). The light energy on the aperture-stop is bounded within one round-shaped area (called the "light envelope") and the size/diameter of the light envelope is determined by the F-number and the maximum acceptance cone angle. There are many light spots of images, like the checkerboard array, in the light envelope, that are formed by the multiple reflections from the inner walls of the integration rod, as shown in Fig. 7-7 (a).

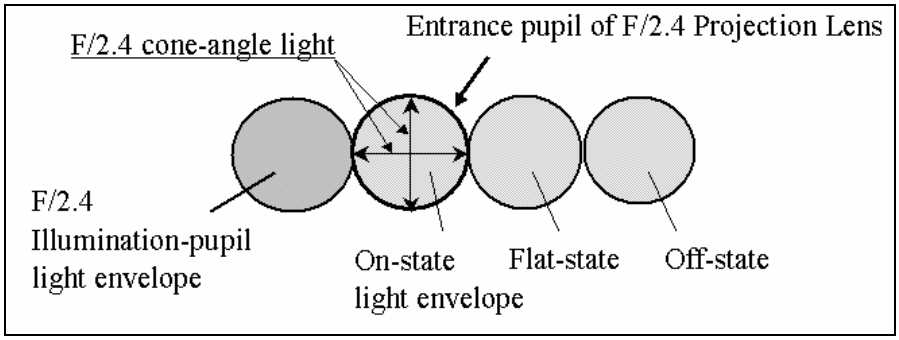

(a)

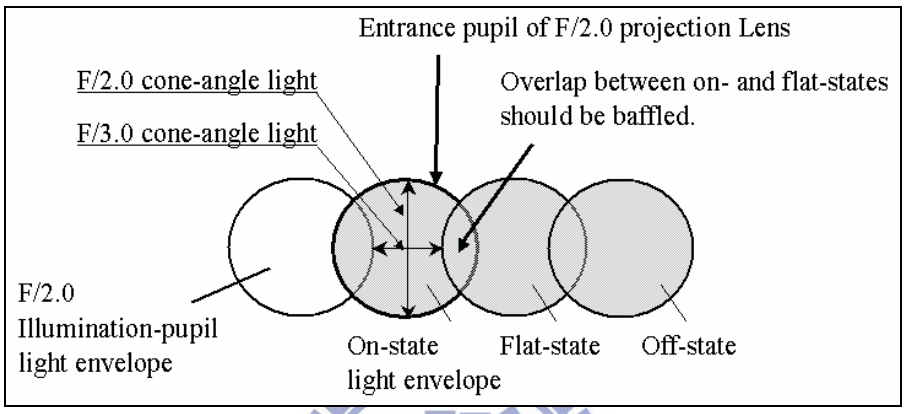

(b)

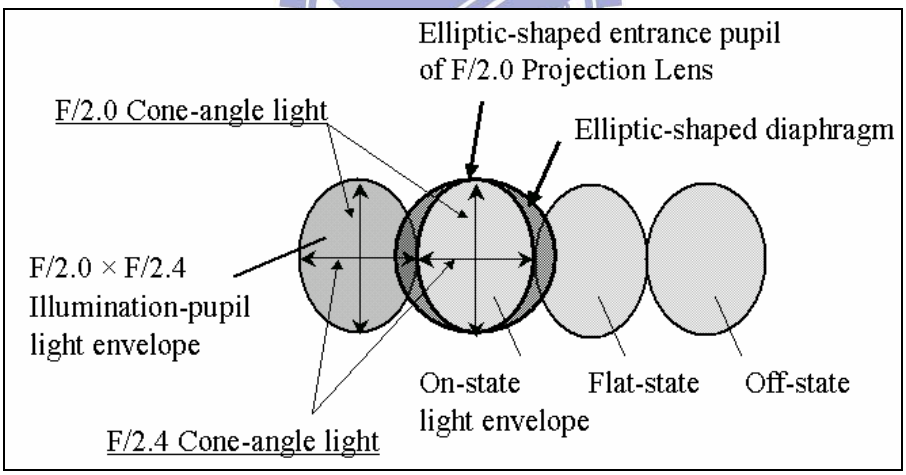

(c)

Figure 7-6 Schematic diagrams of the illumination-pupil stops in the ±12°-tilt-angles DMD™-based projection system. (a) Conventionally optical design of symmetrically single *f* /2.4 system. (b) Optical design of symmetrically single *f* /2.0 system. (c) New optical design of the asymmetrically dual *f*-number (*f* /2.0 × *f* /2.4) system.

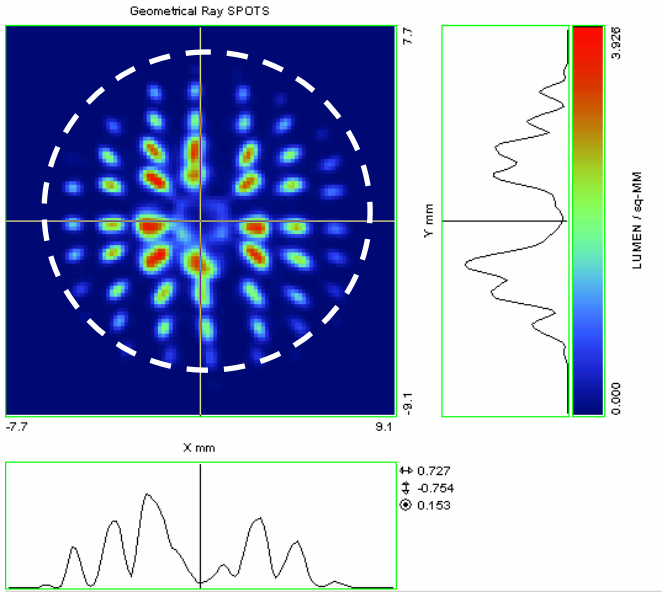

(a)

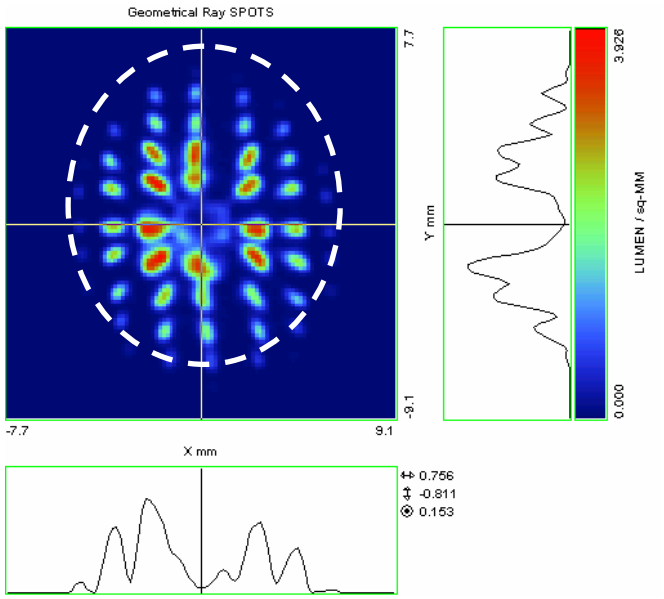

(b)

Figure 7-7 Image of the light envelops in the entrance pupil of the projection lens in the simulation. (a) For the symmetrically single f/2.4 system with the round-shaped illumination-pupil. (b) For the asymmetrically dual f-number (f/2.0 × f/2.4) system with the elliptic-shaped illumination-pupil.

Two kinds of the optical designs with the asymmetry-shaped apertures in the illumination system and the projection lens have been proposed to improve the contrast ratio [66, 67]. The functionalities of the asymmetry-shaped apertures are to

baffle the scattered lights and diffracted lights from the illumination system. For those designs, the minimum *f*-number is still determined by the tilt-angle on DMD™ and the baffling apertures will lead to the reduction in the optical efficiency significantly.

Because of the limitation of *f* /2.4 in the illumination system, the brightness of DMD™-based projector is limited on the specific maximum value unless we could enlarge the acceptance cone angle in the system. If we enlarge the acceptance cone angle to the greater-than ±12°-one, for example ±14.48° that corresponds to *f* /2.0, as shown in Fig 7-6 (b), there exits the overlap of light envelopes between on-state and flat-state. This result is possible to cause a poor contrast ratio, the stray light and the ghost image through the projection lens on the screen. Of course, we can design a baffle at the edge of aperture stop to cut-off the overlay of the light envelopes at the aperture-stop in the projection lens. In this case, the sagittal direction of the aperture stop becomes *f* /3.0 restrictively even though the tangential direction is *f* /2.0. This kind of the design is not able to increase the optical efficiency significantly more than the conventional *f* /2.4 illumination system.

The solution proposed here is a new design of the elliptic-shaped illumination-pupil to improve the *f*-number limitation, as mentioned above, in the optical system of DMD™-based projector. Either an elliptic-shaped obscuration aperture or an anamorphic lens between the lamp's reflector and the integration rod in one *f* /2.0 optical system, as Figs. 7-5 (a) and 7-5 (b), have been proposed [68,69]. These methods are able to "re-shape" the illumination-pupil from symmetrically round light-envelope to asymmetrically elliptic one at the aperture-stops of the illumination system and the projection lens, respectively, as shown in Figs. 7-5 (a) and 7-5 (b). In other words, the tangential direction of the illumination pupil still keeps the *f* /2.0 light cone-angle, but the sagittal direction of the illumination pupil is compressed to *f* /2.4 cone-angle light by either the elliptic-shaped obscuration aperture

or an anamorphic lens. Another design with an ellipsoid-shaped diaphragm at the aperture-stop in the projection lens to prevent the flat-state light through the aperture-stop for the high contrast ratio on the screen, as shown in Fig. 7-6 (c), is also proposed.

In other words, the design proposed here utilizes either an elliptic-shaped obscuration aperture or an anamorphic lens to generate the "dual *f*-number", for example *f* /2.0 × *f* /2.4, in the illumination system of DMD™-based projector. The "dual *f*-number" means that the tangential F-number value is not equal to the sagittal one, and the shape of the illumination pupil is elliptic but not round. By means of this design, the brightness enhancement against the *f* /2.4 limitation can be established. Additionally, optical system that with the F-number more than *f* /2.0, for example *f* /1.8, *f* /1.6 and so on, can be developed along the design flow illustrated above. Small *f*-number stands for the larger acceptance cone-angle and higher optical efficiency in the optical system. Of course, there remain the trade-off issues in considering the cost-and-performance ratio and the requirements of the product specification.

It should be noted that the dual *f*-number design is also able to prevent the overlap between on-state and flat-state of DMD™ at the entrance pupil of the projection lens, and some stray lights or the ghost images on the screen while the tangential *f*-number is greater than *f* /2.4. Therefore, the dual *f*-number does not only increase the brightness but also keeps the contrast ratio in the DMD™-based projector at the same time.

7.4 Simulation exploration of dual-*f*/# illumination system

7.4.1 Ètendue simulation of lamp coupling system

In the beginning of optical design for the illumination system with specific *f*-number, we should estimate the maximum collection efficiency of light source by the Ètendue calculation in Eq. (2-22). The simulation of the collection efficiency is performed by the ray-tracing program of Advanced Systems Analysis Program (ASAP) [70] and the light source model is a Radiant Imaging data file [71] of an ultra-high-pressure mercury lamp with 1.3mm arc-gap, an ellipsoidal reflector (R=24.858, k=-0.596) and maximum half cone-angle $\pm 30^{o}$ (i.e. f /1.0). The geometrical model of lamp coupling system is shown as Fig. 7-8. We fixed the *f*-number (i.e. the cone angle) of the lamp coupling system and regarded the value of acceptance area (i.e. the entrance area of the illumination system) as the variables to calculate the relationship between the Ètendue in Eq. (2-22) and the collection efficiency of the acceptance area. In the ASAP ray-tracing program, 1,000,000 rays are created at the Radiant Imaging source and then traced randomly through the geometrical model of lamp coupling system.

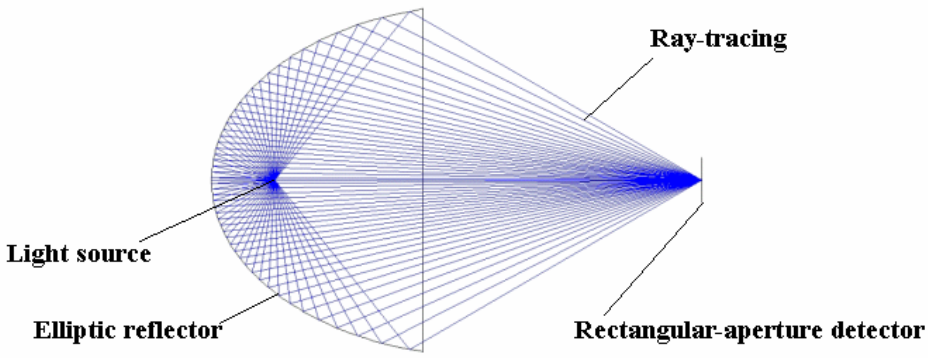

Figure 7-8 Schematic diagram of the lamp coupling system that consists of a light source, one elliptic reflector and one rectangular-aperture detector.

The simulated data of the collection efficiency versus Ètendue was plotted in Fig. 7-9, and then we fitted the set of data to a formula as the function of Ètendue as shown in the view box of Fig. 7-9. The symbols in view box of the Fig. 7-9 are defined as Chi^2/DoF is χ^2 –value, R is the correlation factor and the second terms of a, b, c parameters are the standard errors of a, b, c values, respectively, in the mathematical statistics. According to this fitted formula, the collection efficiency for the specific Ètendue that is a function of the dual *f*-number and acceptance area (i.e. the entrance area of the integration rod) in DLP-based illumination system can be calculated. By this simulation method, we can estimate the lamp coupling efficiencies for the different dual *f*-number configurations before designing the illumination systems.

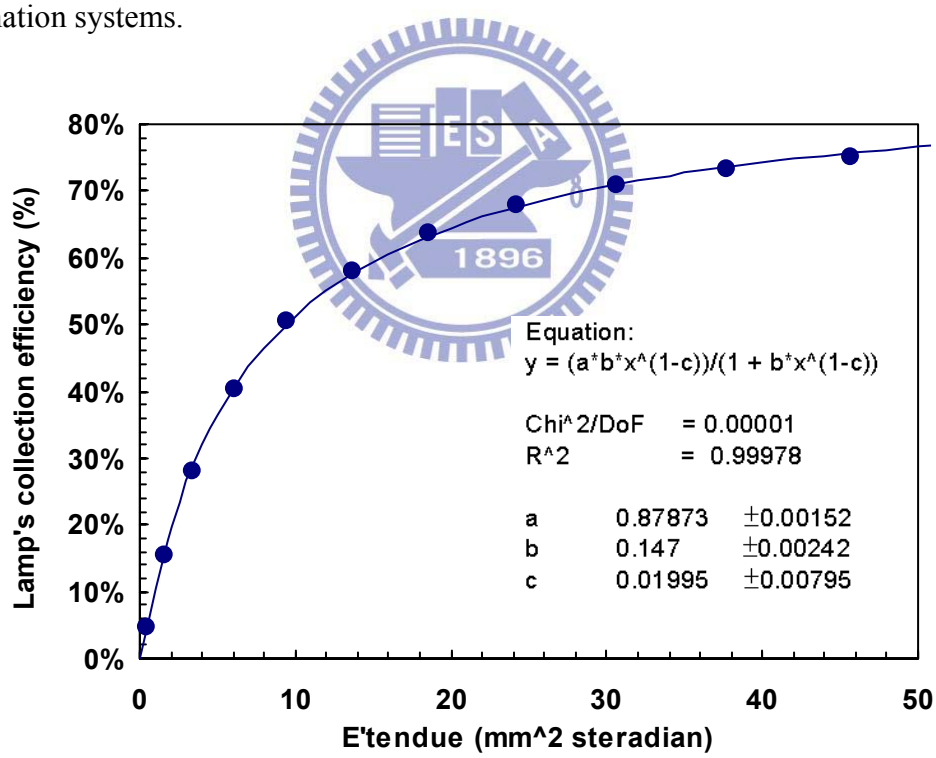

Figure 7-9 Simulated data of the collection efficiency versus Ètendue is plotted as the filled-circle dots. The solid curve and the equation is the fit to the simulated result of lamp coupling system.

The Ètendue of the specific dual *f*-numbers are estimated in Table 7-1. The percentage of the lamp coupling efficiency for dual *f* /2.0 x *f* /2.4 is 68.97%, that for

dual f/2.2 x f/2.4 is 67.54 % and that for single f/2.4 x f/2.4 is 66.18 %. As expected, coupling efficiency can be improved.

Table 7-1 Lamp's Coupling Efficiencies vs. Ètendue.

f-number configuration	Ètendue (mm^2 steradian)	Collection efficiency (%)
f/2.4 x f/2.0	26.490	68.97%
f/2.4 x f/2.1	25.228	68.25%
f/2.4 x f/2.2	24.081	67.54%
f/2.4 x f/2.3	23.034	66.85%
f/2.4 x f/2.4	22.075	66.18%

7.4.2 Optical efficiency of the illumination system

The geometrical model of the optical system is described in section 7.3 as shown in Fig 7-5 (a). Again, the simulation is performed by the ASAP program and the light source model is a Radiant Imaging data file of the same lamp model mentioned in above section. In simulation, typically 1,000,000 rays are created at the Radiant Imaging source and then traced randomly through the geometrical model of the optical system.

The simulated data of the collection efficiency in the DMD active area is shown in Table 7-2. Comparing with single f/2.4 illumination system, the percentage of the increase of the optical collection efficiency on DMD active area for the dual f/2.0 x f/2.4 is 6.2%, that for dual f/2.2 x f/2.4 is 3.6 %. The light-spot shape and the intensity distribution of the illumination-pupil at the entrance pupil of projection lens

is simulated and showed in Fig. 7-7 (b). The result indicated that the illumination-pupil becomes the elliptic-shaped from the single *f*-number to dual one.

Table 7-2 Optical Collection Efficiencies on DMD's active area

f-number configuration	DMD active area Collection efficiency (%)	Overfill (%)	Ratio
f/2.4 x *f*/2.0	63.05%	9.07%	1.062
f/2.4 x *f*/2.1	62.35%	9.02%	1.050
f/2.4 x *f*/2.2	61.53%	8.92%	1.036
f/2.4 x *f*/2.3	60.63%	8.87%	1.021
f/2.4 x *f*/2.4	59.39%	8.81%	1.000

To briefly summarize, the dual *f*-number design utilizes either an elliptic-shaped obscuration aperture or an anamorphic lens between the lamp's reflector and the integration rod to generate the "dual *f*-number", for example *f*/2.0 × *f* /2.4, in the illumination system of DMD™-based projection system. This optical design is able to enlarge the acceptable cone-angle, i.e. the optical efficiency, in the tangential axes at the entrance pupil of the projection lens, and prevent the overlap between on-state and flat-state of DMD™ in the sagittal axes from the some stray light or the ghost image on the screen. By the design proposed here, the percentage of the lamp coupling efficiency for the dual *f*/2.0 x *f*/2.4 is 68.97% and that for dual *f* /2.2 x *f*/2.4 is 67.54 %. Comparing to the conventionally single *f*/2.4 illumination system, the simulated data of the optical collection efficiency increase on DMD active area for the dual *f*/2.0 x *f*/2.4 is 6.2%, that of the lamp coupling efficiency for dual *f* /2.2 x *f*/2.4 is 3.6 %. Overall, the dual *f*-number design can get rid of the *f*/2.4

constraint, due to the light-steering action of narrow ±12°-tilt angles on DMD™ and enables a lower-than- *f*/2.4 optical design with a significantly brightness increase and an adequate contrast ratio in the DMD™-based projectors.

7.5 Summary and remarks

In summary, the design of a dual- *f*-number illumination system and its application to projection display has been investigated. The Ètendue formula of an elliptic-shaped illumination-pupil has been derived. This formula can be used to estimate the optical collection efficiency before designing the illumination optics. Illustrations based on classical Cooke triplet and potential application to a DMD™ projector system has been provided.

It should be noted that the dual *f*-number optical system design could also be applied to any on-axis or off-axis projection-lens or camera-lens systems with not only the higher illumination but also the lower aberrations of coma and astigmatism on the image plane by the elliptic-shaped diaphragm. The design presented here also infers the possibility and feasibility of the multiple *f*-numbers and the anamorphic illumination pupil or diaphragm in the optical system.

Chapter 8

Conclusions and future works

8.1 Conclusions

We develop either an analytical or a semi-analytical model by the use of optical transfer function (OTF) and illumination formations and put emphasis on the study of imaging and non-imaging qualities in the incoherent imaging system. Since the illumination light could vary the intensity distribution of the reflective light from an object, we could no longer assume the OTF or MTF of the object equal to unity in an imaging system. In this thesis, we make the in-depth investigation into the relationship between OTF and the illumination light distribution by calculating the OTF using the pupil function with the amplitude transmittance function $T'(x, y)$ in Eq. (2-1) and the wave aberration function $W(x, y)$ in Eq. (2-2). The amplitude transmittance function $T'(x, y)$ stands for the term given to the characteristic of a non-imaging system. The wave aberration function stands for the term given to the characteristic of an imaging system. One of main contributions of this thesis is to implement and demonstrate the effective factor of the non-imaging system (i.e., illumination light) in OTF calculation for assessing and specifying the performance of the imaging system.

Then, a new approach for extending the depth of focus (EDOF) in an incoherent imaging system with a programmable shaped pupil using structured light has been demonstrated, which provides the connection between non-imaging and imaging systems for enhancing the image quality in the conventionally incoherent imaging systems such as light pipe, photography, microscopy and projector with

embedded illumination modulator. We calculated the OTFs and illumination formations, and analyzed the optical performances for the following four subjects.

A. Subject-1: Optical transfer functions for the specific-shaped apertures generated by illumination with a rectangular light pipe

The pupil function and the corresponding OTFs of the specific shaped aperture generated by illumination with a rectangular hollow light pipe have been investigated in the aberration-free and defocused optical systems, respectively. In conclusion, (1) the OTF values of the even-peak frequencies can decrease when the size of the Lambertian light source decreases, (2) if there are a total of $n \times n$ individual apertures within the pupil, then there are n near-periodical peaks on the OTF curve. (3) The OTF's values remain almost unchanged with the different length of the light pipe, (4) the geometric structure of the light pipe does not affect the resolution limit of the optical system, and the case of the defocused system can coincide with that of the aberration-free system under the condition of a larger defocused coefficient ω_{20}.

B. Subject -2: Programmable apodizer in incoherent imaging system using a digital micromirror device

We have provided a new approach for improving the image quality for the incoherent imaging systems, including photography, projector and microscopy, with a specific illuminator modulator. The semi-analytical results using the optical transfer function (OTF) indicated that the depth of focus can be extended with specifically shaped illumination, which is generated by a digital micromirror device or LED array, on the aperture stop in the imaging system with a specific defocus coefficient, and the specific coefficients for spherical aberration and coma aberration. It has been shown that a shaped pupil with a scale ratio K equal to 0.05 is more helpful for extending the

depth of focus at low spatial frequency, while a shaped pupil with a scale ratio K equal to 0.3 is more useful for extending the depth of focus at high spatial frequency. Furthermore, the image quality could not be significantly influenced as the fill factor (i.e. aperture ratio) of the spatially shaped pupil varied from 100% to 80%.

C. Subject -3: Illuminance formation and color-difference of mixed-color LEDs in a rectangular light pipe: an analytical approach

An analytical method of illuminance formation generated by illumination using a rectangular hollow light pipe and mixed-color LEDs were investigated. The corresponding ANSI light uniformity, ANSI color uniformity and color-difference were derived for single LED and multi mixed-color LEDs. The analytical results indicate that the distributions of illuminance and color-difference vary with the different geometric structures of the light pipes and the location of the light sources. Both ANSI light and color uniformities at the exit plane of the light pipe with mixed-color LED light sources can be reduced exponentially by increasing the length of the light pipe, but can be increased exponentially by increasing the height ratio *b/a* of the light pipe. In the case of the length scale L/A being greater than unity, the mixed-color LED sources on the entrance plane are uniformly illuminated with the acceptable uniform brightness and color images.

D. Subject -4: Design of a dual-*f*-number illumination system and its application to DMD™ projection displays

The design of a dual-F-number illumination system and its application to projection display has been investigated. The Ètendue formula of an elliptic-shaped illumination-pupil was derived. This formula can be used to estimate the optical collection efficiency before designing the illumination optics. Illustrations based on

classical Cooke triplet and potential application to a DMD™ projector system has been provided.

8.2 Future works

In this thesis, we have analytically and numerically demonstrated the feasibility of extending the depth of focus with structure light (i.e. non-imaging illumination) on the aperture stop in the incoherent imaging system by the use of the pupil function and the optical transfer function. Furthermore, an analytical model of the non-imaging system by the use of illumination formations has also been demonstrated. The preliminary results as described in this thesis could provide us either analytical or semi-analytical tools for optimization and simulation in designing an advanced optical system with the imaging lens system and the embedded illumination modulator before we start the experiment. The explorations of the algorithm development in optical optimization and simulation, and its implement in the experiments and real optical devices will be my future works. We propose three primary directions extending our previous works as follows, and the roadmap of my future works is shown in Fig 8-1.

(1) Toward an entirely analytical model for optimization in optical design:

In our previous study, only an analytical or semi-analytical model using OTFs and pupil functions was discussed, and the image quality of the imaging system was investigated just with defocus, spherical and coma aberrations. While exploring to realistic situation, we have to consider more monochromic aberrations such as astigmatism, field curvature and distortion, and chromatic aberrations such as longitudinal color and lateral color for a real optical system in our analysis model. Besides image evaluation, the optimization algorithm should be further developed for dealing with the more and more complicated and compact optical system design

including imaging and non-imaging, for example, how to connect between the scale ratio *K* (a term of non-imaging property) and OTF (a term of imagining performance) will be a critical issue in optical design and optimization.

(2) Toward an experimental analysis on image evaluation in the conventionally imaging systems:

In this thesis, we just demonstrated our research and development using the numerical approach and computed image processing without the experimental verification although we believe the numerical support and exploration will also help the clarification. We understand the importance of experimental realization of proposed schemes, and therefore we will plan a serious of experimental analyses on modulation-transfer-function (MTF) measurement and image evaluation in the conventionally imaging systems especially for photography and microscopy with an imaging system and the specific illumination modulator with the characteristics of either incoherent or coherent light.

(3) Toward new implements and applications in medical imaging of *BioOptics*:

Medical imaging is the state-of-the-art technology to provide two- or three-dimensional images of the living body for clinical purposes or medical science. Imaging studies can diagnose disease or dysfunction from outside the body, providing information without exploratory surgery or other invasive and possibly dangerous diagnostic techniques. In the field of *BioOptics*, medical imaging incorporates medical photography and microscopy, endoscopy, optical coherence tomography, ophthalmoscopy and so on. Since most of observed organs and tissues are three-dimensional objects, the extending the depth of image field is necessarily required in medical imaging system design. From the point of view of potential

applications, as well as from a purely academic perspective, it will be worthwhile to explore new approaches to extending the depth of focus (EDOF) leveraging with our previous works on embedded illumination modulator for optically medical imaging systems in the future.

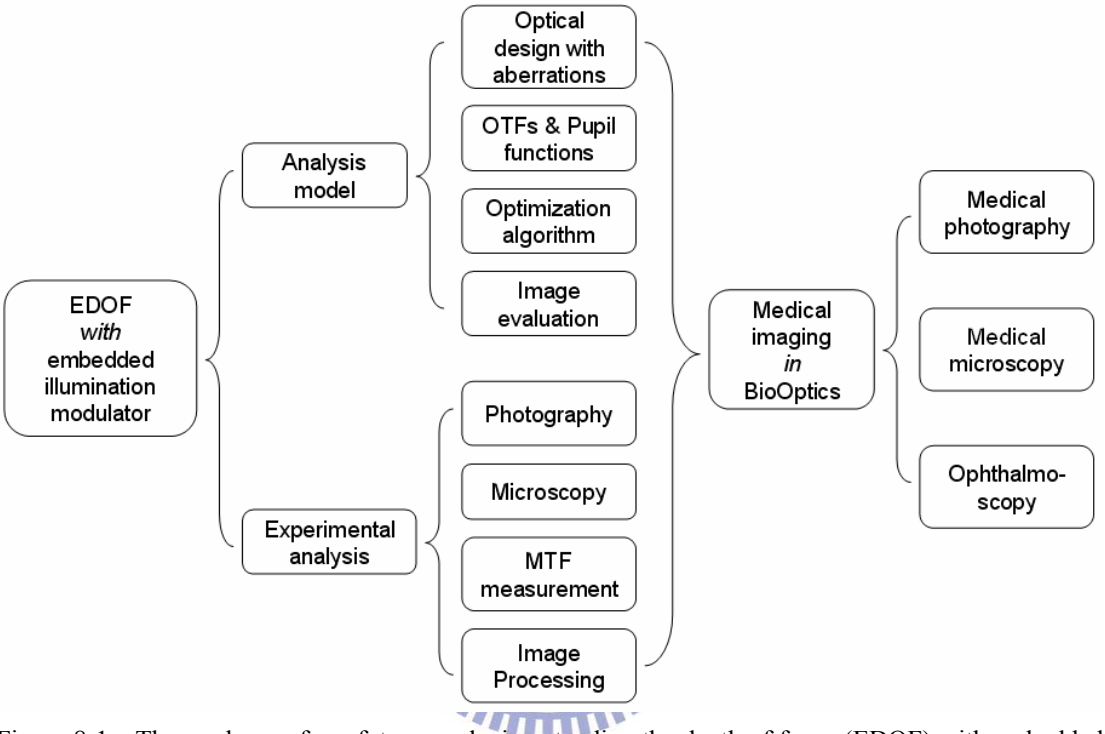

Figure 8-1 The roadmap of my future works in extending the depth of focus (EDOF) with embedded illumination modulator.

Reference

1. J. W. Goodman, *Introduction of Fourier Optics*, 3rd. ed. (Roberts & Company, 2005).
2. V. N. Mahajan, *Optical Imaging and Aberrations, Part II. Wave Diffraction Optics*, (SPIE Press Book, 2001).
3. J. Ojeda-Castaneda, P. Andrea, and A. Diaz, "Annular apodizers for low sensitivity to defocus and to spherical aberration," Opt. Lett. **1**1, 487 (1986).
4. J. Ojeda-Castaneda, L. R. Berriel-Valdos, and E. L. Montes, "Bessel Annular Apodizers: Imaging Characteristics," Appl. Opt. **26**, 2770 (1987).
5. L. N. Hazra and A. Guha, "Far-Field Diffraction Properties of Radial Walsh Filters," J. Opt. Soc. Am. **A 3**, 843 (1986).
6. M. Mino and Y. Okano, "Improvement in the OTF of a Defocused Optical System Through the Use of Shaded Apertures," Appl. Opt. 10, 2219 (1971).
7. C. S. Chung and H. H. Hopkins, "Influence of Nonuniform Amplitude on the Optical Transfer Function," Appl. Opt. 28, 1244 (1989).
8. E. R. Dowski, Jr. and W. T. Cathey, "Extended depth of field through wave-front coding," Appl. Opt. 34, 1859 (1995).
9. J. van der Gracht, E. R. Dowski, M. G. Taylor, and D. M. Deaver, "Broadband behavior of an optical-digital focus-invariant system," Opt. Lett. 21, 919 (1996).
10. E. Reinhard, G. Ward, S. Pattanaik, and P. Debevec, "High Dynamic Range Imaging: Acquisition, Display, and Image-Based Lighting" (The Morgan Kaufmann Series in Computer Graphics, 2006).
11. G. Petschnigg, R. Szeliski, M. Agrawala, M. Cohen, H. Hoppe, and K. Toyama, "Digital photography with flash and no-flash image pairs", in *Proceedings of the*

2004 SIGGRAPH Conference, (Association for Computing Machinery, New York, 2004), pp. 664-672.

12. E. Eisemann and F. Durand, "Flash photography enhancement via intrinsic relighting", in *Proceedings of the 2004 SIGGRAPH Conference*, (Association for Computing Machinery, New York, 2004), pp. 673-678.
13. W. Cassarly, "Non-imaging Optics: Concentration and Illumination", in *OSA Handbook of Optics,* 2nd edition, Vol. III (McGraw-Hill, New York, 2001), pp. 2.28-2.32.
14. C. M. Chang and H. P. D. Shieh, "Design of illumination and projection optics for projectors with single digital micromirror device," Appl. Opt. **39**(19), 3202-3208 (2000).
15. W. N. Partlo, P. J. Tompkins, P. G. Dewa, and P. F. Michaloski, "Depth of focus and resolution enhancement of i-line and deep-UV lithography using annular illumination," *Proc. SPIE*, **1927**, 137-157 (1993).
16. H. H. Hopkins, "Physics of the fiberoptics endoscope," in Endoscopy, G. Berci, ed. (Appleton-Century-Croft, New York, 1976), pp27-63.
17. T. Hough, J. F. V. Derlofske, and L. Hillman, "Management of light in thick optical waveguides for illumination: an application of radiometric principles," *SAE Technical Paper Series*, 940512 (1994).
18. W. J. Smith, *Modern Optical Engineering* (McGraw-Hill, New York, 2000).
19. Y. K. Cheng and J. L. Chern, "Irradiance Formation in Hollow Straight Light Pipes with Square and Circular Shapes," J. Opt. Soc. Am. **A 23**, 427-434 (2006).
20. D. G. Pelka and K. Patel, "Invited Paper: an Overview of LED Applications for General Illumination," *Proc. SPIE*, **5186**, 15-26 (2003).
21. J. F. V. Derlofske and T. A. Hough, "Analytical model of flux propagation in light pipe system, " Opt. Eng. (Bellingham) **43**, 1503-1510 (2004).

22. E. H. Stupp and M. S. Brennesholtz, *Projection Display*, (John Wiley & Sons, England, 1999).

23. T. Nakano and Y. Tamagawa "Design of a wide-angle fast optical system with anamorphic mirrors," in *International Optical design Conference 2002*, Proc. SPIE **4832**, 502-509 (2002).

24. S. Magarill, "Optical system for projection display," US patent #5,552,922 (12 April, 1993).

25. S. Shikama, H. Suzuki and K. Teramoto "Optical system of ultra-thin rear projector equipped with refractive-reflective projection optics," in *SID 02 digest*, 1250-1253 (2002).

26. W. T. Welford and R. Winston, *High Collection Non-imaging Optics*, (Academic, San Diego, 1989).

27. R. McCluney, *Introduction to Radiometry and Photometry* (Artech house, Inc. 1994).

28. G. Wyszecki and W. S. Stiles, *Color Science- Concept and Methods, Quantitative Data and Formulae* (John Wiley & Sons, 2000), Chap. 3, pp. 143-167.

29. W. J. Cassarly, "The art of making efficient illuminator design fun," *Proc. SPIE*, **5186**, 1-4 (2003).

30. F. Zhao, N. Narendran, and J. F. V. Derlofske, "Optical elements for mixing colored LEDs to create white light", *Proc. SPIE*, **4776**, 206-214 (2002).

31. See http://www.bowerusa.com/catalog.php?item=300%7C331.

32. See http://en.wikipedia.org/wiki/Digital_single-lens_reflex_camera.

33. See http://www.bunchware.de/html/optoma_ep755.htm.

34. See http://zeiss-campus.magnet.fsu.edu/articles/lightsources/lightsourcefundamentals.html.

35. See http://micro.magnet.fsu.edu/primer/anatomy/kohler.html.

36. T. L. Williams, *The optical transfer function of imaging systems*, (Taylor & Francis, 1999).

37. H. H. Hopkins, " The Frequency Response of a Defocused Optical system," *Proc. Roy. Soc.* (London) **A231**, 91 (1955).

38. American National Standard for Audiovisual Systems- Electronic Projection- Fixed Resolution Projectors, ANSI/NAPM IT7.228-1997 (American National Standards Institute, 1997).

39. M. S. Brennesholtz, "Light collection efficiency for light valve projection systems," in *Projection Display II*, M. H. Wu, ed., Proc. SPIE **2065**, 71-79 (1996).

40. J. W. Harris and H. Stocker, *Handbook of Mathematics and Computational Science,* (Springer-Verlag, New York, 1998).

41. Mathematica version 4, Wolfram Research, Inc., 100 Trade Center Drive Champaign, IL 61820-7237, USA.

42. See http://www.microscopyu.com/articles/optics/mtfintro.html.

43. See http://www.bobatkins.com/photography/technical/mtf/mtf2.html.

44. See http://en.wikipedia.org/wiki/1951_USAF_resolution_test_chart.

45. E. M Sabatke and J. H. Burge "Basic Principles in the Optical Design of Imaging Multiple Aperture systems," in *International Optical design Conference 2002*, Proc. SPIE **4832**, 236-248 (2002).

46. R. Barakat, " Diffraction Electromagnetic Fields in the Neighborhood of the Focus of Paraboloidal Mirror Having a Central Obscuration, " Appl. Opt. **26**, 3790 (1987).

47. E. Hecht, *Optics* (Addison Wesley, 2002) pp. 543-544.

48. H. H. Hopkins and M. J. Yzuel, “The Computation of Diffraction Patterns in the Presence of Aberrations,” *Opt. Acta* **17**, 157 (1970).

49. H. H. Hopkins, “ Calculation of the Aberration and Image Assessment for a General Optical System, “ *Opt. Acta* **28**, 667 (1981).

50. J. A. Davis, J. C. Escalera, J. Campos, A. Marquez, and M. J. Yzuel, “Programmable axial apodizing and hyperresolving amplitude filters with a liquid-crystal spatial light modulator,” Opt. Lett. **24**, 628 (1999).

51. A. Marquez, C. Iemmi, J. Campos, J. C. Escalera, and M. J. Yzuel, “Programmable apodizer to compensate chromatic aberration effects using a liquid-crystal spatial light modulator,” Opt. Exp. **13**, 716 (2005).

52. D. Dudley, W. Duncan, J. Slaughter, “Emerging Digital Micromirror Device (DMD) Application,” in *MOEMS Display and Imaging Systems*, Proc. SPIE **4985**, 14-15 (2003).

53. F. Bernardini and H. E. Rushmeier, “The 3D Model Acquisition Pipeline”, in *Comput. Graph. Forum*, (Eurographics Association and Blackwell Publisher, 2002), pp. 149-172.

54. B. Curless, “From Range Scans to 3D Models”, ACM SIGGRAPH Computer Graphics, **33**, 38–41 (2000).

55. M. A. A. Neil, R. Juskaitis, and T. Wilson, "Method of obtaining optical sectioning by using structured light in a conventional microscope," Opt. Lett. 22, 1905-1907 (1997).

56. See http://www.stockeryale.com/i/lasers/structured_light.htm.

57. See http://mesh.brown.edu/3DPGP-2009/homework/hw2/hw2.html.

58. L. J. Hornbeck, “Digital light processing for high-brightness, high resolution applications,” in Projection Display III, M. H. Wu, ed., Proc. SPIE **3013**, 27-40 (1997).

59. Y. Kwak and L. MacDonald, “Characterisation of a desktop LCD projector”, Display, **21**, 179-197 (2000).

60. See http://www.eronn.net/camera/test-chart.

61. See http://www.osram-os.com/ostar-projection/technical.php.

62. G. H. Moss, R.G. Fielding, M. Kavanagh, and B. R. Critchley, “A high-luminance large-screen projection system using the digital micromirror device (DMD),” *in SID ’96 International Symposium Digest of Technical Papers* (Society for Information Display, Santa Ana, Calif., 1996), pp. 907-910.

63. M. Laikin, *Lens design*, (Marcel Dekker, Inc. New York, 1990).

64. S. K. Eckhardt, “Fixed-focus triplet projection lens for overhead projectors,” US patent # 5,596,455 (1997).

65. OSLO version 6.2, Lambda Research Corporation, 25 porter road, Littleton, Massachusetts.

66. Peter J. Janssen and Jeffrey A. Shimizu, "High contrast illumination system for video projector," US patent #5,442,414 (1994).

67. D. Scott Dewald, D. J. Segler, and Steven M. Penn, "Advances in contrast enhancement for DLP projection displays", *J. Soc. Inf. Display* **11**, 177 (2003).

68. C. M. Cheng and Y.-H. Kang, “Illumination system and method for improving asymmetric projection,” T.W. patent No. 90,128,276 (2002).

69. C. M. Cheng and Y.-H. Kang, “Illumination system and method for improving asymmetric projection,” US patent No. 7,290,886.

70. ASAP version 6.6, Breault Research Organization, Inc., 6400 East Grant Road, Tucson, Ariz. 85715, USA.

71. Radiant Source™ models and Prosource ™, Radiant Imaging, Inc., 15321 Main St. NE, Suite 310 PO Box 5000 Duvall, WA 98019.

Author's Biography

姓　名	鄭竹明	學　號	9224817	
學　歷	交通大學光電工程研究所 博士班			
經　歷	揚明光學股份有限公司 資深研發處長 從事微型投影機技術與產品研發工作 12 年			
E-mail	chuming.eo92g@nctu.edu.tw ; stsfanc@ms47.hinet.net			
指導教授	陳志隆 教授			
論文題目	成像與非成像光學系統之光學傳遞函數分析與應用 Optical transfer function and its applications to imaging and non-imaging optical systems			
專利著作	台灣專利: 56 篇、美國專利: 11 篇、中國大陸專利: 17 篇，共計 84 篇			
得獎紀錄	1. 98 年『國家發明創作獎』發明金牌獎(個人) –數位光源處理投影裝置。 2. 94 年『國家發明創作獎』發明銀牌獎(個人)–顯示裝置之投影方法。			

Publication List

Journal Papers

1. **C. M. Cheng** and J. L. Chern, "Projection quality improvement with embedded illumination modulator in projector system," Appl. Opt. **49**, 3128-3139 (2010).
2. **C. M. Cheng** and J. L. Chern, "Programmable apodizer in incoherent imaging systems using a digital micromirror device", Opt. Eng. **49**, 023201 (2010).
3. **C. M. Cheng** and J. L. Chern, " Illuminance formation and color-difference of mixed-color LEDs in a rectangular light pipe: an analytical approach," Appl. Opt. **47**, 431-441 (2008)
4. **C. M. Cheng** and J. L. Chern, "Optical transfer functions for specific-shaped apertures generated by illumination with a rectangular light pipe," J. Opt. Soc. Am. **A 23**, 3123-3132 (2006).
5. **C. M. Cheng** and J.-L. Chern, "Design of a dual- *f* -number illumination system and its application to projection display with DMD™," J. Soc. Inf. Disp. **14**, 819-827 (2006).